Christian Landfester

Development of a High-Speed Annular Sector Cascade

for Film Cooling Measurements in Nozzle Guide Vanes with Contoured Endwalls

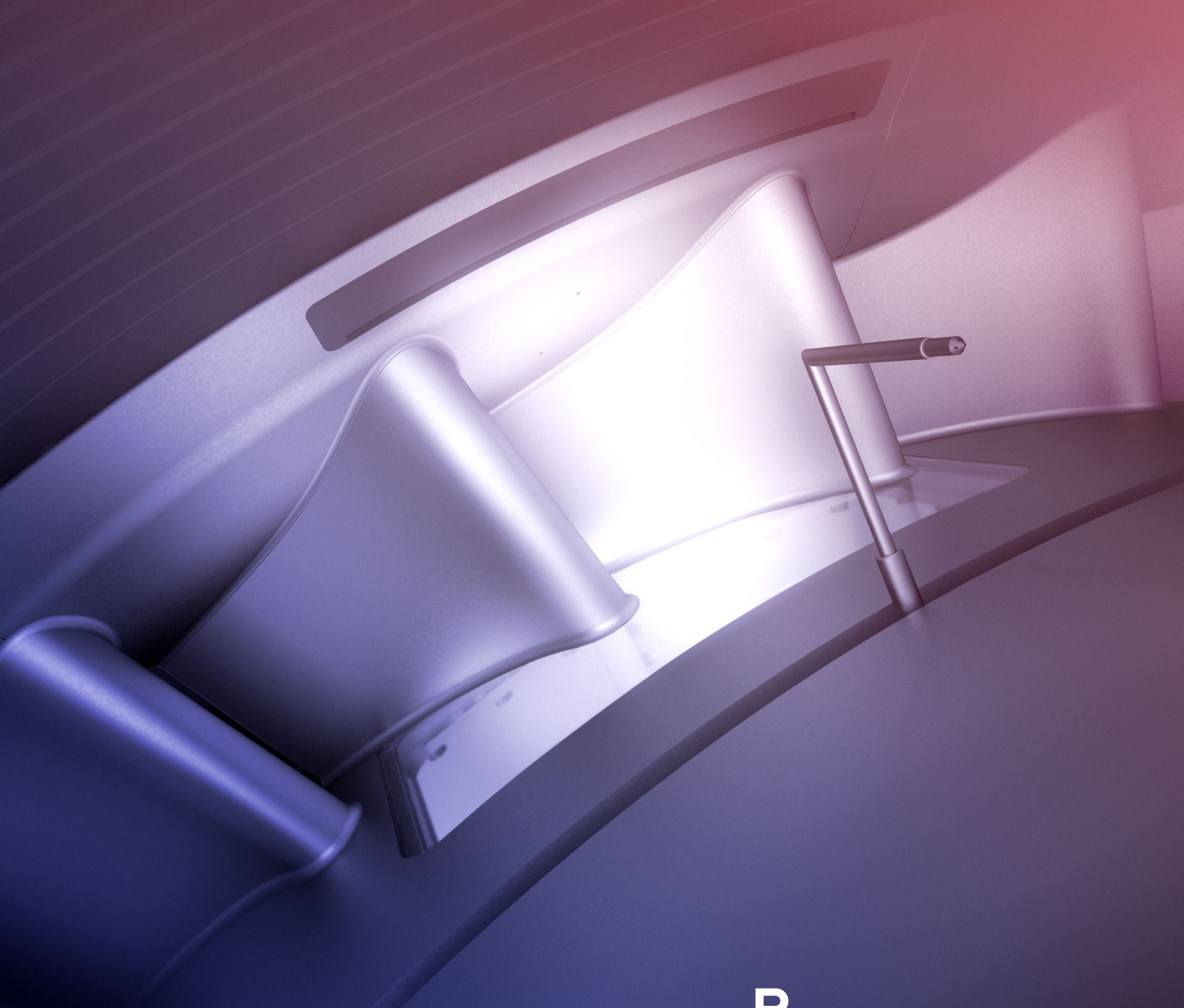

RPTU Rheinland-Pfälzische Technische Universität Kaiserslautern Landau

Development of a High-Speed Annular Sector Cascade for Film Cooling Measurements in Nozzle Guide Vanes with Contoured Endwalls

Vom Fachbereich Maschinenbau und Verfahrenstechnik
der Rheinland-Pfälzischen Technischen Universität Kaiserslautern-Landau
zur Verleihung des akademischen Grades

Doktor-Ingenieur (Dr.-Ing.)
genehmigte
Dissertation

von
Christian Landfester, M.Sc.
aus Neuwied

Tag der Einreichung:	27.02.2023
Tag der mündlichen Prüfung:	23.05.2023

Dekan des Fachbereichs:	Prof. Dr. rer. nat. Roland Ulber
Vorsitz der Kommission:	Prof. Dr.-Ing. Erik von Harbou
Erster Berichterstatter:	Prof. Dr.-Ing. Marin Böhle
Zweiter Berichterstatter:	Prof. Dr.-Ing. habil. Alexander Wiedermann

D 386

Herausgeber:
Rheinland-Pfälzische Technische Universität Kaiserslautern-Landau
Lehrstuhl für Strömungsmechanik und Strömungsmaschinen
Prof. Dr.-Ing. Martin Böhle
Gottlieb-Daimler-Straße
67663 Kaiserslautern

Verfasser:
Christian Landfester

Druck:
Print Simply GmbH
Berner Straße 38
60437 Frankfurt am Main

Acknowledgements

I would like to express my sincere gratitude to all those who have contributed to the successful completion of this dissertation during my tenure as a research assistant at the Institute of Fluid Mechanics and Turbomachinery at the University of Kaiserslautern-Landau, formerly the University of Kaiserslautern.

First, I am grateful to my academic supervisor, Prof. Dr.-Ing. Martin Böhle, for his constant support, guidance, and permissiveness regarding the development of my research work. I am thankful for the opportunity to work at his institute's high-speed turbine test rig. I would also like to thank Prof. Dr.-Ing. habil. Alexander Wiedermann for his kind interest in my work and the spot-on remarks. I am also grateful to Prof. Dr.-Ing. Erik von Harbou for chairing the examination committee.

Additionally, I would like to acknowledge Prof. Dr.-Ing. Robert Krewinkel for his extended and unwavering support, technical expertise, and diligent proofreading of this dissertation. I am also grateful to Dr.-Ing. Clemens Domnick for his scientific advice and assistance in navigating the various intricacies of numerical problems.

Furthermore, I would like to express my appreciation to Dr.-Ing. Roman Franze for his pioneering work in developing and constructing the first version of the high-speed turbine test rig. I am also grateful to my former and current colleagues for the stimulating conversations, their valuable feedback, and their support throughout my research.

I would like to further thank the student assistants Sebastian Schmoll, Sebastian Bellaire, Yannick Nicola, Prinon Chowdhury, Maximilian Kölzer, and Tim Ettrich for their help in setting up the test rig and performing the measurements. Moreover, I would like to thank the metal and electronics workshops, especially Michael Dunkel, Roger Edrich, Pascal Fleischmann, Willi Giebler, Jochen Hoffmann, Kevin Müller, Jörg Neufing, Mike Schneider, and Matthias Piechaczek for their support.

Constructing and operating the test rig was not only challenging but also very costly: Therefore, I would like to acknowledge the financial support of MAN Energy Solutions and AG Turbo over the past years.

Last but not least, I would like to thank my long-time project partner, Dr.-Ing. Gunther Müller, who has always reminded me not to neglect private matters in the struggle to make progress on the project.

Kaiserslautern, June 2023 Christian Landfester

Abstract

Facing the demands of the energy transition, gas turbines require continuous development to improve thermal efficiency. Since this can be achieved by further increasing the turbine inlet temperature, advanced cooling techniques are required to protect the highly loaded turbine components. This includes the first nozzle guide vane, which is located just downstream of the combustion chamber. Film cooling, i.e., injecting coolant into the hot-gas path, has been a cornerstone of turbine cooling. While the coolant film is typically supplied through discrete cooling holes, design-related gaps, e.g., the purge slot between the transition duct and the vane platform, can be utilized for injecting coolant. Since the coolant is drawn from the compressor, potentially offsetting thermal efficiency gains from increased turbine inlet temperatures, efficient use of the coolant is critical. In this context, experimental data obtained under engine-like flow conditions, i.e., matching the Mach and Reynolds numbers that are present in the engine, are indispensable for assessing the film cooling performance. Existing research on upstream slot injection has a blind spot, as all high-speed studies were conducted in linear cascades. This approach neglects, by principle, the influence of the radial pressure gradient that naturally occurs in swirling flows and potentially affects coolant propagation. Therefore, a high-speed annular sector cascade has been developed: It allows testing the film cooling performance and aerodynamic effects of coolant flows from various upstream slot configurations, not only at engine-like Mach and Reynolds numbers but also considering the radial pressure gradient. The cascade is equipped with nozzle guide vanes with contoured endwalls representing state-of-the-art turbine design. The results to be expected from the test rig are, therefore, of great relevance.

The annular sector cascade is integrated into the existing high-speed turbine test facility at the Institute of Fluid Mechanics and Turbomachinery (University of Kaiserslautern-Landau), which was previously used for testing a linear cascade with the same nozzle guide vane design. It incorporates various measurement techniques such as five-hole probes, pressure-sensitive paint, and infrared thermography to investigate both the thermal and aerodynamic aspects of film cooling. This thesis provides a detailed description of the cascade development, starting from the aerodynamic design up to the structural implementation. It also includes the results of the previous measurements in the linear cascade, as they provided the basis for refining the measurement methods.

Kurzfassung

Im Zuge der Energiewende müssen Gasturbinen fortwährend weiterentwickelt werden, um den thermischen Wirkungsgrad zu verbessern. Da dies durch eine weitere Erhöhung der Turbineneintrittstemperatur erreicht werden kann, sind fortschrittliche Kühltechniken erforderlich, um die hochbelasteten Turbinenkomponenten zu schützen. Dies schließt die erste Leitschaufelreihe ein, die sich unmittelbar stromabwärts der Brennkammer befindet. Die Filmkühlung, d. h. die Einleitung von Kühlluft in den Heißgaspfad, ist ein Eckpfeiler der Turbinenkühlung. Während der Kühlfilm in der Regel durch diskrete Kühlbohrungen zugeführt wird, können auch konstruktiv bedingte Spalten, z. B. der Spalt zwischen dem Übergangsstück und der Leitschaufelplattform, für die Einleitung von Kühlluft genutzt werden. Da diese aus dem Verdichter entnommen werden muss und somit den Effizienzgewinnen aus der Erhöhung der Turbineneintrittstemperaturen entgegensteht, ist eine effiziente Nutzung der Kühlluft von großer Bedeutung. Hierbei sind experimentelle Daten, die unter maschinenähnlichen Bedingungen, d. h. bei ähnlichen Mach- und Reynolds-Zahlen, gewonnen wurden für die Bewertung der Kühlleistung unerlässlich. Die bisherige Forschung zur Einleitung von Kühlluft aus stromaufwärts gelegenen Spalten weist einen blinden Fleck auf, da sämtliche Untersuchungen unter kompressiblen Strömungsbedingungen in linearen Kaskaden durchgeführt wurden. Dieser Ansatz vernachlässigt prinzipiell den Einfluss des radialen Druckgradienten, der in drallbehafteten Strömungen naturgemäß auftritt und die Kühlmittelausbreitung potenziell beeinflusst. Daher wurde eine gekrümmte Kaskade entwickelt, mit der die Kühlwirkung und die aerodynamischen Effekte von Kühlluftströmungen aus verschiedenen Spaltkonfigurationen nicht nur bei maschinenähnlichen Mach- und Reynoldszahlen, sondern auch unter Berücksichtigung des radialen Druckgradienten untersucht werden sollen. Die Kaskade ist mit konturierten Leitschaufeln ausgestattet, die dem neuesten Stand der Turbinentechnik entsprechen. Die zu erwartenden Ergebnisse des Prüfstandes sind daher von großer Relevanz.

Die Kaskade wurde in den High-Speed-Turbinenprüfstand am Lehrstuhl für Strömungsmechanik und Strömungsmaschinen (RPTU Kaiserslautern-Landau) integriert, der zuvor für die Untersuchung einer linearen Kaskade mit identischem Leitschaufeldesign verwendet wurde. Die vorliegende Arbeit beschreibt die Entwicklung der gekrümmten Kaskade, beginnend mit der aerodynamischen Optimierung bis hin zur konstruktiven Umsetzung. Sie schließt auch die Ergebnisse der vorangegangenen Messungen an der linearen Kaskade ein, da sie die Grundlage für die Optimierung der Messmethoden bildeten.

Contents

Nomenclature

Lower Case Latin Symbols

c	$\mathrm{m\,s^{-1}}$	Velocity
d	mm	Diameter
h	$\mathrm{W\,m^{-2}\,K^{-1}}$	Heat transfer coefficient
h	mm	Span
k	-	Five-hole probe coefficient
k_1	$\mathrm{m^2}$	Permeability
k_2	$\mathrm{m^{-1}}$	Non-Darcy flow coefficient
l	mm	Length
$\dot{m}$	$\mathrm{kg\,s^{-1}}$	Mass flow
m	mm	Module
p	Pa	Pressure
$\dot{q}$	$\mathrm{W\,m^{-2}}$	Heat flux
r	mm	Radius
r	-	Radial coordinate (cylindrical)
s	mm	Pitch
s	-	Safety factor
t	mm	Thickness
w	mm	Width
x	-	Axial coordinate (cartesian, cylindrical)
y	-	Pitchwise coordinate (cartesian)
y^+	-	Dimensionless wall distance
z	-	Spanwise coordinate (cartesian)

Upper Case Latin Symbols

A	-	First Stern-Volmer coefficient
A	$\mathrm{m^2}$	Area

B	-	Second Stern-Volmer coefficient
BR	-	Blowing ratio
C	mm	Chord length
C	-	Third Stern-Volmer coefficient
C	-	Concentration, mass fraction
C_1	$\mathrm{W\,m^2}$	First radiant constant
C_2	$\mathrm{m\,K}$	Second radiant constant
D	-	Fourth Stern-Volmer coefficient
DR	-	Density ratio
E	$\mathrm{W\,m^{-2}}$	Emissive power
I	-	Momentum flux ratio
I	counts	Intensity
K	mm	Equivalent sandgrain roughness
L	mm	Slot distance to leading edge
M	$\mathrm{W\,m^{-2}\,\mu m^{-1}}$	Spectral exitance
M	mm	Mesh size
M	Nm	Torque
Ma	-	Mach number
MFR	%	Mass flux ratio
$NHFR$	-	Net heat flux reduction
Nu	-	Nusselt number
P	W	Power
Pe_β	-	Periodicity benchmark: inlet pitch angle
$Pe_{\dot{m}}$	-	Periodicity benchmark: mass flow
Pe_{Ma}	-	Periodicity benchmark: Mach number
Pe_F	-	Periodicity benchmark: loading
ΣPe	-	Aggregated periodicity benchmark
Pr	-	Prandtl number
Re	-	Reynolds number
SP	-	Value span
T	K	Temperature
Tu	%	Turbulence level
W	mm	Slot width
W	$\mathrm{g\,mol^{-1}}$	Molecular weight

Lower Case Greek Symbols

α	$^\circ$	Slot angle
α	-	Deflection ratio
β	$^\circ$	Pitch angle
β	-	Open-area ratio
β	%	Porosity
ϵ	-	Emissivity
η	-	Film cooling effectiveness
η	-	Mechanical efficiency
γ	$^\circ$	Yaw angle
γ	-	Isentropic exponent
κ	$\mathrm{W\,m^{-1}\,K^{-1}}$	Thermal conductivity
λ	$^\circ$	Stagger angle
λ	nm	Wavelength
λ_p	-	Pipe friction factor
μ	Pa s	Dynamic viscosity
μ	-	Friction coefficient
ν	$^\circ$	Porous-fluid interface opening angle
ρ	$\mathrm{kg\,m^{-3}}$	Density
ρ	$^\circ$	Probe angle
ρ	-	Reflectivity
σ	-	Standard deviation
τ	-	Transmissivity
τ	-	Transmission ratio
φ	$^\circ$	Circumferential direction (cylindrical)
ζ	-	Total pressure loss coefficient

Upper Case Greek Symbols

Φ	W	Radiant flux
Π	-	Pressure ratio
Θ	-	Dimensionless temperature ratio

Subscripts

$\square_{0}$	Uncooled
$\square_{5h}$	Five-hole probe
$\square_{0...5}$	Pressure taps of five-hole probe
$\square_{a}$	Ambient
$\square_{ad}$	Adiabatic
$\square_{air}$	Air as coolant
$\square_{AW}$	Auxiliary wall
$\square_{ax}$	Axial
$\square_{b}$	Black image
$\square_{b}$	Base plate
$\square_{baf}$	Baffle
$\square_{BB}$	Black body
$\square_{\beta}$	Pitch angle
$\square_{BL}$	Boundary layer
$\square_{c}$	Coolant
$\square_{ch}$	Channel
$\square_{cl}$	Cooling liquid
$\square_{CP}$	Cover plate
$\square_{Cu}$	Copper
$\square_{EP}$	Evaluation plane
$\square_{ETFE}$	Ethylene tetrafluoroethylene
$\square_{ex}$	Extension
$\square_{f}$	Cooled
$\square_{fg}$	Foreign gas as coolant
$\square_{fl}$	Fluid
$\square_{g}$	Grid
$\square_{\gamma}$	Yaw angle
$\square_{h}$	Hub
$\square_{in}$	Inlet
$\square_{is}$	Isentropic
$\square_{m}$	Mainstream
$\square_{M}$	Stepper motor
$\square_{MFA}$	Mass-flow average
$\square_{max}$	Maximum
$\square_{mid}$	Midspan
$\square_{min}$	Minimum
$\square_{o}$	Infrared optics

$\square_{O_2}$	Oxygen
$\square_{off}$	Offset
$\square_{out}$	Outlet
$\square_{p}$	Pressure
$\square_{p}$	Peak
$\square_{r}$	Recovery
$\square_{R}$	Annular gear rack
$\square_{REF}$	Reference
$\square_{ref}$	Reference image
$\square_{s}$	Shroud
$\square_{s}$	Static
$\square_{s}$	Screen
$\square_{S}$	Sensor driving gear
$\square_{S\text{-}S}$	Solid-solid interface
$\square_{\Sigma}$	Weighted average
$\square_{sl}$	Slot
$\square_{t}$	Total
$\square_{T}$	Traverse driving gear
$\square_{tb}$	Tailboard
$\square_{w}$	Wall
$\square_{W}$	Worm gear box
$\square_{ZnS}$	Zinc sulfide

Superscripts and Accent Marks

$\square'$	Axial projection
$\square''$	Probe plane projection
$\overline{\square}$	Area average/arithmetic mean
$\widetilde{\square}$	Lateral average

Lower Case Abbreviations

ann	Annular
ax	Axisymmetric
bd	Blow down
bfs	Backward facing step
ffs	Forward facing step

fl	Flat
hs	High speed
lin	Linear
ls	Low speed
n-ax	Non-axisymmetric
ns	No step
ol	Open loop
rd	Rounded
sp	Sharp

Upper Case Abbreviations

5HP	Five-hole probe
BA-IN	Initial geometry
CHT	Conjugate heat transfer
sCMOS	Scientific complementary metal–oxide semiconductor
DN	Nominal pipe size
EP	Evaluation plane
ETFE	Ethylene tetrafluoroethylene
FEM	Finite element method
FIN	Final geometry
HW	Hot wire
IR	Infrared
L2F	Laser-2-focus
LDA	Laser Doppler anemometry
LE	Leading edge
LED	Light-emitting diode
LIF	Laser-induced fluorescence
LTE	Lower trailing edge
MJP	Multijet printing
N 1…4	Vane 1 to 4
NGV	Nozzle guide vane
OP	Operating point
P	Passage
PIV	Particle image velocimetry
PN	Pipe class rating
PS	Pressure side

PSP	Pressure-sensitive paint
PT	Pressure tap
PtTFPP	Platinum porphyrins luminophores
ROI	Region of interest
S	Saddle point
SEC	Secondary flow
SLM	Selective laser melting
SNR	Signal-to-noise ratio
SS	Suction side
TC	Thermocouple
TLC	Thin layer chromatography
UTE	Upper trailing edge
UV	Ultraviolet

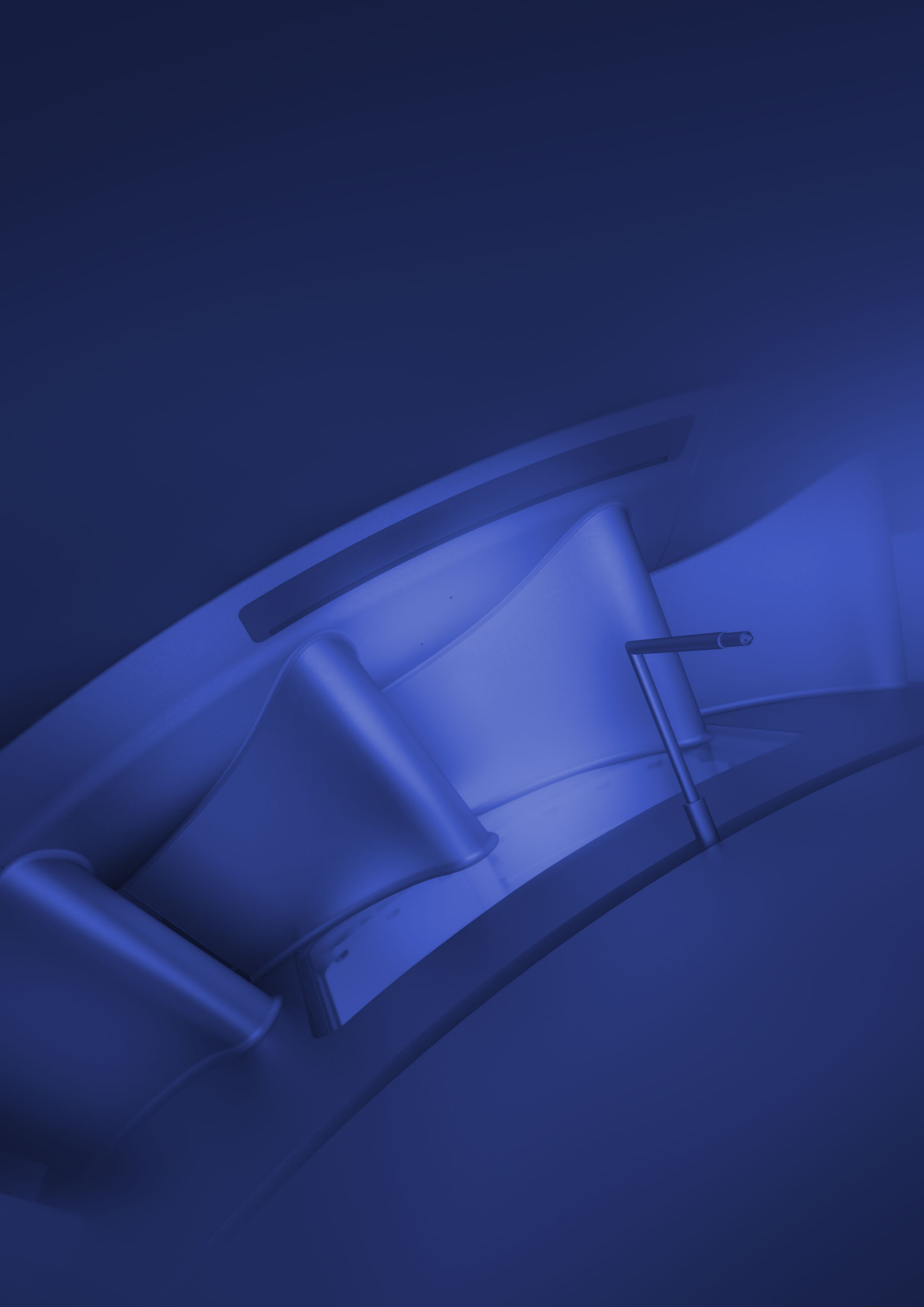

Introduction

Although its share of global power generation is stagnating, natural gas currently provides 22 % of the world's electricity and is responsible for 25 % of power sector emissions.[1] However, the global roadmap to net-zero emissions in 2050 recently reported by the International Energy Agency highlights that the combustion of natural gas will be indispensable for generating energy for the foreseeable future [1]. Thus, the further development of gas turbines to increase fuel efficiency remains essential.

1.1 Motivation

In addition to higher pressure ratios, the efficiency of the underlying Brayton cycle can be improved by raising the turbine inlet temperatures. Therefore, great efforts have been made in the past decades to increase the firing temperatures. However, the demand for higher turbine inlet temperatures has necessitated the use of cooling techniques to protect turbine components from failure.

Starting with internally cooled turbine blades used in the Junkers Jumo 004 jet engine in the mid-1930s, these cooling techniques have been continuously refined. In addition to the use of high-temperature alloys and thermal barrier coatings, the combined application of internal and external cooling techniques allows the turbine inlet temperatures of stationary gas turbines to be raised to currently more than 1650 °C, i.e., far beyond the melting temperatures of the components involved [2].

In contrast to internal cooling, external cooling involves the injection of coolant into the hot gas path through the internal channels of the component to be protected. An essential element of external turbine cooling is the application of film cooling. As stated by Goldstein [3], film cooling involves

1 According to https://ember-climate.org/topics/gas/

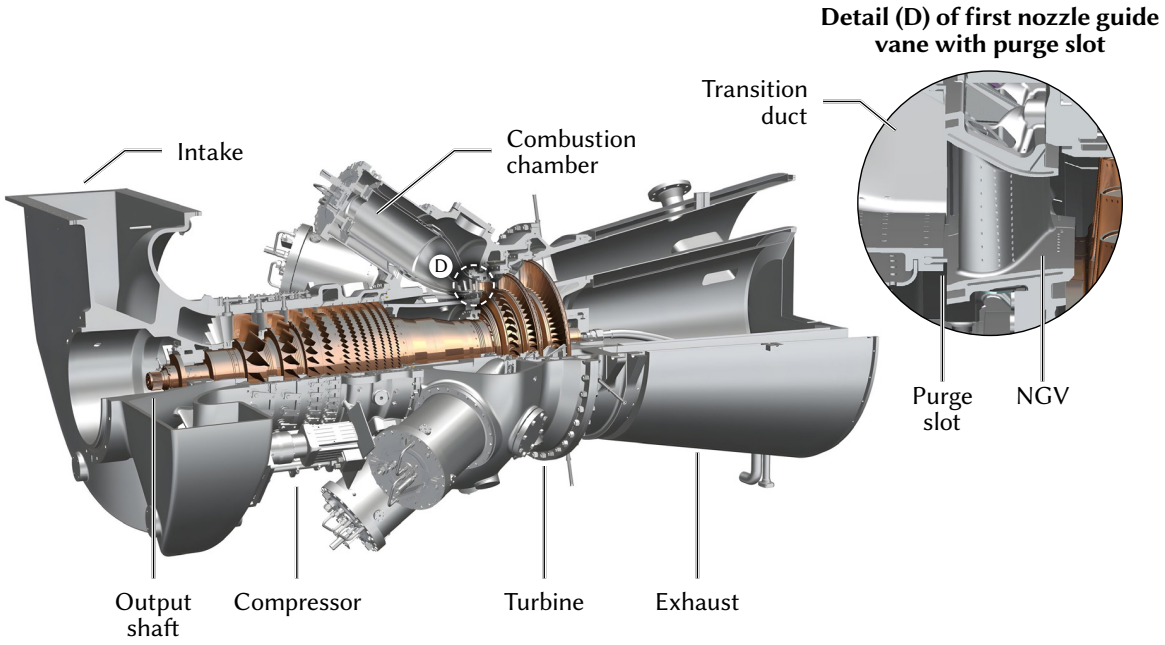

Figure 1.1: Design of a modern stationary gas turbine (illustration by courtesy of MAN Energy Solutions, Oberhausen)

the introduction of a coolant at discrete locations along a surface to protect that surface not only in the immediate vicinity of the injection but also in the downstream area from a high-temperature environment.

Since the coolant used for external cooling must be provided at a pressure level that allows the injection at the respective location of the hot gas path, it is taken from the upstream compressor. However, extracting air from the compressor incurs a penalty to thermal efficiency as the bypassed air does not completely participate in the Brayton cycle. The efficiency gain from increasing the turbine inlet temperatures must always be weighed against the losses from the coolant supply. To maximize the cooling performance while minimizing the coolant consumption, extensive knowledge of the propagation of the coolant and its effects on heat transfer is required [4].

This knowledge has been accumulated through many experimental and numerical investigations over the past decades, focusing on those components that are exposed to the highest thermal loads in the engine. These include the first nozzle guide vane (NGV) situated downstream of the combustion chamber, as shown in Figure 1.1. For structural reasons, coolant is still primarily injected from discrete cooling holes on the vane surface and endwalls. However, the discrete nature of these cooling holes usually fails to provide a full coverage coolant film, as the coolant jets induce vortices that can significantly reduce the cooling performance [5]. Thus, developing optimized hole geometries is an ongoing part of film cooling research [6].

From an aerothermal point of view, providing coolant from a tangential slot is superior to discrete cooling holes as an ideal slot injection would provide a full-coverage coolant film [3]. Although the addition of slots is structurally unfavorable, design-related gaps can be, in principle, utilized for injecting coolant on the endwall surfaces as the cavities beneath these gaps are already pressurized with purge air to prevent hot gas ingestion. This also includes the so-called purge slot that is located between the transition duct and the platform of the NGV, as shown in the detail of Figure 1.1.

Since the turbine components in the actual engine experience expansions and contractions within different operational cycles, the dimensions of this gap can change. It can also be influenced by design modifications at the combustor-turbine interface. Moreover, driven by temperature and pressure variations of both coolant and mainstream, injection-related parameters may change between idle, partial, and full load.

For dimensioning the cooling air system, assessing the cooling performance of these coolant flows is vital. Due to the three-dimensional, highly turbulent nature of the turbine flow and the significant influence of the so-called secondary flow on the coolant distribution, experimental data are still indispensable, preferably obtained under flow conditions close to the engine.

Here, it is first and foremost important to match the Mach and Reynolds numbers that characterize turbine flow in the engine. This includes experimental testing under high-speed conditions to reproduce the compressibility effects present in the high subsonic regions of turbine flows.

Prior investigations have shown that the secondary flow field in an annular turbine guide vane is highly influenced by the radial pressure gradient that naturally occurs in swirling flows [7]. These differences manifest in a highly asymmetrical pressure loss pattern when comparing the hub-side and shroud-side half spans of the outlet flow of a cylindrical vane. It, therefore, stands to reason that the film cooling performance will differ between the hub and shroud under the influence of the radial pressure gradient. Testing this hypothesis implies the reproduction of this gradient which is, by principle, only possible in an annular cascade of turbine vanes.

Although many studies on the cooling performance of upstream slot injection have shed light on the influences of various parameters, none of them was performed in an annular cascade under high-speed conditions (see Table 2.2 in Chapter 2). This is where the present work picks up by developing an annular sector test rig that allows testing of the film cooling performance and aerodynamic effects of coolant flows from various upstream slot configurations at engine-like Mach and Reynolds numbers.

1.2 Placement of this Work

The groundwork for investigating turbine flows at the institute was laid by Franze [8], who developed and commissioned the high-speed turbine test rig that allows testing under engine-like Mach and Reynolds numbers. The test rig is equipped with a gas burner that enables tests in a wide temperature range from 20 °C to 400 °C.

Since then, several studies have been conducted on the film cooling performance and aerodynamic influence of upstream slot injection: While the first studies were performed with a cylindrical vane design [9, 10], the latest measurements were carried out with a state-of-the-art contoured nozzle vane design that utilizes measures to reduce secondary flow [11, 12]. All of these studies were conducted in linear cascades.

The annular sector test rig to be integrated into the test architecture adopts the nozzle guide vane design with a contoured shroud from the previous investigation. Concerning the influence of the endwall design on film cooling performance, the results to be expected from the test rig are, therefore, of great significance. At the same time, the measurements to be performed on the test rig will allow a detailed evaluation of the influence of the radial pressure gradient on film cooling performance and aerodynamics by comparing these results with the findings from the linear cascade tests.

1.3 Thesis Outline

The paper begins with two introductory chapters to familiarize the reader with the subject and experimental methods. The main section starts with a discussion of the findings from the previous measurements in the linear cascade. Then, the development of the annular sector cascade is presented in detail:

Chapter 2: Background and State of the Art

This chapter covers different aspects related to turbine flows and film cooling. It starts by discussing the secondary flow field of a turbine flow and measures to reduce it. Then, it briefly introduces the concept of film cooling and important parameters to evaluate its performance. The chapter then presents a detailed literature review of experimental studies on film cooling using upstream slot injection. The modeling approaches for investigating turbine flows are discussed, focusing on annular cascades and their advantages. Finally, the chapter concludes by formulating research objectives based on the state-of-the-art research presented.

Chapter 3: Experimental Methods and Setup

The third chapter is dedicated to the specifications of the test rig and the annular cascade. In addition, the major measurement methods, namely five-hole probes, pressure-sensitive paint, and IR thermography, are presented in detail, focusing on the application in the annular cascade.

Chapter 4: Preliminary Investigation of the Linear Cascade

This chapter presents the results of the preliminary investigation of the linear cascade. The first part of this chapter includes the experimental results obtained through oil flow visualization, pressure-sensitive paint, and five-hole probe measurements. The second part presents the results of the heat

transfer measurements, along with a description of the measurement module. The chapter concludes with an evaluation of the measurement methods and their implementation to identify improvement potentials in the development of the annular cascade.

Chapter 5: Design and Construction of the Annular Sector Cascade

In this chapter, the aerodynamic design and construction of an annular sector test rig are presented. It first introduces the experimental constraints and requirements, followed by an in-depth discussion of the numerical investigation that was carried out to optimize the fluid volume of the annular cascade. The chapter then presents the design of the cascade, the measuring equipment, and the components required for conditioning the inlet and outlet flow.

Chapter 6: Summary and Outlook

A summary of the main results is given, followed by an outlook on the measurements to be carried out in the annular sector test rig.

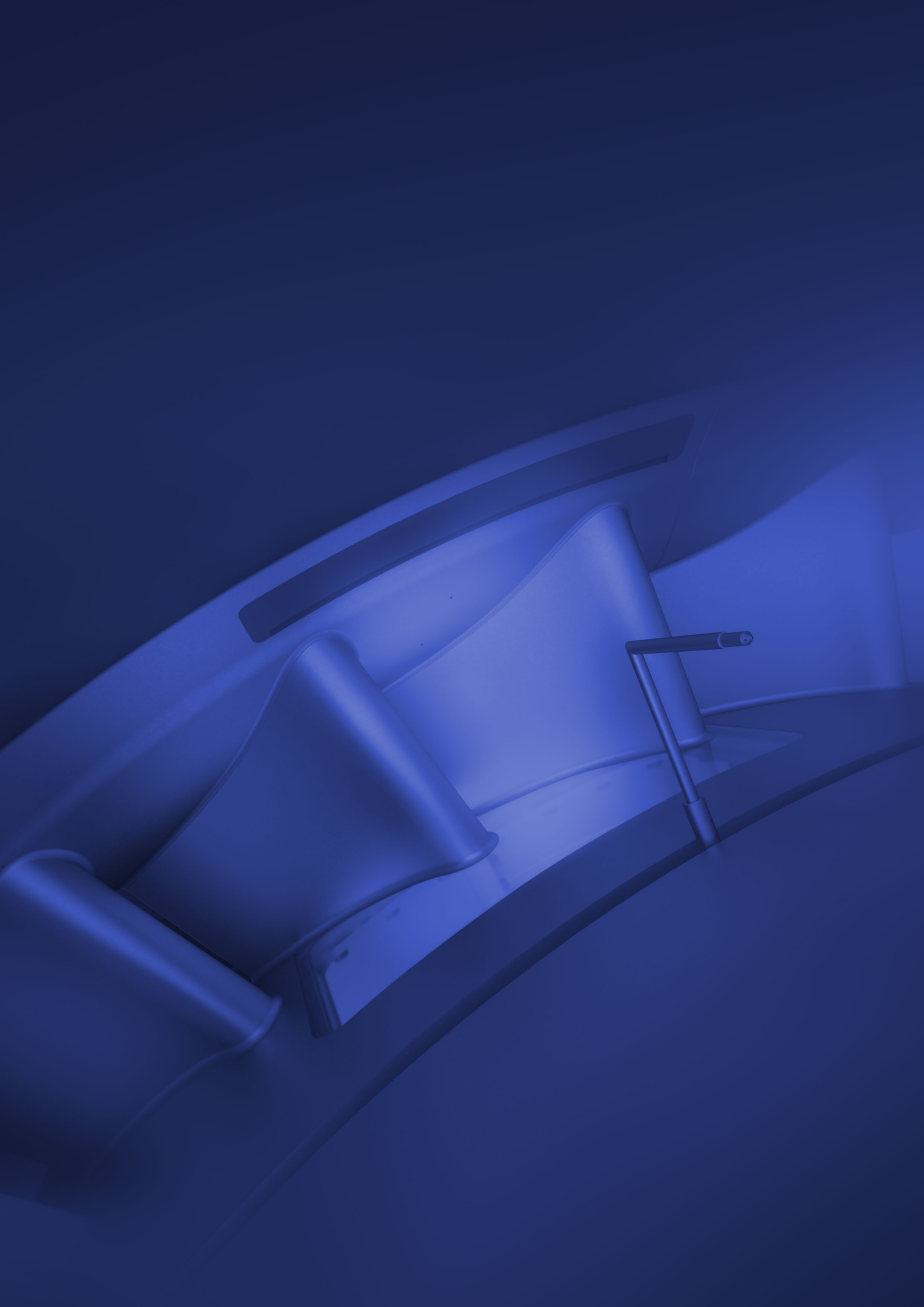

Background and State of the Art

Since the film cooling performance is significantly influenced by secondary flows, the first section of this chapter outlines the secondary flow field of a turbine flow between the stator vanes and presents measures that are applied to reduce secondary flows. After a brief introduction to the principle of film cooling and important parameters for evaluating film cooling performance, a detailed literature review of experimental studies on film cooling by upstream slot injection is presented. This is followed by an overview of modeling approaches for the experimental investigation of turbine flows, with a particular focus on annular cascades and their advantages over linear cascades. The chapter concludes with the formulation of the research objectives, which are derived from the state-of-the-art research presented above.

2.1 Secondary Flow in Turbine Cascades

Secondary flow is generated whenever a sheared flow passes around an obstacle or is deflected through a channel or cascade. While the former phenomenon is mainly driven by viscous effects, the latter is caused by an imbalance between the normal pressure gradient and the centripetal acceleration, which results in an overturning of the shear layer, thereby developing a crossflow toward the suction side [13]. Large flow-turning angles and the presence of a thick leading edge cause the secondary flow in a turbine to be much more complex than in compressors or pumps, with secondary flow-related losses typically accounting for up to 20 % of the total loss for an inlet stator row [14].

Secondary flow not only plays an important role in loss generation, but it also significantly influences the heat load on the vane and endwall, as already shown by Graziani et al. [15] and Blair [16] in early studies on heat transfer. Finally, film cooling is significantly impacted by secondary flow, as it restricts the propagation of the coolant and draws it away from the surface to be cooled, thereby compromising the cooling performance.

2.1.1 Secondary Flow Vortex Model

While Hawthorne [17] pioneered the identification of recirculating flow in a cascade, Langston et al. [18] provided the first comprehensive experimental analysis of secondary flow patterns in turbine cascades, in particular on the role of the leading-edge horseshoe vortex. Since then, these models have been extended and refined by numerous experimental and numerical works. Perhaps the most detailed contribution was made by Wang et al. [19], who documented the endwall flow utilizing laser light and multiple smoke wires. Regarding the secondary flow reduction measures that are also utilized in the vane design presented in Chapter 3, it is important to emphasize that these models can only provide a rough orientation for classifying certain flow phenomena. Since the measurement techniques used in the Institute's turbine test rig do not allow for the breakdown of small-scale vortices, a simplified model is applied for the present work. It is shown in Figure 2.1 and adapted with slight modifications concerning the saddle point region from the work of Takeishi et al. [20].

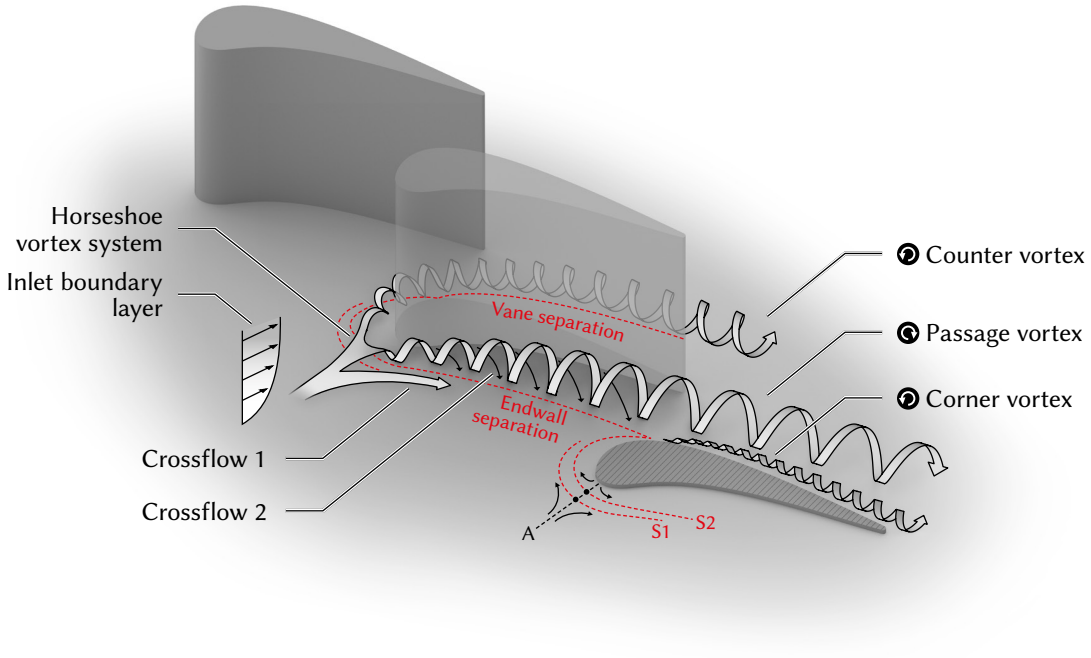

Figure 2.1: Simplified secondary flow vortex model (based on Takeishi et al. [20])

When the endwall boundary layer approaches the vane, a horseshoe vortex system is formed near the intersection of the leading edge and the endwall, similar to that observed in a flow around a cylinder. The driving force of this vortex system is a static pressure gradient in the spanwise direction that originates from the decreasing stagnation pressure between the freestream and the boundary layer. This pressure gradient generates a downward flow along the leading edge that rolls up and splits into a pressure-side and a counter-rotating suction-side leg. It is fed by the incoming boundary layer that separates upstream the leading edge due to the adverse pressure gradient, which is present in the stagnation area. On the endwall upstream of the leading edge, two major separation lines appear: While the first separation line (S1) is attributed to the separating boundary layer ahead of the horseshoe vortex, the second separation line (S2) corresponds to the lift-off of the vortex itself [21]. At the so-called attachment line (A), which is not to be confused with reattachment lines, the incoming flow separates into the adjacent passages. The intersection points between the attachment line and the two separation lines are usually referred to as the so-called saddle points, which are marked with black dots in the illustration [22]. In case of a symmetrical flow around a cylinder, the characteristics of this region, i.e., the strength of the horseshoe vortex and the position of the saddle points, dependent mainly on the thickness of the incoming boundary layer and the cylinder diameter [23]. However, in the context of turbine flow, the pressure field, which is influenced by both the vane design and operating conditions, has a major impact on these characteristics [14].

As shown in the study of Wang et al., but not included in the illustration for clarity, both legs of the horseshoe vortex are initially composed of several sub-vortices, which gradually changed to a single-vortex pattern when entering the passage. Driven by the strong cross-passage pressure gradient, the pressure-side leg is drawn to the suction side, where it encounters its weaker suction-side counterpart. There is a consensus in the literature that the pressure-side leg of the horseshoe vortex merges into the passage vortex while being intensified by the passage crossflow (2) and gradually lifted away from the endwall. However, the downstream interaction of the two legs is presented differently, with the representation in Figure 2.1 following the model introduced by Goldstein and Spores [22]. According to this, the suction-side leg lifts off the endwall and continues as the so-called counter vortex downstream along the suction surface adjacent to the passage vortex. Other authors like Sharma and Butler [24] suggested that the suction-side leg orbits around the outside edge of the passage vortex. Wang et al. concluded that, to some extent, the suction-side leg could be considered as a small part of the larger passage vortex system. Regardless of these differences, there is agreement that the passage vortex is the largest single contributor to loss generation in the passage, as shown, e.g., in an experimental investigation by Moore and Adhye [25]. Furthermore, the passage vortex is also a major obstacle to endwall cooling in the mid and rear passage, as it draws parts of the coolant away from the endwall [26].

Typically, a vortex, such as the horseshoe vortex, generates further counterrotating secondary vortices of lower intensity, which occur in particular at the junction between the obstructive body and the endwall [27]. These so-called corner vortices may also occur in a turbine flow and have been observed in the above-mentioned investigations at the leading edge and at both the suction and

pressure side. However, rounding corners with fillets can reduce or eliminate such vortices, as shown, e.g., in an investigation of Zess and Thole [28]. For illustration purposes, the suction-side corner vortex is included in Figure 2.1. It originates downstream of where the passage vortices lift off from the endwall and is driven by an interaction of the passage vortex with the suction surface [22].

2.1.2 Measures for Reducing Secondary Flow

Recognizing the importance of secondary flow in cascade losses, measures have been developed and tested over the past decades to reduce secondary flow and optimize overall aerodynamic efficiency. These measures, exemplarily shown in Figure 2.2, can be divided into endwall profile adjustments, vane-endwall junction modifications, especially in the leading-edge area, and 3D vane design.

Endwall contouring: Endwall contouring was first introduced by Deich et al. [29] as an axisymmetric reduction of the span between the leading edge and trailing edge by profiling one endwall. The idea of this kind of contouring is to decrease the flow velocity in the high-turning upstream part of the vane, thus mitigating the emergence of passage crossflow, whereas in the downstream region, the passage contraction induces an acceleration that thins the endwall boundary layer, further decreasing the potential of secondary flow [30, 31]. The optimal contraction depends primarily on the aspect ratio, i.e., the ratio between inlet span and chord length. Vane designs with a low aspect ratio benefit from a stronger contraction, as endwall-related losses are more pronounced in relation to the total loss when compared to high-aspect ratio designs [32].

The first experimental investigations on axisymmetric contouring under high-speed conditions were conducted by Kopper et al. [33] in a linear cascade of high-pressure turbine inlet guide vanes. The results obtained for the contoured endwall demonstrated a 17 % reduction of the mass averaged total pressure loss relative to the flat endwall configuration. Remarkably, five-hole probe measurements at

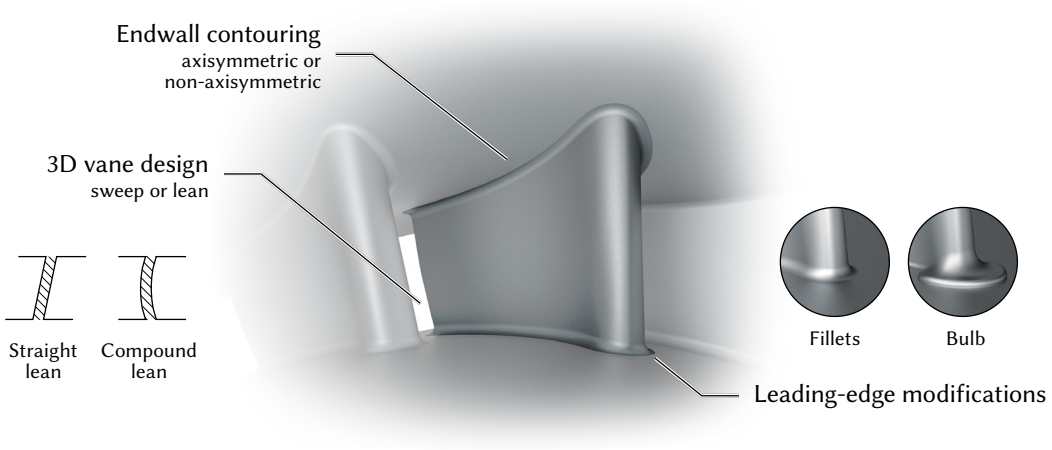

Figure 2.2: Vane design measures for reducing secondary flow

the outlet revealed that most of the improvement resulted from reduced secondary loss on the planar wall side of the contoured cascade. These findings were supported by a similar study conducted by Dossena et al. [34], who performed numerical analyses in addition to experimental investigations. They found that the secondary flow structure on the flat half span is similar to the typical configuration of straight cascades but characterized by lower vortex intensity. Whereas on the contoured half span, the contraction inhibits the formation of a proper passage vortex and its migration toward the midspan. The better performance of the flat half span, as already observed by Kopper et al., was attributed to both the prolongation of the contoured wetted surface and the steeper re-compression at the passage exit, promoting the diffusion of the boundary layer.

Another investigation to be highlighted was conducted by Boletis [35] in an annular cascade, albeit under low-speed conditions. When comparing the contoured half span to the flat half span, he found that the overall loss reduction was higher in the former, unlike in studies on linear cascades. The flow field measurements taken at different axial positions within the passage revealed that a low static pressure area near the suction side of the shroud endwall counteracted the radial pressure gradient generated by the annular shape. Boletis postulated that this effect led to a decrease in the inward migration of low-momentum material along the blade's suction side surface.

Little data is available on the extent to which contouring changes the thermal load on the endwall, as most authors did not provide results from a planar passage as a baseline for comparison to the contoured configurations. In this context, the study by Thrift et al. [36] stands out, who performed heat transfer measurements on the endwalls of both a planar and contoured passage. Their results indicate that the heat transfer is reduced on both endwalls of a contoured passage. The authors attribute this to the reduction of secondary flows, primarily the weakening of the horseshoe vortex. However, it is not clear to what extent the results, which were obtained under low-speed conditions, can be transferred to the real engine, considering that the intended thinning of the boundary layer in the downstream part of the passage may potentially increase the heat transfer.

Non-axisymmetric endwall contours, which should be mentioned here only for the sake of completeness, were first introduced in the late 1980s: The idea of this kind of contouring, i.e., shaping the endwall in the pitchwise direction, is to smooth out the cross-passage pressure gradient in the upstream part of the passage [37]. In this respect, the intended effects are, therefore, somewhat similar to those of the 3D vane profiling techniques mentioned below [38]. Experimental investigations of numerically optimized contours suggest that secondary flow-related losses can be reduced by up to 30 % [39].

Leading-edge modifications: Modifications to the leading edge include both fillets[2] and larger bulb-like geometries. While fillet geometries, especially at the leading edge, are meant to reduce the strength of the horseshoe vortex system [40], the bulb modification is intended to weaken the passage vortex by intensifying the counter-rotating suction-side leg of the horseshoe vortex. Sauer et al. [41]

2 It should be mentioned that fillets are an integral part of the casted vane platform, i.e., they are already integrated into the vane design for manufacturing and structural reasons. Designs without fillets are, therefore, rather academic cases for the purpose of simplification.

observed in an experimental investigation on different bulb geometries a reduction of endwall losses by approximately 50 %. However, a study of Becz et al. [42] investigating similar leading-edge geometries did not show the same level of loss reduction.

Regarding the use of fillets, the first experimental investigations on linear and curved fillets were conducted by Kubendran and Harvey [43]. Although the study was directed to a wing-fuselage junction and is, thus, not fully transferable on the flow field of a high-turning turbine cascade, they reported that the overall drag for both the filleted cases is lower than that for the reference case without fillets. However, a very similar investigation in terms of fillet design and test conditions conducted by Devenport et al. [44] yielded a different result, stating that the fillet actually increases the size and strength of the horseshoe vortex.

Focusing on the vane-endwall junction, Zess and Thole [28] investigated an asymmetric leading-edge fillet that was numerically optimized to mitigate the effect of the leading-edge pressure gradient by accelerating the incoming boundary layer. Subsequent flow field measurements on the pressure side of the optimized vane indicated the elimination of the horseshoe. The comparison of the studies shows that the use of fillets to suppress secondary flow may not be achieved by simple fillets with a constant radius but requires a design optimized for the geometry and flow conditions.

3D vane design: Cylindrical vanes are typically designed to operate at midspan with maximum efficiency. However, this design approach does not account for the radial equilibrium, resulting in spanwise loading variations that can promote secondary flow-related losses. Three-dimensional vane design addresses this issue and includes both sweeping and leaning: A vane is considered "swept" if its leading edge is not perpendicular to the incoming flow or its trailing edge is not perpendicular to the outgoing flow. On the other hand, a vane is considered "tilted" if the intersection of the vane surfaces with a plane perpendicular to the engine axis is inclined to the radial direction [45].

While sweeping is primarily applied in compressor design to improve the stall margin, the primary purpose of lean is modifying the spanwise pressure distribution, thereby weakening the radial pressure gradient, which is assumed to intensify secondary flow in an annular cascade. Harrison [46] compared straight and curved leaned designs and found that a compound lean, as shown exemplarily in Figure 2.2, was most effective in reducing the downstream mixing losses. His findings were supported by another study on a compound leaned turbine blades conducted by Schobeiri et al. [47]. Their results indicated that the leaned configuration effectively reduced the extent of the secondary flow.

2.2 Film Cooling

As already outlined in the introduction, the working principle of film cooling is to inject coolant from the inside to the outside surface of the component to be protected, forming an insulating layer between the surface and the hot mainstream. Unlike transpiration cooling, film cooling is not primarily designed to protect the surface at the point of coolant injection but rather to protect the region

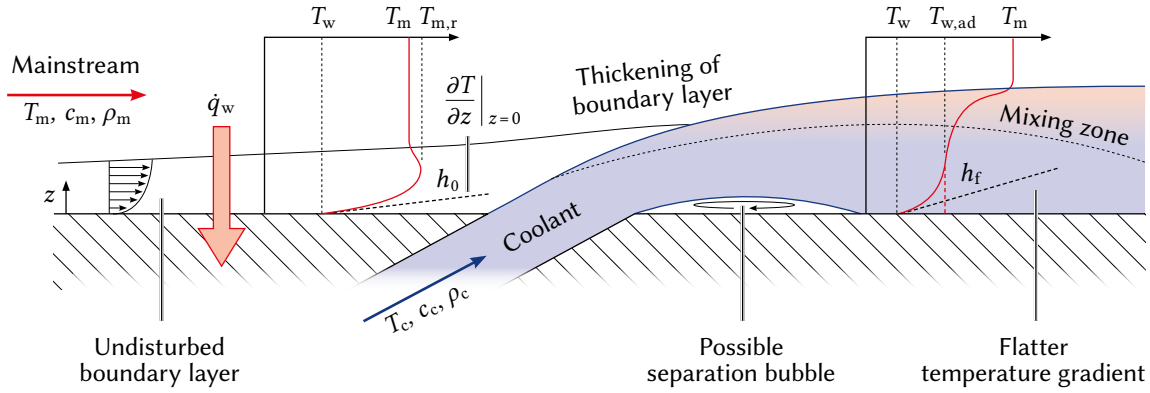

Figure 2.3: Principle of film cooling

downstream of the injection location, as illustrated in Figure 2.3. The film cooling performance is therefore influenced by parameters that are related to both the injection and surface geometry and coolant-to-mainstream conditions [3].

2.2.1 Thermal Analysis

The convective heat transfer $\dot{q}_w$ between a fluid and a solid is governed by the thermal conductivity of the fluid κ_{fl} and the temperature gradient $\partial T/\partial z$ in direct proximity to the surface, with the gradient being dependent on the thickness and shape of the thermal boundary layer. By lowering the local temperature of the fluid adjacent to the surface, the temperature gradient is flattened, and thus the driving potential for heat transfer to occur is reduced. Since this gradient is difficult to measure, the heat transfer is usually related to the difference between the surface temperature T_w and a fluid reference temperature T_{REF} by a proportional factor, namely the heat transfer coefficient h [48]:

$$\dot{q}_w = \kappa_{fl} \cdot \left.\frac{\partial T}{\partial z}\right|_{z=0} = h \cdot (T_w - T_{REF}) \tag{2.1}$$

Accordingly, h reflects the properties of the (thermal) boundary layer, whereas the temperature difference is solely a thermodynamic quantity. For an uncooled case, it is convenient to reference the heat transfer coefficient h_0 to the fluid temperature T_m far from the surface. However, for high-speed flows ($Ma > 0.3$) typically encountered in high-pressure turbines, h_0 should be referenced to the local recovery temperature $T_{m,r}$ of the fluid (see Chapter 4.6.2):

$$h_0 = \underbrace{\frac{\dot{q}_w}{T_w - T_m}}_{\text{Low speed}} = \underbrace{\frac{\dot{q}_w}{T_w - T_{m,r}}}_{\text{High speed}} \tag{2.2}$$

For the film-cooled case, the appropriate reference temperature is not obvious because the local fluid temperature varies greatly depending on the mixing state between the main flow and the coolant. If the mainstream temperature were used as a reference, h_f would be a function of both the flow field and the coolant temperature. For decoupling h_f from the coolant temperature, it is common practice to utilize the adiabatic wall temperature $T_{w,ad}$ as it represents the driving temperature of the coolant film:

$$h_f = \frac{\dot{q}_w}{T_w - T_{w,ad}} \tag{2.3}$$

The heat transfer coefficient can be non-dimensionalized by κ_{fl} and a characteristic length to define Nusselt's number:

$$Nu = \frac{h \cdot L}{\kappa_{fl}} \tag{2.4}$$

The Nusselt number is often preferred in heat transfer analyses because it not only takes into account the flow regime but also incorporates the effect of geometric scale and fluid properties. From equation 2.2, it can be recognized that Nu is equal to the non-dimensional value of the temperature gradient at the wall [13].

2.2.2 Film Cooling Performance

The adiabatic wall temperature is a crucial parameter in evaluating film cooling performance, as it provides information about the fluid temperature above the wall. To eliminate the dependence on both the absolute coolant and mainstream temperature, the adiabatic wall temperature is non-dimensionalized into what is known as the adiabatic film cooling effectiveness:

$$\eta_{ad} = \frac{T_{m,r} - T_{w,ad}}{T_{m,r} - T_c} \tag{2.5}$$

The film cooling effectiveness varies between 0 and 1 and can be interpreted as a concentration measure of the coolant. Film cooling efficiencies close to 1 can be achieved providing that the cooling film neither separates nor mixes with the main flow. However, as indicated in Figure 2.3, the coolant typically mixes rapidly with the mainstream. Thus, even for a non-separating cooling film from an angled hole ($\alpha = 30^\circ$), the film cooling effectiveness has already reduced to less than 0.5 at a downstream distance of 5 bore diameters, as shown, e.g., in an investigation by Baldauf et al. [49].

The film cooling effectiveness will only allow conclusions to be drawn about the actual heat load if the flow field and thus the heat transfer coefficient are not changed by injection, i.e., $h_f = h_0$. While this is usually true far downstream of the injection location, it has been found, e.g., in an investigation on film cooling hole geometries by Crawford et al. [50] that the heat transfer coefficient changes

considerably in the near field of the coolant injection. Regarding the inclined slot injection, Burd et al. [51] observed an increase of the local heat transfer coefficient in the order of 25 % with a local maximum approaching 70 %.

Therefore, as suggested by Sen et al. [52], the overall benefit of film cooling can be evaluated by using a simple relationship that relates the heat transfer that would have occurred without film cooling to that with film cooling. The so-called Net Heat Flux Reduction (*NHFR*) is defined as follows:

$$NHFR = 1 - \frac{\dot{q}_{\mathrm{w,f}}}{\dot{q}_{\mathrm{w,0}}} = \frac{h_{\mathrm{f}} \cdot \left(T_{\mathrm{w}} - T_{\mathrm{w,ad}}\right)}{h_0 \cdot \left(T_{\mathrm{w}} - T_{\mathrm{m,r}}\right)} \tag{2.6}$$

A *NHFR* close to 1 is thus achieved when the heat flux with coolant injection becomes very small compared to the situation without cooling. Conversely, the heat flow balance may deteriorate if the heat transfer coefficient is increased by the injection more than the local temperature is decreased. In the above formulation, *NHFR* depends on the specific temperature conditions of the investigation. To determine the reduction for arbitrary mainstream and coolant temperatures, *NHFR* can be expressed using a dimensionless temperature ratio Θ:

$$NHFR = \frac{h_{\mathrm{f}}}{h_0} \cdot (1 - \eta_{\mathrm{ad}} \cdot \Theta) \quad \text{with} \quad \Theta = \frac{T_{\mathrm{m}} - T_{\mathrm{c}}}{T_{\mathrm{m}} - T_{\mathrm{w}}} \tag{2.7}$$

2.2.3 Fluid Dynamic Parameters

The distribution of the coolant film depends not only on the bore or slot geometry but also to a large extent on fluid dynamic parameters. Besides the mainstream turbulence degree, the blowing ratio *BR*, also referred to as mass flux ratio *MFR*, and the momentum flux ratio I were identified in previous studies as significant factors influencing film cooling performance [48]. The former is defined as follows:

$$BR = \frac{\rho_{\mathrm{c}} \cdot c_{\mathrm{c}}}{\rho_{\mathrm{m}} \cdot c_{\mathrm{m}}} \tag{2.8}$$

It was found that the cooling effectiveness is directly proportional to the blowing ratio as long as the coolant film remains attached to the surface. However, once the blowing ratio exceeds a certain critical point, the film cooling effectiveness decreases. This decline is caused by film-cooling lift-off, where the high-momentum film-cooling jet is unable to attach to the plate surface and instead penetrates the mainstream [53]. The coolant jet separation characteristics were found to scale with momentum flux ratio I, which is defined as follows [48]:

$$I = \frac{\rho_{\mathrm{c}} \cdot c_{\mathrm{c}}^2}{\rho_{\mathrm{m}} \cdot c_{\mathrm{m}}^2} \tag{2.9}$$

A study by Thole et al. [54] identified three distinct regimes that were related to the momentum flux ratio: one where the coolant jet remained fully attached to the surface ($I \leq 0.4$), another where the coolant jet detached and reattached ($0.4 < I \leq 0.8$), and a third where the coolant jet was completely detached ($I > 0.8$).

Finally, the density ratio between the mainstream and the coolant plays an important role, as it is included in both the blowing ratio and the momentum flux ratio. It is defined:

$$DR = \frac{\rho_c}{\rho_m} \tag{2.10}$$

Typically, the DR varies between 1.4 and 2 in the real engine because of the temperature difference between the mainstream and the coolant. However, due to the difficulty of reproducing these ratios in experimental setups, many film cooling studies have been performed with a unity density ratio. It is therefore important to consider and evaluate the effect of DR on film-cooling performance [48]. In general, increasing DR at a constant blowing ratio yields higher effectiveness, particularly at higher blowing ratios, as the momentum flux of a high-density coolant, and thus the tendency to lift-off is lowered [53].

2.3 Endwall Cooling by Upstream Slot Injection

The investigation of air injection through slots dates back to the 1940s. Wieghardt [55], for example, investigated the thermal effects of discharged heated air for the purpose of wing de-icing in an experiment with a slotted flat plate. Goldstein [3] provides an extensive overview of the variety of further experiments up to 1970 that focused on different aspects of film cooling through slots and holes. However, most of these experiments were not directly related to vane endwall cooling but were intended to establish general relations that were utilized in various engineering fields, e.g., rocket nozzles, combustion chambers, or re-entry vehicles. Since these relationships were derived primarily from flat plate tests, their applicability to the flow conditions of a turbine passage was limited.

Compared to the performance of discrete film cooling holes, a slot basically introduces the coolant in a relatively uniform layer that has less mixing with the overflowing mainstream. However, since the high stresses experienced by turbine components would not allow for additional slots, the applicability is mainly limited to design-related slots, such as the purge slot between the transition duct and the vane platform [48].

2.3.1 Overview of Experimental Research

One of the first investigations focusing on turbine endwall cooling was conducted by Blair [16], who studied the distribution of coolant ejected from an inclined slot located upstream of the leading edge. He found that the endwall coolant performance is strongly affected by secondary flow: Driven by

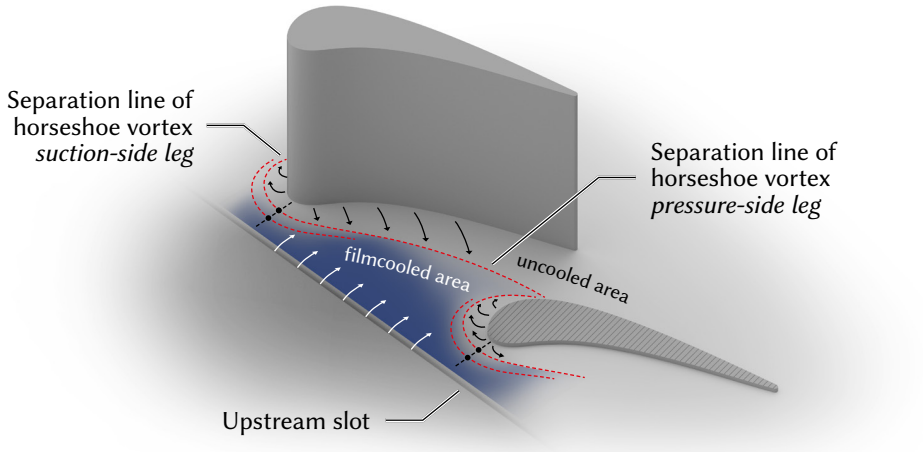

Figure 2.4: Typical endwall coolant distribution for inclined injection with medium-momentum coolant

the passage crossflow, the coolant is swept away from the pressure side and accumulates near the suction side. The results of his comparison demonstrate the failure of previously available correlations of film cooling effectiveness to predict the pitchwise variations that occur on turbine endwalls. Since then, many other experimental investigations of endwall cooling by upstream slot injection have been performed, refining Blair's findings and providing data on the influence of slot, coolant, and mainstream-related aspects.

Although statements about endwall coolant coverage cannot be fully generalized, as it is highly dependent on the parameters discussed in the next section, at least an inclined injection with medium-momentum coolant will usually result in a distribution that is schematically shown in Figure 2.4: While the stagnation pressure in the leading-edge area counteracts the uniform coolant discharge, the coolant propagation in the upstream part of the passage is limited by the horseshoe vortex system. The passage crossflow transports the coolant towards the suction side, where it is carried away from the endwall by the separating passage vortex. As a result, large parts of the endwall, i.e., the area around the leading edge, the pressure side, and the downstream part of the passage, do not experience significant cooling.

In addition to the following discussion of essential parameters that govern the cooling performance of an upstream slot injection, a (non-exhaustive) overview of experimental investigations is given in Table 2.1. It contains both the test rig and slot specifications as well as the respective measurement scope. Also included are tests that have already been performed and those that are currently planned on the institute's own high-speed turbine test rig.

The overview reveals that, firstly, the majority of the studies were performed under low-speed conditions, i.e., engine-like Mach numbers and their effects on secondary flow have not been reproduced. For example, in a study concerning the influence of Mach number on turbine aerodynamics, Perdichizzi [56] has shown that the passage vortex migrates toward the endwall for increasing Mach numbers. Regarding the strong dependence between coolant distribution and secondary flow, it must therefore

be noted that the findings from low-speed tests may not be fully transferable to the conditions in the actual engine. Secondly, it is apparent that all previous studies have been performed in linear cascades, thus neglecting possible influences of the radial pressure gradient, which is to be addressed with the test rig presented in this thesis.

2.3.2 Governing Parameters for Film Cooling Performance

The film cooling performance of an upstream slot injection is influenced by both injection-related parameters discussed in Chapter 2.2.2 and parameters concerning the slot and vane design. In particular, the slot geometry can vary due to design changes but also due to operational variations. While the injection angle of the slot flow can be influenced by design changes of the combustor-turbine interface, the slot width can change significantly due to thermally induced expansions of the turbine components. For the dimensioning of the secondary air system, it is, therefore, necessary to assess the range of possible parameter changes and their effects on the film cooling performance. Concerning the definition of the slot-related parameters, please refer to Figure 3.2.

Influence of coolant mass flux and momentum: Blair's research [16] already showed that the extent of endwall cooling generally increases with higher coolant mass flow, nota bene using an inclined slot with $\alpha = 30^\circ$ located immediately upstream of the leading edge. His findings were supported by Granser and Schulenberg [57], who conducted an investigation under high-speed conditions with a similar slot design but positioned further upstream. They found that the average film cooling effectiveness increases monotonically with the blowing ratio as long as the coolant flow is attached to the wall. However, if the coolant momentum ratio exceeds a critical value of, in this case, 1.25, the film lifts off and mixes with the mainstream, thus limiting the maximum coolant coverage.

Regarding the local distribution of the coolant, it is generally observed that a low-momentum injection prevents the coolant from overcoming the counteracting stagnation pressure upstream of the leading edge and thus exits the slot very non-uniformly. Second, it is found that the low-momentum coolant, driven by the passage crossflow, accumulates on the suction side, leaving the leading-edge area and the pressure side uncooled. When the coolant momentum is increased, the distribution is progressively equalized in the pitchwise direction, thus extending to the previously uncooled areas, provided that the coolant does not separate.

Influence of density ratio: The influence of the density ratio is related to the effects of varying the coolant momentum since a lower density ratio necessarily yields a higher coolant velocity if the blowing ratio is kept constant. However, only little data are available since the majority of investigations were carried out at a constant density ratio. In this context, a study by Chen et al. [58] is to be highlighted, who investigated the cooling effectiveness of an inclined slot injection ($\alpha = 25^\circ$) for a wide range of density ratios. They concluded that the cooling effectiveness worsens at higher density ratios, as the high-density but low-momentum coolant is blocked by the leading-edge stagnation pressure

Table 2.1: Overview of experimental investigation of purge slot cooling in turbine vanes. Own investigations marked with ∗.

Investigation		Test rig				Scope				Slot geometry			Injection			Measuring technique
Author	Year	①	②	③	④	η_{ad}	h_f	ζ	SEC	$\alpha/^\circ$	$\#W$	L/C_x	BR	$MFR/\%$	DR	
Blair [16]	1974	ls	lin	1	fl	●	●	○	○	30	1	0.04	0.5, … , 1.0	-	1.05	TC
Granser and Schulenberg [57]	1990	hs	lin	1	fl	●	○	○	●	36	1	0.46	0.097, … , 2.3	-	0.81	TC, Oil
Burd and Simon [59], [51]	2000	ls	lin	2	ax	●	●	●	○	45	1	0.1	0, … , 1.59	-	≈ 1	TC, HW, Pitot
Kost and Nicklas [60], [61]	2001	hs	lin	12	fl	●	●	●	●	45	1	0.2	1.3	-	0.81, … , 1.09	IR, L2F, Pitot
Zhang and Jaiswal [62]	2001	hs	lin	4	fl	●	○	○	○	45	1	0.2	-	0.5, … , 3	1	PSP
Oke et al. [63]	2001	ls	lin	2	ax	●	○	○	●	45	1	0.2	-	1.65, 3.3	≈ 1	TC-P, HF-A
Colban et al. [64]	2003	ls	lin	2	fl	●	○	○	●	bfs	1	0.08	0.56, … , 0.8	-	0.97	IR, LDA
Knost and Thole [65]	2005	ls	lin	2	n-ax	●	○	○	○	45	1	0.35	-	0.5, … , 1	1.14	IR
Cardwell et al. [66]	2006	ls	lin	2	fl	●	○	○	○	45	3	0.38	0.22, … , 0.66	-	1.14	IR
Kost and Mullaert [67]	2006	hs	lin	12	fl	●	○	○	●	45	1	0.3	1.3	-	0.81, … , 1.09	IR, L2F
Piggush and Simon [68]	2007	ls	lin	2	ax	○	●	○	○	30	1	0.11	0, … , 2.4	-	≈ 1	TC-Probe
Lynch and Thole [69]	2008	ls	lin	2	fl	●	●	○	○	45	2	0.77	0.19, … , 0.73	-	1.1	IR
Thrift et al. [36, 70]	2011	ls	lin	2	fl, ax	●	●	○	○	90, 74	1	0.17	-	0.25, … , 1	≈ 1	IR
Thrift et al. [71]	2012	ls	lin	2	fl	●	○	○	●	90, 45	3	0.05, 0.17, 0.34	1.67	-	≈ 1	IR, PIV
Takeishi et al. [72][3]	2015	ls	lin	4	fl	●	○	○	●	90, 45	1	0, … , 0.04	0.25, … , 0.75	-	≈ 1	PSP, PIV, LIF
Barigozzi et al. [73], [74]	2017	ls	lin	5	fl	●	●	●	●	90	1	0.158	-	0.5, … , 1.5	1	PSP, TLC, 5HP
Chen et al. [58]	2016	ls	lin	4	fl	●	○	○	○	25	1	0.07	0.5, … , 1.5	-	1, 1.5, 2	PSP
∗ Müller et al. [9], [10]	2019	hs	lin	5	fl	●	○	●	●	90, 45, 30	2	0.14, 0.28 ,0.41	0.25, … , 1.5	-	1, 1.6	PSP, 5H-P, Oil
∗ Landfester et al. [11, 12]	2021	hs	lin	5	ax	●	○	●	●	90, 45, 30	2	0.17, 0.23, 0.35	0.25, … , 1.5	-	1, … , 1.6	PSP, IR, 5HP, Oil
∗ *New Annular Test Rig (plan.)*	2023	hs	ann	5	ax	●	●	●	●	90, 45, 30	2	0.17, 0.23, 0.35	0.25, … , 1.5	-	1, … , 1.6	PSP, IR, 5HP, Oil

① Low-speed/high-speed ② Cascade design (linear, annular) ③ Number of full passages ④ Endwall design (flat, axisymmetric, non-axisymmetric) 3 Investigation of stator/rotor cavity leakage flow

and the passage crossflow. However, when classifying these results, the influence of the injection angle must be taken into account: As to be shown in Chapter 4.4.4, high-density coolant performs slightly better when injected through a perpendicular slot at high blowing ratios since separation and mixing with the mainstream is reduced.

Influence of slot angle: While most of the investigations were carried out with fixed slot inclination, Thrift et al. [71] were the first to directly study the influence of the slot angle under low-speed conditions, using both a 45° and a 90° setup. They observed that the inclined slot provides a substantial improvement in the endwall cooling performance over the perpendicular orientation, as the coolant coverage was increased at every location within the vane passage. These findings were supported by Takeishi et al. [72], who compared inclined and perpendicular slot designs, but for rotor blades. Additional LIF and PIV measurements indicated that the risk of hot gas ingestion at low blowing ratios could be reduced by inclining the slot.

Influence of slot width: A broad investigation on the influence of the slot width was conducted by Cardwell et al. [66] in a low-speed cascade with an inclined slot. When comparing varying slot width while maintaining the mass flux ratio, they found that decreasing the slot width caused the coolant to be more evenly distributed on the endwall, with a substantial increase in cooling on the pressure side. As with the density ratio, these effects must be attributed to the increased coolant momentum. If, instead, the momentum is kept constant, the area of coolant coverage is found to be very similar for all slot widths investigated. However, with the mass flux ratio being reduced, the coolant effectiveness levels from the narrow slot flow are lower relative to the wider slots. These findings are supported by a similar study conducted by Lynch and Thole [69], with the inclined slot positioned at a more upstream position. They pointed out that matching the momentum flux ratio is a more realistic situation for a turbine engine, as the coolant will be supplied at a constant pressure relative to the mainstream.

Influence of slot distance: In addition to the variation of slot angles, the investigation of Thrift et al. [71] provides insights into the influence of the slot position, as they varied the distance between the perpendicular slot and the leading edge in three steps. While the far upstream position was shown to have little impact on the endwall cooling performance, the position closest to the leading edge improved both the local and area-averaged film cooling effectiveness. This was explained by the fact that the separated coolant is quickly turned towards the endwall in the presence of the vane stagnation pressure, thus reducing the mixing length with the mainstream.

However, a study by Kost and Mullaert [67] that was conducted in a transonic cascade with an inclined slot at a constant blowing ratio showed that moving the slot downstream does not necessarily improve film cooling effectiveness but depends on the position of the injection relative to the saddle point, where the migration of coolant away from the endwall is promoted by the emerging horseshoe vortex.

Influence of endwall design: As explained in Chapter 2.1.2, endwall contouring aims to improve aerodynamics by weakening secondary flow. With respect to the strong influence of secondary flow on the coolant propagation, the question arises to what extent the findings of investigations carried out on flat endwalls can be transferred to contoured designs. On this question, to the knowledge of the author of the present work, there is no experimental research available that would compare two endwall designs under otherwise identical main flow and coolant conditions.

An investigation by Thrift et al. [36, 70] in two linear cascades with flat and contoured endwalls revealed that coolant coverage was the largest for the contoured endwall at each flow rate tested. However, concerning the above question, the study is compromised by the fact that the slot angle was slightly varied between the two designs. In addition, with a span ratio of $h_{\mathrm{out}}/h_{\mathrm{in}} = 0.86$, the vane that was used in this investigation, exhibits a relatively low contraction, when compared, for example, to the vane design applied in the present work.

Own investigations [9], which were carried out on flat and contoured vane designs, can only be consulted to a limited extent on this issue since the vanes examined differ considerably in terms of their profiling. Notwithstanding, the comparison also suggests that contouring is, in principle, beneficial for film cooling performance: First, the passage contraction facilitates the reattachment of the separated coolant. Second, the weakening of the horseshoe vortex and the subsequent mitigation of the passage crossflow promote the propagation of coolant.

2.3.3 Interaction of Coolant and Main Flow

Just as the propagation of coolant is affected by secondary flow, the upstream injection of coolant can, in turn, influence the emergence and downstream development of the horseshoe vortex system. However, it is important to stress that no general statements can be made, as the interaction between the coolant and the main flow depends not only on the coolant momentum but on the slot parameters and the vane design as well.

An investigation of Biesinger and Gregory-Smith [75], although not directly related to film cooling, revealed that a low-momentum injection increases the effective inlet boundary layer thickness, resulting in a strengthening of secondary flow. If the coolant momentum, however, is increased, the inlet boundary is re-energized, weakening the passage vortex. Regarding slot inclination, they conclude that a low injection angle is more effective than a high angle in countering secondary flow.

Kost and Nicklas [60], who performed in-passage flow field measurements in the same transonic cascade mentioned above, observed that the horseshoe vortex is strengthened, while the endwall crossflow, and consequently the passage vortex, is weakened by the coolant injection. They concluded that the strengthening effect must be attributed to the location of the inclined slot, being positioned just in the region of the saddle point. However, in the follow-up study by Kost and Mullaert [67] regarding the influence of slot distance, it was shown that the observed intensification of the horseshoe vortex could be avoided by placing the inclined slot further upstream. Other authors confirmed that inclined injection can actually suppress the development of secondary flow, such as Zhang and Jaiswal [62],

who conducted an investigation with a similar inclined slot design on a flat endwall. The same holds true for an inclined injection on an axisymmetrically contoured endwall, as shown by Burd and Simon [59], who observed that the secondary flow structure near the contoured endwall is progressively suppressed for an increasing blowing ratio.

However, if the coolant is injected through a perpendicular slot, secondary flow intensifies, as the incoming boundary layer of the mainstream is forced to separate upstream of the slot. According to Thrift et al. [71] and supported by own investigations at the high-speed turbine test rig [9], the perpendicular injection results in the formation of a large leading-edge vortex, which amplifies the horseshoe vortex by its additional momentum.

With the suppression or amplification of secondary flow, the question arises of how the overall aerodynamic performance of the stage is influenced by the coolant injection. However, only little data are available concerning this question. On the one hand, the results obtained in the low-speed investigation by Burd and Simon mentioned above suggest that the inclined injection is accompanied by no or little aerodynamic penalty. On the other hand, Kost and Nicklas [60] found that the aerodynamic loss was notably increased in a high-speed investigation, which may be attributed to both the amplification of the horseshoe vortex and the intensification of turbulence. Aerodynamic measurements with a five-hole probe at the outlet of a cylindrical vane design, which were conducted at the institute's own high-speed turbine test rig, suggest a more complex relation: While a perpendicular injection induces higher losses throughout all blowing ratios, the inclined injection indicates that the aerodynamic efficiency can be actually improved [10]. However, it must be considered that, firstly, compared to [60], the additional energy introduced by the injected coolant was not balanced and, secondly, the measurements in the immediate vicinity of the endwall could not be carried out due to the limitation of the probe.

2.4 Experimental Modeling Approaches

Experimental modeling of turbomachinery flow in general and of flow through guide vanes, in particular, can be carried out at different levels of abstraction, which are shown schematically in Figure 2.5. Each abstraction level is associated with simplifications that alter the flow in the test compared to the flow in the real engine. A so-called full load shop test (level 0), as described, e.g., by Maekawa et al. [76], is performed on the entire engine. It is, therefore, obviously not only impractical for an application in the academic environment but also rather unsuitable for basic research since the measurement accessibility and test design flexibility are severely limited.

The first step in reducing experimental complexity is to restrict the investigation to one or more stages (level 1) of the turbine. While this approach reproduces the rotor-stator interaction, it neglects the combustor-turbine interaction. However, swirl generators, such as those used at the 1.5-stage

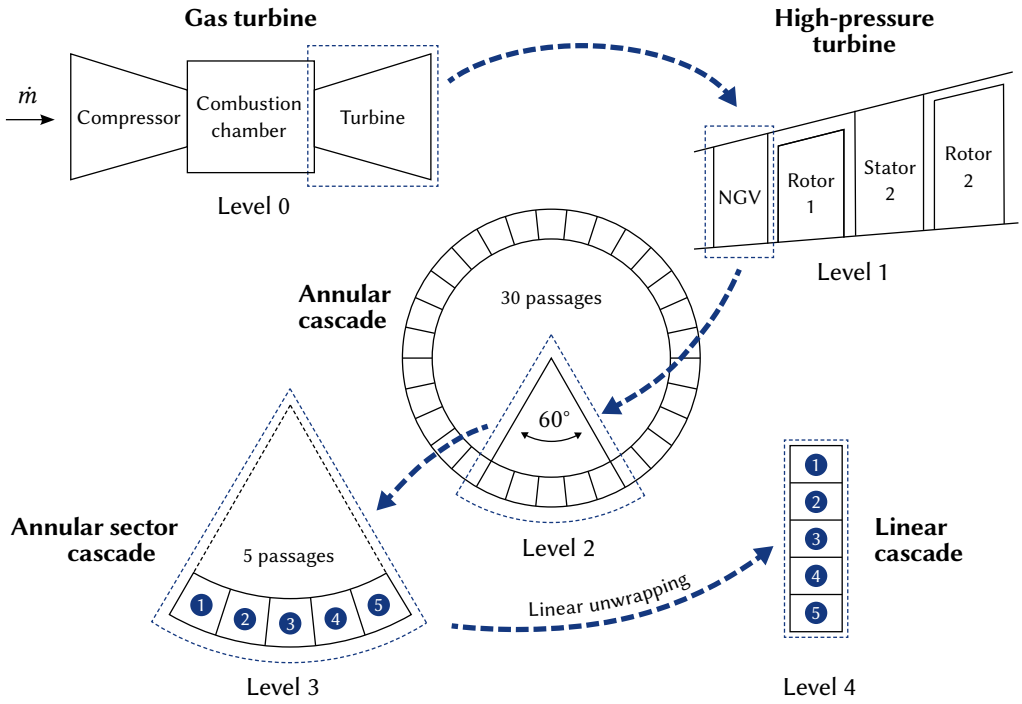

Figure 2.5: Modeling levels of the first nozzle guide vane flow (adapted from Franze [8])

turbine test rig at the Institute of Gas Turbines and Aerospace Propulsion (Technical University of Darmstadt, Germany) that was commissioned by [77] can be utilized to simulate and investigate the effects of a combustion chamber.

The second step of abstraction is realized in an annular cascade (full annulus) that consists of a single row of (rotating) blades or vanes, although some test rigs model a complete stage to reproduce the actual inlet or outlet conditions while still being classified as annular cascades in the literature. Annular cascades tend to play a relatively minor role in turbine studies because they are still relatively costly to build and operate, with the major hurdle being the high mass flow requirement, especially when testing under high-speed conditions is required. This difficulty can be mitigated by limiting the study to one sector, which constitutes the next level of abstraction. Restricting the flow domain to a finite number of blades or vanes on the meridional plane introduces periodicity issues between the individual passages, which have to be addressed by a proper design of the outer passages, e.g., by using tailboards or boundary layer bleeding in the upper and lower channel walls [78].

The vast majority of aerodynamic testing in the field of turbomachinery is conducted in linear cascades, which in the simplest case are derived from unwrapping and flattening out the cylindrical meridional section of the annulus [79]. Low cost, simple design, and easy access for probe and optical measurements are the main reasons for the widespread use of such cascades. They represent the

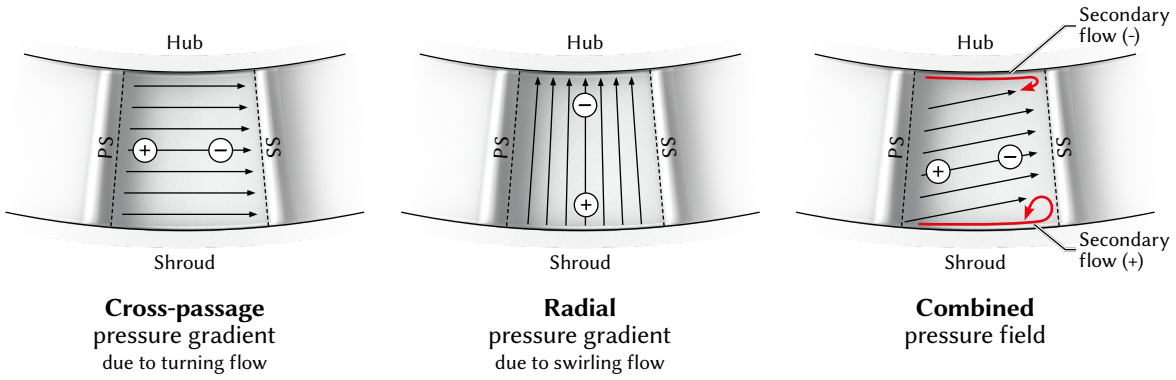

Figure 2.6: Pressure gradients in an annular cascade (adapted from Povey et al. [81])

highest level of abstraction, although it should be mentioned that many landmark studies, especially on film cooling (e.g., Goldstein et al. [80]), have even been performed on a flat plate, neglecting the pressure gradient present in cascade flow.

Pressure gradients in an annular cascade: The general advantage of annular cascades over linear ones arises from the fact that only an annular test design accounts for the radial pressure gradient that naturally emerges from swirling flow. The existence of this radial gradient can be deduced from the simple radial equilibrium equation, which is given for an axisymmetric and inviscid flow by:

$$\frac{\partial p}{\partial r} = \rho \cdot \frac{c_\varphi^2}{r} \tag{2.11}$$

It stated that the centripetal acceleration c_φ^2/r of a fluid particle that keeps the flow moving on a circular path with the tangential velocity c_φ must be balanced by a radial pressure gradient, which always acts in the negative radial direction. Therefore, the static pressure in a swirling flow in an annulus always grows as the radius increases [13].

The pressure field in an annular cascade is thus composed of both a cross-passage pressure gradient (due to the turning flow) and a radial pressure gradient, as shown in Figure 2.6. As it also affects the low-momentum fluid near the endwalls, it promotes the growth of secondary flow in the shroud region while inhibiting the growth of the secondary flow near the hub [81].

The influence of the radial pressure gradient on the flow field was exemplarily demonstrated in an essential study on a cylindrical guide vane in a full annular cascade that was carried out in a low-speed turbine test rig by Sieverding et al. [7]. With a hub-to-tip ratio of ≈ 0.8, it roughly matches the ratio specified for the test rig presented here (see Table 3.1). The flow field was investigated using four-hole pressure probes in twelve axial planes from upstream to far downstream of the vane row.

The study highlights the effects that are, by their very nature, absent in a linear test design: While the radial pressure gradient is still weak at the passage inlet, their results indicate that the radial pressure gradient has taken significant proportions at the passage outlet, in particular near the suction

side where the pressure difference between the hub and the shroud amounts to 30 % of the outlet dynamic head. It is noted that the direct effect of the pressure gradient is amplified by the generation of passage vortices of different strengths at the hub and the shroud, causing significant differences in the loss and flow angle distribution within and downstream of the passage. With respect to loss generation and propagation, they found that the radial pressure gradient is the driving force for the radial migration of low-momentum material from the shroud to the hub.

Exit flow conditioning and periodicity: When setting up the flow conditions at the cascade outlet, a common technique is to allow the exit flow to develop freely through an extended annulus of a constant radius or an axial diffuser before being discharged into a constant pressure plenum. This approach has been successfully field-tested, for example, in the aforementioned study by Sieverding et al.. However, when discharging swirling flow into a plenum of constant pressure, the hub boundary layer may separate, as it is exposed to an adverse pressure gradient toward the exit of the annulus. Thereby, the risk of flow separation increases when the hub-to-tip radius ratio decreases [78, 81]. To overcome this problem, test designs often include a (stationary) row of rotors or de-swirlers behind the vane that turn the swirling flow in the axial direction.

Figure 2.7 provides a schematic representation of the approaches documented in the literature. However, it should be noted that the applicability of these full annulus approaches within a sector cascade is limited due to the lack of rotational symmetry. In particular, the design of a radial diffuser within an annular sector would pose design problems, as the top and bottom walls of the sector would have to follow both the flow path and the diffuser shape.

The rotor-based approach was tested in an investigation by Boletis and Sieverding [82] on the annular test rig that was previously introduced by Sieverding et al. [7]. Accordingly, the presence of a rotor introduced minor changes to the outlet flow field, which were, however, limited to the hub-near half span. They concluded that it is possible to perform annular nozzle tests without a downstream

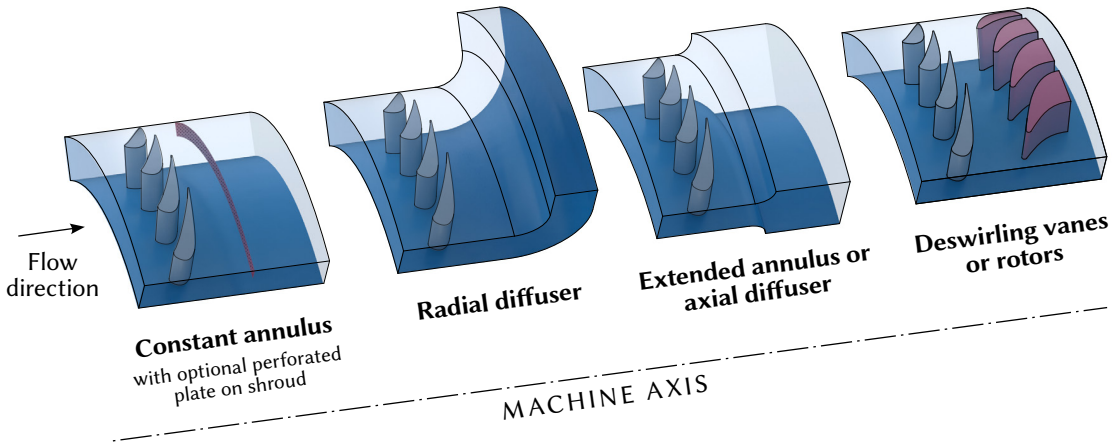

Figure 2.7: Methods of setting annular cascade exit conditions (adapted from Povey et al. [81])

rotor if the outlet duct has an appropriate length. But it is important to note that in the test performed by Boletis and Sieverding, no separation was apparently observed even without a rotor. A high-speed investigation by Williamson et al. [83] came to the opposite conclusion, stating that using a rotor could completely eliminate the separation that sets in on the hub for the vane-only variant. However, when examining the spanwise distribution of pressure losses and flow angles provided in the study, it can be observed that even in the case of flow separation, the changes are virtually limited to the hub-near half span. Considering the research objectives of the cascade presented here, the usefulness of a rotor can therefore be doubted, as the investigation will be limited to the shroud region.

Another method to inhibit flow separation by balancing the radial pressure gradient that is present in the swirling outlet flow was presented by Squire [84] for an annular steam turbine test rig. He used a perforated plate that was mounted on the shroud downstream of the trailing edge and imposed a pressure drop to the flow near the shroud.

However, with regard to the objective of the test rig presented here, the author believes that the optimization of periodicity is of greater importance because it is also likely to have a much greater effect on the flow within the passage: First, non-periodicity originates upstream leading edge and propagates through the whole passage, and second, it extends over the entire span. Unfortunately, there is little data in the literature that addresses periodicity in annular sector cascades. Regarding the overview of annular sector test rigs in Table 2.2, there is only one study to be highlighted: The experimental investigation was carried out by Wiers and Fransson [85] in the high-speed annular sector test rig that was commissioned by Wiers and Fransson [86] at the KTH Royal Institute of Technology (Stockholm, Sweden). The 5-passage cascade with a contoured shroud endwall was tested with six different outlet configurations that utilized both tailboards at the outer vanes and radial diffusers. Remarkably, they found that the best periodicity was obtained in a configuration where both the tailboards and the radial diffuser were dismounted. A dump diffuser, i.e., a constant pressure plenum, downstream of the cascade instead of a smooth guiding had a positive effect on the periodicity because, as they assumed, the exit flow develops as a free jet, and the flow angle adjusts itself to the downstream back pressure. This concept was successfully adapted by Saha et al. [87] in another 4-passage annular sector cascade that was installed in the same test facility.

Povey et al. [81] presented a de-swirling concept for a 5-passage cascade that basically ties into the idea of a fixed rotor. However, the more interesting part of their study concerns the experimental investigation of two upper/lower channel wall designs that bound the transition piece between the guide vane exit and the de-swirling inlet. In principle, these walls act as tailboards, as they impose a defined pitch angle on the exit flow. While the walls of the first design were slightly curved to de-swirl the flow to a certain extent before actually entering the de-swirling vanes, the pitch angle of the second wall design was constant. The pressure distribution downstream of the vane row was highly skewed for the first design, with the pressure ratio between the two outer passages differing by almost 40 %. The second design provided much better periodicity, at least for the three inner passages.

Table 2.2: Overview of annular sector cascades for film cooling investigations

Author	Location	Year	①	②	③	④	T_m / °C	$\dot{m}_m$ / kg s^{-1}	Π_{max}	Technique
Wiers and Fransson [86]	Stockholm, Sweden	1998	ol	hs	5	ax	0 ... 180	4.7	4	PT, TC, 5HP
Rådeklint and Hjalmarsson [88]	Finspong, Sweden	1998	ol	hs	5	fl	130 ... 900	10	20	PT, TC, IR
Povey et al. [81]	Oxford, United Kingdom	2004	bd	hs	5	ax	20 ... 50	2.3	3	PT, TC, TLC
Krivonosova et al. [89]	Saint-Petersburg, Russia	2011	ol	hs	4	fl	1000	10	6	PT, TC
Dees et al. [90]	Niskayuna, New York	2013	n/a	hs	5	ax	120	n/a	n/a	PT, TC
Saha et al. [87]	Stockholm, Sweden	2014	ol	hs	4	ax	30	4.7	4	PT, TC, 5HP

① Wind tunnel typ (open-loop/blow-down) ② Low-speed/high-speed ③ Number of full passages ④ Endwall design (flat, axisymmetric)

Notwithstanding the application of de-swirlers, this study highlights the sensitivity of periodicity to the exit geometry. Regarding the development of the test rig presented here, fixed walls, as used by Povey et al., seem to be rather disadvantageous here due to the lack of adjustability.

A similar finding was obtained by Dees et al. [90], who investigated the periodicity of vane loading and outlet flow experimentally and numerically in a similar 5-passage cascade with fixed upper/lower channel walls. They suggested that the wall respectively tailboard design should be numerically optimized using a full-rig CFD approach, which is adopted in the present work.

2.5 Scope of the Present Work and Research Objectives

The landmark study by Sieverding et al. [7] presented in the previous section has clearly demonstrated the influence of the radial pressure gradient on the generation and propagation of secondary flow in turbine flow. At the same time, it is known from previous research on film cooling performance that secondary flow has a significant effect on coolant distribution. However, the existing research on upstream slot film cooling has a blind spot in this regard, as none of the above studies have experimentally investigated the film cooling performance with respect to the radial pressure gradient using an annular cascade. Furthermore, although many papers provide valuable insights into individual aspects, there are few studies that coherently investigate film cooling effectiveness, heat transfer, and passage aerodynamics. Last but not least, the literature review revealed that the majority of studies have been performed under low-speed conditions, i.e., engine-like Mach numbers and their effects

on the secondary flow have not been reproduced. Therefore, the main objective of this work is to develop an annular sector test rig that allows the investigation of both the thermal and aerodynamic aspects of film cooling from an upstream slot under engine-like conditions concerning Mach and Reynolds numbers.

The contoured nozzle guide vane design to be adopted in the test rig represents state-of-the-art turbine design that utilizes measures for reducing secondary flow, as presented in Chapter 2.1.2. With respect to the influence of vane design on film cooling performance, the results to be expected from the test rig are, therefore, of great significance.

The design of an annular sector cascade is confronted with two major challenges: First, as with linear cascades, the finite number of vanes poses flow periodicity issues that must be addressed by suitable measures. Second, outlet conditions must be established to prevent an (early) flow separation of the boundary layer on the hub, as it is exposed to an adverse pressure gradient. At the same time, the design must provide for integrating the measurement methods, which are explained in detail in the following chapter. Here, the findings and experiences from the previous measurements in the linear cascade, presented in Chapter 4, shall serve as a basis on which to refine the measurement methods. Given the results already available from these measurements, the new test rig also allows for a future evaluation of the influence of the radial pressure gradient, following up on Sieverding's investigation.

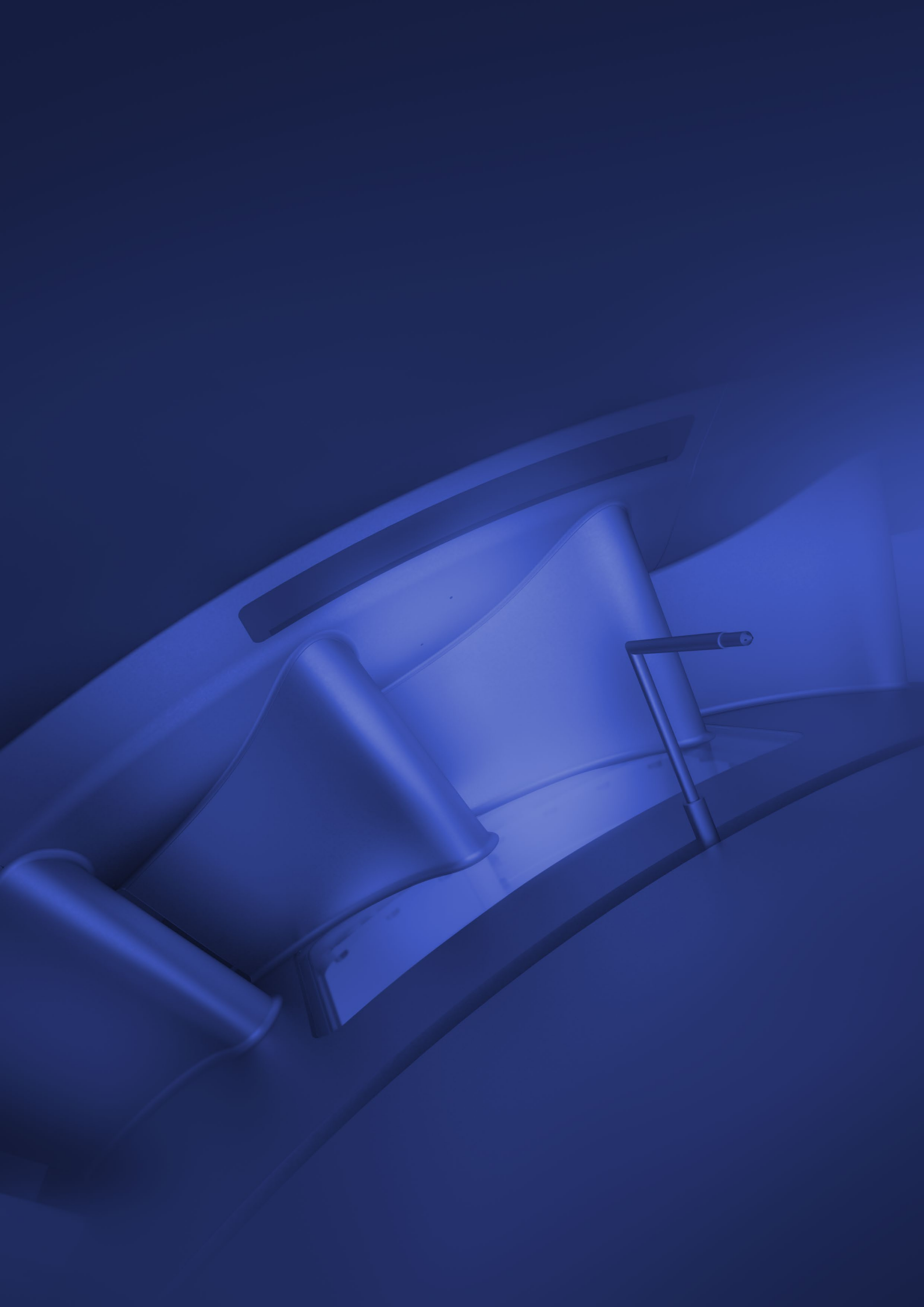

Experimental Methods and Setup

This chapter is dedicated to the specifications of the test rig and the annular cascade. In addition, the major measurement methods, namely five-hole probes, pressure-sensitive paint, and IR thermography, are presented in detail with a focus on the application in the annular cascade. Further details that are necessary for the discussion of the results from the linear measurement campaign are provided in Chapter 4. The endwall oil-flow visualization, which was carried out with a 70:30 mixture of highly viscous silicon oil (5000 cSt) and UV dye, is not covered separately in this chapter, as it is one of the standard methods of flow investigation.

3.1 High-Speed Turbine Test Rig

The high-speed turbine test rig at the Institute of Fluid Machinery and Fluid Dynamics (SAM) of the University of Kaiserslautern-Landau was originally planned and commissioned by Franze [8]. Designed as a pressurized open wind tunnel, the test rig allows the investigation of cascade aerodynamics and film cooling performance under machine-like conditions with respect to Reynolds and Mach numbers.

The flow chart of the turbine test rig, depicted in Figure 3.1, can be divided into a main flow, a coolant flow, and a bypass, which is used for the five-hole probe calibration. The main flow is provided by a screw compressor (Aerzen Delta Screw VML 95) with an electrical power of 250 kW. It supplies a mass flow rate of up to $2.2\,\mathrm{kg\,s^{-1}}$ at a maximum pressure ratio of 2.5, i.e., sufficient reserves are available to match the actual pressure ratio of a single turbine stage. The main flow can also be fed temporarily via a throttled pressure vessel ($\Pi \leq 10$) either to extend the operating range or to perform low-speed probe calibrations. Since the main flow heats up to 125 °C after compression, a cooler ($P \leq 200\,\mathrm{kW}$) is installed downstream to allow tests to be carried out under isothermal

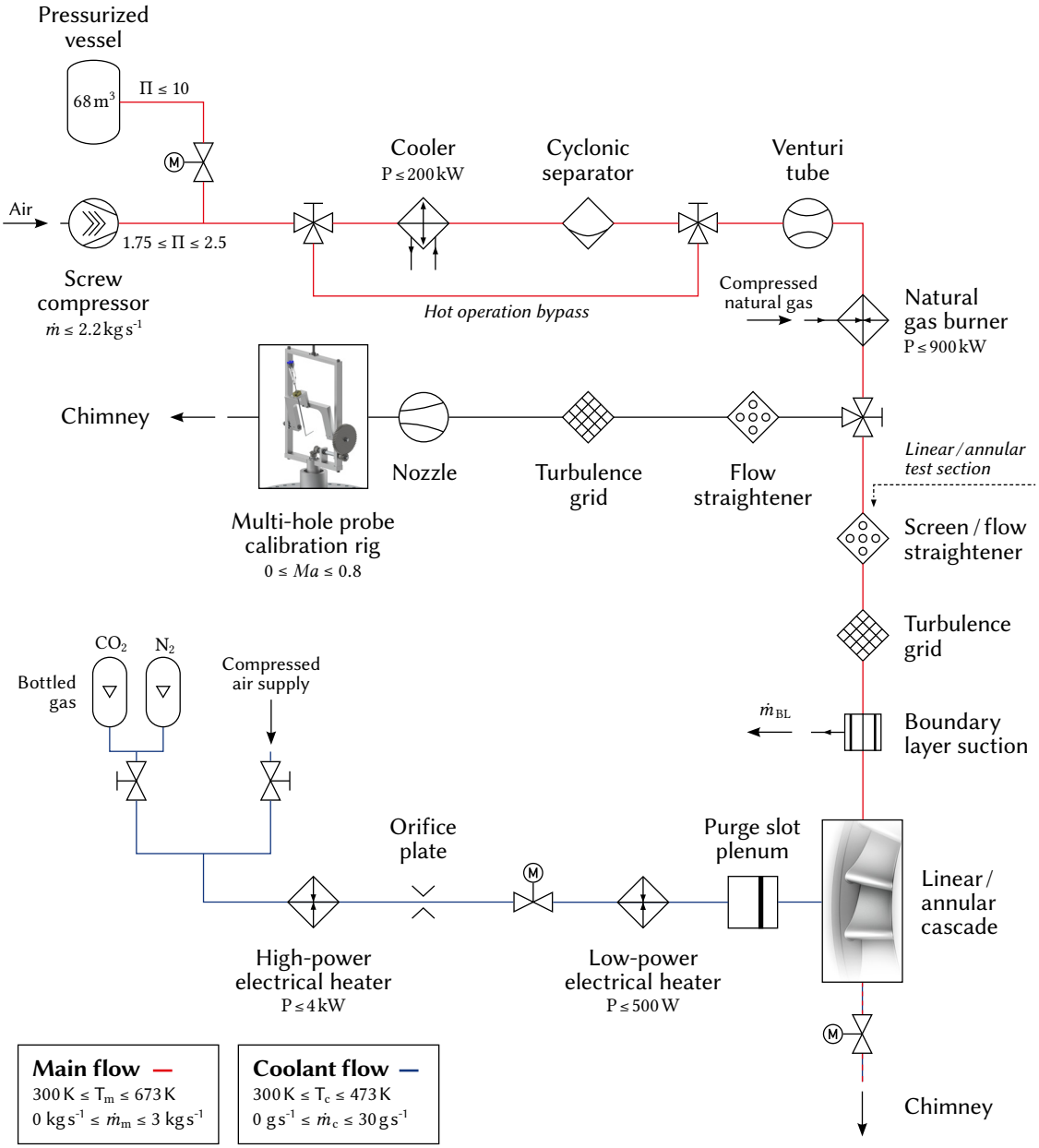

Figure 3.1: Flow chart of the high-speed turbine test rig

conditions within the application limits of pressure-sensitive paint, ranging from 0 °C to 50 °C. A cyclonic separator behind the cooler ensures that these low-temperature tests can be carried out with dry air. Downstream of a Venturi nozzle for mass flow metering, the flow passes through a custom-made gas burner (Seibold FC5, $P \leq 900\,\mathrm{kW}$) which is capable of heating the main flow up to 400 °C at maximum compressor output. The burner is supplied with natural gas that is compressed to an absolute pressure of 3 bar by a single-stage piston compressor (Mehrer TEL 80).

Downstream of the burner, the mainstream can be fed either into the test section or, via a bypass, into the probe calibration section. Within the test section, the circular cross-section is converted to a rectangular respectively annular cross-section using a transition duct before the flow is equalized by screens and straighteners. For the generation of isotropic turbulence, a grid is installed further downstream. Before the flow enters the cascade, the existing boundary layer is separated with a suction unit on the hub and shroud to ensure a defined boundary layer thickness at the cascade inlet. The dimensioning and design of these components for the annular cascade are presented in detail in Chapter 5. The bypass for probe calibration is also equipped with flow conditioning, such as a screen and a straightener. A comprehensive overview of the calibration device can be found in section 3.3.2.

The pressure ratio of the cascade can be readjusted over the entire rotational speed range of the screw compressor by means of a motorized throttle valve at the outlet, which expands the main flow to near ambient pressure before discharging it through a chimney.

The coolant flow is either provided from the university's own compressed air supply system or from bottled gas, which is necessary for the pressure-sensitive paint measurements (see section 3.4.1). A high-power electric heater ($P \leq 4\,\mathrm{kW}$) is used to pre-heat the coolant to a temperature of up to 200 °C. An array of orifice plates is used to measure the mass flow of the coolant, which is adjusted by a motorized control valve. A retrofitted low-power ($P \leq 500\,\mathrm{W}$) heater immediately upstream of the coolant plenum allows for fine-tuning of the coolant temperature with short response times to temperature fluctuations in the main flow or when bottled gas is drawn (see section 3.4.3).

3.2 Specifications of the Annular Cascade

The geometric parameters of the annular cascade are depicted in Table 3.1. As already discussed in the previous chapter, the nozzle guide vane represents a state-of-the-art gas turbine design and was provided by MAN Energy Solutions: It features an axisymmetric contouring of the shroud endwall, which reduces the span at the outlet to 62 % of the inlet height, lowering secondary-flow induced losses and thus increasing aerodynamic efficiency. In addition, the vane profile, which was designed using numerical methods, is slightly twisted for the purpose of equalizing mass throughput over the vane height. Fillets along the vane root also contribute to the reduction of secondary flow, especially with regard to the formation of the horseshoe vortex at the leading edge. For manufacturing reasons, the fillets have been simplified with a constant radius compared to the original design.

Table 3.1: Geometric parameters of the annular cascade

Parameter	Symbol	Value	Parameter	Symbol	Value
Scaling		1.37	Pitch, mid	s_{mid}	90.4 mm
Span, inlet	h_{in}	85.5 mm	Turning angle	$\Delta\beta_{\mathrm{mid}}$	76.3°
Chord length, mid	C_{mid}	100 mm	Stagger angle	λ_{mid}	60.7°
Axial chord length, mid	$C_{\mathrm{mid,x}}$	49 mm	Span ratio	$h_{\mathrm{out}}/h_{\mathrm{in}}$	0.62
Radius hub	r_{h}	389 mm	Aspect ratio	$h_{\mathrm{in}}/C_{\mathrm{mid}}$	0.86
Radius shroud, inlet	$r_{\mathrm{s,in}}$	474.5 mm	Hub-tip ratio, inlet	$r_{\mathrm{h}}/r_{\mathrm{s,in}}$	0.82
Radius shroud, outlet	$r_{\mathrm{s,out}}$	442 mm	Solidity, mid	$C_{\mathrm{mid}}/s_{\mathrm{mid}}$	1.11

The comparatively high aspect ratio of the vane – the usual value for an NGV amounts to approximately 0.6 [92] – is intended to weaken further the influence of endwall-induced secondary flow on the passage flow. Since the circular-annular transition duct that is presented in Chapter 5.4 had already been manufactured for a previous project, the vane design was modestly scaled, matching the hub radius of the inlet segments. Furthermore, the scaling improved accessibility and simplified the integration of the measurement equipment.

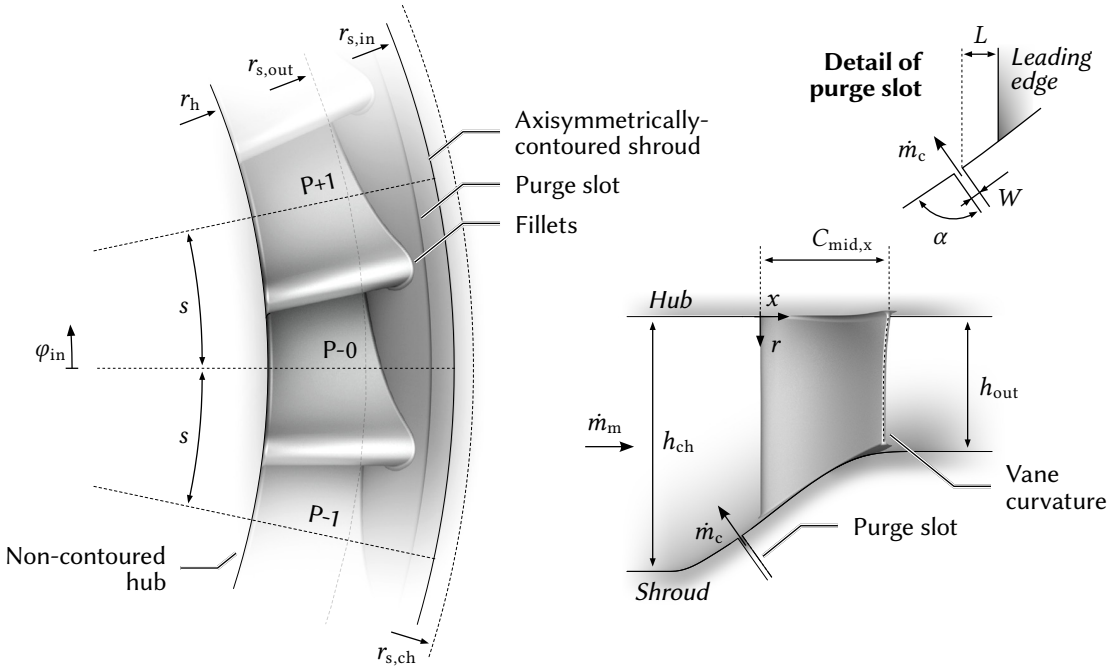

Figure 3.2: Nomenclature of the annular cascade and geometric parameters of the purge slot

Table 3.2: Mainstream and coolant parameters of the linear and annular cascade

Parameter	Symbol	Value
Reynolds number, inlet	Re_{in}	2.35×10^5
Reynolds number, outlet	Re_{out}	2.1×10^6
Mach number, inlet	Ma_{in}	0.067
Mach number, outlet	Ma_{out}	0.76
Inlet turbulence	Tu_{in}	5.2 %
Pressure ratio	Π	1.48
Blowing ratio	BR	$0.25, 0.5, \ldots, 1.5$
Density ratio (PSP)	DR	1 and 1.6
Density ratio (HT)	DR	$1.2, \ldots, 1.44$

The nomenclature of the annular cascade and the geometric parameter definition of the purge slot are illustrated in Figure 3.2. The central passage containing the slot insert is designated P-0. Since the local main flow direction is relevant to the interaction with the coolant, the slot angle α is defined on the local wall, normal to the shroud endwall that was linearly extended in the upstream direction along the platform angle of 30° to meet the channel height of 100 mm provided by the inlet segments.

The aerodynamic specifications of the mainstream and coolant are depicted in Table 3.2. The Reynolds numbers and Mach numbers that can be realized in the test rig correspond to the actual flow conditions in the real engine. As already discussed in the previous chapter, film cooling effectiveness is highly sensitive to changes in the coolant mass flux. In the actual engine, the blowing ratio can be adjusted in the design process within certain limits by the stage-wise positioning of the compressor bleeding points. To reflect the typical range found in the relevant literature, the blowing ratio was adjusted in small steps between 0.25 and 1.50. The density ratio between the coolant and the mainstream is varied for the PSP measurements by using foreign gases of different molecular weights, with the unity density ratio obtained by ejecting nitrogen and the high-density ratio setup realized by ejecting carbon dioxide. As already discussed in Chapter 2, $DR = 1$ is only an academic test case, while in the actual engine, DR typically ranges between 1.4 and 2 due to the inherent temperature difference between the coolant and the main flow. However, this configuration is intended for comparison with literature data and to reveal the influence of the density ratio. Furthermore, performing five-hole probe measurements in cold operation can only be implemented with compressed air ejection since the consumption of foreign gas would exceed the capacity of the cylinder bank due to the long duration of the measurement.

In principle, the density ratio in the heat transfer measurement campaign can be adjusted continuously by selecting the main flow and cooling air temperature within the operational limits of the components according to section 3.1. While the test rig architecture was originally designed for

main flow temperatures up to 400 °C, the hot gas operation is limited to 160 °C in order to keep the ambient temperature in the test room at an acceptable level, therefore limiting the density ratio to 1.44 with $T_c = 20\,°C$. To exploit the temperature capabilities of the test rig in future investigations retrofits such as a high-performance air conditioning system in the test room are required, which could not be realized within the scope of the current project. The results of linear measurement campaign, as presented in Chapter 4.6, were obtained with $DR = 1.2$ and $DR = 1.3$ at mainstream temperatures of 90 °C respectively 160 °C.

Table 3.3 summarizes the geometric parameter combinations of the purge slot that are realized in both the linear and the annular measurement campaign. The parameter set is inspired by specifications commonly found in the literature (see Chapter 2) and incorporates technical considerations of both turbine design and operation. Thus, the slot width W was varied between 1 mm and 2 mm to reflect dimensional changes in clearance caused by thermal expansion of the turbine components. The variation of slot distance L, which ranges between 9 mm and 18 mm, accounts for the fact that the axial length of the vane platform can be adjusted within certain limits in the design process. The same applies to the slot angle α, which is varied between 90° and 30°, with the slot distance kept constant at 9 mm for the 45° and 30° variant since the slot insert does not provide enough space for positioning the inclined slot further upstream.

Table 3.3: Geometric parameter combinations of the purge slot

		$\alpha/°$		
W/mm	L/mm	90	45	30
1	9	●	●	●
	12	●	○	○
	18	●	○	○
2	9	●	●	●
	12	●	○	○
	18	●	○	○

3.3 Five-Hole Probes for Flow Field Measurements

It is a common practice to use multi-hole pressure probes to determine the local total and static pressure, velocity, and direction in a three-dimensional flow. However, even a simple Pitot tube is subject to a certain dependency between the pressure reading and the flow direction. The magnitude of the deviation from the actual total pressure is dependent on both the probe head geometry and the incidence. If a probe is intended for flow direction measurements, high angular sensitivity is desirable. For this reason, multi-hole pressure probes are applied, which feature additional pairs of symmetrically

distributed peripheral pressure taps to the central tap typical of a Pitot tube. While designs with only one pair of additional pressure taps are used for two-dimensional flow fields, two-pair configurations, i.e., five-hole probes are utilized for three-dimensional flows in a pitch and yaw range of usually ±30°[93]. Due to the highly three-dimensional nature of the cascade flow, especially at the outlet of the passage on account of the secondary flow, five-hole probes are utilized in the present setup.

3.3.1 Measurement Principle and Probe Nomenclature

The L-shaped five-hole probe design, which was developed at the institute and is used for aerodynamic measurements at the inlet and outlet of the cascade, is shown in Figure 3.3. The tip is designed as a cone with a base diameter of 2.45 mm and an aperture of 60° containing forward-facing peripheral bores with 0.3 mm diameter.[4] The pitch and yaw planes are assigned according to the subsequent installation situation, as the probes are inserted laterally via the hub endwall (see Figure 5.38). An additional circumferential static pressure ring allows the static pressure to be measured directly. The dimensions of the probe, i.e., the tip and shaft diameter, are a trade-off between structural robustness and response time on the one hand and the blocking and displacement effect on the other hand [94, 95]. The spatial resolution is furthermore limited, especially in regions with high velocity gradients since pressures from different taps are not measured at the same physical location [96].

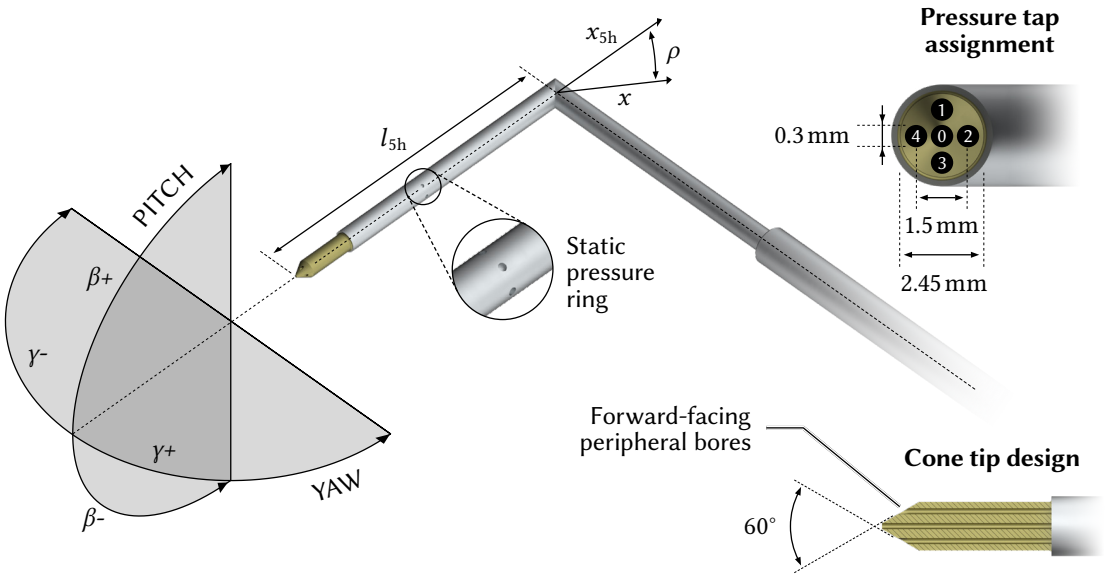

Figure 3.3: Design and nomenclature of the five-hole pressure probe

4 The term 'forward facing' describe the orientation of the peripheral bores in relation to the axis of the probe.

When using multi-hole probes, a fundamental distinction is made between the so-called nulling method and the fixed-position method: While the first requires the probe to be rotated in the unknown flow until the direction-sensing pressures are nulled, the second method, which is applied in the present setup due to its simple integration and fast measurement procedure, involves a correlation-based determination of the flow direction, with the probe alignment being unchanged [97]. Although the pressure distribution could, in principle, be predicted with reasonable accuracy, at least for spherical tips, by applying a potential flow approach, manufacturing inaccuracies and viscous effects necessitate a calibration within the range of yaw and pitch angles to be expected in the later measurement [98].

3.3.2 Probe Calibration

For calibration, the five-hole probe is exposed to a flow of known pressure, velocity, and direction while being rotated stepwise along the yaw and pitch plane. According to Treaster and Yocum [98], the following set of dimensionless coefficients – two for the determination of flow direction and two for the determination of total and static pressure – are calculated in each calibration point:

$$k_\beta = \frac{p_1 - p_3}{\Delta p} \quad (3.1) \qquad k_\gamma = \frac{p_2 - p_4}{\Delta p} \quad (3.2) \qquad k_{\mathrm{p,s}} = \frac{p_0 - p_\mathrm{s}}{\Delta p} \quad (3.3) \qquad k_{\mathrm{p,t}} = \frac{p_\mathrm{t} - p_0}{\Delta p} \quad (3.4)$$

The denominator Δp adapts the normalization approach, which was first introduced by Dudzinski and Krause [97] and can be interpreted as an indicated dynamic pressure.

Since it has been found to be advantageous with regard to the uniformity of the calibration map of the custom probe design, this approach is slightly modified by adding the standard deviation of the probe pressures. It is defined

$$\Delta p = \underbrace{p_0 - \frac{1}{4}\sum_{i=1}^{4} p_i}_{\text{Indicated dynamic pressure}} + \sqrt{\frac{1}{5}\sum_{j=0}^{4}\left(p_j - \frac{1}{5}\sum_{k=0}^{4} p_k\right)^2}. \quad (3.5)$$

An investigation of Dominy and Hodson [99] on the calibration of five-hole probes with different cone tip designs confirmed that the probe coefficients are sensitive to changes in Reynolds number related to the probe tip diameter since the characteristic of flow separation and reattachment on the cone surface is altered. Due to the wide span of flow velocities in the wake of the cascade, the outlet probe was calibrated over a range of $1.2 \times 10^4 \leq Re_{5\mathrm{h}} \leq 4.4 \times 10^4$ with an increment of $\Delta\, Re_{5\mathrm{h}} = 0.8$. The evaluation of the measurement is then performed iteratively, i.e., after an initial determination of the local flow velocity, the evaluation is repeated with the corresponding calibration data set.

Calibration rig: A calibration rig that has been originally developed at the institute is used for the calibration of L-shaped five-hole probes for both high-speed and low-speed applications. It is shown in Figure 3.4 and is integrated into a bypass of the high-speed turbine test rig (see Figure 3.1). While the screw compressor is utilized for high-speed calibrations up to $Ma = 0.8$, low-speed calibrations with $Ma \leq 0.3$ can be carried out with the mass flow drawn from the pressurized vessel, which is continuously supplied by a compressor.

The rig consists of two independently adjustable frames that allow the probe to be rotated about a joint pivot in the pitch and in the yaw direction, whereby the frames are actuated separately by stepper motors. The rotation of the frame for the yaw adjustment is hereby transmitted by a bevel gear connected with a hollow shaft, and the orientation of the probe is measured by flange-mounted inductive angle sensors.

The bypass flow is first equalized using a honeycomb and a screen, which are integrated into the infeed as an intermediate flange. A Prandtl probe and a temperature sensor allow the steady state of the calibration to be monitored, with the upstream throttle valve being readjusted in low-speed operation in the event of pressure fluctuations in the vessel.

The axisymmetric calibration jet is generated by a two-stage nozzle that contracts the initial diameter of $d_{\text{in}} = 267\,\text{mm}$ to $d_{\text{out}} = 70\,\text{mm}$. Utilizing an optional turbulence grid between the two stages, the turbulence level of the nozzle flow can be raised to better reflect the operating conditions of the probe in the later operation. The smooth contraction of the last stage generates a top-hat velocity profile at the nozzle exit, characterized by a flat and uniform velocity distribution across the cross-section. Since

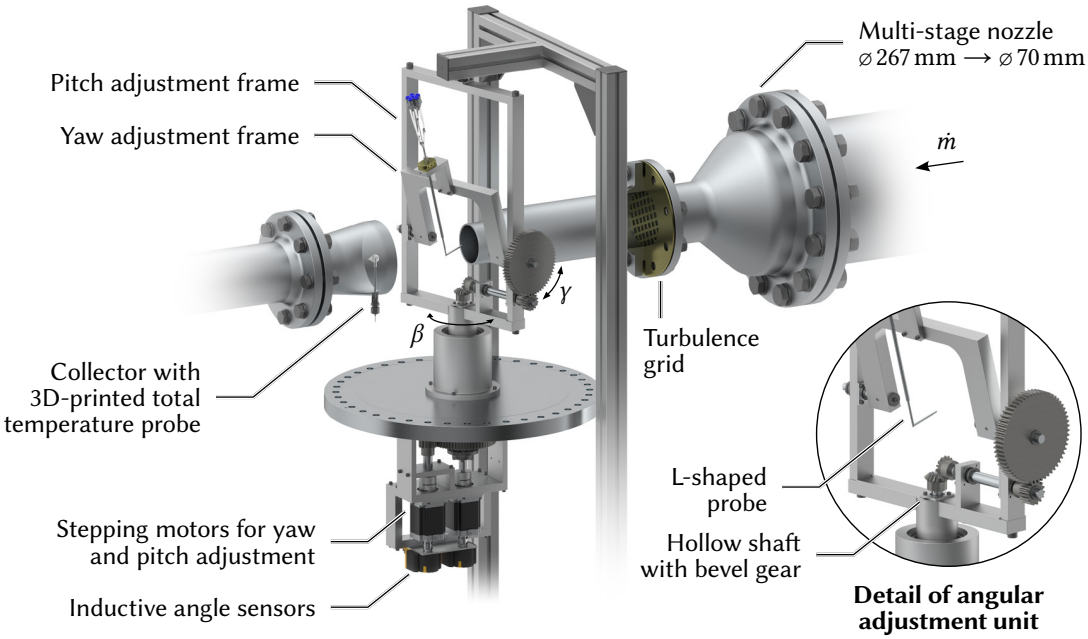

Figure 3.4: Five-hole pressure probe calibration rig

the probe tip is located immediately downstream of the nozzle exit, it is completely enclosed by the conically converging potential core of the jet flow, which is characterized by an almost homogeneous velocity distribution. It extends over a length of $x/d_{\text{out}} \approx 5$ and is surrounded by an expanding shear layer where the jet mixes with the ambient air [100]. Since the calibration is performed under steady-state conditions, it is reasonable to take the total pressure from the center bore at the beginning of the calibration process when the probe is aligned to the flow. According to Tollmien [101], it can further be assumed in good approximation that the static pressure at the probe tip corresponds to the ambient pressure in the test room. A collector, installed at a distance of $x/d_{\text{out}} = 5$ from the nozzle exit, passes the free jet into the piping system of the test rig, with a custom-designed total temperature probe being integrated into the collector.

To reduce the total time of calibration and measurement, an algorithm was integrated into the LabView-based measuring program, which assesses the steady state of the pressure readings at the probe tip by continuously comparing two successive readings i and $i+1$. The final measurement is performed when

$$\Delta p_n = \frac{|p_{n,i} - p_{n,i-1}|}{p_{n,i}} < 0.01 \quad \text{for } n = 1 \dots 5. \tag{3.6}$$

The algorithm reflects the fact that the actual settling times of the probe pressures differ significantly depending on the present velocity and pressure gradients.

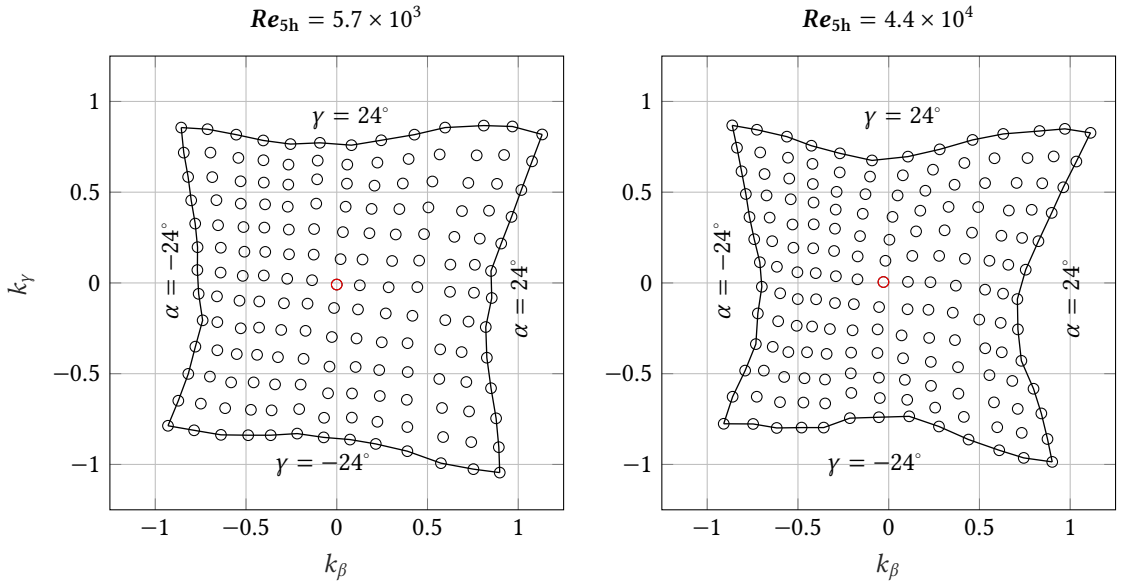

Figure 3.5: Five-hole probe calibration map of k_β over k_γ for low-speed and high-speed conditions, with the red dot indicating $\beta = \gamma = 0°$

Calibration results: Figure 3.5 provides exemplary calibration maps for the low-speed configuration ($Re_{5h} = 5.7 \times 10^3$) and the high-speed configuration ($Re_{5h} = 4.4 \times 10^4$), with each point representing a certain yaw-pitch combination. The calibration was conducted in the range of flow angles from -20° to 20° with an increment of 4°. An ideal probe tip without shape and surface deviations would provide a point-symmetric calibration field. In the present case, the calibration maps are affected by a slight distortion, which can presumably be attributed to manufacturing tolerances. However, as long as the map is non-intersecting, the determined coefficients can be assigned to an unambiguous flow angle combination.

The distribution of the static and total pressure coefficient is shown in Figure 3.6 exemplarily for the calibration at low speed. The latter clearly illustrates the angular sensitivity of the center hole: With $k_{p,t} \approx 0$ within a range of approximately $\pm 5^\circ$, the center hole reading is virtually equal to the actual total pressure. Contrariwise, for larger angles of attack, a significant correction of $k_{p,t} \cdot \Delta p$ is required to obtain the actual total pressure.

The measurement evaluation is performed in two steps: First, the two flow angles are determined from the calibration map shown in Figure 3.5 using a bilinear interpolation method. It is based on the barycentric coordinates of the triangle formed by adjacent calibration points to weigh the influence of each vertex on the value to be interpolated. In the second step, the coefficients $k_{p,s}$ and $k_{p,t}$ for the identified flow direction are interpolated using the calibration maps shown in Figure 3.6. The static and total pressure of the flow can then be obtained from equations 3.3 and 3.4.

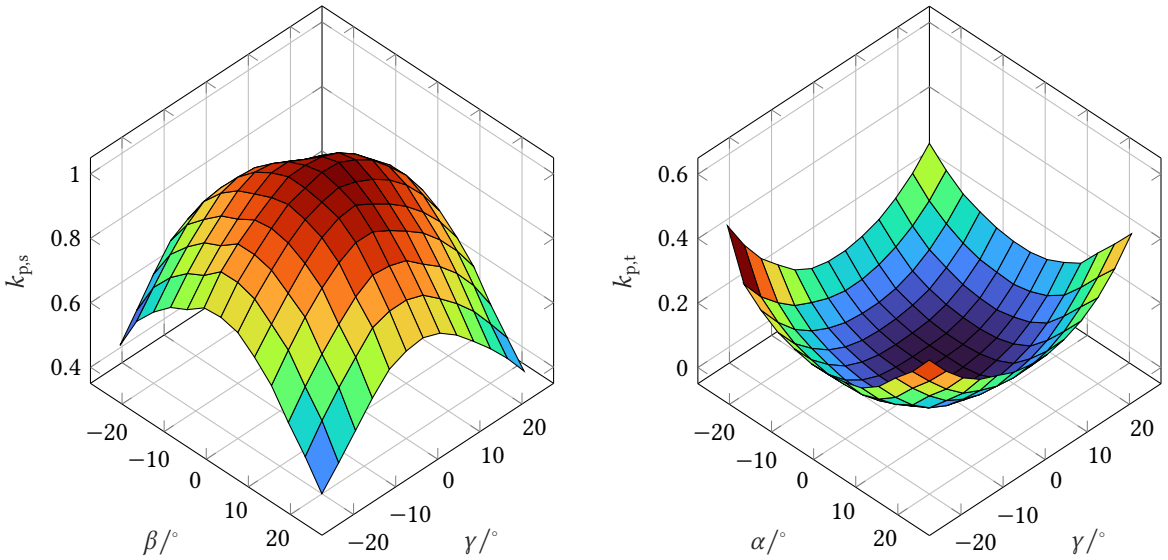

Figure 3.6: Distribution of static pressure coefficient $k_{p,s}$ (left) and total pressure coefficient $k_{p,t}$ (right) for $Re_{5h} = 4.4 \times 10^4$

3.3.3 Application in the Annular Cascade

Due to the limited measuring range, five-hole probes are typically aligned to the main flow direction. For measurements at the outlet of the present cascade, the probe is therefore adjusted by 76.3° according to Table 3.1. For the annular cascade, integrating an inclined L-shaped probe introduces variable geometric offsets, which must be considered in construction and measurement.

Starting with Figure 3.7, the radial and circumferential offsets that need to be considered when generating the measurement field are derived. First, the polar axis of the inlet coordinate system φ_{in} is rotated by φ_{off} to φ_{out}. The polar axis of the outlet coordinate system φ_{out} can be determined by the intersection point between the outlet measuring plane and the streamline starting from the passage center at the inlet. With the outlet measuring plane being positioned at $x/C_{\text{mid,x}} = 1.3$, the offset φ_{off} equals 19.7°. This value is also essential for correctly dimensioning and positioning the probe traversing unit (see section 5.5.6) since the probe feedthrough must reflect the desired measuring span.

The measurement field is spanned by a grid defined by the two increments $\Delta\varphi$ and Δr, where the radial increment is refined near the sidewall to provide better resolution of secondary flow in the later measurement. To allow the probe tip to traverse along the blue trajectory shown in Figure 3.7, the probe shaft must follow the red trajectory, which is derived from the radial offset $r_{\text{5h,off}}$ and the circumferential offset $\varphi_{\text{5h,off}}$.

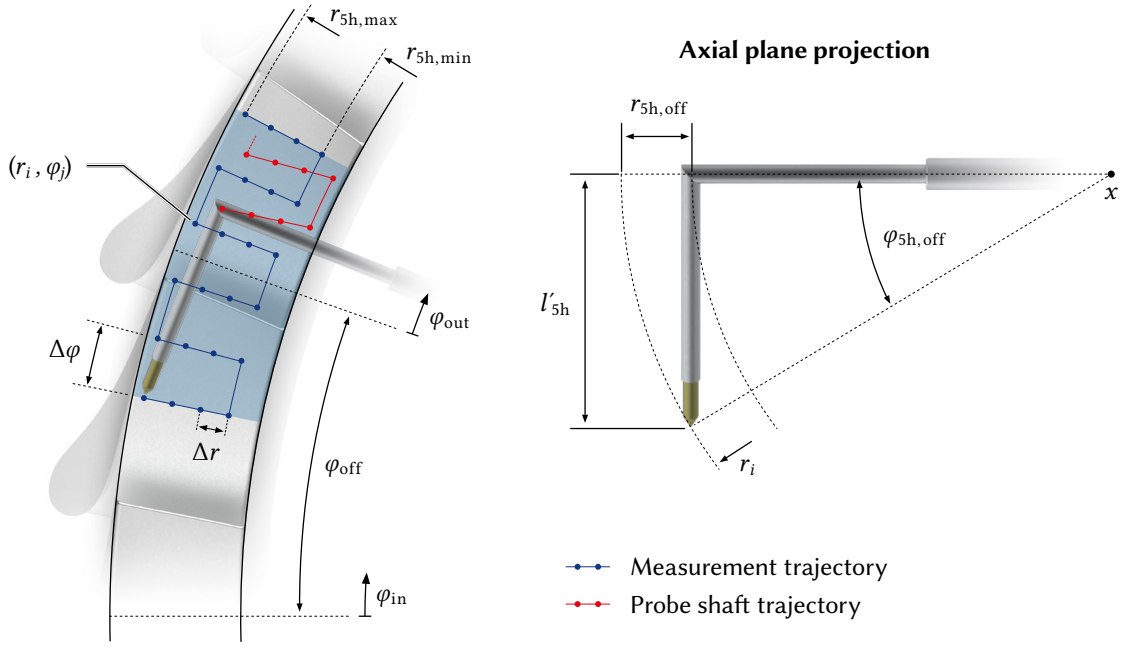

Figure 3.7: Five-hole pressure probe outlet measurement field for the annular cascade

The length of the short side l_{5h} of the probe, projected in axial direction onto the measurement plane, is given by

$$l'_{5h} = \sin\rho \cdot l_{5h} \tag{3.7}$$

where ρ is the probe angle and l_{5h} the length of the short side of the probe. By utilizing trigonometric relationships, the radial offset can then be calculated using

$$r_{5h,off} = r\left(1 - \cos\varphi_{5h,off}\right) \tag{3.8}$$

with the circumferential offset being defined as

$$\varphi_{5h,off} = \arccos\left(\frac{\sqrt{r^2 - l'^2_{5h}}}{r}\right). \tag{3.9}$$

While it is possible to move the probe head closer to the shroud endwall without risking damage to the probe, the proximity to the hub endwall is limited, as the probe would have contact with the endwall at the junction of its short and long side. However, according to a study of Treaster and Yocum [98], the use of free-jet calibrated five-hole probes below a distance of two probe head diameters from the wall is not recommended. While these findings were generally confirmed by Lee and Yoon [102], it could be shown in their investigation that a negative inclination of the probe head with respect to the wall, which necessarily occurs in the annular passage, as shown in Figure 3.8, significantly

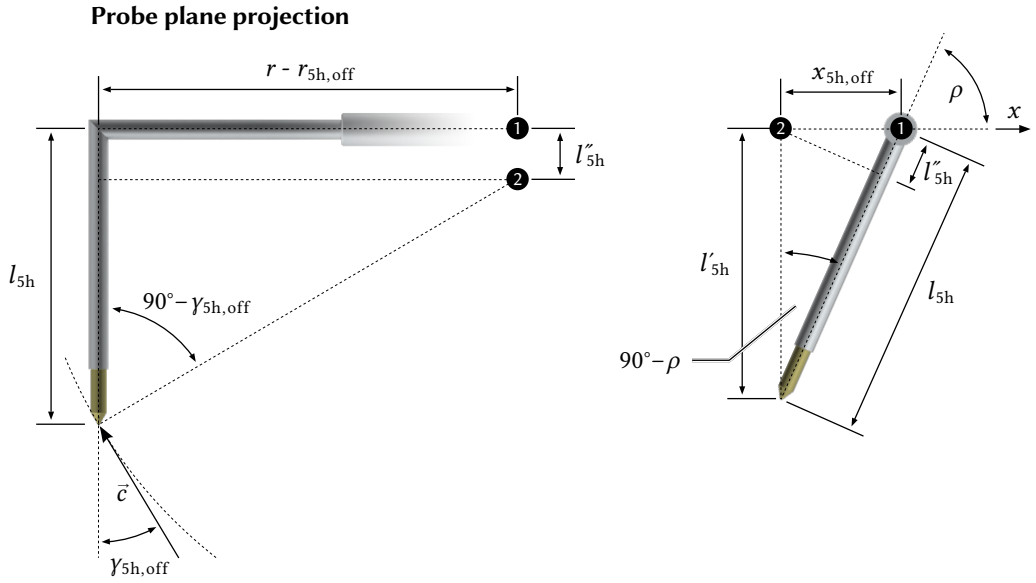

Figure 3.8: Geometric derivation of γ offset

attenuates the wall effect. Since in the present case both the Reynolds number of the probe tip and inclination, which will be derived in the following, are comparable to the aforementioned study, the minimum wall distance is set to one probe tip diameter.

The inclination is equivalent to the yaw offset of the probe at the maximum radial position, which can be derived geometrically according to Figure 3.8:

$$\gamma_{5\mathrm{h,off}} = \arctan\left(\frac{l_{5\mathrm{h}} - l''_{5\mathrm{h}}}{r - r_{5\mathrm{h,off}}}\right) \tag{3.10}$$

with

$$l''_{5\mathrm{h}} = \cos\rho \cdot x_{5\mathrm{h,off}} = \cos^2\rho \cdot l_{5\mathrm{h}}. \tag{3.11}$$

Taking into account the previously mentioned limits and dimensions, the parameters can be obtained for the outlet probe with $l_{5\mathrm{h}} = 85\,\mathrm{mm}$ according to Table 3.4.

Table 3.4: Radial measurement limits and yaw offsets for the outlet probe

Parameter	Near-shroud	Near-hub
r	439.5 mm	399.1 mm
$(r - r_{\mathrm{h}})/h$	0.954	0.191
$\gamma_{5\mathrm{h,off}}$	10.5°	11.6°

3.4 Pressure-Sensitive Paint for Film Cooling Effectiveness Measurements

Pressure-sensitive paint (PSP) is an optical sensor that makes use of oxygen-based quenching of luminescence, allowing the pressure distribution on a surface to be measured in a non-intrusive and non-destructive manner. By utilizing the heat-mass transfer analogy, which refers to the similarity between the equations governing heat transfer and mass transfer, PSP can also be applied for determining the film cooling effectiveness [103]

The application of PSP dates back to the 1980s, when the oxygen quenching effect, discovered as early as the 1930s, was first exploited for pressure measurements in aerodynamic research [103]. Of particular note is a study by Ardasheva et al. [104], who made the very first pressure measurements on the surfaces of various models in a supersonic flow. As an alternative to existing measuring techniques like gas chromatography or thin-film heating, the utilization of PSP for film cooling studies originated in the late 1990s with an investigation of Zhang and Fox [105] respectively Zhang et al. [106]. They measured the film cooling effectiveness of a coolant being ejected from cooling holes

on both a flat plate and a turbine vane. In the meantime, PSP has been established as a well-proven method for film cooling testing and has also been successfully used on the high-speed turbine test rig in previous investigations [9].

3.4.1 Measurement Principle

While there are various formulations of PSP, the paint generally consists of luminescent molecules called luminophores, which are bound in an oxygen-permeable layer and can be excited with light of a specific wavelength, typically in the UV range. As shown schematically in Figure 3.9, the activated luminophores emit light at a specific intensity and wavelength, with the intensity being attenuated by oxygen molecules that permeate the paint and quench the luminescent emission. Since the degree of extinction is proportional to the concentration of oxygen molecules, the luminescent intensity is a decreasing function of the partial pressure of oxygen, which is, in turn, proportional to the absolute air pressure [103].

In the practical implementation of PSP, a fundamental distinction must be made between the intensity-based method, which is applied in the present case, and lifetime-based approaches: While the first relies on the intensity measurement of the light emitted by the paint, the latter refers to the luminescence decay, which is not dependent on the excitation intensity, thus eliminating the need of reference conditions. However, application of the lifetime-based approach requires advanced instrumentation, e.g., pulsed excitation light and synchronized recording techniques with short integration times [107].

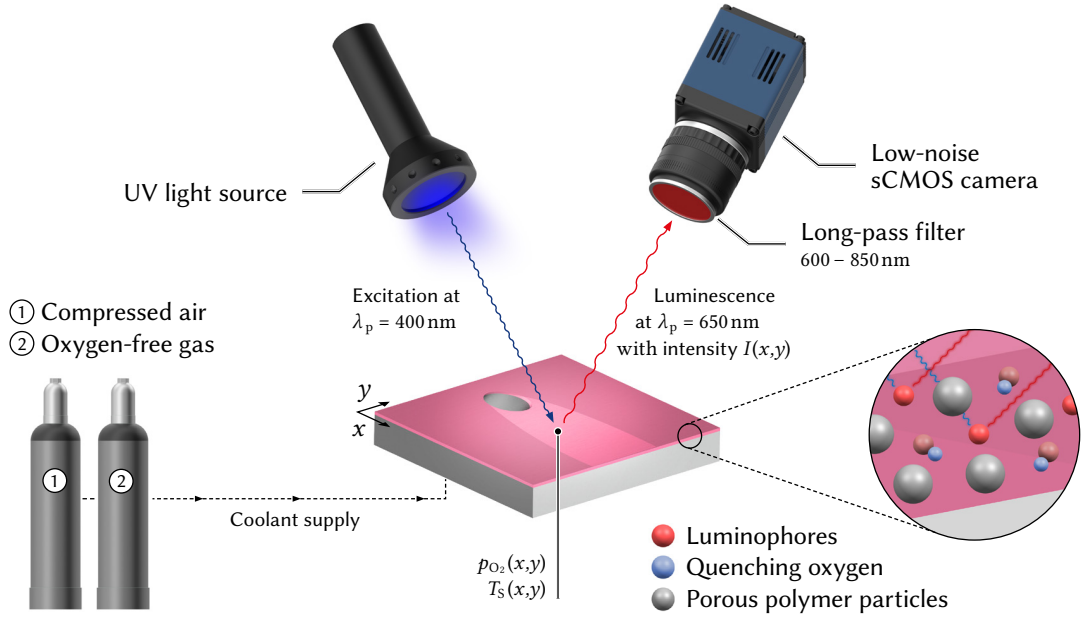

Figure 3.9: Measuring principle of pressure-sensitive paint in the context of film cooling experiments

The dependence between the local intensity I and acting partial pressure of oxygen p_{O_2}, both related to a known reference condition at the same physical location, is given by the Stern-Volmer equation. With the mole fraction of oxygen being constant in air, the partial pressure of oxygen is proportional to the absolute pressure, thus following:

$$\frac{I_{\mathrm{ref}}}{I} = A(T) + B(T) \cdot \frac{p_{O_2}}{p_{O_2,\mathrm{ref}}} = A(T) + B(T) \cdot \frac{p}{p_{\mathrm{ref}}} \tag{3.12}$$

where the empirical coefficients A and B are temperature-dependent, so surface temperatures must be taken into account in both calibration and later application. With the intensity being related to a reference intensity, the evaluation can account for non-uniform illumination, uneven coating, and inhomogeneous luminophore concentration [103].

Heat-mass transfer analogy: Starting with early works of Goldstein et al. [108] respectively Burns and Stollery [109] in the late 1960s, the use of foreign gas in simulating film cooling is a common approach to both determine film cooling effectiveness and to reflect the influences of varying density ratios between the main flow and the coolant under isothermal experimental conditions. Already Schmidt [110] stated the analogy of mass diffusion and heat transfer, which is expressed in the similar structure of the governing differential equations, and which can be used to transfer the results of experiments of one group to the other, and vice versa.

By applying the heat-mass transfer analogy to a turbulent boundary layer, the adiabatic wall temperature for the heat transfer situation according to equation 2.5 can be related to the mass fraction of the foreign gas at a non-penetrable surface according to Pedersen et al. [111] as follows

$$\eta_{\mathrm{ad}} = \frac{T_{\mathrm{w,ad}} - T_{\mathrm{m,r}}}{T_{\mathrm{c}} - T_{\mathrm{m,r}}} \approx \frac{C_{\mathrm{w}} - C_{\mathrm{m}}}{C_{\mathrm{c}} - C_{\mathrm{m}}}, \tag{3.13}$$

where C is the mass fraction of the foreign gas. This relationship holds true when the turbulent Schmidt number Sc_{t} for the mass transfer experiment is equal to the turbulent Prandtl number Pr_{t} for the heat transfer situation, i.e., the turbulent Lewis number $Le_{\mathrm{t}} = Sc_{\mathrm{t}} \,/\, Pr_{\mathrm{t}}$ is unity. According to Kays et al. [112] and other studies [113, 114], this assumption is reasonably valid for gases and gas mixtures in turbulent flow fields.

Since PSP is virtually an oxygen sensor, the mass fraction of coolant can be measured by injecting a foreign gas, which does not contain unbound oxygen, i.e., $C_{O_2,\mathrm{c}} = 0$. By expressing equation 3.13 based on the mass fractions of oxygen, it is obtained [115]

$$\eta_{\mathrm{ad}} \approx \frac{C_{O_2,\mathrm{fg}} - C_{O_2,\mathrm{air}}}{C_{O_2,\mathrm{c}} - C_{O_2,\mathrm{air}}} = 1 - \frac{C_{O_2,\mathrm{fg}}}{C_{O_2,\mathrm{air}}}, \tag{3.14}$$

where $C_{O_2,\mathrm{fg}}$ is the local mass concentration of oxygen inside the coolant film. Following Charbonnier et al. [116], the mass fractions are converted into molecular fractions by the introduction of the molecular weight W of each gas mixture, allowing equation 3.14 to be expressed in terms of partial

pressure of oxygen:

$$\eta_{ad} \approx 1 - \frac{C_{O_2,fg}}{C_{O_2,air}} = 1 - \left[1 + \frac{W_{fg}}{W_{air}} \left(\frac{p_{O_2,air}/p_{O_2,ref}}{p_{O_2,fg}/p_{O_2,ref}} - 1 \right)\right]^{-1} \tag{3.15}$$

When using nitrogen as a foreign gas ($DR = 1$), equation 3.15 simplifies to due to virtually equal molecular weights of nitrogen ($W = 28.01\,\mathrm{g\,mol^{-1}}$) and pure air ($W = 28.96\,\mathrm{g\,mol^{-1}}$) as follows:

$$\eta_{ad} \approx 1 - \frac{p_{O_2,fg}/p_{O_2,ref}}{p_{O_2,air}/p_{O_2,ref}} \tag{3.16}$$

Experimental application: As shown schematically in Figure 3.10, the application of PSP in the context of film cooling measurements requires a certain set of images acquired at different operating states to obtain the partial pressures according to equations 3.15 and 3.16.

The black image (a) compensates for a constant offset in the intensity distribution due to residual light or dark current noise from the camera, with the intensity distribution I_b being subtracted from all further recordings. The so-called wind-off image (b) captures the corresponding intensity distribution I_{ref} of a known reference pressure distribution, typically at atmospheric conditions, i.e., $p_{ref}(x,y) = const. = p_a$. For the determination of the local partial pressure $p_{O_2,air}$ under operating conditions, a wind-on image with I_{air} is obtained with pure air being ejected as coolant. With this data set, the pressure distribution could now be calculated (see section 4.3 for linear cascade results). To determine the film cooling effectiveness, a second wind-on image set with I_{fg} is recorded, in which the cooling air is replaced by the foreign gas while maintaining the mainstream operating conditions. As exemplified in Figure 3.10, due to the lowered partial pressure of oxygen, the areas of high foreign gas concentration, i.e., high film cooling effectiveness, are highly luminescent.

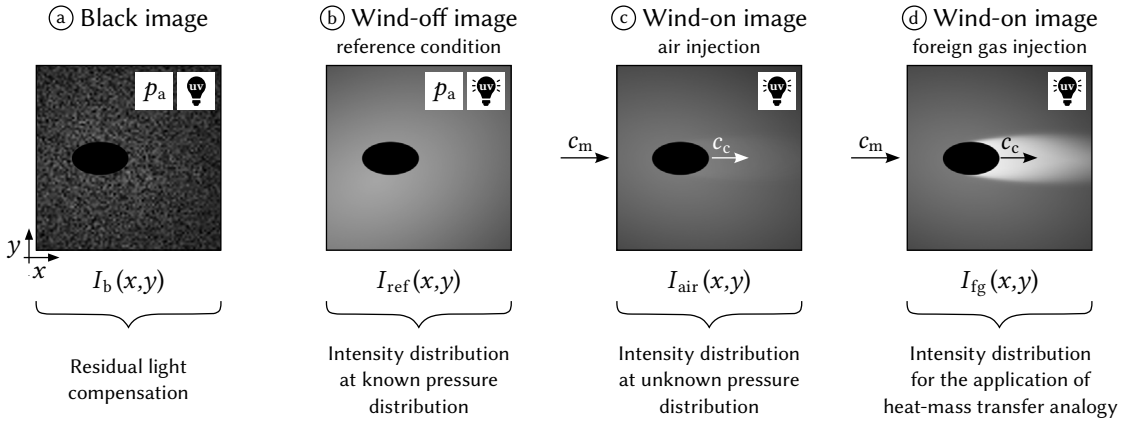

Figure 3.10: Intensity-based PSP image sequence for measuring adiabatic film cooling effectiveness

The luminescence intensity of each image set is typically recorded with a low-noise camera, which is equipped with a long-pass filter to block the excitation light. The spatial resolution of the pressure field is virtually only limited by the optical resolution of the camera. Since the signal-to-noise ratio (SNR) scales with the square root of the number of captured images [117], 20 frames are captured each and averaged in the present case.

While the uncertainty factors to consider when applying PSP are described in detail in Appendix A, three major challenges arise that can seriously compromise the results and are discussed in the following: First, the model may be deformed or shifted under wind-on conditions due to aerodynamic loading, resulting in an erroneous relation of the local intensity values. This issue can, in principle, be addressed in a subsequent image registration process, for example, by using transformation maps that are based on fiducial markers on the model surface [118]. However, this approach only allows limited correction of perspective deviations in the representation of a three-dimensional model. In the present case, the stiff vane and rigid endwall are not significantly deformed, but the test rig is displaced by up to 10 mm in the operating condition due to thermal expansion and pressure loading. As described in detail in the following section, image registration is therefore performed in situ by adjusting the camera position relative to the endwall by means of an industrial robot.

Excitation-related errors are another major source of measurement uncertainty, with changes in local illuminance between the wind-off and wind-on images being the most important. Apart from power fluctuations of the light source, which can be minimized in the current setup by a constant LED operating temperature, these changes are mainly caused by the already mentioned model deformation and displacements resulting in the relative position of the light source being altered. In the current setup, this issue is overcome by mounting the light source directly on the displacing test section, eliminating the need for any correction. However, the use of self-referencing binary paints containing additional pressure-insensitive luminophores is nowadays the most successful approach for illumination compensation when the above measures are not applicable [107].

The third major source of measurement error is associated with unknown or changing temperatures, as luminescence intensity is a function of both pressure and temperature. Particularly in the context of film cooling tests, the main challenge is to establish isothermal conditions, i.e., to keep the mainstream and the coolant at the same temperature, especially when foreign gas is supplied from a high-pressure cylinder bank. The measures implemented for coolant temperature control on the high-speed turbine test rig are explained below. The temperature difference between the wind-on and wind-off images can be minimized by taking advantage of the thermal inertia of the test rig. Under steady-state operating conditions, the test stand heats up to approximately 30 °C, depending on the ambient temperature. After the screw compressor is turned off, the temperature decreases at such a low rate that a reference image can be taken at a virtually constant temperature immediately after the switch-off.

3.4.2 Paint Calibration

As mentioned above, a calibration, either a-priori or in-situ, is necessary to quantify the relation between luminescence intensity, pressure, and temperature, i.e., to determine the Stern-Volmer constants according to equation 3.12. However, various extensions of the Stern-Volmer equation exist which allow a better approximation to the characteristics of particular PSP formulations. In the present case, a suitable fit of the calibration data shown below could be obtained with the following equation according to Hubner and Carroll [119]:

$$\frac{I_{\mathrm{ref}} - I_{\mathrm{b}}}{I - I_{\mathrm{b}}} = A(T) + B(T)\,\hat{p} + C(T)\,\frac{D(T)\,\hat{p}}{1 + D(T)\,\hat{p}} \quad \text{with } \hat{p} = \frac{p}{p_{\mathrm{ref}}} \tag{3.17}$$

with the extended Stern-Volmer constants A, B, C and D. Injecting oxygen-free foreign gas causes the oxygen partial pressure p_{O2} to drop to as low as 0 bar in regions of high foreign gas concentrations, i.e., areas with maximum film cooling effectiveness. For this reason, a-priori calibration is mandatory in the context of film cooling investigations since only the sum of partial pressures, but not a single partial pressure, can be measured with pressure taps. A pressure-based calibration[5] must therefore cover the full range between vacuum and the highest pressures that occur in operation.

Calibration chamber: The self-developed vacuum calibration chamber, depicted in Figures 3.11 and 3.12, was completely redesigned and initially commissioned for the annular test rig. It consists of a welded stainless steel pipe segment that is covered on both sides with blind flanges. The first flange contains the PSP calibration insert, which houses a cooling water cavity for the purpose of temperature control. It is made of highly conductive copper to promote homogeneous tempering. The cavity is supplied by a circulator (Julabo HD) with a temperature stability of ±0.01 K and covered by a stainless steel plate, with the whole assembly being sealed by round chords and bolted to the flange around the circumference.

The opposite flange contains both an acrylic sight glass for optical access and bulkhead fittings for the coolant water supply of the ring-shaped and water-cooled UV LED array ($\lambda_{\mathrm{p}} = 400\,\mathrm{nm}$, $\Phi_{\mathrm{t}} = 4.6\,\mathrm{W}$) which is mounted internally to the flange and powered via a vacuum-tight electrical feedthrough. The chamber pressure is conditioned through a vacuum-tight three-way valve using a rotary vane vacuum pump (final absolute pressure 0.5 mbar) and compressed air, with the chamber pressure being measured by an absolute pressure sensor (0…3000 mbar, full-scale accuracy 0.1 %) which is attached to the chamber via a threaded sleeve. The three-way valve allows the chamber to be first evacuated and then gradually pressurized by the compressed air connector without refitting.

5 An alternative method of calibration involves introducing a specific mixture of air and a foreign gas into the calibration chamber at a constant pressure. Please refer e.g., https://innssi.com/calibration/

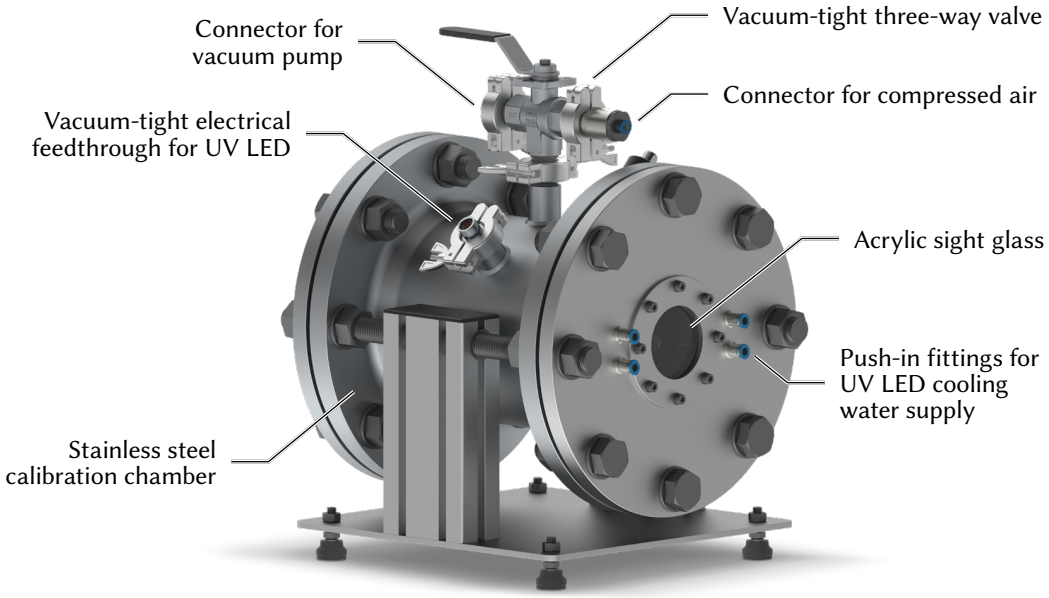

Figure 3.11: PSP calibration chamber

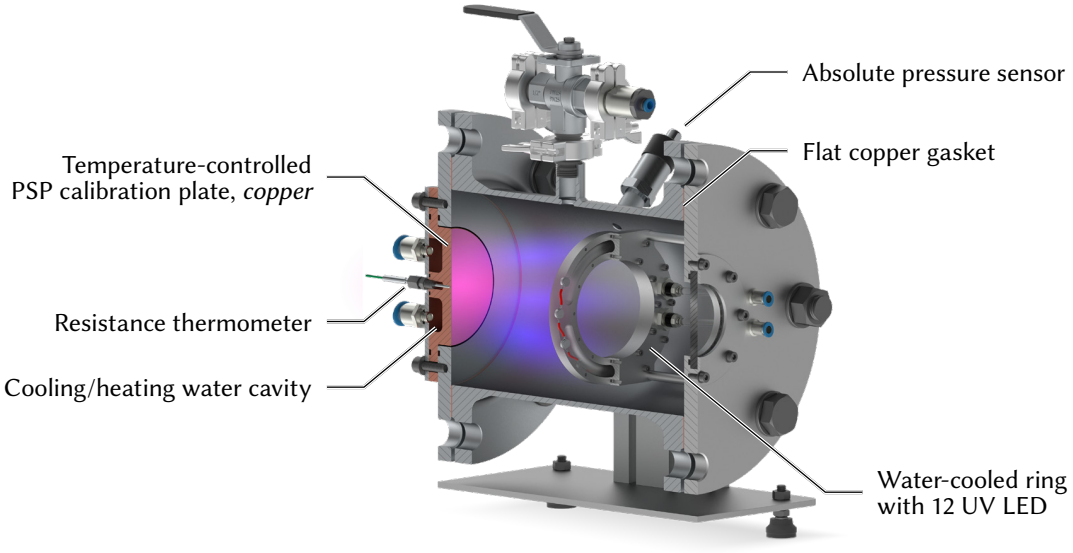

Figure 3.12: PSP calibration chamber (sectional view)

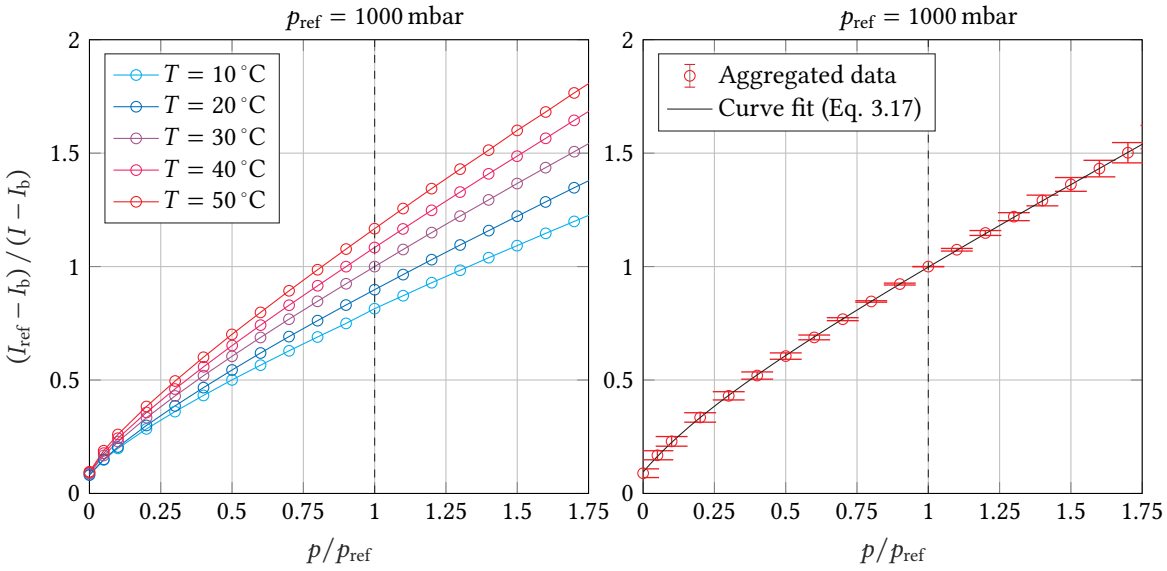

(a) Fixed reference intensity with $T_{\mathrm{ref}} = 30\,^{\circ}\mathrm{C}$ **(b)** Variable reference intensity

Figure 3.13: Calibration curves of PtTFPP PSP (ISSI UniFIB)

Calibration results: The calibration for the commercial paint (ISSI UniFib), which contains platinum porphyrins luminophores (PtTFPP) in a polymer binder, was carried out in a pressure interval between 0 bar and 1.75 bar with temperatures ranging from 10 °C to 50 °C. The results, which are shown in Figure 3.13, have been referenced at 1 bar. To illustrate the influence of the surface temperature, the reference intensity was fixed at $T_{\mathrm{ref}} = 30\,^{\circ}\mathrm{C}$ for the left plot. The non-linear curve progression highlights the importance of the calibration to be carried out at absolute pressures close to respectively equal to 0 bar, as otherwise the measurement of high coolant concentrations would be compromised. When referencing each temperature set with the according intensity obtained at the respective temperature ($T_{\mathrm{ref}} = T$) as proposed by Han and Rallabandi [115] and shown in the right plot, the temperature effect can be compensated to a certain extent allowing the data to be fitted as follows:

$$\frac{I_{\mathrm{ref}} - I_{\mathrm{b}}}{I - I_{\mathrm{b}}} = 0.09455 + 0.6795\,\hat{p} + 0.3143\,\frac{2.471\,\hat{p}}{1 + 2.471\,\hat{p}} \quad \text{with } \hat{p} = \frac{p}{p_{\mathrm{ref}}} \tag{3.18}$$

However, temperature-dependent errors (see error bars) must be accepted here, which is particularly evident at low and high pressures since the intensity ratios obviously do not scale linearly with temperature. For the present case, a temperature-specific evaluation was therefore performed by interpolating the according calibration curve for the temperature measured in operation from the data set shown in Figure 3.13a.

3.4.3 Experimental Apparatus

Excitation: Due to the limited measurement accessibility, along with the aforementioned requirements of a uniform excitation for all image sets, two compact UV floodlights (see Figure 3.14) that can be attached directly to the probe traversing system were developed. Each floodlight consists of an array of 12 UV LEDs ($\lambda_p = 400\,\text{nm}$, $\Phi_t = 4.6\,\text{W}$) which is mounted on a circuit board. The waste heat is dissipated via a water-cooled heat sink providing a steady-state radiant output. This allows the illumination source to be positioned in the immediate vicinity of the optical access without shifting its relative position to the region of interest (ROI) due to test rig displacements. In addition, the position of the floodlight can be optimized for each recording position and approached with high repeatability by using the circumferential probe traversing unit. Due to the twisted vane geometry, optical access to the endwall is severely restricted. For this reason, the excitation unit is provided with a multi-axis adjustment so that the floodlight can be optimally aligned. To obtain a spatially uniform and bright illumination, the floodlight is equipped with a holographic diffuser that has a 60° beam angle and is applied to a polypropylene screen. It scatters light by a thin layer of holographic material with specific diffraction characteristics allowing for control over the angle and intensity of the scattered light [120]. While conventional ground-glass diffusers have a transmission of about 65 % in the UV range, depending on the selected sand roughness, the transmission of the holographic diffuser is 85 % according to the manufacturer's specifications.[6] The higher efficiency and, thus, the higher excitation intensity allows a higher f-number for the same exposure time, which in turn increases the depth of field of the image – a significant aspect since the contoured endwall extends easily beyond the focal plane of the camera with the aperture open.

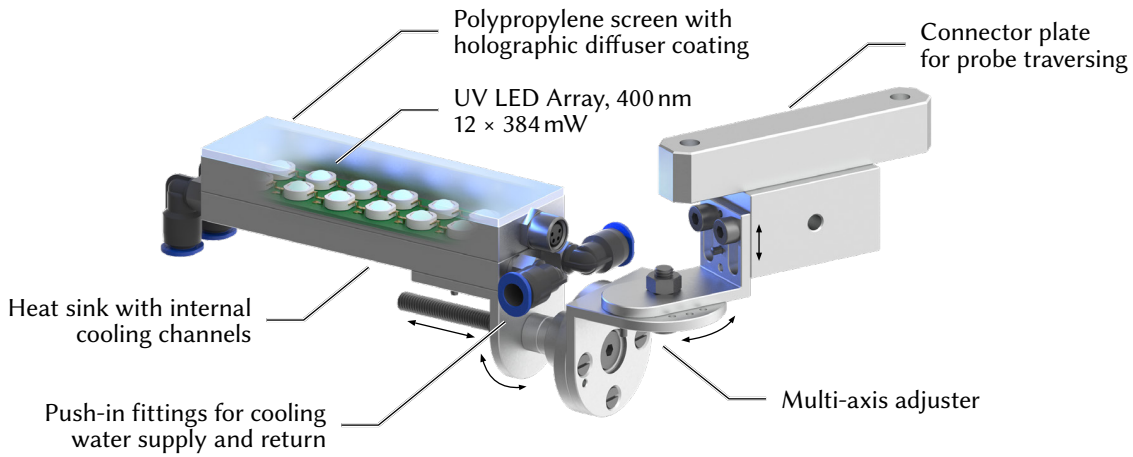

Figure 3.14: Self-developed UV LED floodlight

6 Please refer to https://www.optrovision.de/produkte/luminit-light-shaping-diffuser.html

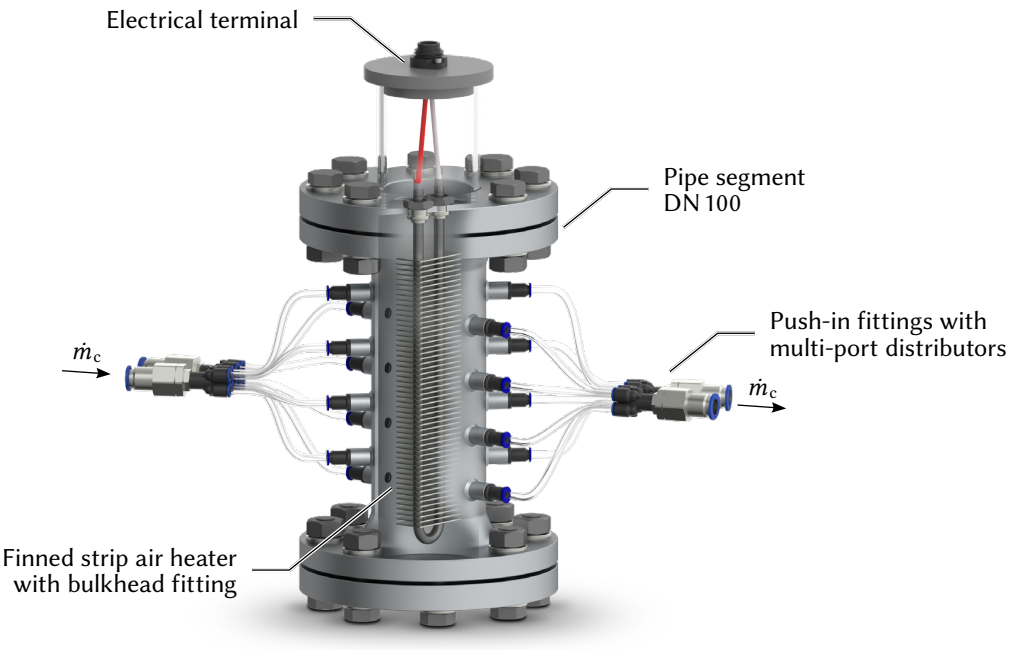

Figure 3.15: Low-power heater for precision control of the coolant flow temperature T_c

To further improve the optical performance of the measurement setup in terms of UV transmissivity and reflectivity, borosilicate glasses with an anti-reflective coating in the range of $380\,\text{nm} < \lambda < 450\,\text{nm}$ were integrated into both the linear and the annular test rig.

Temperature control: Due to the temperature dependence of the luminescence response, it is advisable to equalize the temperature of the main flow and the coolant since a correction in post-processing could only be done iteratively by using the initial film cooling effectiveness to determine local mixing temperatures. The high-power temperature control unit used in the linear measurement campaign is not precise enough for reliable fine control because it has comparatively high response times. Short control times are crucial, especially for foreign gas supply, since nitrogen and carbon dioxide cool down on throttling to the pressure level of the secondary air supply due to the Joule-Thomson effect [121]. For this reason, a low-power heater was developed and installed immediately upstream of the plenum. As shown in Figure 3.15, it consists of a short pipe segment with a finned strip air heater ($P = 500\,\text{W}$) integrated via a bulkhead fitting. To increase the heat transfer between the heating elements and the coolant, the coolant mass flow is fed laterally through eight push-in fittings. The inside of the pipe segment was insulated with a polycarbonate layer to further reduce the thermal inertia of the controlled system. The temperature is adjusted via a PID controller integrated into the power electronics of the heater, with the control value being given by the thermocouple installed in the purge slot plenum.

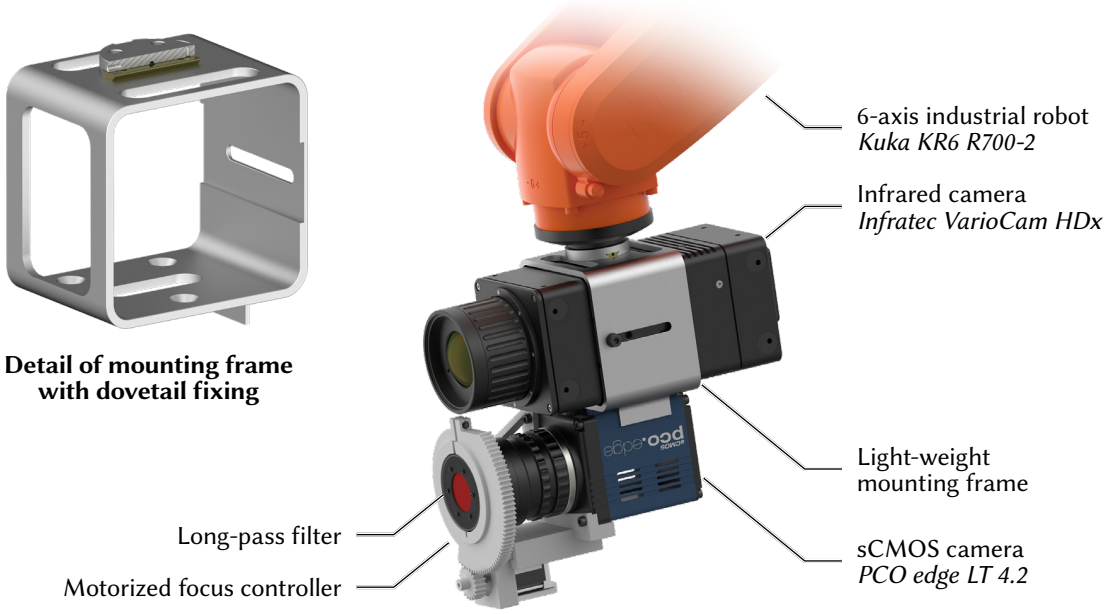

Figure 3.16: Camera setup with light-weight camera mount for Kuka 6-axis industrial robot

Image recording and camera positioning: For the low-noise recording of the luminescence response, a cooled sCMOS camera (PCO edge LT 4.2) with 2048 × 2048 px and a dynamic range of 16 bit is used in the current setup. The camera is equipped with an optical long-pass filter (optical density classification 6) that blocks 99.9999 % of the incoming light up to a wavelength of $\lambda = 600$ nm. This almost completely obstructs the excitation light so that reflections of the UV LEDs on the endwall are practically suppressed.

Since optical access to the end wall is very limited, image acquisitions from different positions are required to capture the entire region of interest in both the PSP and IR measurement campaigns. Due to the aforementioned demands of the PSP measurement technique, an industrial robot is particularly suitable for this purpose, as it allows different positions to be approached with repeatable accuracy throughout the entire measurement campaign. The 6-axis Kuka KR6 R700-2 robot used in the present measurement setup features a pose repeatability 0.02 mm with a payload of 3 kg and maximum reach of 726 mm. To optimize the payload inertia, a light-weight aluminum mounting frame, shown in Figure 3.16, was developed, allowing both cameras to be attached as near as possible at the robot tool flange. The mounting frame has a custom dovetail fixture that enables the entire assembly to be joined to the robot platform via an adapter plate.

During the linear measurement campaign, it was found that due to a lack of motorized focus adjustment of the camera-lens combination, the freedom of position was limited, i.e., only recording positions could be considered that would provide sharp imaging of the end wall with the same focus setting. For this reason, a motorized focus adjustment system was developed as part of a student

research project. It utilizes a stepper motor-driven gear with an integrated friction clutch to adjust the focus ring of the camera lens. The stepper motor can be addressed via an interface in the measuring program so that specific focus setups can be integrated into the PSP measuring sequence.

A mere registration of the recorded images in the post-processing would be insufficient, as the displacement introduces perspective changes that cannot be compensated by translating the images. For this reason, an algorithm was implemented in the LabView-based measurement program: At each recording position and for each image set, a test image is first acquired and compared with a reference image that was taken at the beginning of the measurement campaign. Using a point tracing of the pressure measurement taps on the endwall, the relative displacement can be calculated and transmitted to the industrial robot, which then performs a position correction.

3.5 IR Thermography for Heat Transfer Measurements

As discussed in Chapter 2, using the film cooling effectiveness as a single indicator of surface protection is not sufficient because the flow field may be significantly altered by the coolant injection, thus increasing the local heat transfer coefficients. Therefore, for a complete assessment of the cooling performance, additional investigations on the heat transfer are inevitable.

3.5.1 Measurement Principle

As it is not possible to directly measure heat flux, it must be inferred, e.g., by temperature monitoring across a spatial distance [122]. Convective heat transfer measurement typically requires a heat flux sensor, which implements the underlying thermo-physical model in the test setup, and a thermal transducer for the temperature measurement. Heat flux sensors generally consist of plates with known thermal behavior whose temperature is measured at certain points. The heat transfer measurement setup, which is schematically shown in Figure 3.17, utilizes a so-called auxiliary wall with quasi-isothermal boundary conditions for the implementation of the heat flux sensor.

In contrast to embedded thermocouples, infrared (IR) thermography, as it is used in the present case, constitutes a true two-dimensional temperature measurement allowing the heat flux through the sensor to be measured in two dimensions as well [123]. Since the radiant energy received by the IR detector of the camera depends on both the radiometric properties of the investigated surface and the transmission path, they must be taken into account in the analysis of the IR data in order to infer the actual surface temperatures. In the present case, the pressurized test rig necessitates the use of infrared optics, whose transmission properties must be included in the analysis.

Heat flux sensor: The so-called auxiliary wall can be considered a gradient sensor, where the wall heat flux is inferred from the thermal conduction resulting from the temperature gradient within a solid of constant and isotropic thermal properties [124]. Following Fourier's law of heat conduction,

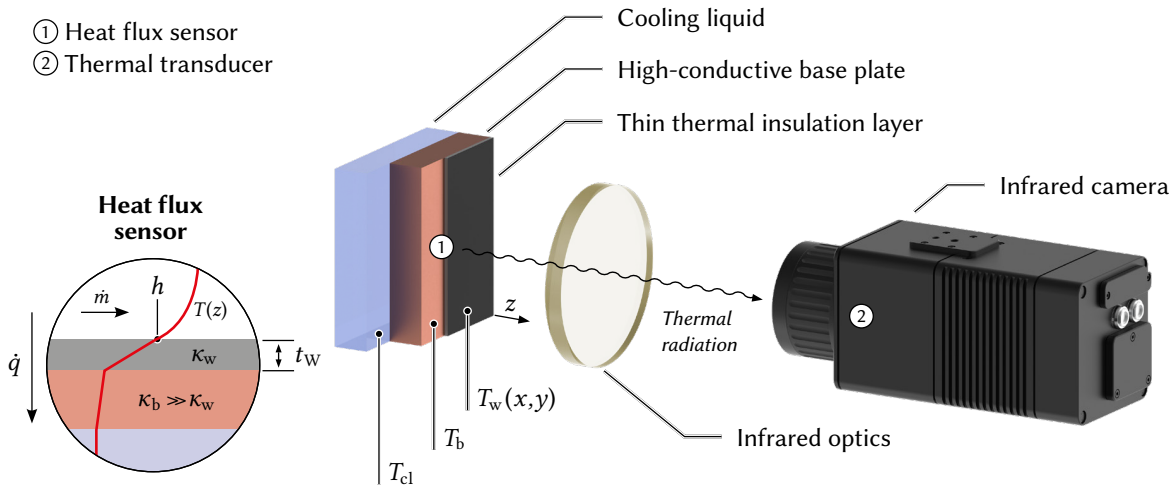

Figure 3.17: Measuring principle for heat transfer measurement

the heat flux in the auxiliary wall is defined by [112]

$$\dot{q}_w = -\kappa_w \nabla T \tag{3.19}$$

If the temperature boundary conditions are known, the gradient field in the solid, and hence the heat flux can be determined analytically or by means of an FE simulation, as demonstrated, for example, by Baldauf et al. [49], who investigated the local heat transfer coefficients on a flat plate surface downstream a row of cylindrical ejection holes. While the surface temperatures were acquired thermographically, the rear temperature distribution was interpolated between thermocouple measuring points. To solve the heat conduction problem without the need for interpolating the backside temperature distribution, a quasi-isothermal approach with a double-layer design is adopted from Laveau [125] in the present case, also eliminating the need for extensive instrumentation. As shown in the left part of Figure 3.17, the water-cooled double-layer wall is made up of a thermally high-conductive base plate and a thin insulating layer with thickness t_w facing the flow, which enables the following assumptions: First, with $\kappa_w \ll \kappa_b$, the backside temperature of the insulating layer T_b is considered to be constant. Second, it is assumed that no significant conductive heat transport occurs in the transversal direction of the insulation layer, i.e., that the heat conduction is virtually one-dimensional since $\partial T/\partial x \ll \partial T/\partial z$. By replacing the gradient in equation 3.19 with the finite difference, it becomes

$$\dot{q}_w(x,y) = \frac{\kappa_w}{t_w} \cdot \big(T_w(x,y) - T_b\big). \tag{3.20}$$

The local heat flux $\dot{q}_w$ into the auxiliary wall is balanced by the convective fraction $\dot{q}_h$ and a radiative fraction $\dot{q}_r$ from the surrounding walls, with the latter being approximated by

$$\dot{q}_{rad} = \sigma\, \epsilon\, (T_m - T_w). \tag{3.21}$$

where σ is the Stefan-Boltzmann constant and ϵ the radiative emissivity of the auxiliary wall. With respect to the temperatures prevailing in the experimental setup, this fraction can be neglected, as it only accounts for less than 3 % of the total heat flux. With equation 2.3 and 3.20, the heat transfer coefficient for the cooled case is therefore:

$$h_\mathrm{f}(x,y) = \frac{\kappa_\mathrm{w}/t_\mathrm{w} \cdot \left(T_\mathrm{w}(x,y) - T_\mathrm{b}\right)}{T_\mathrm{w,ad}(x,y) - T_\mathrm{w}(x,y)} \tag{3.22}$$

Thermal transducer: Since its first documented application in aerodynamic research in 1967, IR thermography has become widely used in both skin friction and heat transfer studies [126]. It utilizes the thermal radiation, which is emitted by each body at temperatures above 0 K, with the intensity being dependent on the wavelength of the radiation and the temperature of the body. The spectral distribution of emissive power of a black body, i.e., radiant flux per unit wavelength emitted by a perfectly absorbing surface, can be described by Planck's law of radiation [127]:

$$M(\lambda,T) = C_1 \cdot \left[\lambda^5 \left(e^{C_2/\lambda T} - 1\right)\right]^{-1} \tag{3.23}$$

where C_1 and C_2 are the first, respectively, the second radiant constant. Accordingly, the intensity distribution shifts towards shorter wavelengths with increasing temperature, with the displacement of the maximum being described by Wien's law:

$$\lambda_\mathrm{max} = 2897.8\,\mu\mathrm{m} \cdot \frac{T}{\mathrm{K}} \tag{3.24}$$

Real objects generally emit or absorb only a fraction ε of the idealized black body radiation. Instead, they reflect a fraction ρ and transmit a fraction τ of the incident radiation. Due to energy conservation, the following applies under steady-state conditions [127]:

$$\varepsilon(\lambda) + \rho(\lambda) + \tau(\lambda) = 1 \tag{3.25}$$

For the evaluation of an IR thermography, it is therefore important to consider the entire radiation chain of the experimental setup. In the present case, the setup, as shown in Figure 3.18, can be simplified by several assumptions: First, the investigated surface can be characterized as both non-transparent ($\tau_\mathrm{w}(\lambda) = 0$) and thermally gray, i.e., emissivity and reflectivity are constant and thus independent of the wavelength. The infrared optics is further non-absorbent, but its transmissivity τ_o is sensitive to the wavelength, which will be addressed by a calibration shown below. Due to the short recording distances of less than 1 m, the transmissivity of the atmosphere in both the duct and in the test room can be assumed to be unity [128]. The total radiation M_t is therefore composed as follows:

$$M_\mathrm{t} = (1-\tau_\mathrm{o}) \cdot M_\mathrm{a} + \tau_\mathrm{o} \cdot \left[\varepsilon_\mathrm{w} M_\mathrm{w} + (1-\varepsilon_\mathrm{w}) \cdot M_\mathrm{m}\right] \tag{3.26}$$

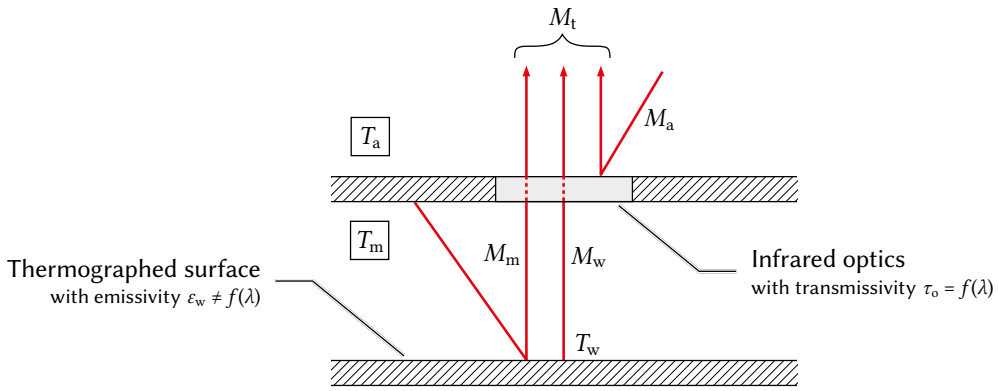

Figure 3.18: Simplified thermal radiation chain

It is further assumed that both the reflected fraction of the inner walls of the channel and the reflected fraction of the ambient are constant with respect to governing temperatures T_m and T_a. Last but not least, a directional dependence of emissivity is neglected since appropriate traversing of the IR camera ensures the ROI to be thermographed at viewing angles $< 60°$, where emissivity starts to change significantly [127, 129]

3.5.2 Experimental Apparatus

The temperature measurements are performed with an IR camera (Infratec VarioCAM HDx head 600) which operates in the long-wavelength infrared band from 7.5 µm to 14 µm. The uncooled microbolometer detector (640 × 480 px) works on the principle of a thermistor, a type of resistor whose resistance varies with the temperature [127]. It features a measurement range of −40 °C to 600 °C with an absolute measurement accuracy of ±2% and a relative temperature resolution of up to 0.03 °C at 30 °C.

Since the detector operates in a spectral band, it captures only a fraction of the total radiant energy which the body emits according to Planck's law. The emissive power of a spectral interval is therefore defined as:

$$E(T)_{\lambda_1}^{\lambda_2} = \int_{\lambda_1}^{\lambda_2} M(\lambda, T)\, \mathrm{d}\lambda \tag{3.27}$$

Regarding optical access, the majority of standard glasses have cut-off wavelengths longer than 2.7 µm, making them unsuitable for IR applications [127]. Therefore, the infrared window used in the present setup is made of zinc sulfide, whose spectral transmission curve is plotted in the left part of Figure 3.19.

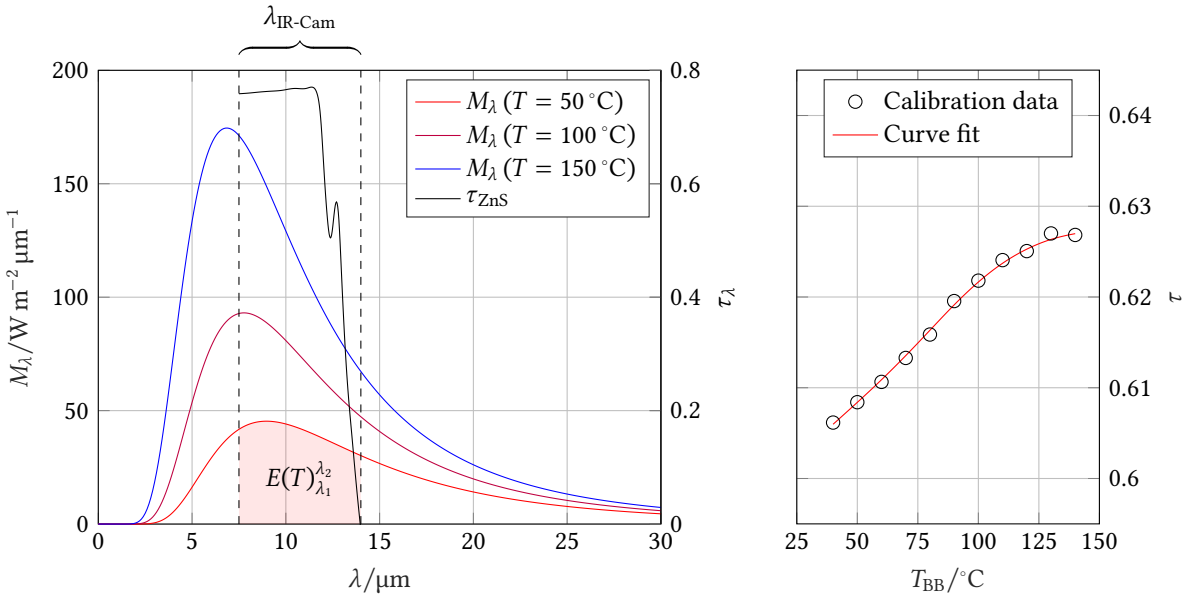

Figure 3.19: Spectral distribution of emissive power M_λ of black bodies with transmission spectrum of zinc sulfide window (left) and temperature-dependent transmission curve (right)

The diagram also contains the spectral distribution of the emissive power of a black body for three distinct temperatures, with the interval in the spectral band of the IR camera being exemplarily drawn for $T = 50\,^\circ\text{C}$.

Since, on the one hand, the spectral transmissivity drops significantly for $\lambda > 11.5\,\mu\text{m}$ and, on the other hand, the spectral exitance distribution shifts to the left for higher temperatures according to Wien's law, the total transmission of the optics is temperature-sensitive. To consider the transmission properties of the glass used in the evaluation of the IR measurements, a calibration was conducted between 40 °C and 140 °C using a temperature-controlled blackbody radiator, with the results depicted in the right part of Figure 3.19. It can be seen that the transmissivity increases slightly from 60.6 % at 40 °C to 62.7 % at 140 °C.

The design implementation of the auxiliary wall method is described in detail separately for linear and annular cascades in sections 4.6.1 and 5.5.5.

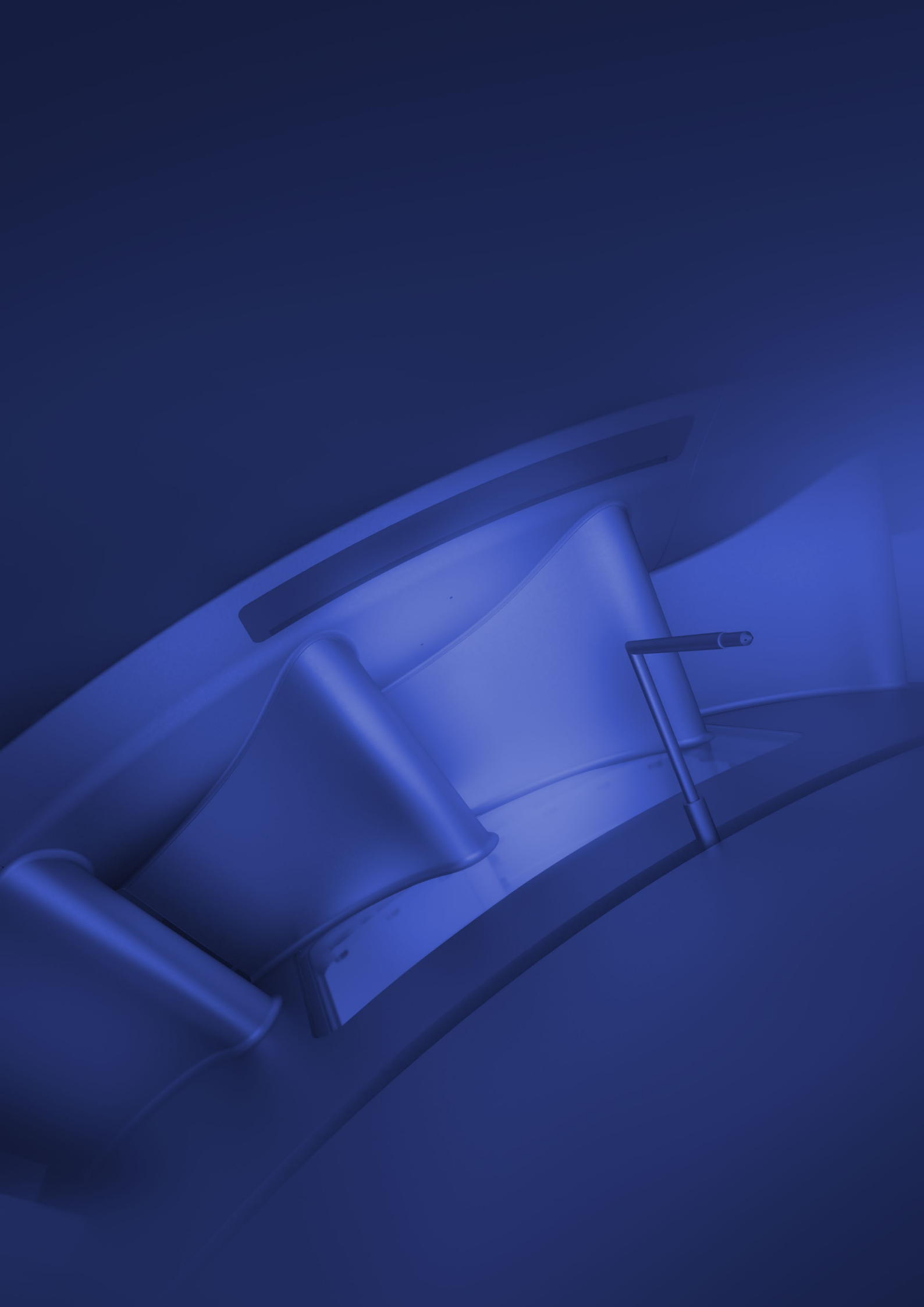

Preliminary Investigation of the Linear Cascade

This chapter presents the results of the preliminary investigation on the linearized design of the vane that was depicted in Chapter 3. The investigation was conducted using a five-passage cascade which was integrated into the high-speed turbine test rig. The main objectives of this preliminary test were twofold: First, the measurement methods to be implemented in the annular test rig were to be field-tested. Second, the investigation provides results that can be used for a later assessment of the influence on film cooling regarding the simplifications associated with linearization.

The first part of this chapter includes the experimental results obtained through oil flow visualization, pressure-sensitive paint, and five-hole probe measurements. These findings have been previously published in Landfester et al. [11, 12]. However, for the present work, the post-processing was fundamentally revised to provide the film cooling and oil-flow results of different recording positions (see Chapter 3.4.3) in a unified and combined manner by utilizing a mapping algorithm developed at the institute. It allows the raw camera data to be mapped seamlessly on the 3D model of the endwall and the vane surface by using a pinhole camera projection approach.

The second part presents the results of the heat transfer measurements, along with a description of the measurement module that was specifically designed for this purpose, implementing the auxiliary wall method. The chapter concludes with an evaluation of the design and the implementation of the measurement methods to identify improvement potentials in the development of the annular cascade.

4.1 Experimental Setup

The linear cascade was integrated into the linear section of the test rig (see Figure 3.1) that was originally developed by Franze [8] and in which similar investigations had previously been carried out on a cylindrical NGV design [9, 10]. The scope of the investigation covers the slot configurations listed in Table 3.3. The denomination and definition of the slot geometries are identical to the nomenclature of the annular cascade presented in the previous chapter.

The characteristics of the linear cascade are depicted in Figure 4.1. The purge slot is positioned upstream of the central passage P-0 on the shroud endwall and has an overlap of 16.5 % to each of the neighboring passages. For a consistent comparison of the different slot positions, the reference area for the averaging of the local film cooling distribution is restricted by the passage inlet and the passage outlet, excluding the upstream area between the leading edge and the slot outlet. The averaging was performed by interpolating the pixel-wise distribution of the surface-mapped camera data onto a grid of regularly spaced points, allowing an equally weighted calculation.

The outlet plane for the five-hole probe measurements extends from the near-shroud region to the midspan since the effects of coolant ejection are limited to this part of the passage flow. Due to the limited applicability of five-hole probe measurements in the immediate vicinity of walls, the measuring plane was restricted to $z/h_{\mathrm{out}} = -0.46$. As schematically depicted in the right part of Figure 4.1, each probe measurement consists of 896 single measuring points that were densified in spanwise direction near the shroud for a better resolving of secondary flows.

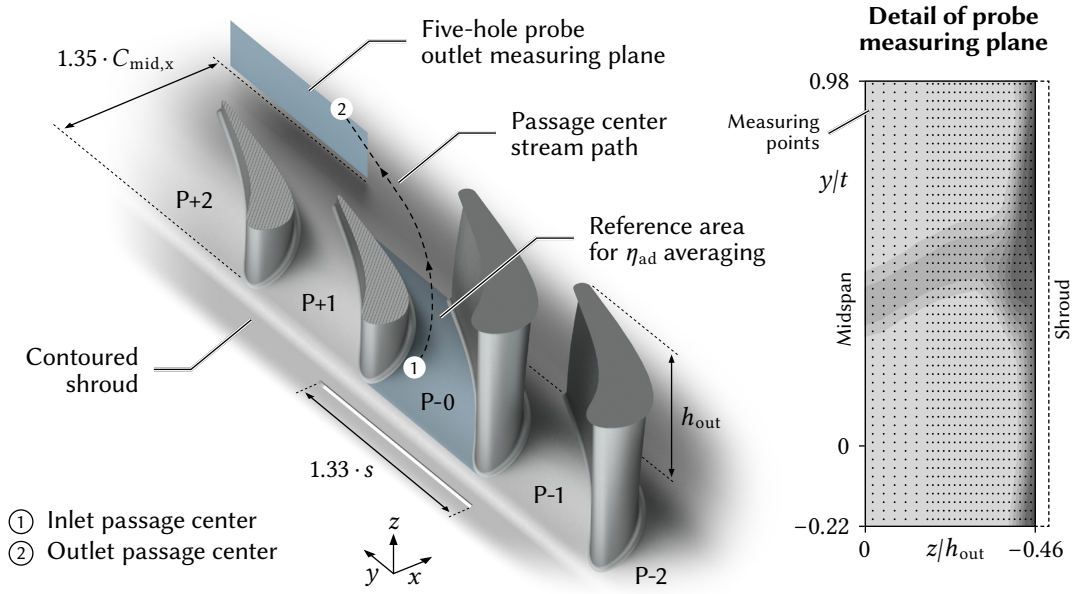

Figure 4.1: Nomenclature of the linear cascade with outlet probe measuring plane and reference area for η_{ad} averaging

For better readability, the coolant configuration with regard to the geometric- and ejection-related parameters is denoted following the structure

$$(\alpha\bigcirc\,|\,W\bigcirc\,|\,L\bigcirc\,|\,BR\bigcirc\,|\,DR\bigcirc),$$

where the circular placeholder is replaced by the actual value if not changed in the corresponding evaluation. Furthermore, the slot distances $L = 9,\ 12$ and 18 mm are paraphrased as near-, medium-, and far-upstream in the following discussion.

Experimental and numerical investigations following the measurement campaign on the linear cascade have shown that the slot flow is adversely affected by the geometry of the upstream plenum. The results of the numerical simulation of the plenum geometry and implications for the redesign of the annular plenum are discussed in detail in Chapter 5.5.4. At this point, however, it should be mentioned that certain singularities, such as streaks, which emerge in the coolant distribution shown below, may be attributed to the plenum characteristics.

4.2 Near-Endwall Flow Visualization

As already discussed in Chapter 2, there is a strong interdependence between the injection and distribution of coolant on the one hand and the formation and downstream progression of secondary flow on the other hand. It is, therefore, reasonable to start with a discussion of the oil flow visualizations before assessing the coolant distribution based on the PSP measurements.

4.2.1 Interference Between the Coolant and the Main Flow

The scale of interference between the coolant and the main flow is illustrated in Figure 4.2, where the base case, i.e., a no-slot configuration with a blind insert, is compared with a perpendicular coolant injection. As to be expected from a highly optimized, aft-loaded vane geometry, the streamline distribution of the base case on the left is rather unspectacular in the sense that no prominent secondary flows can be observed. The saddle point (S), where the reverse flow of the horse-shoe vortex intersects the incoming boundary layer flow, is located in close proximity to the leading edge, indicating that the strength of the horseshoe vortex is significantly attenuated in comparison to cylindrical vane designs without fillets or endwall contouring, as shown, e.g., by Takeishi et al. [20].

When the horseshoe vortex splits up, the two legs propagate downstream into the passage. While the suction-side leg (1) is convected around the leading edge and stays close to the vane root, the cross-passage pressure gradient causes the pressure-side leg (2) to detach from the vane traveling toward the suction side. However, in contrast to the secondary flow model presented in Chapter 2.1.1, it is not evident that it propagates all the way to the adjacent vane and merges with its suction-side counterpart to form the passage vortex. Rather, the vortex re-approaches the pressure side in the mid-passage region (see detail), possibly absorbing the pressure-side corner vortex, which is hardly

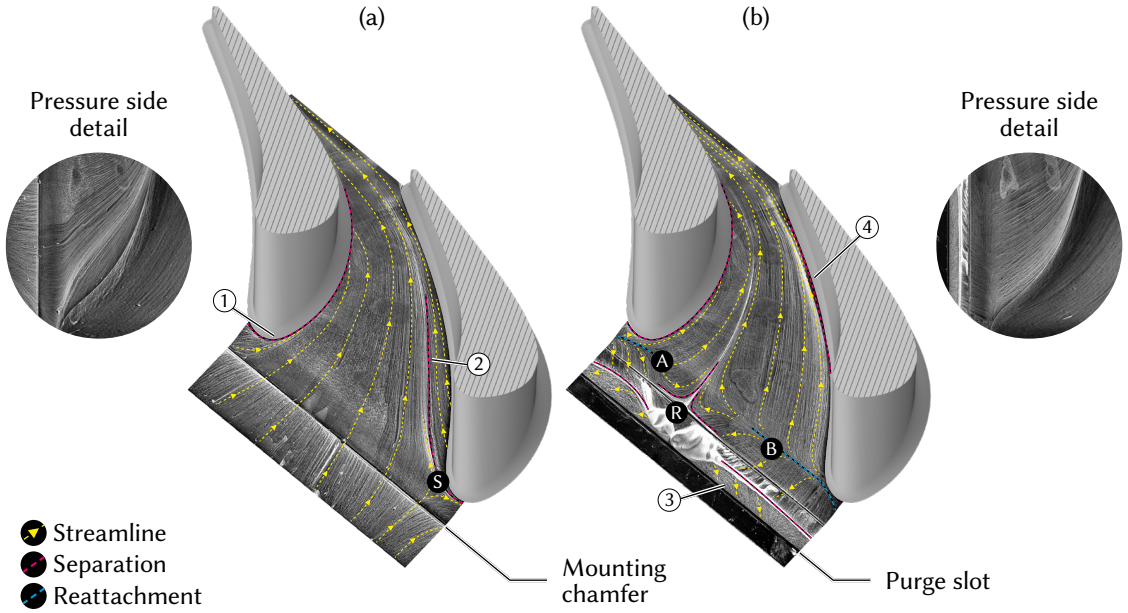

Figure 4.2: Oil flow visualization of (a) base case and (b) exemplary cooling configuration ($\alpha 90\,|\,W1\,|\,L18\,|\,BR1.5\,|\,DR1$)

visible. In the aft of the passage, its track gets lost, indicating that the vortex has detached from the endwall or is dissipated by the main flow. With this in mind, it is clear that the typical division of the endwall into two large crossflow zones separated by the pressure-side leg of the horseshoe vortex does not apply to this extent in the present case. Rather, the passage crossflow, which arises from the altered equilibrium between the reduced centripetal forces in the boundary layer and the imposed cross-passage pressure gradient, originates mainly from the upstream endwall boundary layer.

Anticipating the PSP results, the flow field of the present vane design appears to be particularly advantageous since the coolant propagation is usually limited by the pressure-side leg of the horseshoe vortex for low and medium blowing ratios.

The extent to which the secondary flow field may change when high-momentum coolant is injected into the main flow is shown in the right part of Figure 4.2, exemplary for a perpendicular injection with $BR = 1.5$ at the far-upstream position. It is first noticed that the formerly mentioned flow features at the leading edge and at the pressure side, namely the saddle point and the pressure-side leg of the horseshoe vortex, are no longer visible on the endwall. Rather, the vortex is apparently displaced by the propagating coolant on the vane surface.

Due to its high momentum, the coolant instantly separates at the slot exit and penetrates the main flow before reattaching at the passage inlet. While doing so, it rolls up against the main flow direction and forms two counter-rotating vortices (A) and (B) originating at the leading edge and propagating in the pitchwise direction towards the passage center. The flow field between the vortices and the slot exit is quite complex: The sprinkled distribution of oil paint along a narrow strip (3) indicates a zone

of reduced skin friction, which is enclosed by the detached coolant at the slot exit and the separation lines of the two vortices. The flow direction of this separation bubble cannot be clearly identified due to the faint formation of the streamlines. However, it stands to reason that the circulation is driven by the shear stress of the detached coolant flow, thus pointing to the slot exit at the wall-facing side. This is also supported by the fact that the area has not been completely washed out. Rather, oil paint is continuously drawn from the large accumulation zone, which is formed at the rendezvous point (R) of the two converging vortices that are deflected into the passage. Further downstream at the pressure-side vane root, a separation line (4) appears whose origin cannot be clearly associated with a specific vortex since this may be either the corner vortex or the reattaching horseshoe vortex.

4.2.2 Influence of Blowing Ratio

To evaluate the influence of the coolant momentum, Figure 4.3 depicts three different blowing ratios for a narrow, perpendicular slot at the near-upstream position. Starting with $BR = 0.25$ at the left, it can be seen that the flow field experiences only minor changes. The saddle point (S) is slightly shifted upstream, which is accompanied by a marginal intensification of the horseshoe vortex, with the separation line of the pressure-side leg somewhat moving to the passage center. Contrary to the high-momentum case discussed in the previous section, the coolant seems to reattach to the endwall just downstream of the slot exit, as indicated by the reattachment line and the enclosed oil accumulation. The distribution of the accumulated oil suggests that a pitch-wise crossflow within the small separation

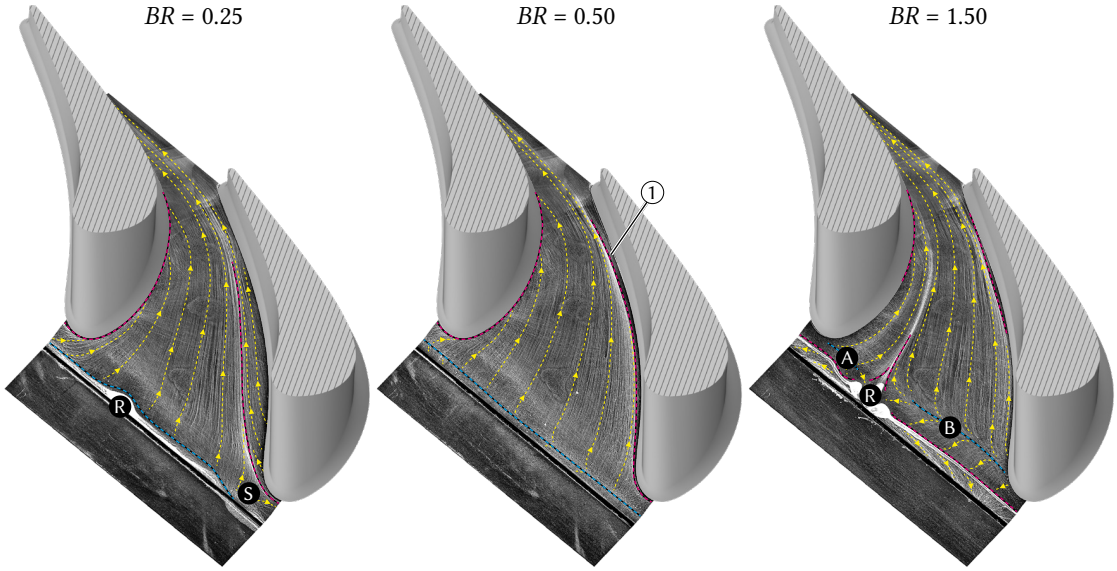

Figure 4.3: Oil flow visualization regarding the influence of BR using the example of cooling configuration ($\alpha 90 \,|\, W1 \,|\, L9 \,|\, BR\bigcirc \,|\, DR1$)

bubble sets in, as the oil is concentrated in a local spot (R). This crossflow is presumably driven by the acting pressure field upstream of the passage, which also confines the coolant exiting the slot near the leading-edge area.

When increasing the coolant momentum to $BR = 0.5$, an almost imperceptible reattachment line extends over the entire length of the slot, with the partial accumulation of oil disappearing completely. This indicates that the coolant crossflow within the separation bubble has vanished, and the coolant exits the slot now much more uniformly. Concerning the main flow, the separation line of the horseshoe vortex is shifted towards the vane root. The densification of the streamlines (1) in the downstream part of the passage near the pressure side suggests that the vortex does not separate from the endwall.

A further increase of the blowing ratio to 1.5 causes a qualitative change in the flow topology, as it is already found in the far-upstream slot configuration discussed in the previous section. Again, the coolant rolls up in two counter-rotating and converging vortices (A) and (B) that are deflected into the passage while the oil paint is accumulated in a large recirculation zone (R) between the vortices and the slot exit. However, compared to the far-upstream injection, these flow features are less pronounced, which in this particular case must be attributed to the special shape of the endwall contouring: As can be seen from the shaded strip in Figure 4.1, there is a bump on the contoured endwall immediately upstream of the passage entrance that promotes a rapid reattachment of the separated coolant.

4.2.3 Influence of Injection Angle

As seen previously, significant changes to the secondary flow field are driven by the extent of flow separation of the coolant at the slot exit. It stands to reason that separation of the coolant and, as a result, increased mixing with the main flow will, first, worsen the cooling effectiveness and, second, be aerodynamically inefficient. Thus, it can be further assumed that an inclined injection, which is also common in film cooling by discrete holes, has less impact on the flow field while increasing the cooling effectiveness.

To confirm this assumption, Figure 4.4 compares the perpendicular configuration with the two inclined variants at the near-upstream position with $BR = 1$. At $\alpha = 90^\circ$, once again, the flow structure, which is already known from the discussion of $BR = 1.5$ in the previous section, emerges but with reduced strength due to the lower blowing ratio. At this point, in view of the PSP results, it should be noted that the transition of the flow topology to the emergence of coolant-induced vortices apparently occurs between $BR = 0.5$ and $BR = 0.75$.

In the case of the two inclined injections, the coolant attaches to the endwall closely behind the slot exit without forming coolant-induced vortices. The accumulation of oil, which indicates the presence of a small separation bubble, gradually weakens with a decreasing slot angle. The flow field further downstream is nearly identical for the two inclined variants. In both cases, the formation and propagation of the horseshoe vortex seem to be mitigated, as the separation line is shifted to the pressure side of the vane root. Furthermore, the boundary layer is re-energized, weakening the endwall crossflow.

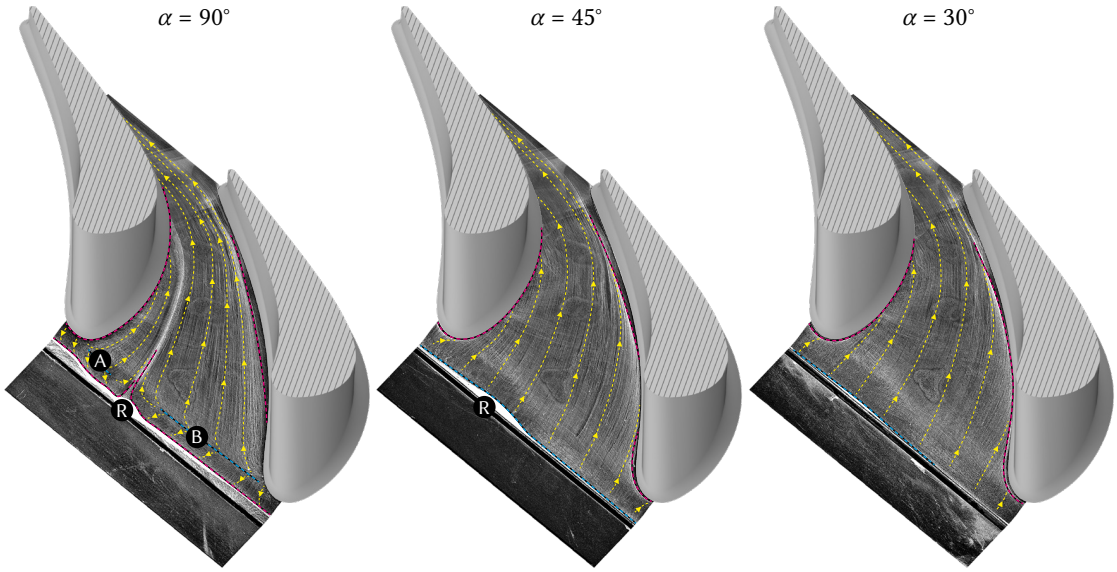

Figure 4.4: Oil flow visualization regarding the influence of α using the example of cooling configuration ($\alpha\bigcirc\,|\,W1\,|\,L9\,|\,BR1\,|\,DR1$)

4.3 Endwall Pressure

To check the plausibility of the PSP measurements, the static pressure distribution on the base case endwall is shown in the left part of Figure 4.5, with the local pressure difference between the PSP and the pressure tap reading being determined. First of all, it is noticeable that the pressure reduction, as to be expected for an aft-loaded vane geometry, is mainly limited to the mid and rear part of the passage. The pressure increase around the stagnation point cannot be resolved with the existing measurement setup since it only amounts to approximately 5 mbar, considering the dynamic pressure at the inlet (see Appendix A).

The right part of Figure 4.5 depicts the chordwise averaged distribution of the static pressure and the corresponding isentropic Mach number. Again, it is evident that the major share of pressure conversion respectively flow acceleration occurs in the downstream half of the passage, with the isentropic Mach numbers rising almost linearly from approximately 0.3 to 0.79.

When comparing the PSP pressure information with the pressure tap reading, it is important to keep in mind that the latter can be biased by the hole geometry. This includes, for example, the Reynolds number related to the borehole diameter as well as the edge treatment or the angle at which the borehole is drilled into the wall [130]. While the first three pressure taps indicate slightly lower pressures than the PSP, the reading of the last tap is somewhat higher. This deviation, which increases in absolute numbers in the rear part of the passage, must be understood as a superposition of several potential measurement errors, which will be discussed in detail in Appendix A. However, it can be

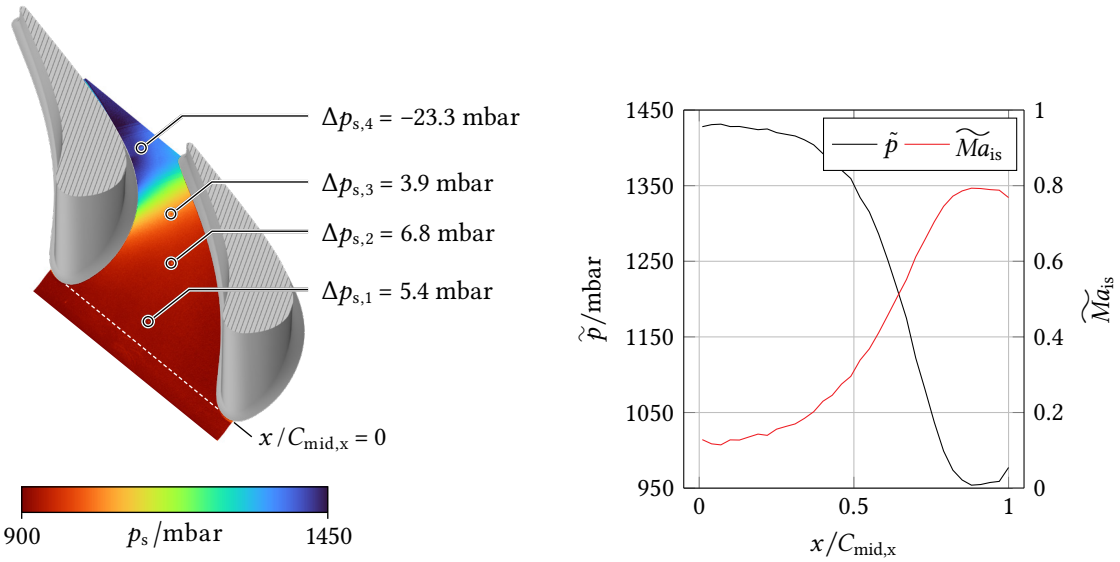

Figure 4.5: PSP-based pressure distribution with deviation $\Delta p_{s,i}$ from pressure tap readings i and chordwise averages with isentropic Mach number

assumed that the deviation of the last bore is mainly caused by both the decreasing fluid temperatures due to pressure conversion and the – for constructive reasons – inclined orientation of the pressure tap related to the local wall normal. While the first effect increases the luminescence intensity and thus decreases the obtained pressure information assuming a constant reference temperature, the latter leads to a slight exaggeration of the tap reading. In summary, it can be stated that the PSP setup provides reliable pressure readings – especially considering that the span in the partial oxygen pressures is substantially increased when using foreign gas.

4.4 Endwall Film Cooling Effectiveness

The next section presents the results of the film cooling effectiveness measurements. Before examining the influence of the individual parameters, it will first be shown how the development of secondary flow and coolant distribution are related. For this reason, Figure 4.6 superposes the secondary flow field with the distribution of adiabatic film cooling effectiveness for the perpendicular slot at the near-upstream position.

With $BR = 0.25$ in the left part, it can be seen that the highest cooling effectiveness is obtained in the small strip that is associated with a separation bubble (R) directly downstream of the slot. As indicated by the course of the reattachment line and confirmed by the coolant distribution, the coolant does not exit the slot uniformly along the slot length, rather being concentrated in the center. While the coolant effectiveness rapidly decreases downstream of the reattachment line, the coolant is strongly constricted by the pressure-side leg of the horseshoe vortex (1) with its accompanying passage crossflow. A similar

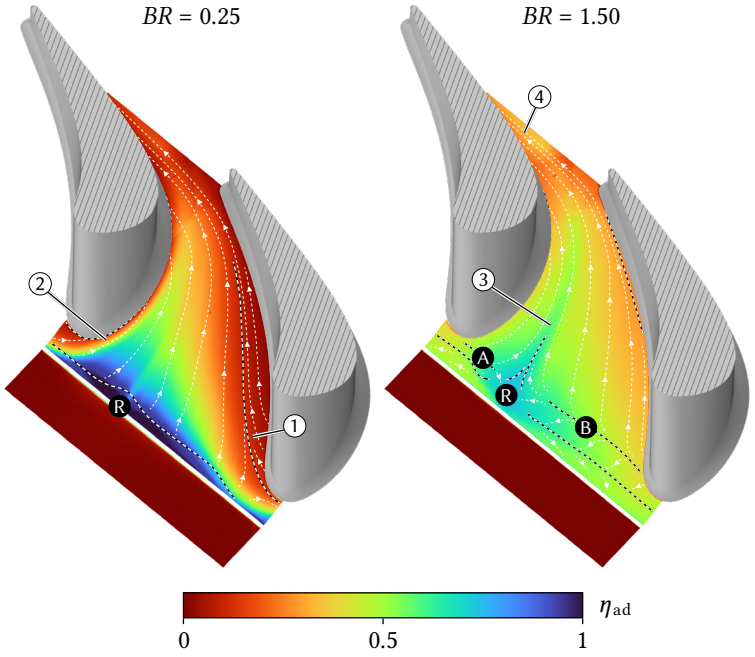

Figure 4.6: Superposition of secondary flows derived from oil flow visualization with the distribution of η_{ad} for cooling configuration ($\alpha 90 \,|\, W1 \,|\, L9 \,|\, BR\bigcirc \,|\, DR1$)

effect, albeit much less pronounced due to its position, is generated by the suction-side leg of the horseshoe vortex (2), which stays close to the leading edge. It presumably causes the narrow region around the vane root not to be covered by the coolant.

The high-momentum injection ($BR = 1.5$) reveals a distinct change in the coolant distribution. As a result of the much stronger initial mix-out with the main flow, the effectiveness immediately downstream of the slot is considerably reduced compared to the previous case. Both coolant-induced vortices (A) and (B) obviously transport the coolant in the area (R) that is associated with the large accumulation of oil paint. Where the vortices converge and are deflected into the passage, a coolant streak (3) appears that extends from the accumulation zone to the rear part of the passage. Even though the maximum effectiveness is significantly reduced compared to the low-momentum variant, the coolant-infused main flow apparently spreads enough coolant in the passage to provide cooling even to those areas previously shielded by the horseshoe vortex.

In the aft of the passage, a local increase of the film cooling effectiveness (4) can be observed, which also appears in other cooling configurations shown below. It cannot be ruled out that this phenomenon might be caused by an interaction with the passage vortex, which transports the coolant back to the endwall. However, it is more likely that this is a systematic measurement error due to an unavoidable reflection of the UV light source, which in turn is owed to limited optical accessibility in the aft part of the passage.

4.4.1 Influence of Blowing Ratio and Injection Angle

While the blowing ratio constitutes an important parameter that can be adjusted by regulating the feeding pressure of the cooling cavities in the real engine, the injection angle can be modified by design changes of the vane platform. The influence of both parameters is illustrated in Figure 4.7 for a narrow slot at the near-upstream position, with the area-averaged results being added to the respective contour plots. To reflect the conditions in the actual engine, this and the following comparisons are provided with the engine-like density ratio.

For all cases, a decrease in the coolant concentration can be observed along the passage, which presumably can be attributed to diffusion and secondary flow-related mixing with the main flow. For both the perpendicular and the inclined injection, albeit less pronounced, the coolant exits the slot very non-uniformly at $BR = 0.25$, probably due to the local pressure peak in the leading-edge area. In the case of the inclined configuration, a narrow band of reduced cooling effectiveness (1) can be seen immediately downstream of the slot. This phenomenon may be caused by local separation, possibly due to minimal surface defects in the coated endwall, as it also occurs at other blowing ratios and slot angles.

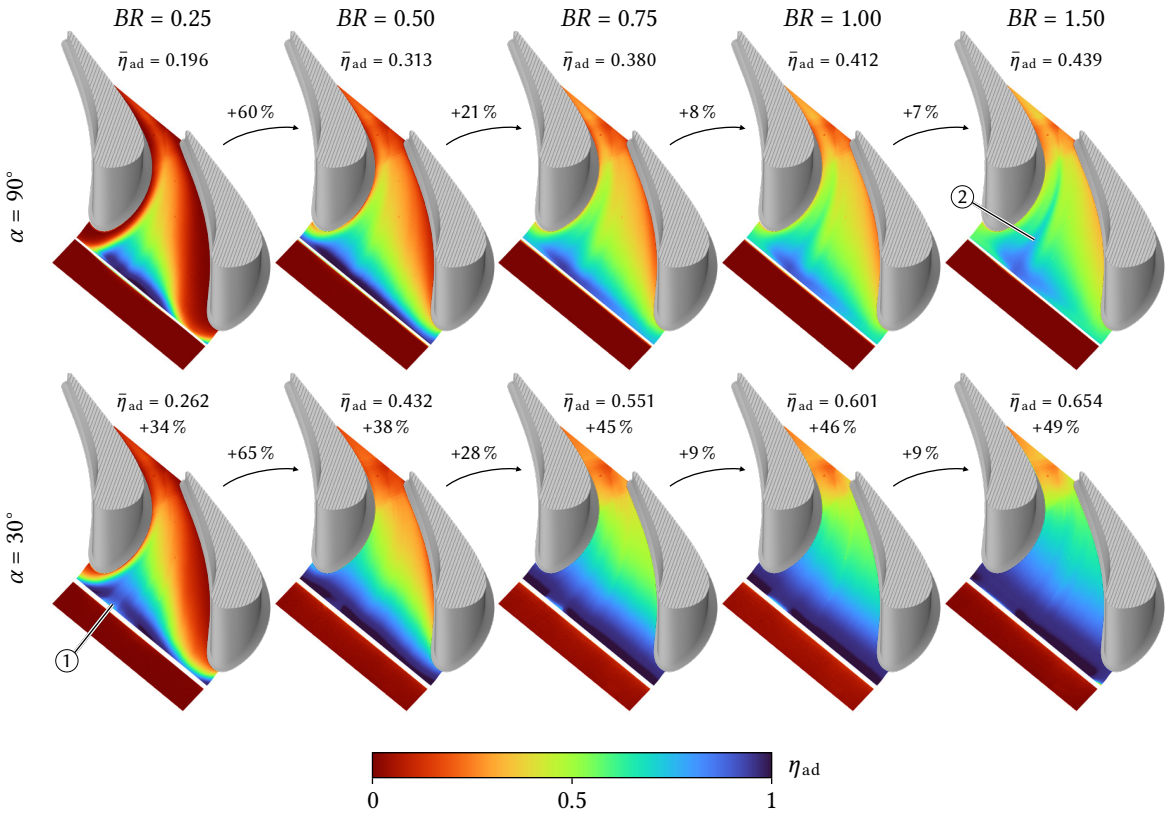

Figure 4.7: Influence of BR and α on η_{ad} for exemplary film cooling configuration ($\alpha\bigcirc\,|\,W1\,|\,L9\,|\,BR\bigcirc\,|\,DR1.6$)

In the passage, the coolant forms a triangular shape which is limited by the separation lines of the horseshoe vortices. Thus, critical areas, e.g., the vane leading edge and pressure side, remain uncooled. Consequently, a slight increase of the coolant momentum ($BR = 0.5$) results in a more even injection along the slot length, whereby the sharp limitation of the triangular shape vanishes, as the pressure-side leg of the horseshoe vortex is shifted towards the vane root.

Increasing the coolant momentum beyond $BR = 0.75$ yields only minor effectiveness gains for the perpendicular injection since the coolant separates and mixes with the main flow. With recourse to the findings of the oil flow visualization, it can be seen that the coolant-induced vortices increasingly draw the coolant away from the leading-edge area, concentrating it in their convergence zone. At the same time, the coolant streak (2), which is formed by the deflected vortices, becomes more and more visible.

While the pressure side remains nearly uncooled for the highest coolant momentum at perpendicular injection, all critical areas in the upstream half of the passage are covered with coolant for the inclined injection at $BR \geq 0.75$. Since the coolant does not separate even at the highest blowing ratios, significant gains in cooling effectiveness can be realized. However, the coolant still mixes with the main flow in the rear part of the passage. On the one hand, this may certainly be attributed to turbulent diffusion and the interaction with secondary flows. On the other hand, the convex shape of the very rear part of the endwall (see Figure 3.2) might contribute to this, as it promotes the separation of the coolant film.

Concerning the averaged results and the influence of the slot angle, it is obvious that the inclined injections outperform the perpendicular injection for all blowing ratios, whereby the lead increases for higher blowing ratios, as the perpendicular injection is more and more affected by separation and turbulent mixing. It can be concluded that the propagation of the coolant relies to a large extent on the initial mixing with the main flow, which in turn depends on whether the coolant separates at the slot outlet.

Regarding the influence of the blowing ratio, it is evident that the biggest gain in cooling coverage can be achieved in the transition from $BR = 0.25$ to $BR = 0.50$ with 60 % respectively 65 % as the coolant can overcome the counteracting pressure at the leading edge for both perpendicular and inclined injection. The relative enhancement of the coolant coverage decreases then progressively for higher blowing ratios and finally amounts to only 7 % respectively 9 %.

4.4.2 Influence of Slot Width

To investigate the influence of the slot width W, it is reasonable to compare different widths at equal coolant mass flows since the influence of W would otherwise be superimposed by the mass flow variation. Figure 4.8 shows the two slot widths at two mass flow equivalent BR cases for both a perpendicular and an inclined injection at the medium- respectively near-upstream position.

Starting with the perpendicular injection, it can be seen that the narrow slot benefits slightly from the increased coolant momentum since the coolant exits the slot more evenly compared to the wide slot injection at $BR = 0.25$. Here, the coolant is mainly concentrated in the part of the passage that is enclosed by the two legs of the adjacent horseshoe vortices. At higher blowing ratios, the opposite

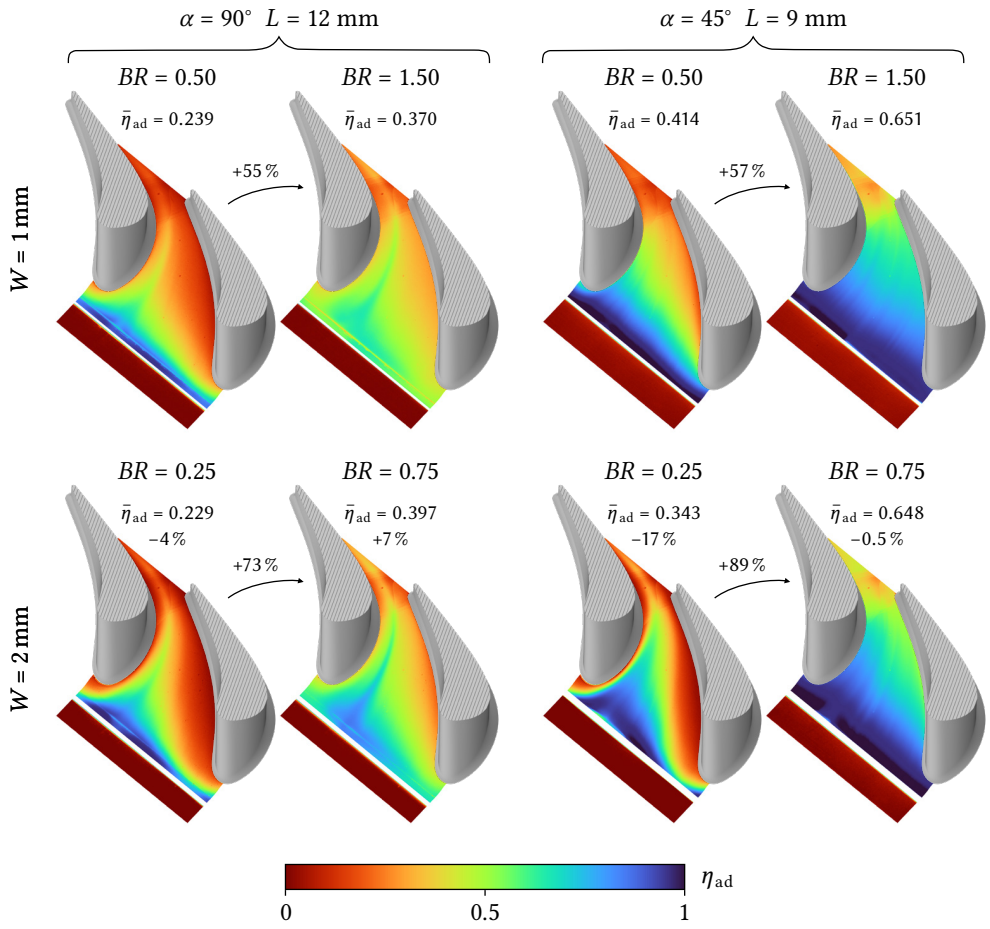

Figure 4.8: Influence of W on η_{ad} at mass-flow equivalent BR for exemplary film cooling configuration ($\alpha\bigcirc\,|\,W1\,|\,L\bigcirc\,|\,BR\bigcirc\,|\,DR1.6$)

occurs: The high-momentum injection through the narrow slot causes the coolant to separate and mix with the main flow to a larger extent. Thus, the wide slot variant performs better, at least in terms of average values. However, for the narrow slot, the coolant-infused main flow propagates the coolant to the thermally critical pressure side to a somewhat larger extent.

Since separation occurs only on a small scale with the inclined variants, the advantages associated with a higher coolant momentum prevail. This is particularly evident for the low-momentum comparison, where the narrow slot configuration provides already good coolant coverage over the entire pitch in the upstream half of the passage, whereas the performance of the wide slot suffers from the acting counter-pressure at the leading edge and the shielding effect of the horseshoe vortex. For higher blowing ratios, these differences almost completely level out, as the wide and narrow slot variants perform virtually the same, both in terms of local distribution and averaged values.

4.4.3 Influence of Slot Distance

The slot distance depends on the axial dimension of the vane platform, which in turn can be adjusted in the design process. To investigate the influence of this distance, Figure 4.9 depicts the results for the wide and perpendicular slot at the near-upstream and far-upstream position. First, it is striking that the coolant exits the far-upstream slot more evenly at low blowing ratios since the upstream position is not exposed to the counter-acting pressure field at the leading edge to the same extent. At the same time, the coolant coverage in the passage deteriorates, as indicated by the significantly lowered averaged values. Moreover, in the areas with high thermal load, i.e., the leading-edge region and the pressure side, the local film cooling effectiveness is reduced for this latter case. These phenomena have to be attributed to both the prolonged mixing length and the progression of the endwall contouring that promotes a rapid reattachment of the separated coolant at the near-upstream position, as explained before. For this reason, considerably higher local maxima in cooling coverage can be obtained with the slot at the near-upstream position, especially in the convergence zone of the coolant-induced vortices at high blowing ratios. In terms of overall coverage, it can be concluded that the near-upstream position is beneficial for both low and high blowing ratios.

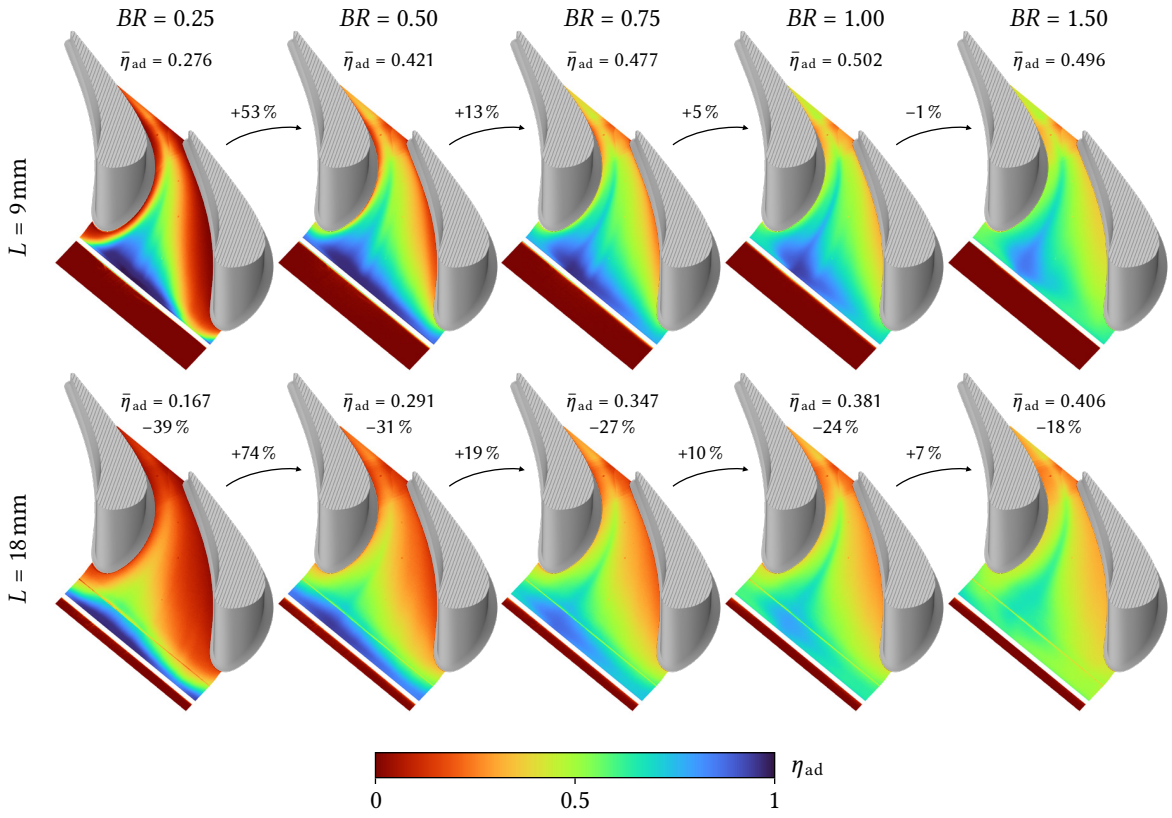

Figure 4.9: Influence of L on η_{ad} for exemplary film cooling configuration ($\alpha 90 \,|\, W2 \,|\, L\bigcirc \,|\, BR\bigcirc \,|\, DR1.6$)

4.4.4 Influence of Density Ratio

Figure 4.10 provides a comparison between the – in terms of practical considerations – academic configuration with $DR = 1$ and the engine-like configuration with $DR = 1.6$ for both a perpendicular and an inclined injection at the lowest respectively highest blowing ratio. Since the mass flow is held constant in this comparison, the higher density ratio is accompanied by a lower exit velocity and, thus, a lower momentum flux. For low BR the film cooling effectiveness is significantly overestimated by using a coolant of the same density because the higher plenum pressure facilitates a homogeneous ejection for both the perpendicular and the inclined slot. At high coolant momenta, the engine-like density configuration is advantageous, but to different extents regarding the perpendicular and inclined slot. While the first clearly profits from reduced separation and turbulent mixing, the latter benefits only to a very small extent.

It can be concluded that the density ratio should be included in the analysis whenever the coolant momentum is suspected of playing a major role in the coolant distribution.

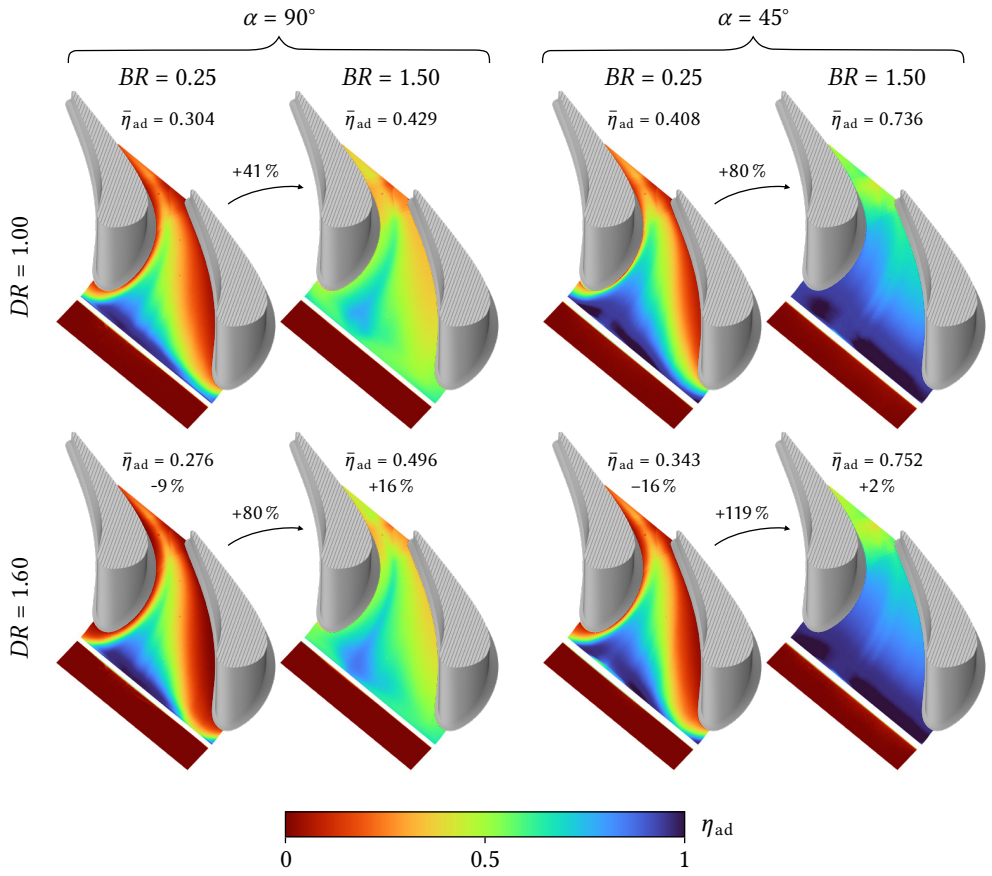

Figure 4.10: Influence of DR on η_{ad} for exemplary film cooling configuration ($\alpha\bigcirc\,|\,W2\,|\,L9\,|\,BR\bigcirc\,|\,DR\bigcirc$)

4.5 Outlet Flow Field

The injection of coolant upstream of the leading edge, so to say in the nucleus of secondary flow emergence, can significantly affect the near-endwall flow field of the passage, as seen before. It can therefore be assumed that these changes propagate downstream and influence the overall vane aerodynamics. For this reason, the results of the five-hole probe measurements on the outlet plane are compared in the following section.

Figure 4.11 presents the flow field of the uncooled base case broken down by the pressure ratio Π, the total pressure loss coefficient ζ and the pitch and yaw angles with a superimposed secondary flow field. Starting with the distribution of the pressure ratio (a), it can be seen that the midspan flow field is dominated by cross-passage pressure gradients originating from the vane pressure and suction side. The central passage P-0 is separated from its adjacent passage P+1 by the vane wake flow, with its center being indicated by the dashed line. Since the chord length decreases from the shroud to the hub, the wake has an oblique orientation on the axial measurement plane. Near the shroud, the secondary flows and the endwall boundary layer appear through a reduction in static pressure (1).

The total pressure loss (b) distribution of a subsonic nozzle guide vane can be divided into three zones of different loss regimes, with the nearly lossless freestream dominating the flow field from the midspan to the near-endwall region. The profile loss, which is mainly two-dimensional in nature, originates from both the boundary layer separation at the vane trailing edge and from viscous and turbulent effects, which are caused by the non-uniform velocity profile in the vane wake [13]. In the

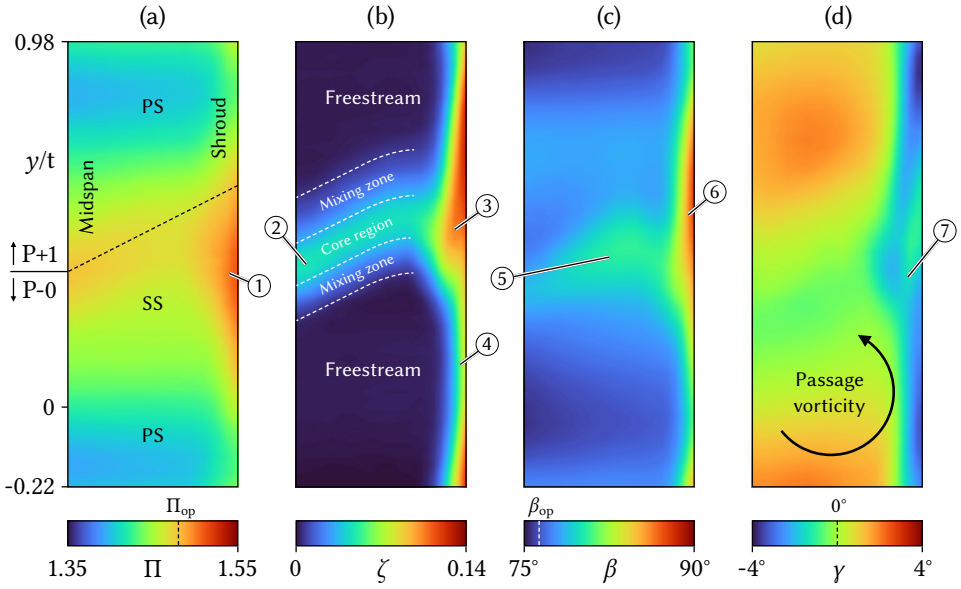

Figure 4.11: Base case distribution of loss coefficient ζ and flow angles β and γ with superimposed secondary flow field

present case, the wake is clearly separated into a narrow core region of medium losses (2), which originates presumably from the separated boundary layers, and a low-loss zone in which the wake mixes with the freestream.

The third regime is characterized by endwall losses, which are three-dimensional by nature, as they are caused by both secondary flow and the growth of the endwall boundary layer. As already discussed in Chapter 2, these losses account for a significant portion of total losses. Given the design features of the vane and the analysis of the near-endwall flow field in section 4.2, it is therefore not surprising that in the present case, these losses are significantly reduced compared to non-optimized designs, e.g., the cylindrical vane, which was previously investigated in the high-speed turbine test rig [10]. As already found by Dossena et al. [34] in a study on a similarly contoured vane design, the contraction of the passage restrains the formation of a proper passage vortex. This inhibits the transport of low-energy fluid from the endwall boundary layer toward the midspan. In the present case, characteristic vortex structures cannot be clearly identified since the limitation of the probe restricts flow measurements in the immediate vicinity of the shroud. Considering the flow angles shown on the right, the loss maximum (3) in the wake extension may be attributed to the passage vortex. The thickening of the endwall boundary layer, which is promoted by the convex shape of the endwall in the rear part of the passage, must account for the loss accumulation at the outer edge of the measurement field (4).

Concerning the pitch angle (c), the freestream is characterized by an almost homogeneous distribution approximating the turning angle of the design point. The slight over-turning of the flow in parts of the wake region (5) can be traced back to the twisted trailing edge of the vane, which increases the local turning angle from the hub to the shroud. In the immediate vicinity of the wall (6), the strong over-turning of the boundary layer flow becomes apparent. The yaw angle distribution (d) exhibits a passage vorticity that transports fluid from the midspan pressure side to the endwall and then back to the midspan. The region close to the wall where the highest pressure losses occur is characterized by a close juxtaposition of large and small yaw angles (7), indicating the presence of the passage vortex. However, the vorticity shown in the secondary flow field is superposed by the strong over-turning near the endwall.

Impact of perpendicular coolant ejection: To assess the effects of coolant ejection on the outlet flow field, the discussion starts with Figure 4.12 depicting the loss distribution for the perpendicular slot at the near-upstream position, with base case contour line for $\zeta = 0.1$ being overlaid. The mass flow averaged pressure loss is added below.

First, it is striking that even for the highest blowing ratio, the effects of coolant injection are limited to the near-endwall region, while the width and the loss level of the wake at the midspan remain virtually unchanged. With increasing *BR*, the local loss maximum, which is associated with the passage vortex, moves gradually toward the midspan. At maximum *BR* it starts to separate from the endwall boundary layer (1) and mix with the mainstream. With recourse to the oil flow visualization in Figure 4.3, this phenomenon can be traced back to the initial displacement of the pressure-side leg of the horseshoe vortex. The thickness of the endwall boundary layer (2) is not altered by the injection.

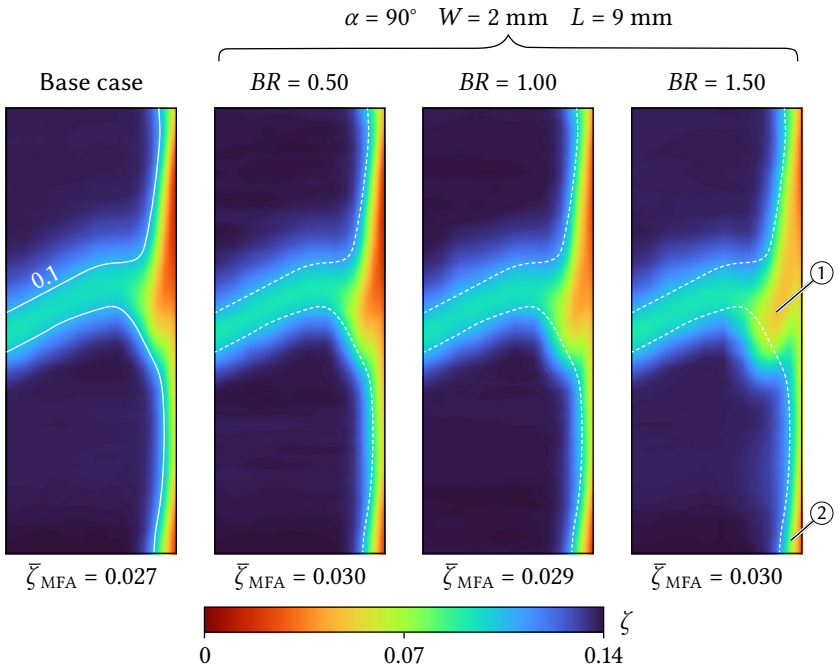

Figure 4.12: Influence of BR on ζ for perpendicular injection

In terms of total losses, it can be concluded that the perpendicular injection worsens the aerodynamic performance of the vane, as the mass flow averaged losses increase slightly. However, it should be noted that significant portions of the endwall flow field are not covered by the measurement plane due to the spatial limitations of the probe.

Impact of inclined coolant ejection: The loss distribution of the inclined injection is depicted in Figure 4.13. Surprisingly, the flow field does not differ qualitatively much from the perpendicular injection – unlike the previous investigation on the cylindrical vane, where almost complete extinction of the passage vortex was observed. In the present case, the loss core (1) is marginally displaced in the direction of the midspan, with the loss maximum being slightly reduced compared to the perpendicular injection. It is, however, noticeable that the endwall boundary layer thickness (2) is significantly reduced when compared with the base case. It stands to reason that the inclined injection introduces high-energy fluid into the boundary layer, thus counteracting the thickening. This is also reflected in the mass-averaged values, as the inclined injection provides a gross loss reduction, i.e., without balancing the energy input of the injected coolant, which would be necessary for a net analysis.

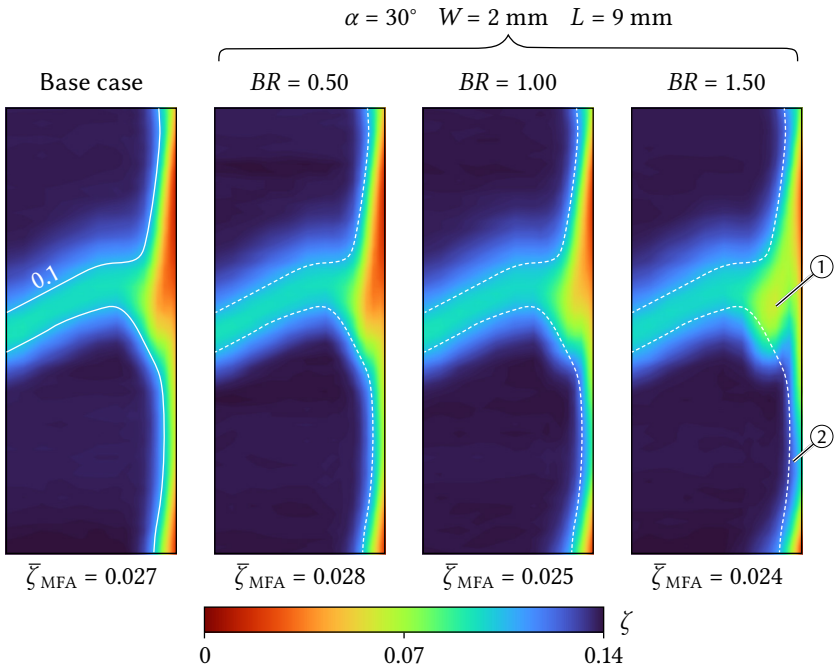

Figure 4.13: Influence of BR on ζ for inclined injection

4.6 Endwall Net Heat Flux Reduction

The next section reports the results of the linear heat transfer measurement campaign. The discussion of results is preceded by the presentation of the linear measurement module since design decisions for the annular measurement module (see Chapter 5.5.5) are derived from the experience with the linear module and its shortcomings. Table 4.1 summarizes the operating conditions of the two thermal setups that have been realized. While the first operating point was realized by uncooled bypass operation utilizing the heat of the screw compressor, the gas burner was switched on at minimum power in the second operating point, with the slot parameter set being reduced to lower gas consumption.

To allow the extrapolation of the adiabatic wall temperatures according to a superposition approach, introduced by Gritsch et al. [131], three heat flux setups were established by adjusting the cooling water temperatures in three steps for each operating point. Due to the shortcomings of the measurement setup that will be explained in the following section, the measurement module could only be operated with reduced cooling water throughput, therefore limiting its cooling capacity. To reduce the heat flux transferred from the main flow to the endwall, the cooling water temperatures were thus raised for the second operating point.

Table 4.1: Operating conditions of heat transfer measurement campaign

Parameter	OP 1	OP 2
DR	1.2	1.3
T_m	85 °C	160 °C
T_c	25 °C	60 °C
T_cl	(5, 10 and 15) °C	(30, 40 and 50) °C

4.6.1 Heat Transfer Measurement Module

The two-part heat transfer measurement module, shown in Figure 4.14, constructively implements the auxiliary wall method explained in Chapter 3: To obtain a homogeneous temperature distribution, the base body is made from high-conductive copper ($\kappa_\mathrm{BP} = 401\,\mathrm{W\,m^{-1}\,K^{-1}}$) and contains a full-surface cooling water cavity, which encloses the slot insert and is capped by a bolted stainless steel cover plate ($\kappa_\mathrm{CP} = 15\,\mathrm{W\,m^{-1}\,K^{-1}}$). Sealing is ensured by circumferential round cords which are inserted into the sealing grooves of the base body. Its flow-facing side was fully coated with ETFE ($\kappa_\mathrm{AW} = 0.25\,\mathrm{W\,m^{-1}\,K^{-1}}$). The coating was provided with an allowance so that it could be milled to a constant thickness of 0.5 mm in a further processing step. The cooling water cavity is supplied via

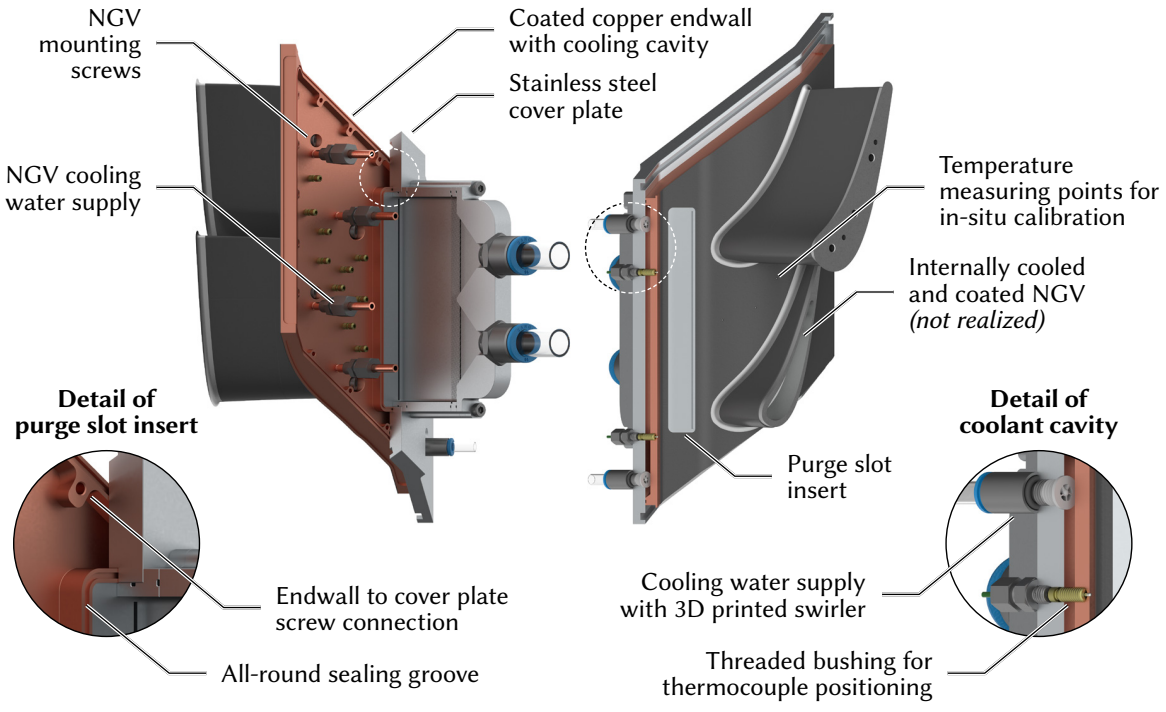

Figure 4.14: Heat transfer measurement module for the linear cascade

six push-in fittings distributed on the back of the cover plate. To avoid impingement cooling effects and ensure a more even distribution of the cooling water, self-developed and 3D-printed swirlers are screwed into the back of the cover plate. For temperature monitoring of the cavity as well as for in-situ calibration of the IR camera, 12 sheath thermocouples (⌀ 1 mm) are integrated into the endwall, which are guided and sealed through the cavity via threaded inserts. The thermocouples for the camera calibration are routed to the surface via a continuous bore in the base body and the coating.

An internal cooling concept for the NGV was developed to extend the heat transfer measurements to the vane surface while also minimizing parasitic heat fluxes from the vane into the endwall, which would potentially affect measurement accuracy in the vane root region. The design includes a cooling water cavity, which is supplied through a separate cooling water circuit. The cooled NGVs were manufactured additively using the so-called Selective Laser Melting (SLM) process, a method of 3D printing that uses a laser to build metal parts layer by layer from powdered metal [132]. Since the raw surface of such printed parts is not hydraulically smooth, the vanes were reworked by milling before the ETFE coating should have been partially applied. For time and cost reasons, however, the concept could not be realized, as the manufacturing of the vane was severely delayed. Additionally, one of the two vanes warped considerably during the printing process, making reworking impossible. Nevertheless, the successful reworking of the second vane demonstrated the feasibility of the concept in principle. Pictures of the post-processed vanes, one being sliced for examination purposes, can be found in the appendix under C.4 and C.5.

Shortcomings of the measurement setup and implications for evaluation: Owing to the component warpage of the cover plate and excessive manufacturing tolerances, the tightness of the cooling water cavity was not given at high cooling water flow rates: Cooling water entered the purge-slot plenum through the inner sealing surface and was discharged into the cascade via the slot insert. By subsequently sealing the cavity with silicone, it was possible to achieve sufficient tightness, at least for a reduced cooling water pressure. However, by reducing the cooling water mass flow, it was not possible to obtain a uniform temperature distribution across the base body. At the same time, the number of temperature measurement points in the base body was too small to interpolate the temperature distribution on the back of the auxiliary wall for calculating the actual wall heat flux.

In addition, the surface thermocouples could not be used for reliable in-situ calibration of the IR camera because the measured value was corrupted by the high temperature gradient inside the auxiliary wall. For this reason, the radiometric correction of the IR data could only be performed with the calibration curve for the transmissivity of the zinc sulfide window obtained ex-situ (see Figure 3.19).

Eliminating these shortcomings would have required reengineering and remanufacturing the measurement module, which was not possible due to project-related time and budget constraints. However, these findings have been incorporated into the development of the annular measurement module presented in section 5.5.5.

As the following section shows, the determination of valid heat transfer coefficients and derived quantities, such as the Nusselt number, is not possible with the current design since the actual heat fluxes cannot be reliably calculated. The obtained measurement data can, however, be used to derive the temperature-dependent formulation of the *NHFR* according to equation 2.6 since it is based on the ratio of the heat fluxes in the cooled and uncooled case.

4.6.2 Heat Transfer Coefficient for Base Case

The discussion starts with the heat transfer coefficient of the uncooled base case, as it reveals not only the effects of the passage flow characteristics on heat transfer but also the shortcomings of the measurement setup. Given the high subsonic flow regime in the rear part of the passage, it is advisable to incorporate the local adiabatic recovery temperature $T_{m,r}$ in the determination of the heat transfer coefficient in the uncooled case. For a turbulent boundary layer, it is defined [100]:

$$T_{m,r} = T_{m,t} \cdot \underbrace{\frac{1 + \sqrt[3]{Pr} \cdot \frac{\gamma-1}{2} Ma_{is}^2}{1 + \frac{\gamma-1}{2} Ma_{is}^2}}_{\leq 1} \quad \text{with} \quad Pr\,(T = 160\,^{\circ}\text{C}) \approx 0.705 \tag{4.1}$$

In the present case, the isentropic Mach number distribution on the endwall could be derived from the PSP measurement, as the inlet and outlet Mach numbers were kept nearly constant by adjusting the total pressure level during hot gas operation. As shown in the left part of Figure 4.15, $T_{m,r}$ drops by approximately 6 °C near the suction side in the downstream half of the passage.

The distribution of the heat transfer coefficient for the base case (OP 2) is shown in the right part of Figure 4.15. While the overall distribution describes a plausible trend of a downstream increasing convective heat transfer, the excessively high values with $h_0 \gg 1000\,\text{W}\,\text{m}^{-2}\,\text{K}^{-1}$ in the rear part of

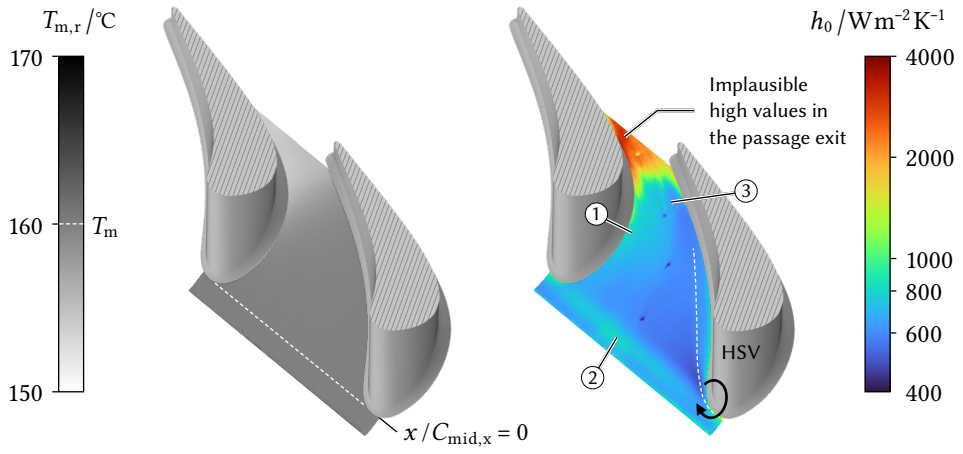

Figure 4.15: Base case recovery temperature $T_{m,r}$ and heat transfer coefficient h_0 for OP 2

the passage are very likely caused by the insufficient and inhomogeneous cooling of the measuring module, with the upper part of the endwall being most affected due to the installation situation. As a result, the actual auxiliary wall temperature T_b is probably much higher than assumed, thus establishing a new local temperature equilibrium with an increased endwall temperature T_w. However, since the unknown variation of T_b cannot be accounted for in the calculation of q_w, the heat transfer coefficient is overestimated.

This notwithstanding, the distribution, particularly in the passage entrance, reveals characteristics that can be attributed, at least qualitatively, to specific flow phenomena: The pressure-side leg of the horseshoe vortex becomes apparent by large gradients near the leading edge. While the area of reattachment in the immediate vicinity of the vane root exhibits an increased heat transfer due to the impingement effect, the separation zone indicated by the dashed line is characterized by lowered heat transfer. In contrast, no delicate structures can be identified along the suction side (1), which suggest the presence of the suction-side leg of the horseshoe vortex. This finding is, however, supported by the oil flow visualization from Chapter 4.2 and prior investigation by Thrift et al. [36], who found similar characteristics at the leading edge of an axisymmetrically contoured vane design. The general increase in convective heat transfer from the pressure to the suction side is presumably caused by the acceleration of the fluid and the resulting thinning of the boundary layer.

The already mentioned bump (2) in the progression of the endwall contouring stands out with locally increased values. The same is true for the third thermocouple bore (3), where a turbulent streak forms, likely due to a surface defect or burr at the hole's edge.

4.6.3 Net Heat Flux Reduction

The effects on the heat flux distribution by coolant injection are discussed on the basis of the temperature-dependent formulation of the net heat flux reduction according to equation 2.6. With respect to the full scope of the parameter set, the discussion is focused on operating point 1 ($DR = 1.2$), with the single results of the three cooling water temperatures being averaged. The compilation of the results corresponds to the parameter sets discussed in the section on film cooling effectiveness. However, when directly comparing the results, it must be taken into account that the density ratios do not match.

Furthermore, a comparison of the two operation points with regard to the influence of the density ratio is not meaningful since the investigation would be superimposed by the effect of changed temperature ratios between the main flow, the coolant, and the coolant liquid. With recourse to Chapter 2.2, the temperature-dependent formulation of *NHFR* as used here is necessarily related to the temperature ratio

$$\frac{\Delta T_f}{\Delta T_0} = \frac{T_c - T_b}{T_{m,r} - T_b}. \tag{4.2}$$

as it sets the upper limit of the *NHFR* that can be obtained in the corresponding measurement. For example, with $T_c < T_b$, it would be possible that *NHFR* locally exceeds 1 as the direction of heat flux would possibly be reversed in regions of high coolant concentration.

Influence of blowing ratio and injection angle: Figure 4.16 depicts the results for both a perpendicular and an inclined slot at the near-upstream position, with the area-averaged values and their relative change being added. First of all, it is striking that $NHFR \geq 0$ for all blowing ratios, i.e., in the present thermal configuration, the near-upstream slot does not worsen the thermal loading of the endwall, as negative values would appear yellow to red with the present colormap. The distributions show both similarities and differences to those found for the film cooling effectiveness. Thus, as the coolant concentration decreases further downstream due to turbulent mixing with the main flow, *NHFR* also declines. Moreover, the non-uniform coolant injection along the slot length and the downstream accumulation of coolant (1) at the lowest blowing ratio are reflected by both locally very large *NHFR*, while the leading-edge area and the pressure side are fully exposed to the hot gas. With

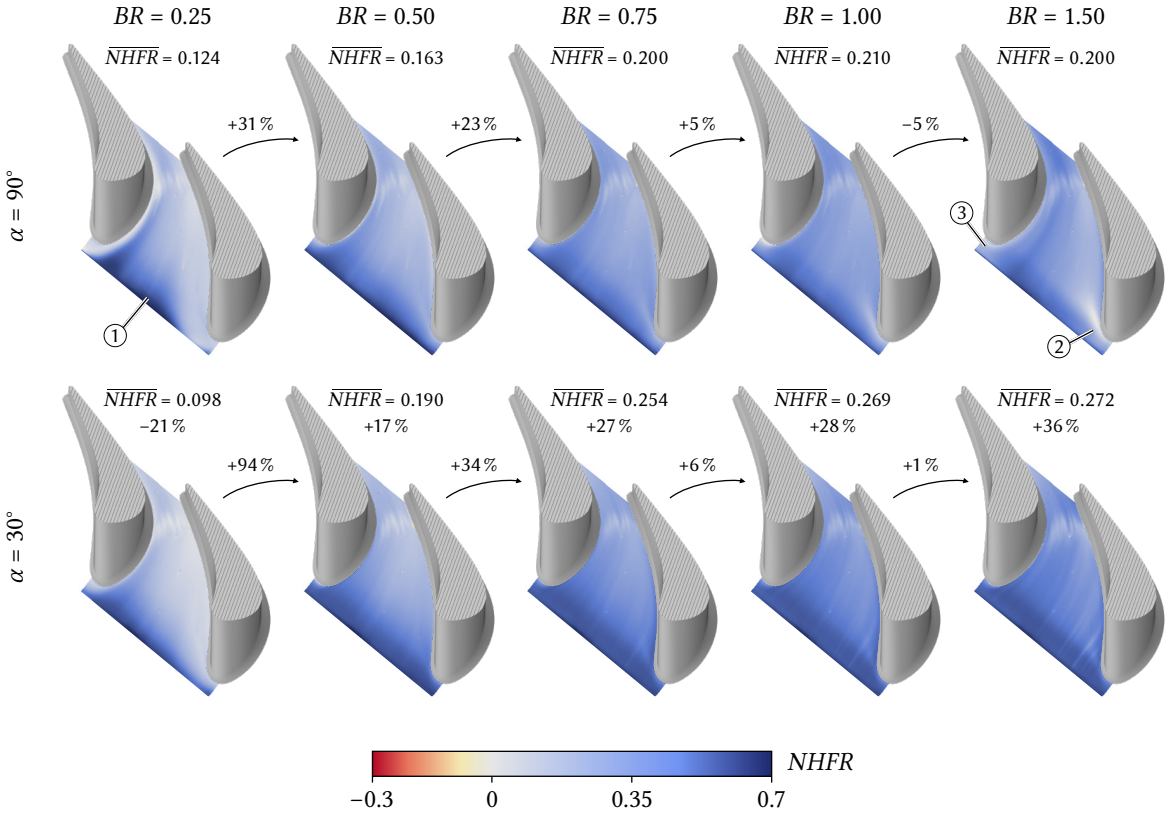

Figure 4.16: Influence of *BR* and α on *NHFR* for exemplary film cooling configuration ($\alpha\bigcirc\,|\,W1\,|\,L9\,|\,BR\bigcirc\,|\,DR1.2$)

recourse to the results of the oil flow visualizations, the low-momentum injection does not intensify secondary flow to a significant extent. It is, therefore, not surprising, but only consistent with the prior findings, that areas not being covered by coolant do not suffer from increased net heat flux.

By raising the blowing ratio up to $BR = 1$, the heat flux reduction and its homogeneity in pitchwise direction are improved, especially in the upstream half of the passage for both the perpendicular and the inclined injection. As indicated by the averaged values, a further increase in the coolant momentum does not reduce the thermal load. For a perpendicular injection, there is even an opposite effect, both locally and on average, as $\overline{NHFR}$ drops by 5 % compared to $BR = 1$. On account of the amplification of secondary flows, the leading-edge area on both the pressure (2) and the suction side (3) experiences a significant drop in *NHFR*.

Comparing the averaged values, it stands out that the inclined slot performs worse than the perpendicular slot at $BR = 0.25$. Considering the previous results, this stems more likely from a systematic measurement error or, more precisely, from corrupted assumptions regarding the coolant temperature than from a flow phenomenon. Since the slot inserts are made of stainless steel due to a lack of manufacturing alternatives and exposed to the hot gas on the flow-facing side, it cannot be ruled out that the coolant in the slot heats up, with the degree of temperature increase being dependent on the inner surface of the slot insert. Because by design, the inclined slot inserts have a larger inner surface area, it can be assumed that the coolant heats up more.[7]

Influence of slot width: The influence of varying slot widths is illustrated in Figure 4.17 for a perpendicular and inclined slot at the medium- and near-upstream position, whereby the comparison is carried out at mass flow equivalent blowing ratios, as already explained in Chapter 4.4.2.

Starting with the perpendicular injection, it can be seen that the wide slot configuration considerably reduces the thermal load on the endwall. Especially at higher coolant momenta, the *NHFR* gains are substantial as the area-average increases by 280 %. Driven by the intensification of the coolant-induced vortices, the high-momentum injection through the narrow slot at the medium-upstream position actually worsens the thermal loading in the leading-edge area compared to the base case. As shown in Figure 4.8, the corresponding film cooling distribution – ignoring the comparatively small influences of the changed density ratio – indicates an increased mixing of the coolant with the main flow, which appears rather advantageous considering the uniformity of the coolant distribution. At this point, it becomes clear why an isolated analysis of film cooling effectiveness may not provide a complete understanding of film cooling performance in certain cases, i.e., when the flow field is substantially changed by the coolant injection.

The results of the inclined slot roughly follow the trends derived from the corresponding film cooling effectiveness study, at least for the low coolant momentum comparison. Here, the disadvantage of the lower momentum prevails, as the coolant flow is displaced by the stagnation pressure and the

7 Supporting CFD calculations are currently being performed to estimate the heating of the coolant for various slot configurations. Since the results are currently not yet fully available, they could not be considered for this work.

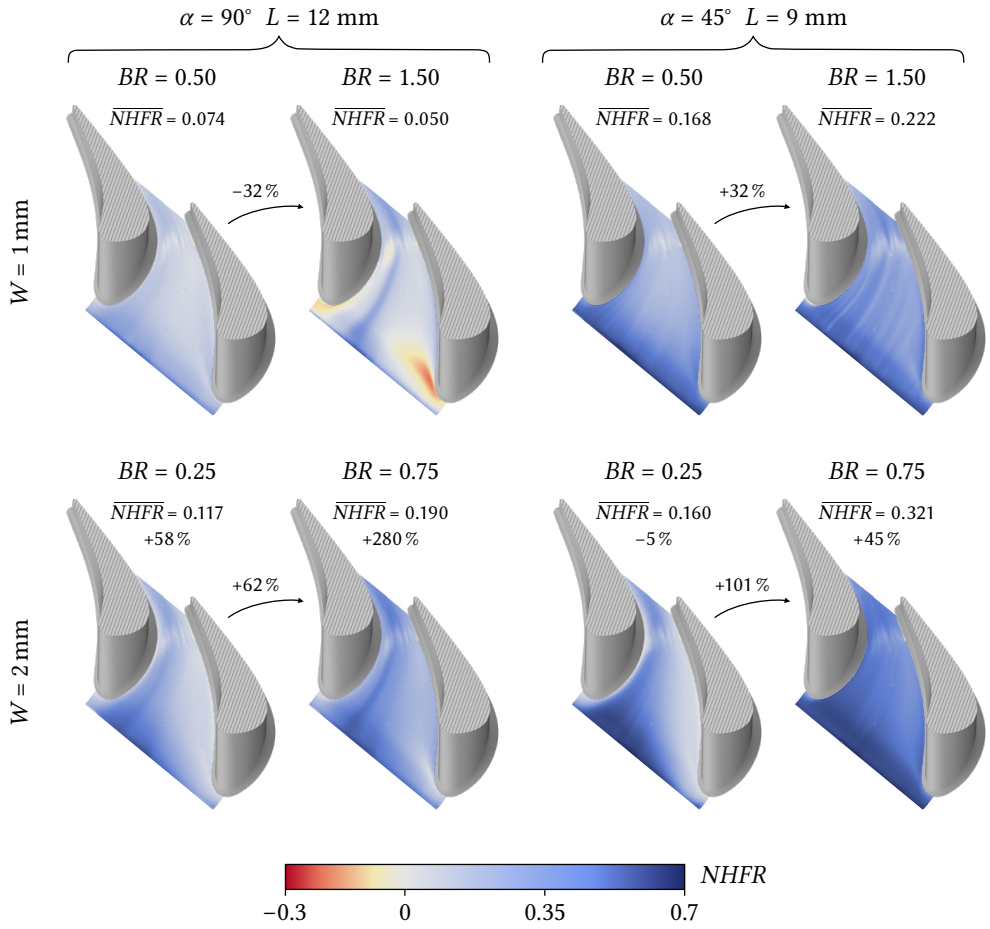

Figure 4.17: Influence of W on $NHFR$ at mass-flow equivalent BR for exemplary film cooling configuration ($\alpha\bigcirc\,|\,W1\,|\,L\bigcirc\,|\,BR\bigcirc\,|\,DR1.6$)

passage crossflow. At higher blowing ratios, the results differ from the previous findings: While the film cooling effectiveness distribution does not indicate a substantial change between the narrow and the wide slot, the thermal load is significantly higher for the narrow configuration. It can be assumed that the boundary layer is thinned out when injecting high-energy coolant, i.e., with $BR > 1$ through the inclined slot, thus increasing the local heat transfer.

Influence of slot distance: Figure 4.18 presents the $NHFR$ distribution for a perpendicular slot at the near- and far-upstream position. It is evident, and consistent with the findings of the cooling effectiveness results (see Figure 4.9), that the far-upstream slot performs worse at both low and high blowing ratios. The trends, however, are contrary: While the performance gap with respect to the film cooling effectiveness steadily narrows for higher blowing ratios, it widens in terms of thermal load for $BR > 0.5$. Here, the effects previously mentioned are manifested: With the emergence of the coolant-induced vortices at high BR, it can be assumed that the heat transfer coefficient is locally increased compared to the base case. For the near-upstream slot, this surge can be compensated – nota

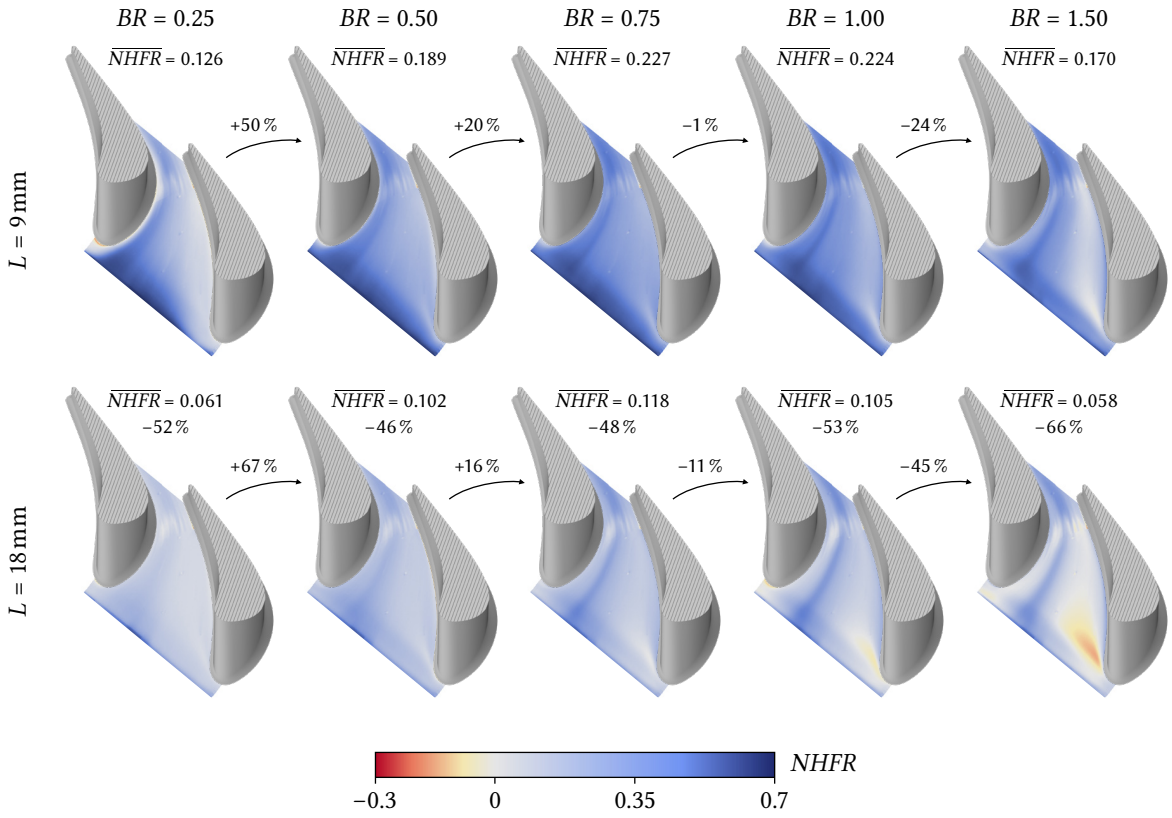

Figure 4.18: Influence of L on $NHFR$ for exemplary film cooling configuration ($\alpha 90 \,|\, W2 \,|\, L\bigcirc \,|\, BR\bigcirc \,|\, DR1.2$)

bene for the present thermal setup – by a sufficiently high coolant concentration such that the driving temperature difference is small enough to provide a net heat flux reduction. For the far-upstream slot, however, the amplification of secondary flow is accompanied by such an increased coolant dilution that the thermal load deteriorates locally compared to the base case.

These correlations are also confirmed for the narrow slot in Figure 4.19, where the film cooling effectiveness is contrasted with the net heat flux reduction for all three slot distances. To make the findings of the film cooling effectiveness and heat transfer study comparable with respect to the density ratio, $\overline{\eta}_{\mathrm{ad}}(DR = 1.2)$ was linearly interpolated from the results for $DR = 1$ and $DR = 1.6$.

Again, it is obvious that the coolant concentration and the heat flux reduction are strongly correlated with the slot distance, as positioning the slot further upstream worsens the results throughout all investigated BR. However, the influence of BR differs significantly: The film cooling effectiveness shows a nearly similar trend for all slot distances, with the maximum occurring at $BR = 1.25$. While the net heat flux reduction also reaches a maximum at $BR = 1.25$ for the near-upstream slot, it deteriorates for the medium- and far-distance slot with $BR > 0.75$. This again underlines that an evaluation of film cooling performance based solely on film cooling effectiveness is insufficient.

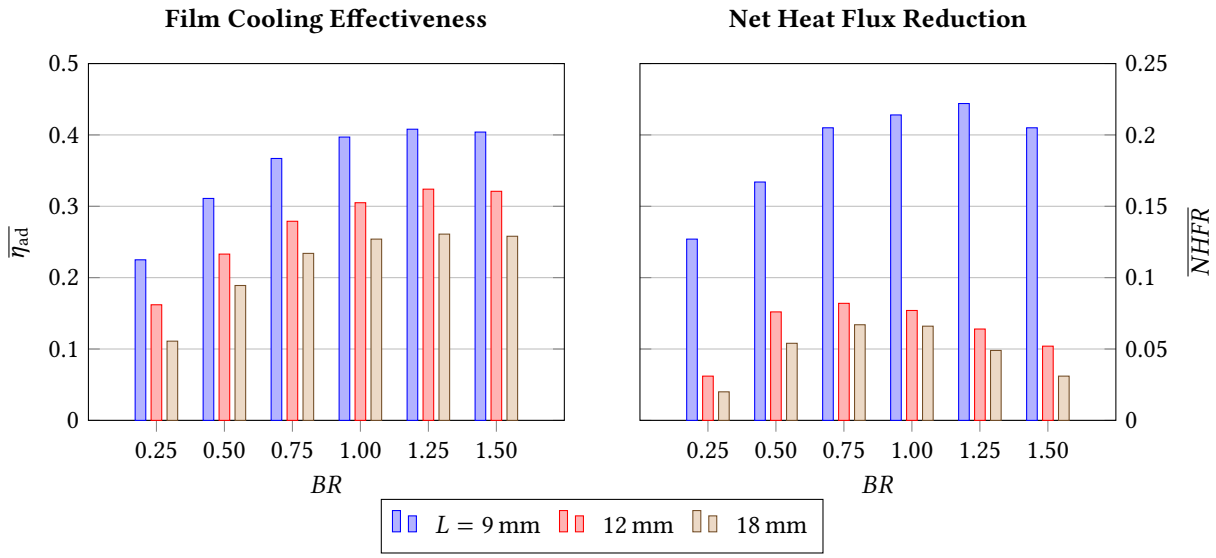

Figure 4.19: Influence of L on $\overline{\eta}_{ad}$ and $\overline{NHFR}$
for exemplary film cooling configuration ($\alpha 90\,|\,W1\,|\,L\bigcirc\,|\,BR\bigcirc\,|\,DR1.2$)

4.7 Aggregated Analysis

To evaluate the influence of the geometry-related slot parameters aggregated over all blowing ratios, the average of the obtained area-averaged film cooling effectiveness and net heat flux reduction, each weighted with BR, was calculated for each slot configuration. It is defined:

$$NHFR_\Sigma = \frac{\sum_i \overline{NHFR}_i \cdot BR_i}{\sum_i BR_i} \quad (4.3a) \qquad \eta_\Sigma = \frac{\sum_i \overline{\eta}_{ad,i} \cdot BR_i}{\sum_i BR_i} \quad (4.3b)$$

The results of the weighted averages are depicted in Figure 4.20 subdivided by slot angle and distance for the narrow and wide slot respectively. The percentage changes added to the bars relate to the perpendicular and upstream slots, respectively.

Starting with the injection angle (upper row), it is obvious that a slot inclination is clearly beneficial for the film cooling effectiveness, as the film cooling effectiveness is improved by at least 46.7 %. While the narrow slot profits from a further inclination of 30°, the results for the wide slot are practically identical. It is conceivable that, due to the high mass flow, the near-endwall flow in the upstream and midstream part of the passage is fully coolant-saturated, i.e., $\eta_{ad} \to 1$ for both inclined variants. In the downstream part of the passage, mixing with the main flow then predominates. The $NHFR$ results show a similar trend, although the rates of increase differ significantly. However, with reference to the discussion in the previous section, these results must be interpreted taking into account the possible heating of the inclined slot flow. This would explain why the narrow and inclined slot provides only a minor improvement of 6.9 % respectively 27.6 %, while the gains of the wide inclined slot exceed 70 % since the ratio of slot volume to slot surface has changed to favor the former.

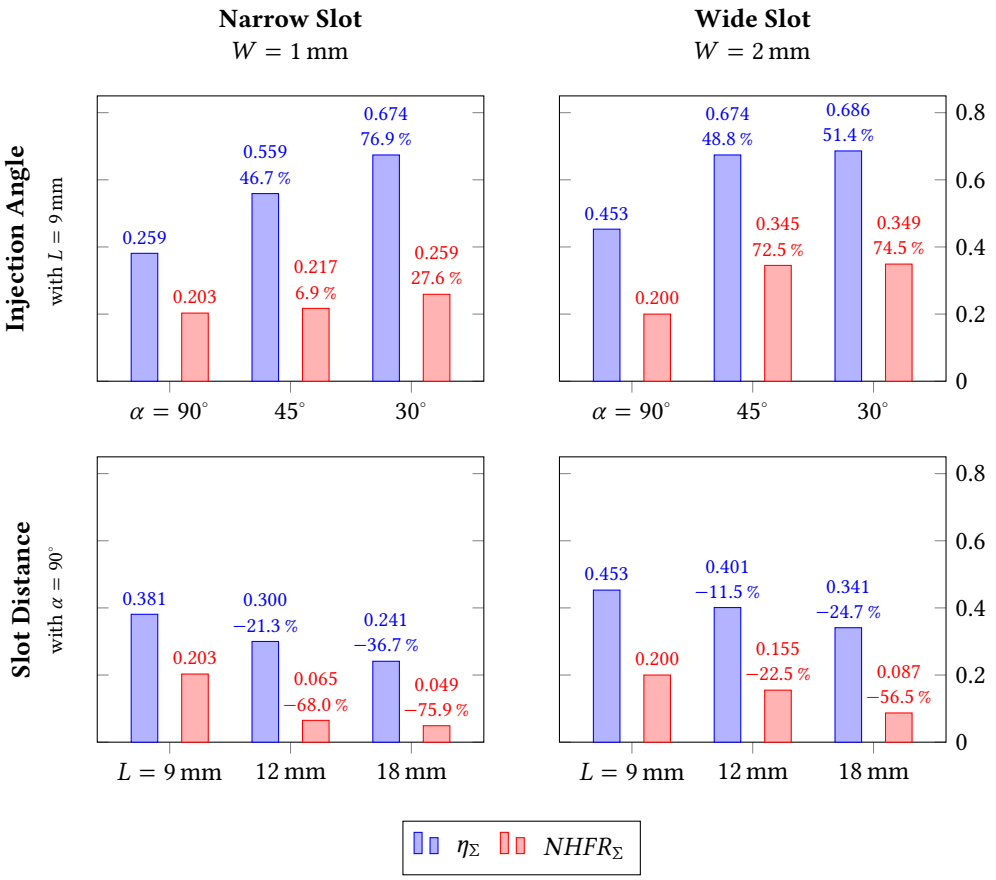

Figure 4.20: Aggregated analysis of geometric slot parameter with weighted averages for $DR = 1.2$

The results concerning the influence of the slot distance illustrate that the heat flux reduction is degraded to a much larger extent compared to the film cooling effectiveness when moving the slot further upstream. With recourse to the findings of the previous section, this has to be attributed to the amplification of secondary flow, which locally increases the thermal load beyond that of the base case. This is especially the case for the narrow slot where a reduction of thermal loading is virtually non-existent.

4.8 Lessons Learned for the Design of the Annular Cascade

The design of the linear cascade has revealed some weaknesses in its operation, which need to be addressed in the development of the annular cascade. Here, general aspects concerning the overall design have to be distinguished from shortcomings in the implementation of specific measurement techniques.

The linear cascade has been designed as a stainless steel multi-part construction with screw and clamp connections. Excluding the flow conditioning inserts, the inlet segment shown in Figure 4.21 consists of 19 individual parts that have to be bolted together and sealed off from each other. At the same time, large wall thicknesses of up to 35 mm, which were applied under consideration of constructional strength and stiffness, worsen the handling due to the weight of the individual components. For example, the endwall plate, which had to be dismantled for maintenance work on the flow conditioning inserts, weighs 60 kg. In addition, some parts suffered from production-related warpage, which may be attributed to the challenging machinability of the selected steel (1.4571/AISI 316Ti) and caused leakage, as sealing tolerances were not met.

For these reasons, the design and manufacturing concept of the annular cascade has been fundamentally revised by utilizing welded structures for the pressurized vessels and casings. By means of FEM analyses, it was possible to significantly reduce material usage while retaining safety tolerances. Apart from that, as already mentioned in section 4.1, the linear plenum did not provide a spatially uniform coolant supply, so the design has been completely reworked for the annular cascade. Further details of the construction are given in the next chapter.

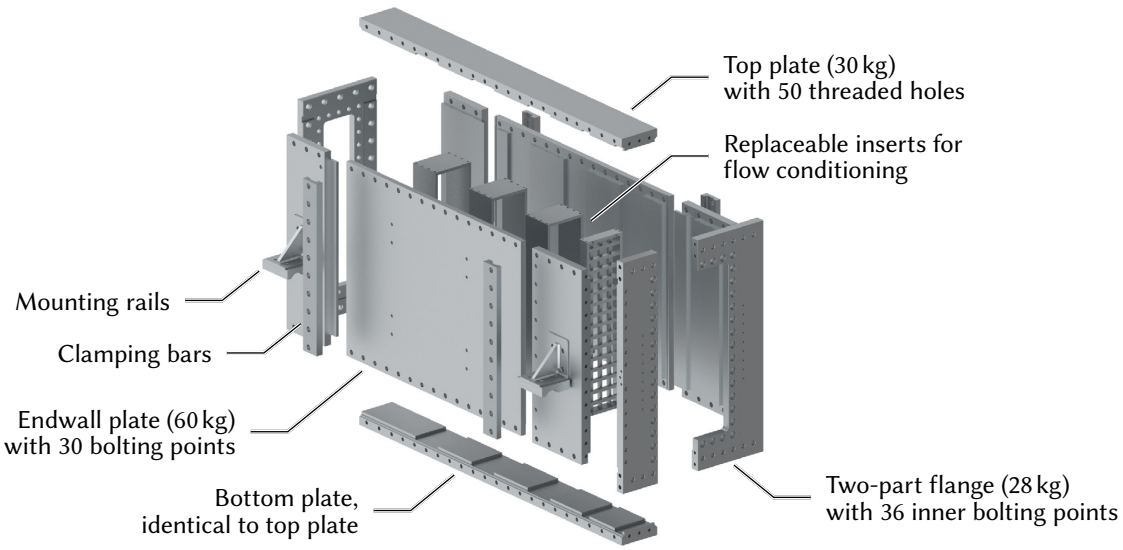

Figure 4.21: Exploded view of multi-part inlet segment with total weight of 350 kg

Regarding the requirements of the PSP measurement, the setup that was established for the linear cascade has proven reliable. Notwithstanding this, an additional fast-responsive secondary air heater, which was already presented in Chapter 3.4.3, has been developed to speed up the measurement sequence, thus reducing the consumption of foreign gas.

As discussed in section 4.6.1, the shortcomings of the design of the heat transfer measurement module require a complete revision. Here, both the lack of tightness of the cooling water cavity and the parasitic heat fluxes were identified as major issues, which are addressed in the annular design by downsizing the tempered endwall surface and utilizing low-conductive materials for the slot insert.

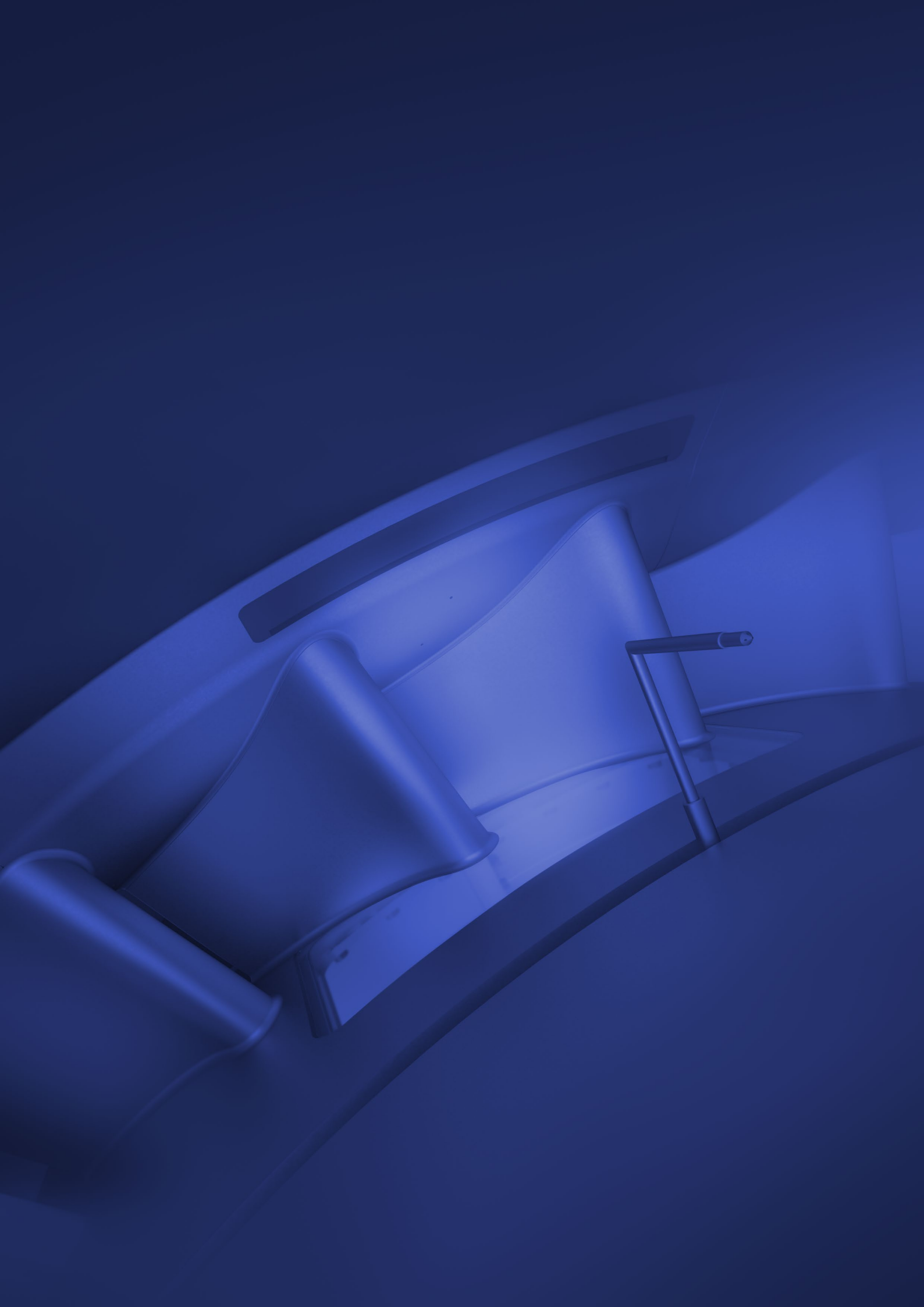

Design and Construction of the Annular Sector Cascade

In this chapter, the aerodynamic design of the annular cascade and the construction of the entire annular test rig and its parts are presented. After a brief explanation of the experimental constraints and requirements, section 5.2 presents the numerical investigation that was carried out to optimize the fluid volume of the annular cascade in terms of flow periodicity. Here, a benchmark approach was utilized to systematically investigate and evaluate the influences of the geometry parameters. The constructional design of the cascade, the measuring equipment, and the components required for the conditioning of the inlet flows are presented in sections 5.3 to 5.6. In addition, figures showing the manufactured parts and mounted assemblies are included in appendix C.

5.1 Experimental Constraints and Requirements

The entire annular test rig had to be integrated into the existing test facility architecture (see Fig. 3.1) since time and budget constraints precluded rebuilding the test housing or the inlet and outlet ducts. Figure 5.1 illustrates the spatial constraints of the existing test room. A distance of 2800 mm between the main gate valve (nominal width DN 250, pressure tread PN 16) and the opposite wall of the test room is provided for the annular test rig. The inlet and outlet duct are separated by a height difference of 990 mm. While the bypass for the pressure probe calibration and parts of the coolant air system are located in the rear area of the test room, the front area is occupied by measurement equipment and a cylinder bank for the supply of foreign gas as coolant.

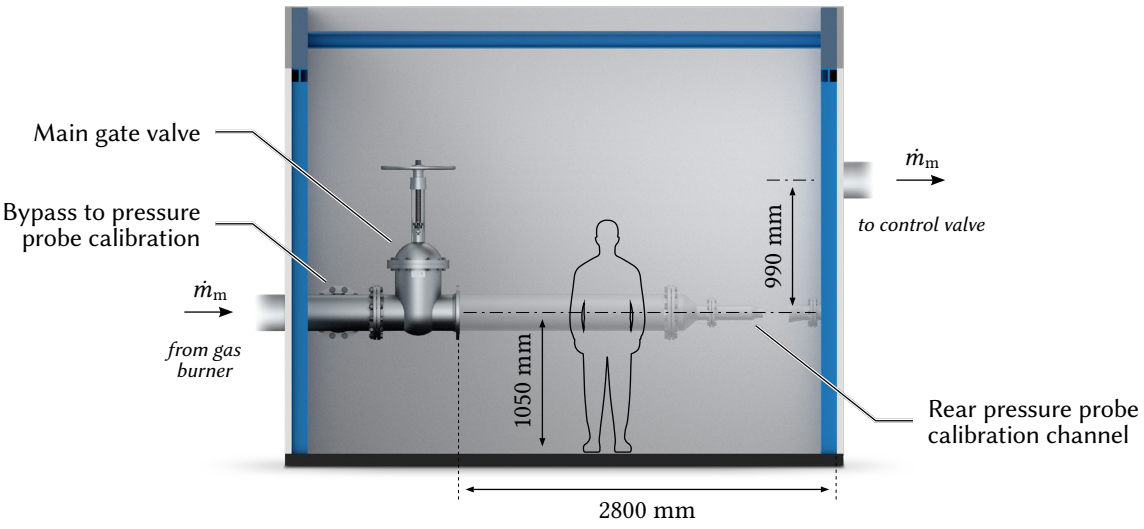

Figure 5.1: Existing test room and spatial restrictions for the design of the annular cascade

Regarding the operating boundary conditions of the test rig, the entire construction had to be designed to withstand a maximum absolute pressure of 2.5 bar. With respect to the measures to improve flow periodicity (see Chapter 2.4), the required pressure resistance as well as the spatial constraints, therefore, limit the reasonable volume of the outlet geometry.

Based on the trade-off between operational steady-state and measurement uncertainty made in Chapter 4.6, the maximum inlet temperature for conducting the heat transfer measurement campaign was reduced from 400 °C to 160 °C. With this temperature limitation, the selection of suitable construction materials was extended to include heat-resistant aluminum alloys, which have lower yield and tensile strength properties compared with stainless steels, but advantages in terms of machinability [133]. This is particularly important, as the manufacturing of the contoured endwall segments involves a high level of machining. Furthermore, it allows the use of 3D-printed polymer parts, which can be freely shaped and have low thermal conductivity, thus being particularly suitable for insulating components like the purge slot inserts.

Since the measurements already conducted on the linear cascade are to be carried out to the same extent on the annular cascade, the design must meet the following instrumentation requirements:

- Optical access for PSP and IR measurements
- Feedthrough and traversing units for five-hole probes at cascade inlet and outlet
- Interchangeability of the central passage endwall (shroud) for conducting oil flow visualizations
- Interchangeability of the purge slot geometry
- Footprint for industrial robot

Within the inlet section, the circular cross-section behind the main gate valve first has to be transitioned to an annular sector segment of 60°. At the entrance of the cascade, defined inlet conditions are required with respect to turbulence intensity, velocity distribution, and boundary layer thickness. Therefore, suitable flow conditioning measures, i.e., screens, straighteners, and boundary layer control, must be integrated into the inlet.

5.2 Numerical Optimization of the Fluid Volume

For optimizing the flow periodicity at the inlet and outlet of the cascade, numerical calculations were performed, including various geometric design parameters, which are shown in Figure 5.2 and will be discussed in the following subchapter.

The integration of rotors or de-swirling vanes to improve periodicity was not considered for several reasons: First, it would have significantly increased manufacturing costs. Second, the required axial overall length of the cascade would have been notably increased, as the outlet flow behind the rotor would have been turned back in the axial direction. The decision against the use of a rotor is also

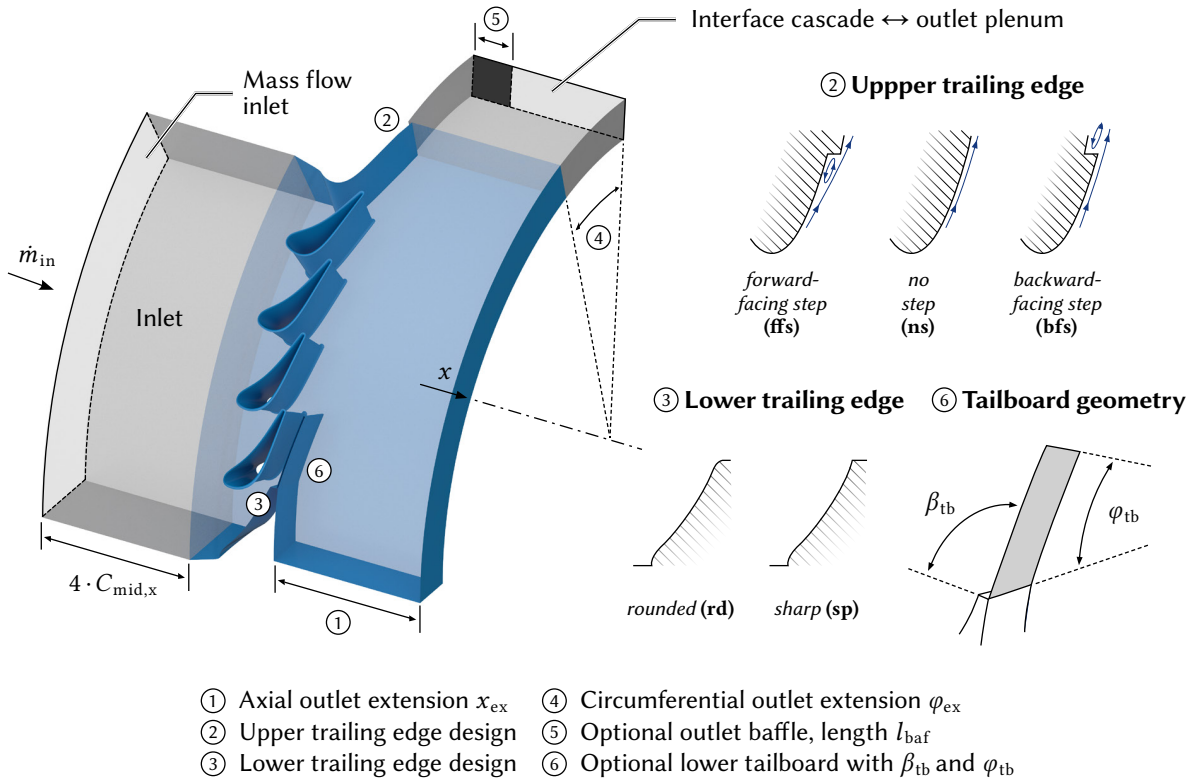

Figure 5.2: Geometric parameters and boundary conditions for the numerical optimization of the annular cascade fluid volume

supported by previous studies: According to Boletis and Sieverding [82], who studied the flow field behind an annular nozzle guide vane ($r_h/r_s = 0.94$, $t_h/C_s = 0.8$) with and without a downstream rotor under low-speed conditions, no fundamental flow changes were observed. Especially near the shroud, the flow field remained virtually unchanged. This is contrasted with a study by Williamson et al. [83], who performed a similar investigation but under transonic flow conditions for a high turning angle vane. They concluded that a realistic assessment of the vane performance might require appropriate testing with a rotor. However, a closer look at their results shows that the exit tip flow in terms of flow angle and pressure losses is hardly influenced.

Therefore, the initial geometry is based on a cascade design by Saha [91], who successfully implemented a 4-passage annular sector cascade with a similar turning angle of 71° and both-sided endwall contouring into a high-speed test rig. The outlet geometry is realized as a dump diffuser at constant annulus without tailboards, rotors, or de-swirling vanes and is followed by a linear transition ($r \to \infty$) which leads the flow to the outlet plenum. According to Wiers and Fransson [85], the idea of a dump diffuser outlet is to allow the exit flow to develop as a free jet and the flow angle to adjust itself to the downstream back pressure.

Like the linear cascade, the annular cascade is to be implemented as a 5-passage model. This is beneficial since the central passage to be investigated is flanked by two neighboring passages each. The upper and lower cascade limitations correspond to the pressure and suction side geometry of the vane, but without fillets for manufacturing reasons.

5.2.1 Geometric Design Parameters and Numerical Setup

The geometric parameters for the numerical optimization include the axial extension x_{ex} and circumferential extension φ_{ex} of the outlet volume. Furthermore, the trailing edge shape of the upper and the lower cascade limitations were varied. Following Saha [91], an optional baffle was added at the interface between the outlet and the plenum to influence the outflow angle of the upper passage (P+2) as a recirculation flow emerges upstream of the baffle. Due to design considerations, i.e., manufacturing requirements and the integration of the probe traversing system, the geometry of the outlet volume was modified during the optimization process, as shown in Figure 5.3.

All calculations were performed with the commercial solver ANSYS CFX (2019 R3). It solves the compressible Reynolds-averaged Navier-Stokes (RANS) equations based on a finite volume discretization. Due to a large number of geometric variants, the meshing of the computational domain was performed automatically with the ANSYS Meshing Tool (2019 R3). While a mesh with an average of 3×10^6 nodes (medium mesh) was used for the optimization process, the number of nodes was increased to 1.4×10^7 nodes (fine mesh) for the evaluation of the final geometry to resolve the development of secondary flow more accurately within the cascade. The free flow volume of the inlet was discretized with hexahedral elements, while tetrahedral elements were used for the discretization of the cascade and the outflow volume. The RANS-based k-ω SST model by Menter [134] was chosen for

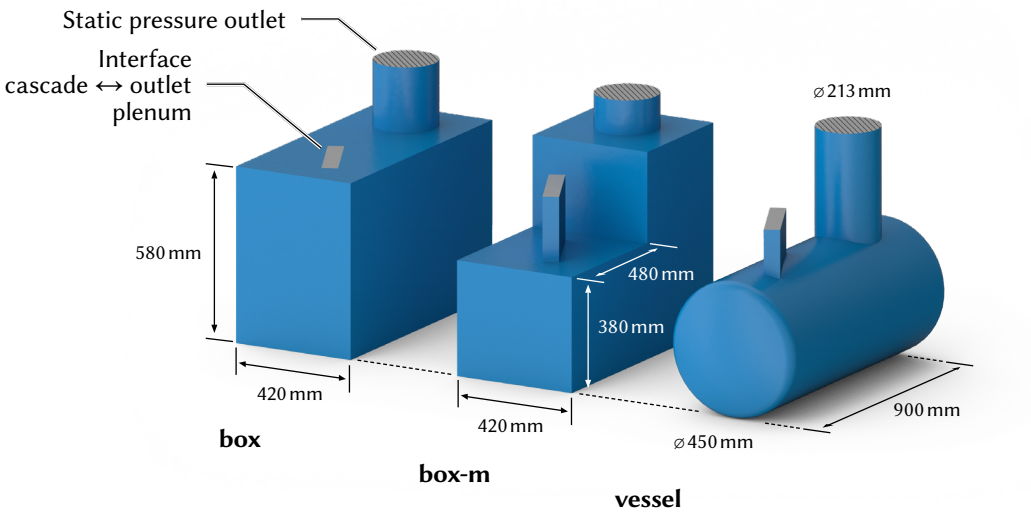

Figure 5.3: Outlet volumes for the numerical optimization of the annular cascade fluid volume

the closure of the RANS equations, as the 2-equation model yields good results concerning turbulent boundary layers and the prediction of secondary flows, e.g., Reviol et al. [135]. It utilizes the k-ω model within the boundary layer and switches to the standard k-ϵ model in outer flow regions.

The boundary layer was resolved by a maximum number of 30 prism layers with an inflation factor of 1.2 starting at 3×10^{-6} mm for the medium mesh respectively 1×10^{-6} mm for the fine mesh. Across the cascade volume, $y^+ < 3$ (medium mesh) respectively $y^+ < 1$ (fine mesh) was obtained, i.e., the first cell is located inside the viscous sublayer, which allows the velocity distribution in the boundary layer to be calculated without a wall function. All solid walls were assumed adiabatic and hydraulically smooth. To assess the convergence of the calculation, flow variables were evaluated pointwise (Ma_{in}) and integrally (vane loading $|\boldsymbol{F}|$, cascade pressure ratio Π) in addition to the residuals.

Table 5.1 summarizes the main parameters of the numerical study. To easily evaluate differences in terms of pressure losses between the geometric variants and to include the pressure ratio of the passage as a benchmark parameter, the pressure at the outlet was not adjusted throughout the optimization. The outlet pressure for evaluation of the final geometry (fine mesh) was set to obtain $\Pi = 1.48$.

5.2.2 Benchmark Approach for Periodicity Optimization

To systematically evaluate and compare the influence of the geometric variants on the periodicity at the inlet and outlet of the cascade, a benchmark approach was developed. The normalized sum of the deviation from the central passage respectively from the average over all vanes is formed for relevant quantities at the inlet and outlet and summarized in an aggregated benchmark $\sum Pe$. The calculation specifications of the benchmark are given in Table 5.2. By definition, lower values of the aggregate benchmark correspond to better periodicity.

Table 5.1: CFD setup for the optimization and evaluation of the annular cascade fluid volume

Parameter	**Medium mesh** for fluid volume optimization	**Fine mesh** for final geometry evaluation
No. of mesh nodes[8]	3×10^6	1.4×10^7
y^+	< 3	< 1
Viscous model	k-ω SST	⟶
Time	steady-state	⟶
$\dot{m}_{\text{in}}$	$2\,\text{kg}\,\text{s}^{-1}$	⟶
Re_{in}	2.34×10^5	⟶
T_{in}	$30\,^\circ\text{C}$	⟶
Tu_{in}	5 %	⟶
$p_{\text{s,out}}$	1.25 bar	1.175 bar

Mach numbers, passage mass flows, vane loadings, and inflow angles at different axial positions (see Figure 5.4) are included in the calculation. The cascade pressure ratio under constant pressure at the plenum outlet is taken into account as a denominator so that configurations with a higher pressure ratio are uprated. In contrast, the maximum Mach number in the cascade is used as a numerator to account for the undesirable velocity increase with $Ma > 1$ that typically occurs in the lower passage due to the reduced pressure within the recirculation zone of the lower part of the outlet.

Table 5.2: Benchmark definitions for numerical optimization

Benchmark	**Definition**	**Type**	**Location**
Mach number periodicity	$Pe_{Ma} = 1/\,Ma_0 \cdot \sum_{i=-2}^{2} \lvert Ma_i - Ma_0 \rvert$	pointwise	In1, Le, Out
Mass flow periodicity	$Pe_{\dot{m}} = 1/\dot{m}_0 \cdot \sum_{i=-2}^{2} \lvert \dot{m}_i - \dot{m}_0 \rvert$	mass-flow average	Le
Loading periodicity	$Pe_F = 1/\bar{F} \cdot \sum_{j=1}^{4} \lvert \boldsymbol{F}_i - \bar{\boldsymbol{F}} \rvert$	mass-flow average	NGV
Inlet pitch angle deviation	$Pe_\beta = \sum_{j=1}^{4} \lvert \beta_i \rvert$	mass-flow average	In2
Aggregated benchmark	$\sum Pe = Ma_{\max}^2 \,/\Pi \cdot \left(1/3 \cdot \sum Pe_{Ma} + Pe_{\dot{m}} + Pe_F + Pe_\beta \right)$		

8 The number of nodes varies due to the different fluid volumes. The number given here for the middle mesh refers to the initial variant

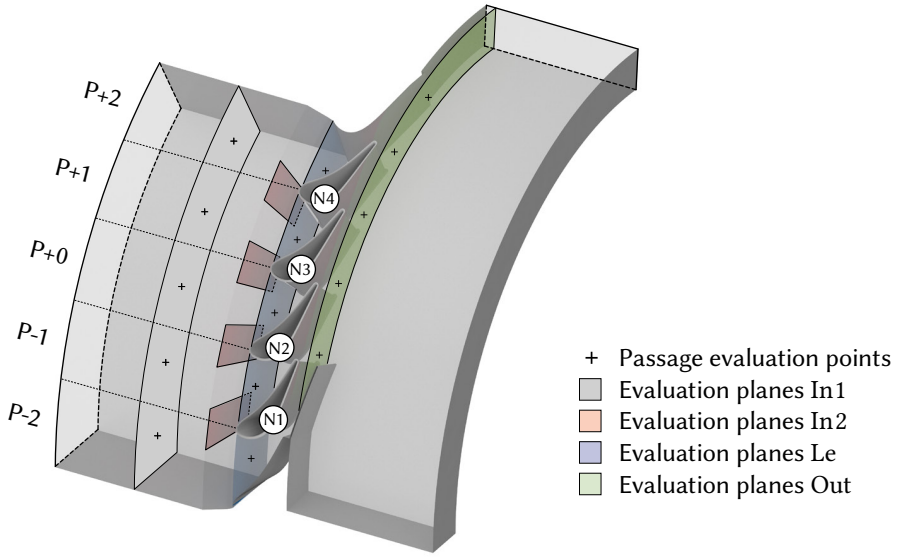

Figure 5.4: Periodicity evaluation planes and points for the numerical optimization

5.2.3 Benchmark Results

The benchmark results of the investigated geometric variants are summarized in the following Tables 5.3 to 5.6.[9] For better visibility, the aggregated benchmarks have been highlighted with a color grading in the range between 10 and 50.

The results of the base case configuration, i.e., without tailboard or baffle, can be taken from Table 5.3. Concerning the influence of the axial outlet expansion x_{ex} (BA-IN – BA05), it is evident that smaller outlet volumes significantly worsen the periodicity. For case BA-01, the two lower passages P-2 and P-1 experience a significant mass flow increase of 12.8 % respectively 4.4 %. This can be attributed to the uneven distribution of outlet back pressure which in turn can be traced back to the blocking effect due to pronounced flow separation on the hub side in the lower region of the outlet volume. From a length of 250 mm, however, the influence of x_{ex} weakens. A minimum can be found at an outlet length of 300 mm. Therefore, this configuration was adopted for all other variants.

Taking a closer look at the outlet Mach number distribution of the no-step variants, it is noticeable that the flow is over-accelerated at the no-step trailing edge of the upper cascade limitation. This results from the fact that the flow does not separate at the trailing edge but follows the contour up to a turning angle of 90°. The use of a forward-facing step leads to separation at the trailing edge. This significantly reduces the over-acceleration in the upper passage (P+2) from 11.3 % (BA-07) to −2.6 % (BA-10), resulting in a better aggregated benchmark despite higher pressure losses.

9 A more detailed breakdown of the benchmarks with their underlying individual values, which are referred in the discussion of the following results, can be found in appendix B.

The results of the baffle variants are shown in Table 5.4. Given the nominal turning angle of 76.3°, the theoretically optimum length of the baffle can be determined by the intersection point between the cascade-outlet interface and the corresponding helical flow path starting from the upper trailing edge. This results in 58 mm for $\varphi_{ex} = 30°$ respectively 31 mm for $\varphi_{ex} = 15°$. In the BAF-01 to BAF-07 variants, the length of the baffle was gradually increased from 20 to 70 mm. Up to a length of 40 mm, the baffle has no noticeable influence on the periodicity, especially on the over-acceleration in the upper passage, which remains stable at approximately 11 % compared to the central passage. From a length of 50 mm, the baffle shows a clear effect, which increases up to a length of 60 mm, as expected. In this range, the periodicity of the exit Mach number seems to be particularly sensitive to length changes. Thus, the relative over-acceleration in the upper passage drops from 4.9 % for $l_{baf} = 55$ mm to −3.1 % for $l_{baf} = 60$ mm. For this reason, an adjustment option should be considered in the test rig to allow the periodicity to be optimized under real conditions.

The introduction of a forward-facing step for the upper cascade geometry and a sharp trailing edge for the lower geometry further improves the periodicity significantly. The additional blocking effect of the forward-facing step equalizes the flow field in the upper passage (P+2) by reducing the averaged inlet flow angle from 2.5° to 0.5°. The excess mass flow rate of approximately 8 % in the lower passage for the rd variants can be explained by the fact that the rounded trailing edge results in increased turbulent mixing of the wake flow with the recirculation zone in the lower part of the outlet. As this is associated with reduced back pressure, a sharp tear-off edge leads to an equalization of the pressure distribution in the outlet and, thus, to a more homogeneous distribution of the mass flows and consequently to a further harmonization of the Mach number distribution and the vane loading.

Table 5.3: Evaluation of selected base geometry variants

Variant	x_{ex} /mm	φ_{ex} /°	UTE	LTE	Outlet plenum	Ma_{max}	Π	$\sum Pe_{Ma}$	Pe_F	$Pe_{\dot{m}}$	Pe_β	$\sum Pe$
BA-IN	**150**	30	ns	rd	box	1.07	1.40	34.2	14.4	13.5	2.4	34.3
BA-01	**100**	30	ns	rd	box	1.01	1.28	111.8	22.9	22.3	8.0	71.4
BA-02	**200**	30	ns	rd	box	1.07	1.42	32.2	10.0	9.7	5.0	28.4
BA-03	**250**	30	ns	rd	box	1.04	1.42	31.9	7.9	10.1	5.6	25.9
BA-04	**300**	30	ns	rd	box	1.02	1.41	32.5	8.9	9.7	4.1	24.6
BA-05	**350**	30	ns	rd	box	0.99	1.40	35.5	9.0	10.1	4.0	24.7
BA-06	300	**10**	ns	rd	box	1.01	1.41	33.3	9.0	10.1	3.9	24.6
BA-07	300	**15**	ns	rd	box	1.01	1.41	32.8	9.0	9.7	4.0	24.5
BA-08	300	**20**	ns	rd	box	1.02	1.42	32.4	8.9	9.5	4.2	24.6
BA-09	300	**40**	ns	rd	box	1.02	1.41	33.3	9.0	9.9	4.1	24.8
BA-10	300	15	**ffs**	rd	box	1.01	1.38	24.1	8.9	9.5	3.8	22.3

(UTE) Upper trailing edge (LTE) Lower trailing edge · Please refer to Figure 5.2 and 5.3 for geometric parameters.

Table 5.4: Evaluation of selected baffle geometry variants with $x_{ex} = 300\,mm$

Variant	φ_{ex} /°	l_{baf} /mm	UTE	LTE	Outlet	Ma_{max}	Π	$\sum Pe_{Ma}$	Pe_F	$Pe_{\dot{m}}$	Pe_β	$\sum Pe$
BAF-01	30	**20**	ns	rd	box	1.01	1.41	32.9	8.9	9.8	4.1	24.4
BAF-02	30	**30**	ns	rd	box	1.01	1.41	34.3	8.9	9.8	4.0	24.6
BAF-03	30	**40**	ns	rd	box	0.99	1.39	32.9	8.9	10.2	3.9	23.8
BAF-04	30	**50**	ns	rd	box	0.98	1.38	29.2	9.0	10.5	3.9	23.0
BAF-05	30	**55**	ns	rd	box	0.97	1.37	27.5	8.8	10.7	3.9	22.5
BAF-06	30	**60**	ns	rd	box	0.98	1.37	24.4	8.9	9.8	3.7	21.7
BAF-07	30	**70**	ns	rd	box	0.97	1.35	26.5	9.0	9.9	3.6	21.9
BAF-08	15	30	**ns**	rd	box	0.98	1.38	24.2	8.9	9.9	3.9	21.3
BAF-09	15	30	**ffs**	**sp**	box-m	0.96	1.37	20.1	7.3	7.6	3.3	16.7
BAF-10	15	30	ffs	**sp-l**	box-m	0.99	1.36	21.5	9.2	8.9	4.2	21.2
BAF-11	15	30	ffs	**sp-s**	box-m	1.11	1.33	42.8	13.4	26.8	16.9	65.5

(UTE) Upper trailing edge (LTE) Lower trailing edge (sp-l) sharp prolonged (sp-s) sharp shortened

Nevertheless, variant BAF-09 still has an increased relative mass flow of 5.9 % in the lower passage. Therefore, it was investigated to what extent an axial extension (BAF-10) or reduction (BAF-11) of the lower passage geometry could further improve the mass flow distribution. It turns out that periodicity reacts very sensitively to changes in the length of the lower passage limitation. Here, the shortened variant leads to a considerable worsening of flow periodicity. Since no improvement could be achieved with any of these variants, this approach was not taken any further.

Parallel to the variants with baffle, it was investigated to what extent a change to a backward-facing step of the upper cascade limitation could further improve the periodicity. For this purpose, four sub-variants were developed, with their geometries shown in Figure 5.5 and their results summarized in Table 5.5. In conjunction with the sharp lower trailing edge, it was possible to obtain even better results

Table 5.5: Evaluation of selected base geometry variants with modified upper trailing edge design

Variant	x_{ex} /mm	φ_{ex} /°	UTE	LTE	Outlet plenum	Ma_{max}	Π	$\sum Pe_{Ma}$	Pe_F	$Pe_{\dot{m}}$	Pe_β	$\sum Pe$
BA-BFS-01	300	15	**bfs-a**	sp	box-m	1.02	1.46	29.6	7.2	7.4	2.8	19.5
BA-BFS-02	300	15	**bfs-b**	sp	box-m	1.03	1.44	22.2	7.2	7.3	2.8	18.0
BA-BFS-03	300	15	**bfs-c**	sp	box-m	0.99	1.41	16.4	7.2	7.6	3.0	16.4
BA-BFS-04	300	15	**bfs-d**	sp	box-m	1.01	1.42	15.7	7.2	7.4	2.9	16.2

(UTE) Upper trailing edge (LTE) Lower trailing edge

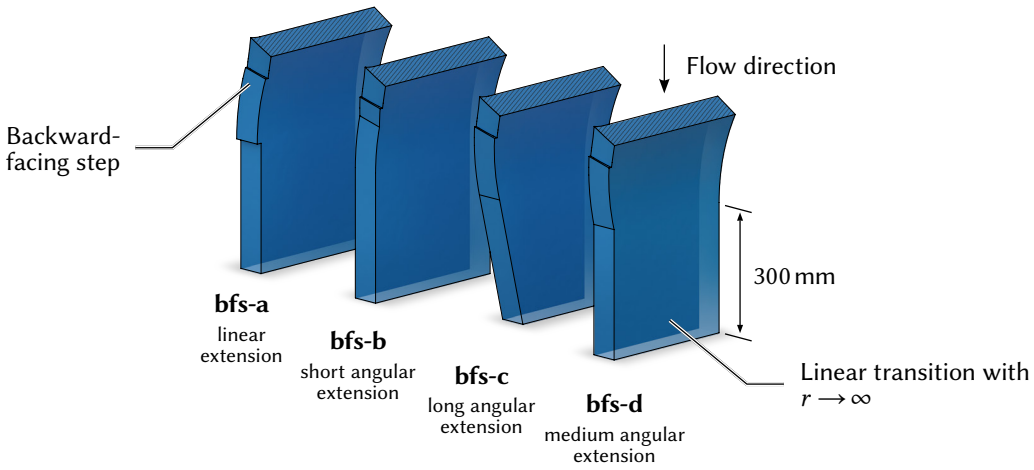

Figure 5.5: Sub-variants of the upper trailing edge geometry with backward-facing step and linear transition

without the use of a baffle by suppressing the over-turning at the upper passage (P+2) with a tilted tailboard behind the backward-facing step (variant BA-BFS-03 and BA-BFS-04). With the latter variant, the excess acceleration in the upper passage could be completely eliminated while simultaneously reducing the pressure losses. After this optimization step, the remaining aperiodicity is mainly limited to the lower passage with an excess mass flow rate of 5.3 %. For this reason, a tailboard was added to the lower passage for further investigation. The benefit of this approach, which has already proven advantageous for the linear cascade, is that the major parameters, i.e., the pitch and length or the circumferential extension, can be adjusted with little effort under real test conditions.

Table 5.6 summarizes the results of the tailboard variants. The pitch angle β_{tb} was varied within a range of 76° to 78°, and the circumferential extension between 10° to 15°. The final geometry is based on variant TB-04 but with a modified outlet plenum since a vessel-shaped geometry proved to be a more feasible alternative in terms of material requirements, manufacturing costs, and test rig integration.

Looking at the results for case TB-01 ($\beta_{\mathrm{tb}} = 76°$) and TB-02 ($\beta_{\mathrm{tb}} = 77°$), it is evident that even small pitch angle variations have a significant effect on periodicity. The tailboard configuration of the TB-01 variant directs large parts of the mass flow through the lower passage. Hence, the flow is accelerated to $Ma_{\mathrm{max}} = 1.29$, substantially increasing the loading of the lower vane (N1) by 10.6 %. A steeper adjustment of the tailboard provides a significant improvement in periodicity by constricting the outlet cross section and, therefore, raising the local backpressure.

Due to the comparatively low maximum Mach number, the variant TB-03 ($\beta_{\mathrm{tb}} = 78°$) is preferred over TB-02 and, therefore, used for further evaluation. However, the uneven distribution of the loading at the expense of the lower vane (−6.8 %) is striking. By shortening the tailboard, the blocking effect can be reduced gradually, thus increasing the loading of the lower vane (N1). Configuration TB-04 proves to be optimal among the test geometries. At this point, it did not seem reasonable concerning

Table 5.6: Evaluation of selected tailboard geometry variants based on geometry BA-BFS-04

Variant	β_{tb} / °	φ_{tb} / °	Outlet	Ma_{max}	Π	$\sum Pe_{Ma}$	Pe_F	$Pe_{\dot{m}}$	Pe_β	$\sum Pe$
TB-01	**76**	15	box-m	1.29	1.41	20.1	21.2	11.1	5.6	52.7
TB-02	**77**	15	box-m	1.04	1.42	18.2	3.3	7.4	3.1	15.2
TB-03	**78**	15	box-m	0.91	1.43	17.8	13.7	3.4	4.6	16.0
TB-04	78	**12.5**	box-m	0.95	1.43	15.5	3.9	4.3	1.5	9.4
TB-05	78	**10**	box-m	1.03	1.43	16.7	5.4	7.4	3.0	15.7
FIN	78	12.5	**vessel**	0.94	1.41	16.4	4.0	4.4	1.5	9.6
FIN-OP	78	12.5	vessel	1.04	**1.48**	16.7	4.3	4.2	1.5	11.5
FIN-OP-FINE	78	12.5	vessel	1.10	**1.48**	16.5	3.7	4.4	1.6	12.3
Linear cascade				1.05	1.48	20.2	2.7	5.8	2.2	12.9

(OP) Operating point

computational costs to calculate further tailboard variants. Rather, on account of the high sensitivity of periodicity to changes in the tailboard parameters, an adjustment was integrated into the test section so that the best point could be determined under real conditions (see Chapter 5.5.2).

For the evaluation of the final geometry at the design point, the outlet pressure for variant FIN-OP was lowered until a pressure ratio of $\Pi = 1.48$ was obtained. Except for a small benchmark penalty due to the expected increase in the maximum Mach number, the periodicity is not affected. Neither does the recalculation with the fine mesh (FIN-OP-FINE) significantly worsen the benchmark. The downgrading from 11.5 to 12.3 is mainly caused by a peaking Mach number due to the mesh refinement.

To classify these results, the benchmark was also applied to the numerical investigation of the linear cascade, which was conducted as part of the former design and optimization process. This reveals that the quality of the periodicity has even slightly improved.

5.2.4 Evaluation of the Final Geometry

To evaluate the outcome of the optimization process in detail, the vane loading and the outlet flow of the final geometry (FIN) are compared to the results of the initial geometry (BA-IN). Figure 5.6 depicts the chordwise distribution of the isentropic Mach number Ma_{is} at different spanwise positions (near hub, midspan, near shroud) for vane N1 to N4.

The general distribution is characterized by a uniform acceleration of the flow along the suction side. The highest aerodynamic load is present in the mid to rear part of the profile so that it can be considered mid-to-aft-loaded. Due to the shroud endwall contouring, the flow near the shroud experiences a

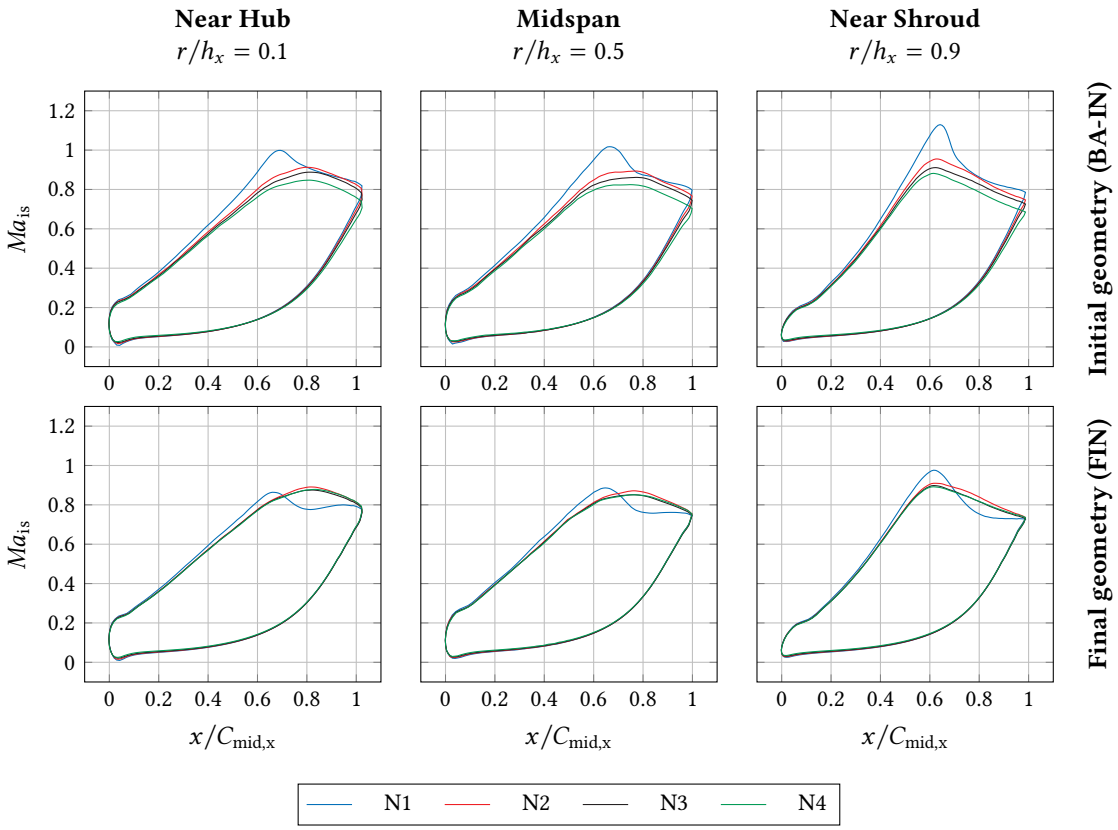

Figure 5.6: Comparison of vane loading between initial and final geometry

delayed but stronger acceleration when compared to the midspan and hub. With reference to the investigation by Boletis [35], it can be assumed that the associated load reduction at the leading edge contributes significantly to the reduction of secondary flow.

Across all spanwise sections, the initial geometry is specified by an uneven distribution of the loading, which gradually decreases from the lower to the upper vane. In conjunction with the dump diffuser design of the outlet, the rounded trailing edge of the lower cascade limitation causes a significant loading peak due to the over-acceleration at the suction side of vane N1.

In the final geometry, the vane loadings were clearly harmonized, with the loading of N4 being virtually identical to that of N3. Caused by the step at the transition from the trailing edge of the lower cascade limitation to the tailboard, the opposite suction side of vane 1 is still exposed to a slight over-acceleration, followed by deceleration due to the steep pitch adjustment of the tailboard. By flush-fitting the tailboard to the trailing edge of the lower cascade limitation, the loading of the lower vane could presumably be further equalized. However, constructional considerations stand against this, as the endwall contouring extends beyond the twisted trailing edge of the vane (see fig. 3.2). Thus, this could only have been implemented with a rigid, freeform-shaped tailboard at the expense of adjustability.

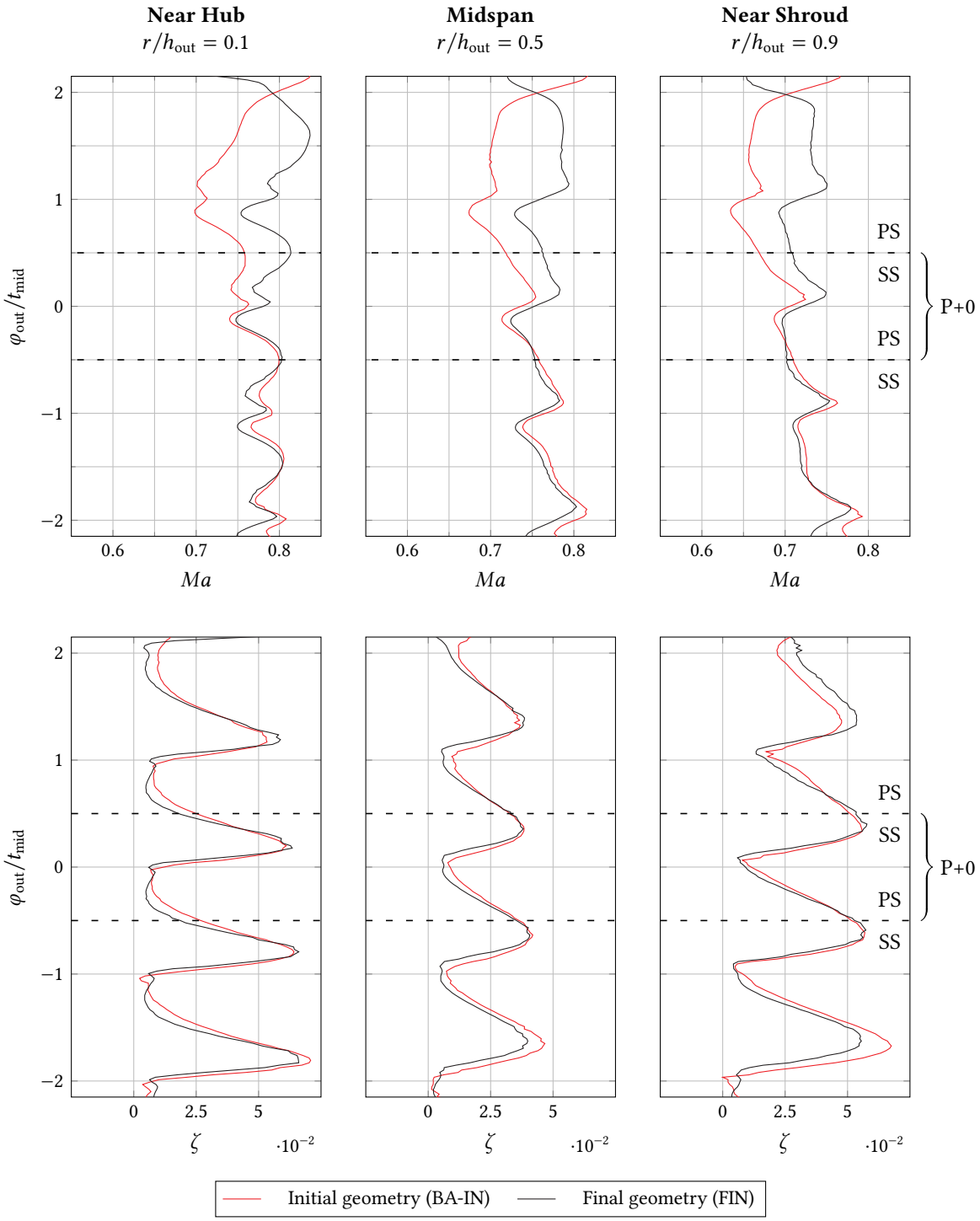

Figure 5.7: Comparison of Mach number and total pressure loss coefficient distribution on outlet measuring plane between initial and final geometry

To evaluate the periodicity at the outlet, Figure 5.7 presents the Mach number *Ma* and total pressure loss distribution ζ in pitchwise direction at the same three spanwise positions mentioned before. Starting with the Mach number distribution, it can be generally stated that within each passage, there is a strong variation in both spanwise and pitchwise direction – a result of the complex flow field, which is driven by strong pressure gradients in both directions (see discussion of Figure 5.8).

Concerning periodicity, there is a strong gradient between P+1 and P-1 at all spanwise positions for the initial geometry. Furthermore, due to the no-step design of the upper cascade geometry, the flow is strongly accelerated at the upper passage. In contrast, the optimized geometry shows a much more periodic pattern at all spanwise positions. Particularly at the important near-shroud position, the two adjacent passages have a very good agreement with the central passage. In the lower passage (P-2), however, the curve shows an overall upward trend indicating that the tailboard setup, as mentioned before, can still be optimized.

At the midspan, the distribution is characterized by a periodic alternation between the medium loss wake region and the nearly lossless freestream. Driven by secondary flow and the growth of the endwall boundary layer, the loss level is significantly increased in the near-hub and near-shroud regions. Especially near the shroud, the high-loss area extends over a large part of each passage. In comparison to the Mach number distribution, the periodicity of the losses may appear to be more robust to geometry changes, as even the initial geometry shows no essential changes of the loss pattern in the pitchwise direction. The higher Mach numbers in the lower passages are only evident in higher peak losses. However, an even more periodic distribution could be achieved even with the optimized geometry, as the loss levels at midspan and shroud are almost identical across the passages.

In-depth evaluation with fine mesh setup: The calculation of the final geometry with significantly increased mesh density (see Table 5.1) within the cascade allows a more detailed flow analysis: Figure 5.8 depicts the normalized outlet pressure distribution and the total loss coefficient downstream of the central passage, with the secondary flow superimposed. The static pressure distribution is dominated by a strong gradient pointing from the pressure side outlet flow near the shroud (+) to the suction side outlet flow near the hub (-). It results from the superposition of the radial and cross-passage pressure gradients, as discussed in Chapter 2.6. With respect to the findings of Chapter 4, the strength of the radial gradient clearly underlines the necessity of incorporating endwall curvature into the modeling approach for a more realistic assessment of the passage flow.

The loss distribution is characterized by a complex interaction of profile, wall, and secondary flow-induced losses: At the midspan (1), the losses of the vane wake flow dominate, which has already mixed significantly with the main flow due to viscous and turbulent effects. The elliptical-shaped local loss maximum (2) near the shroud can be attributed to the passage vortex. Compared with its hub-side counterpart (3), it has widened considerably, shifted toward the center of the passage, and smoothed out with the freestream. The assumptions of Chapter 2, i.e., the amplification of secondary flows on the shroud, are found to be valid in the numerical model. This also holds true for the endwall losses

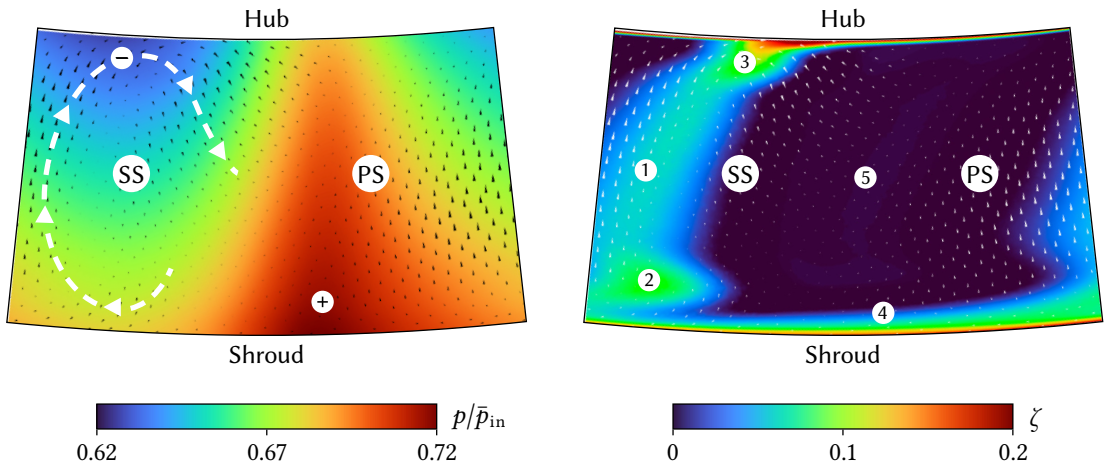

Figure 5.8: Distribution of normalized static pressure and total pressure loss coefficient with secondary flow overlay at central passage outlet plane for final geometry (FIN-OP-FINE)

on the shroud (4), which propagate significantly towards the passage center, while the hub losses are concentrated in the immediate vicinity of the endwall. However, it must be taken into account that these effects may be partly attributed to the contouring of the shroud endwall. Along with the results of Boletis [35], the linear cascade measurements also indicate that at least a significant portion of the thickening of the endwall losses can be attributed to contouring.

Concerning the secondary flow field, the vorticity of vortices, e.g., the passage vortex, is clearly superposed by a large-scale circulation, which extends over the entire span and is highlighted in the static pressure plot. Driven by the strong radial pressure gradient, the circulation transports low-momentum fluid through the wake from the shroud to the hub. From there, the flow is redirected back to the center of the passage but deflected in the pitchwise direction due to the strong counteracting pressure gradient. Along a narrow corridor (5) between the passage-wise circulation, secondary flow weakens considerably.

To assess the periodicity of the final geometry under design point flow conditions, the pitch and yaw flow angles β and γ are plotted over all passages in Figure 5.9. The freestream in the central and adjacent passages is characterized by a periodic flow deflection (1) of approximately 76°, whereas in the upper passage (P+2), the flow is slightly over-deflected (2). Due to the reduced velocity and the associated lower inertial resistance near the shroud endwall, the flow is overturned (3) by the imposed pressure gradient pointing from the pressure to the suction side. Since the boundary layer at the hub endwall is considerably thinned, this effect is limited to the shroud. Rather, the deflection at the hub endwall (4) is partially lowered by the passage-wise circulation. Across all passages, these patterns recur with sufficient periodicity.

It is noticeable that the range of the pitch and yaw angles differs significantly: While the radial circulation is accompanied by very high (5) and very low (6) yaw angles in the range of approximately −15° to 15° degrees, only the near-wall regions stand out with both considerably increased and

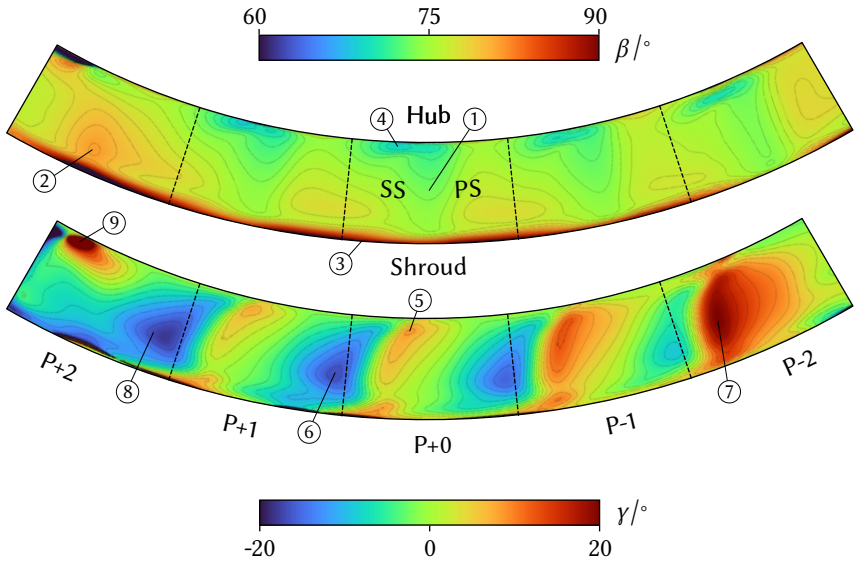

Figure 5.9: Distribution of flow angle β and γ on outlet plane for final geometry (FIN-OP-FINE)

decreased pitch angles. Concerning periodicity, there is an intensification of secondary flow pointing towards the hub region within the lower passages (7). At the upper passage, an inverse amplification of the secondary flow toward the shroud region emerges (8), with a flow separation occurring at the junction of the upper cascade limitation and the hub endwall (9). The periodicity of the central passage is only moderately affected, and it can be assumed that an optimized tailboard setting can mitigate these phenomena.

The total pressure loss coefficient and Mach number distribution are shown in Figure 5.10. The characteristic loss pattern with the oblique wake region, the vortex-induced secondary flow losses, and the thickened shroud endwall losses are periodically repeated in the adjacent passages. Minor deviations in periodicity can be found in the lower passage (P-2): While the near-hub loss center of the passage vortex (1) is shifted towards the passage center, the near-shroud counterpart (2) is pushed towards the endwall. This can be attributed to the formerly discussed amplification of the flow circulation pointing toward the shroud. The flow separation on the hub endwall within the upper passage (P+2) is evident by increased losses.

The passage-wise Mach number distribution can be divided into distinct sections: The low-pressure but high Mach number flow (3) originates from the suction side, while the high-pressure but low Mach number flow (4) emerges from the pressure side. The wake region (5) with the prominent passage vortex (6) and the thickened shroud endwall boundary layer (7) show up with likewise reduced flow velocities. Concerning periodicity, the two-dimensional distribution confirms what has already been observed at the three spanwise positions: The two adjacent passages P-1 and P+1 show an almost identical Mach number distribution when compared to the central passage. As discussed earlier, the stepped junction between the lower cascade limitation and the tailboard results in an over-acceleration

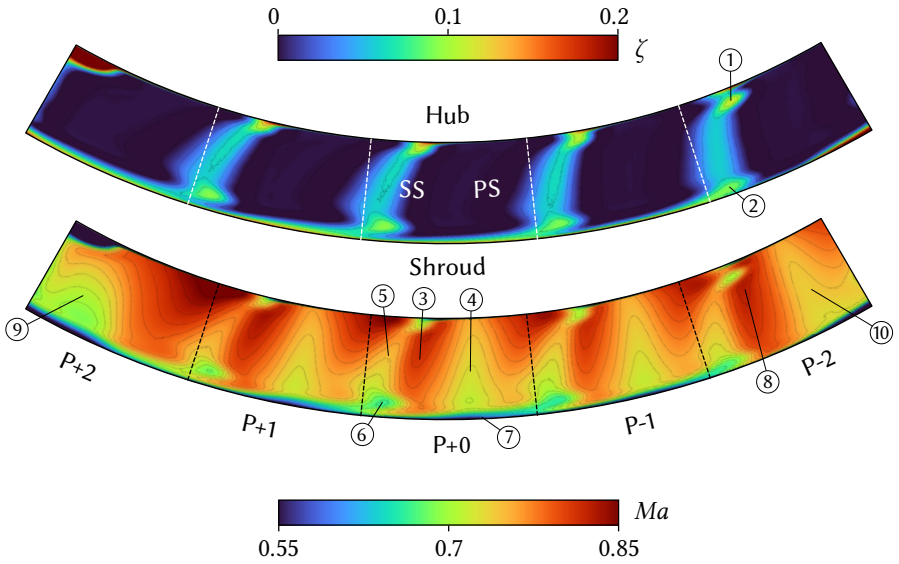

Figure 5.10: Distribution of Mach number and total pressure loss coefficient ζ on outlet plane for final geometry (FIN-OP-FINE)

of the suction-side flow of vane N1, which is clearly evident in the two-dimensional distribution (8). However, considering the sensitivity of the tailboard setting, it can be assumed that this lack of periodicity can be further compensated in real operation. The aperiodicity in the region of the upper (9) and lower (10) cascade limitations cannot be avoided by design since the lack of a suction-side and pressure-side flow affects the evolution of the secondary flow. To limit the effects of boundary layer growth and, therefore, to improve periodicity in the upper and lower passage, in many cases a boundary layer bleeding system is integrated into the test rig immediately upstream of the upper and lower passage limitation [136]. Since this is only a critical issue in compressor cascades and, in the present case, a satisfactory periodicity was obtained in the three inner passages, the integration of such a system was not put into practice.

Table 5.7 summarizes the mass flow averaged inlet conditions obtained at the operating point for the final geometry, which will be used for subsequent dimensioning calculations.

Table 5.7: Derived inlet conditions at operating point for final geometry (FIN-OP-FINE)

Parameter	Value	Parameter	Value
Static pressure $\overline{p}_{\text{in}}$	1.64 bar	Density $\overline{\rho}_{\text{in}}$	$1.89\,\text{kg}\,\text{m}^{-3}$
Velocity $\overline{c}_{\text{in}}$	$23\,\text{m}\,\text{s}^{-1}$	Dyn. Viscosity $\overline{\mu}_{\text{in}}$	$1.85 \times 10^{-5}\,\text{Pa}\,\text{s}$

5.3 Overview of the Annular Sector Cascade

Overview of the Annular Sector Cascade The annular test rig consists of segmentally constructed components connected by flanged joints: Functional parts, such as the turbulence grid, are integrated as intermediate flanges. This design allows simple assembly and quick replacement of individual components. In contrast to the linear cascade, the individual segments were designed as welded structures for several reasons: First, the use of welded components significantly reduced the complexity of the sealing system, as the individual segments can be sealed via ordinary flat gaskets. Secondly, a welded structure facilitates the use of bent sheet metal parts to realize the annular endwalls since the use of milled components would have involved significantly higher material consumption and a larger number of parts. Finally, the use of a welded structure and the associated reduction in complexity led to simplified structural strength analyses to determine wall thicknesses and reinforcements. With a wall thickness of 6 mm, the total weight of the inlet section could thus be drastically reduced from approximately 350 kg to 100 kg compared to the linear cascade.

The reduction of the design temperature from 400 °C to 160 °C allows, in principle, the application of aluminum components. However, due to strength considerations, the welded structures are made of 1.4307 (AISI 304L), a low-carbon austenitic and general-purpose stainless steel with particularly good weldability. With an ultimate tensile strength[10] of 600 MPa, it has at least twice the strength of aluminum alloys with good weldability, e.g., Al-Mg alloys [137]. Furthermore, the significantly lower thermal conductivity of $16\,\mathrm{W\,m^{-1}\,K^{-1}}$ compared to $117\,\mathrm{W\,m^{-1}\,K^{-1}}$ simplifies temperature control during heat transfer measurements, as less heat is dissipated to the test room environment.

Before the individual components are presented in detail, the following section will provide an overview of the entire annular test rig: Figure 5.11 shows the test rig from the shroud view, with the flow coming from right to left. A welded transition duct (1) converts the circular cross-section of the upstream attached valve into an annular sector cross-section of 60°. This is followed by the first inlet segment (2) for flow conditioning, which houses a turbulence screen as well as a flow straightener and provides measurement access for monitoring the inlet conditions. To set a defined level of turbulence at the inlet of the cascade, a turbulence grid (3), designed as an intermediate flange, is mounted between the first and second (4) inlet segments, with the latter one containing a second measurement access. Immediately upstream of the cascade inlet, a hub- and shroud-side boundary layer suction (5) is installed, which is also realized as an intermediate flange. The entire inlet section as well as the outlet tubing of the boundary layer suction is supported by an aluminum frame. The annular cascade casing (6), which was designed around the optimized fluid volume, not only contains the five-passage cascade but integrates the necessary measurement instrumentation. The contoured endwalls of the shroud with the central purge slot measurement module are designed as separate inserts that are held in place by clamping jaws. The cascade casing is followed by the outlet vessel (7), which collects the

10 According to the material certificate of the used batch

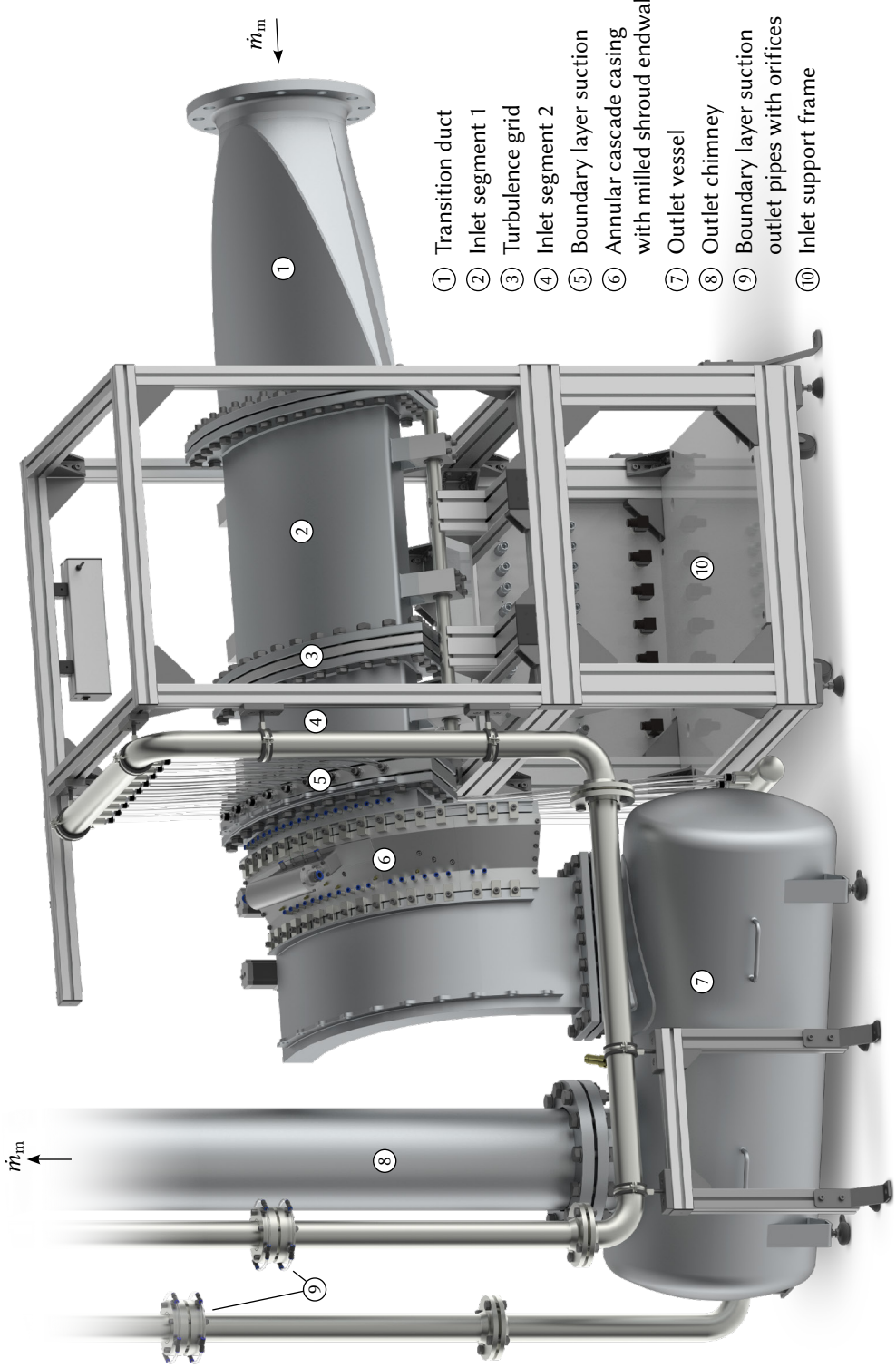

Figure 5.11: Shroud-side overview of the annular test rig

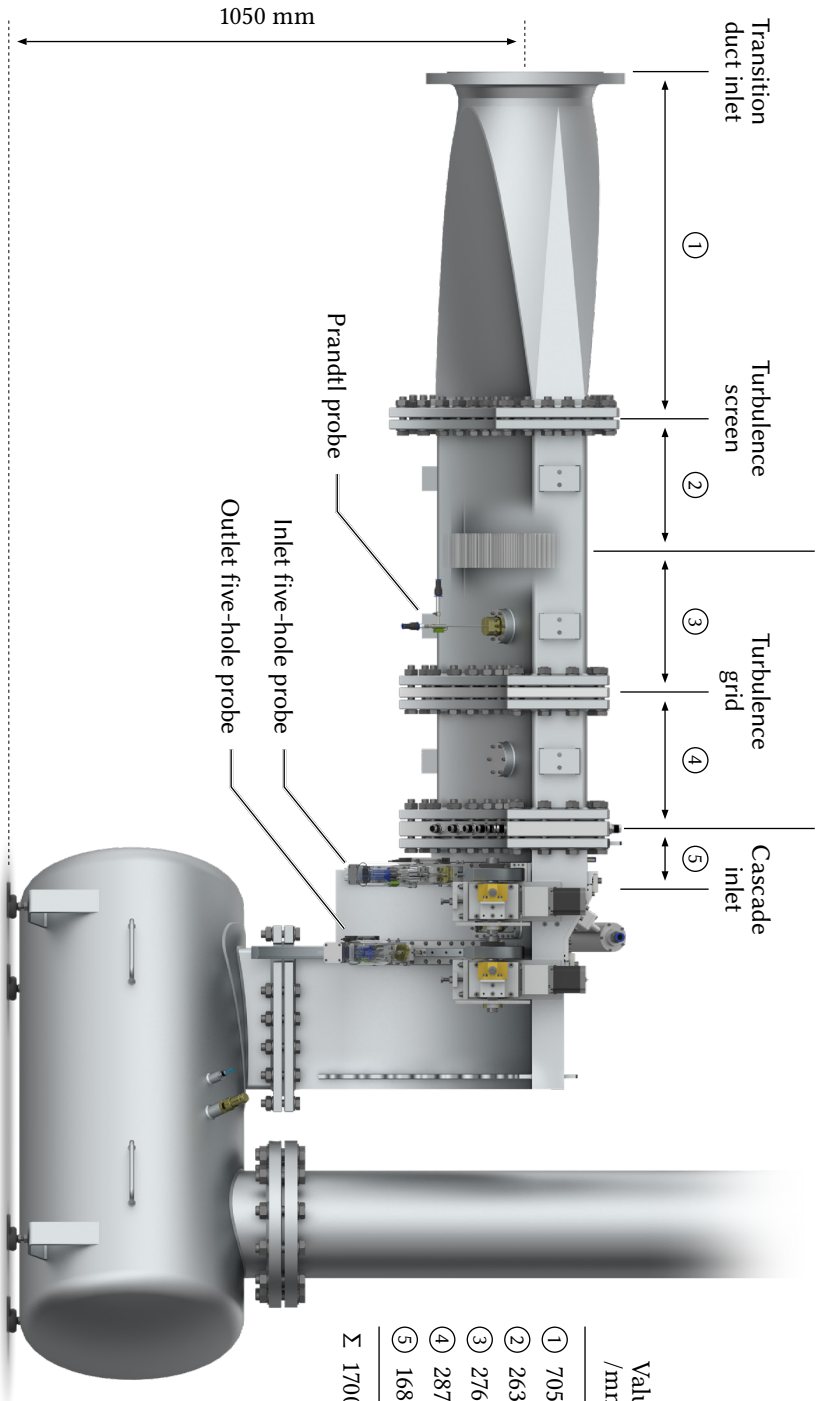

	Value /mm	Value /$C_{mid,x}$
①	705	14.39
②	263	5.37
③	276	5.63
④	287	5.86
⑤	168	3.43
Σ	1700	34.7

Figure 5.12: Hub-side overview of the annular test rig

flow and guides it into the chimney (8). The diverted flow of the boundary layer suction is discharged via parallel pipes. By means of integrated orifice plates and downstream control valves, the diverted mass flow for the shroud and hub can be measured and adjusted separately.

The hub-side view of the test rig with the relevant axial dimensions is shown in Figure 5.12. As the purge slot is located on the shroud, the accesses for probe and optical measurements are provided on the hub. To reduce pre-existing turbulence and to equalize the flow velocity profile directly behind the transition duct, the turbulence screen is integrated into the flange of the first inlet segment. Following the design guidelines by Mehta and Bradshaw [138], a honeycomb is positioned further downstream of the transition duct. The axial position of the turbulence grid between the first and second inlet segment was deducted from the dimensioning process following Roach [139]. The boundary layer suction is located in close proximity to the cascade inlet to limit the re-growth of the boundary layer. As mentioned before, for the evaluation of the inlet and outlet flow field, two independent probe traverse units are integrated into the cascade casing, with the circumferential traversing units mounted at the bottom plate of the cascade casing.

5.4 Inlet Flow Guidance and Conditioning

The transition duct, shown in Figure 5.13, was already developed and manufactured as part of a previous project: It has a length of 705 mm and consists of two multi-folded half-shells, which are made of 6 mm thick stainless steel sheets (1.4571/316Ti) and welded together along the two end faces. The welded half shells are enclosed in two welding neck flanges. While the annular sector flange has an angle of 60° with a channel height of 100 mm, the circular flange has an inner diameter of 260.4 mm.

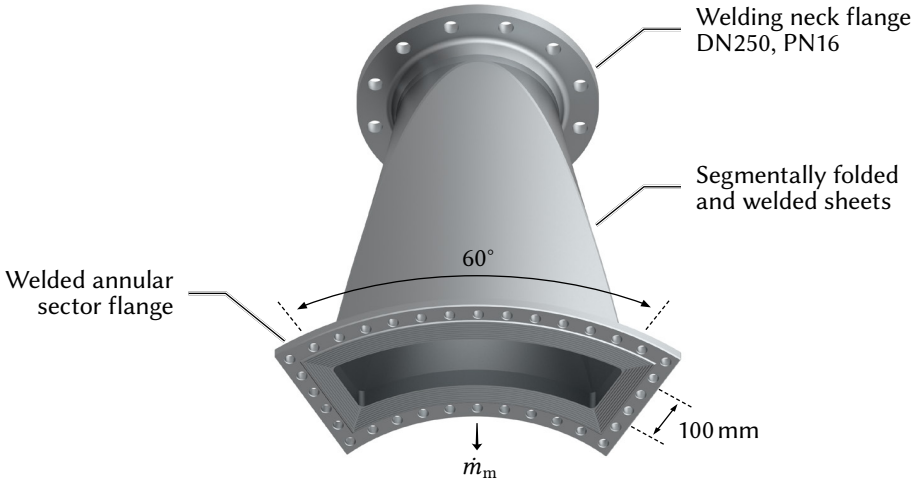

Figure 5.13: Circular-annular transition duct

This results in an area ratio of $A_{\text{out}}/A_{\text{in}} = 0.86$, i.e., the flow is slightly accelerated within the transition duct. With recourse to the study of Mehta [140], flow separation is unlikely despite the comparatively high divergence angle of about 20° between the upper and lower channel walls of the annular sector.

5.4.1 First Inlet Segment with Turbulence Screen and Flow Straightener

The first inlet segment, depicted in Figure 5.14, is intended to equalize the flow exiting the transition duct by means of a screen and a downstream flow straightener. It consists of two welded half-shells enclosed by two socket weld flanges. For flexible integration of the turbulence screen, the upstream flange is provided with a pocket in which the screen holding frame is inserted. U-shaped profiles are welded to the end faces of the casing: They are necessary for mounting the shaft brackets by which the inlet segment is braced in the support frame. To monitor the inlet flow conditions, a Prandtl probe with an integrated thermocouple is mounted downstream of the honeycomb. For a correct probe alignment, the brass probe holder, which is sealed by an O-ring in the welded socket, can be rotated freely. Considering the required level of turbulence $Tu_{\text{in}} = 5.2\,\%$ at the entrance of the passage, the turbulence level should be lower upstream of the turbulence grid.

Screen dimensioning: Screens are commonly used for equalizing the velocity profile by imposing a static pressure drop proportional to the velocity of the incoming flow. Furthermore, they deflect the incident flow towards the local normal and reduce the turbulence intensity [138]. Concerning

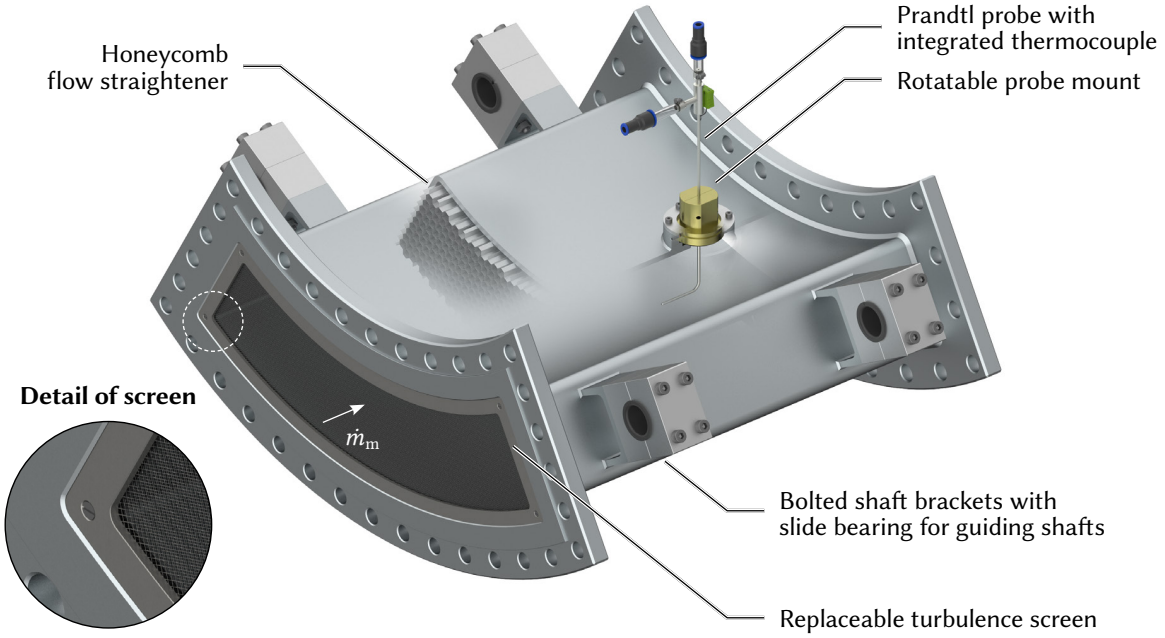

Figure 5.14: First annular inlet segment

the characteristics of the incoming flow in the test rig, it can be assumed that a fully developed turbulent pipe flow is present. According to Basse [141], the average turbulence intensity $\overline{Tu}_\mathrm{p}$ in both smooth- and rough-walled pipes is a function of the pipe friction factor λ_p and can be estimated by the following empirical formula:

$$\overline{Tu}_\mathrm{p} = \frac{9}{10\sqrt{2}} \cdot \sqrt{\lambda_\mathrm{p}} \tag{5.1}$$

Since the upstream pipes of the test rig are not entirely made of stainless steel, the pipe walls cannot be considered hydraulically smooth. Assuming a wall roughness of $K \leq 0.4$ [142] and a pipe Reynolds number of $Re = 7 \times 10^5$, the maximum pipe friction factor can be obtained by Moody's chart [143] with $\lambda_\mathrm{p} = 0.022$ leading to $\overline{Tu}_\mathrm{p} \approx 9\,\%$. According to Prandtl [144], the turbulence intensity is reduced by a single screen in the ratio of $1/\sqrt{1+\zeta_\mathrm{s}}$. The screen pressure loss coefficient ζ_s can be estimated following the formula by Wieghardt [145]

$$\zeta_\mathrm{s} = f(Re_\mathrm{s}) \cdot \frac{1-\beta_\mathrm{s}}{\beta_\mathrm{s}^2} \tag{5.2}$$

where β_s is the open-area ratio of the screen and Re_s the Reynolds number related to the wire diameter d_s. Experimental data suggest that the function $f(Re_\mathrm{s})$ reaches a constant value of approximately 0.5 for $Re_\mathrm{s} > 250$ [146]. To prevent additional turbulence generation due to vortex shedding, the wire diameter should be chosen so that $Re_\mathrm{s} < 60$ [147]. However, in the present case, the wire diameter d_s and mesh size M_s must be sufficiently large to prevent clogging during operation since a very small amount of flash rust is carried along with the flow. Furthermore, the additional small-scale turbulence decays rapidly according to a study of Groth and Johansson [148]. They stated that the distance required for the intensity to fall below the incoming level is about 15 mesh sizes for supercritical screens. With these limitations, a screen with $d_\mathrm{s} = 0.2\,\mathrm{mm}$, $M_\mathrm{s} = 0.7\,\mathrm{mm}$ and $\beta_\mathrm{s} = 0.51$ was chosen for the annular test rig. The downstream honeycomb is placed in a relative distance of $375 \cdot M_\mathrm{s}$. With $Re_\mathrm{s} \approx 500$, the loss coefficient can be estimated to $\zeta_\mathrm{s} = 1.42$ resulting in a turbulence damping factor of 0.64.

Honeycomb dimensioning: According to Mehta and Bradshaw [138], honeycombs are particularly effective in eliminating swirl, aligning the flow with the axis of the pipe, and reducing lateral turbulence. The hexagonal honeycombs used here are made from aluminum foil with a thickness of 80 µm and have a cell size of 6.4 mm. With a length of 50 mm, the crucial length-to-size ratio equals 7.8, meeting the general design rules for the application of flow straighteners. Approximately 1300 cells are allocated across the annular cross-section.

The lateral and axial turbulence damping factors of the honeycomb can be estimated with recourse to measurements conducted by Scheiman and Brooks [149] who investigated similarly sized, but slightly shorter, honeycombs under similar flow conditions. They found a lateral damping of 0.47

and an axial damping of 0.62. Assuming that the turbulence intensity of the incoming pipe flow does not exceed 9 %, the combination of screen and honeycomb provides sufficient overall damping in the range of 0.3 to 0.4.

The honeycomb was manually cropped to the annular shape using waterjet-cut templates with an oversize of 2 mm and pushed into the channel. With a pressure loss coefficient of 0.2 [150] and a total pressure loss of approximately 120 Pa, the acting force on the honeycomb structure is about 5 N at design point flow conditions. Due to the clamping effect and in consideration of the low drag, no additional axial securing is necessary. To avoid stalling of the honeycomb cells, the yaw angles of the incoming flow should not exceed 10°. Following Mehta and Bradshaw [138], the deflection ratio α_s of the screen, i.e., the ratio between the outlet and inlet angles, can be estimated by

$$\alpha_s = 0.66 + \frac{0.31}{\sqrt{1 + \zeta_s}} \tag{5.3}$$

i.e., the present screen reduces yaw and swirl angles by a factor of approximately 0.86. Regarding the maximum half divergence angle of about 10° in the transition duct, stalling in the honeycomb can therefore be ruled out.

5.4.2 Turbulence Grid

The turbulence grid, shown in Figure 5.15, is required to ensure a defined turbulence intensity across the inlet of the cascade. It differs from a screen mainly by a significantly higher Reynolds number based on the characteristic length of the grid elements [151]. For easy integration into the test rig, it is designed as an intermediate flange, which is mounted between the first and second inlet segments.

The variety of turbulence generators being used is wide and ranges from passive elements, such as perforated sheets and gridded bars or rods [152], to active elements like motor-adjustable grids [153] or grids with jet injection [154]. In the present case, a simple radial arrangement of square bars is used, as this setup is the most robust and easy to integrate into the annular cross-section. The rectangular profile is furthermore particularly insensitive to Reynolds number variations [139] and can be manufactured in a single step on a waterjet cutting machine. The actual grid is inserted into a milled pocket of the flange, allowing different turbulence settings to be investigated with little changeover costs.

The turbulence, generated by a grid, decays with distance downstream, as there is no continuing source of turbulent energy. The rate of this energy decay is very equal to the rate of viscous dissipation [155]. With reference to an analysis of Roach [139], it can be described for a square bar by the following equation

$$Tu(x) = 1.13 \cdot \left(\frac{x}{w_g} \right)^{-5/7} \tag{5.4}$$

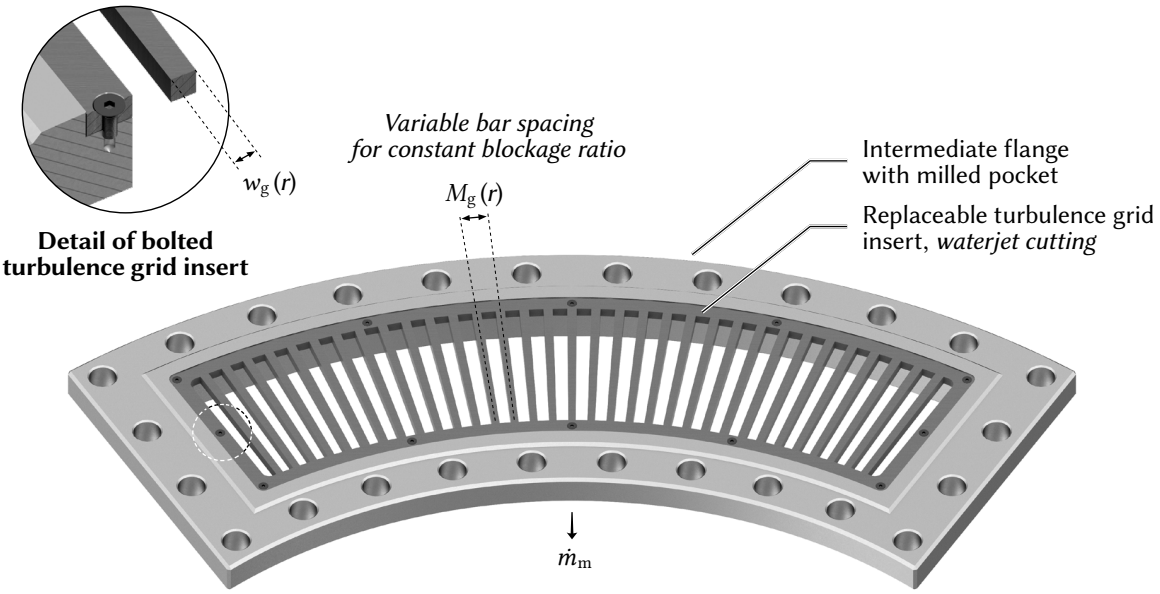

Figure 5.15: Turbulence grid design adapted from Saha [91]

where w_g is the width of the bar and x the downstream distance from the grid. The associated pressure loss coefficient can be calculated within a Reynolds number range $10^2 < Re_d < 10^4$ by [139]

$$\zeta_g = 0.98 \cdot \left(\frac{1}{\beta_g^2} - 1 \right)^{1.09} \tag{5.5}$$

Since the pressure loss depends mainly on the open-area ratio $\beta_g = 1 - w_g/M_g$, a uniform bar width across the radius would inevitably result in an increasing blockage from shroud to hub. This would, in turn, induce a radial gradient in flow velocity and create flow instabilities if β_g falls below 0.5. With $\beta_g = 0.6$ and $w_g(r) = w_{g,s} \cdot r/r_{s,in}$, the open-area ratio is therefore kept constant over the channel height at the cost of slightly reduced turbulence. To overcome this difficulty, a circumferential arrangement of the bars can be considered as an alternative but was not implemented here for reasons of structural stability. The main parameters of the grid used here can be taken from Table 5.8 below. The presented grid configuration is a compromise between the turbulence requirements, the relative distance from the grid to the cascade inlet, and the axial footprint of the second inlet segment. Depending on the Reynolds number, isotropic turbulence is typically obtained after 40 to 50 mesh lengths or bar spacings [156]. Therefore, it could be objected that the selected distance is too small. However, the slight contraction from $r_{s,ch} = 489\,\text{mm}$ to $r_{s,in} = 474.5\,\text{mm}$ at the cascade inlet should improve isotropy according to previous studies [155].

Table 5.8: Main parameters of the used turbulence grid on shroud and hub

Parameter	Shroud	Hub
Bar width w_g	6.1 mm	4.9 mm
Bar spacing M_g	15.3 mm	12.2 mm
Open-area ratio β_g	0.6	0.6
Relative distance x/M_g	29.8	37.4
Inlet turbulence intensity Tu_{in}	5.2 %	4.4 %
Reynolds number Re_d	1.4×10^4	1.13×10^4
Pressure loss Δp_g	9.2 mbar	9.2 mbar

5.4.3 Second Inlet Segment with Boundary Layer Suction

The second inlet segment, manufactured in the same way as the first segment and depicted in Figure 5.16, provides the necessary inlet distance between the turbulence grid and the boundary layer suction. It has additional measurement and instrumentation access, which can be used, e.g., for turbulence measurements with hot-wire anemometry. The bolted shaft brackets already mentioned are shown here in detail: They consist of two milled aluminum half-shells with dry-running flanged sleeve bearings (Igus G300) inserted.

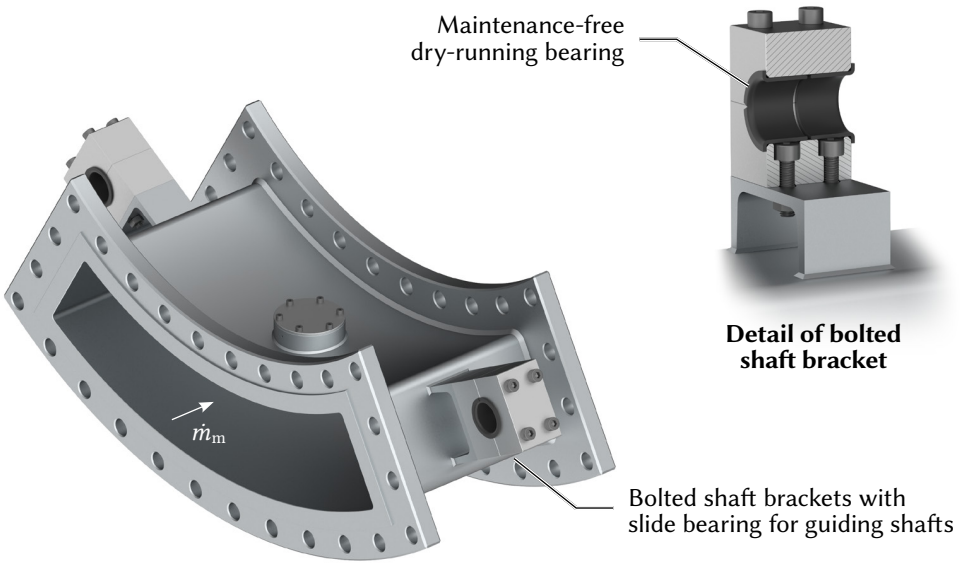

Figure 5.16: Second annular inlet segment

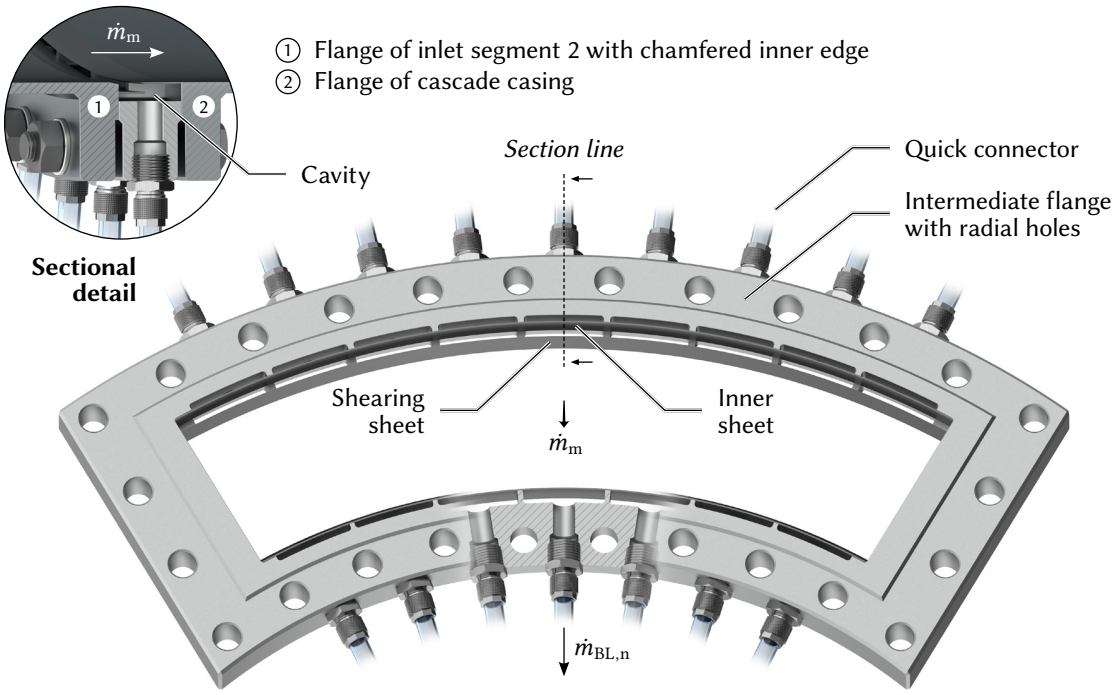

Figure 5.17: Boundary layer suction

The need for boundary layer suction arises from the fact that a boundary layer of unknown thickness has formed at the end of the inlet segments. For this reason, the existing boundary layer must be removed through suction, allowing a new boundary layer to develop with a uniform, known thickness across the entire endwall. In previous tests with the linear cascade, it was found that the boundary layer suction also helps to create a more uniform velocity distribution across the channel's height by a fine adjustment of the suction rate.

The boundary layer suction, illustrated in Figure 5.17, is designed as an intermediate flange with milled ribs, cavities, and bores. The incoming boundary layer on the hub and shroud is separated via circumferential shear sheets, collected in cavities, and discharged via radial bores with partial threads. To prevent the formation of a detachment bubble at the sharp edge of the shear sheet, the inner edge of the upstream flange is provided with a chamfer, which directs the flow slightly downwards and, therefore, facilitates a seamless attachment of the highly turbulent outer flow on the surface of the sheet. For this reason, the downstream installation of a trip wire, as used in the linear cascade, was omitted. Additional sheets between the shear sheets and the bores are intended to equalize the suction in the circumferential direction. All sheets are fixed to the ribs of the flange with high-temperature adhesive. The extracted flow is transferred to the outlet collector pipes using quick connectors and polymer tubes. As mentioned above, the extracted mass flow can be adjusted independently at the hub

and at the shroud by means of control valves integrated into the outlet piping. Additionally, if needed, the suction rate for each bore can be independently regulated by retrofitting each tube with a separate valve. An active suction is not required, as the test rig is operated under overpressure.

The major dimension of the sheets and cavities were optimized based on a numerical investigation by comparing the thickness of a tripped boundary layer upstream and downstream of each configuration. The evaluation of the final geometry suggests that the boundary layer suction works best at a total suction rate of $\dot{m}_{\mathrm{BL}}/\dot{m}_{\mathrm{m}} = 2\,\%$.

5.4.4 Inlet Support Frame

The framework of the inlet support, shown in Figure 5.18, is made from prefabricated T-slotted aluminum profiles. The inlet segments are guided and supported by parallel shafts, which are fixed to the framework by separately adjustable shaft supports. This allows easy and precise assembly and alignment of the inlet segments and simplifies revision work, as the flange joints can be loosened without additional support. For convenient transport and positioning in the test room, the support frame is equipped with retractable casters, which allow the frame to be firmly attached to the floor at its final position. The upper part of the frame is used, among others, for mounting the pipes of the boundary layer suction system. Furthermore, the cantilever serves for safe cable and tube routing of both five-hole probe measuring systems and the connecting tubes of the static pressure ports, which is particularly important considering the integration of the industrial robot.

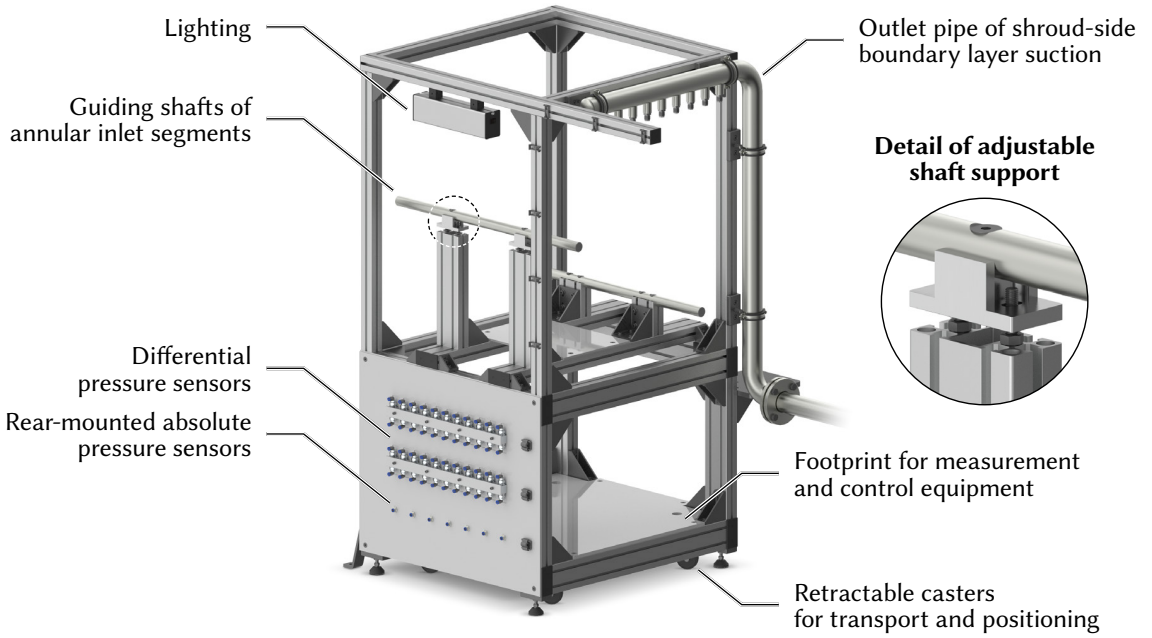

Figure 5.18: Support frame for annular inlet segments

The front of the frame is used for mounting the pressure sensors at a close distance from the actual measuring position. This allows short sensor response times, which are crucial for efficient five-hole probe field measurements since the settling time for a steady-state signal is proportional to the pneumatic tube length [157]. Both absolute and differential pressure sensors are used in the test rig, with the latter being applied for measurement tasks that require high accuracy over a small measuring span. In addition, differential pressures at the opposing holes of the five-hole probes can be determined directly. A summary of the sensors used, their measurement location, and their error margin can be found in appendix A.

5.5 Annular Test Section

In the following subchapter, the structure of the test section is first presented before the individual components are explained in detail. The focus of the presentation is on the design of the welded cascade casing, the redesign of the plenum geometry, and the dimensioning of the measuring module for heat transfer measurements.

5.5.1 Annular Cascade Casing

Figures 5.19 and 5.20 depict the welded cascade casing with the endwall inserts and the attachments for probe traversing and optical access. By using bent sheets with a thickness of 6 mm for the endwalls on the shroud and hub with a constant radius, it was possible to reduce the number of parts required and thus the complexity and material usage of the overall construction. The contoured shroud endwalls are realized by milled segments that can be inserted into the casing and fixed with clamping jaws. The attachments for the probe traversing are fixed both to the reinforced base plate and to welded-on mounting frames. To further simplify the cascade casing, the cascade limitation of the upper passage (P+2) was realized with milled inserts that are bolted to both the casing and the endwall.

The sectional view (b) in Figure 5.19 shows the passage nomenclature, with the central passage module containing the purge slot insert and the feed. The axial length of the endwall segments was chosen so that the transition from the milled segments to the welded casing is located downstream of the outlet measurement plane, which helps to avoid any edge effects on the near-wall flow. As the cross section narrows in the radial direction, the optical window must be inserted from the inside into the cutout. Finally, static pressure taps are integrated into the casing and endwall segments to allow for operating point monitoring at the inlet and outlet positions.

Structure of the welded design: The cascade casing illustrated in an exploded view in Figure 5.21 consists of 16 individual parts welded together. All milled and waterjet-cut stainless steel parts (dark grey) were prefabricated in the university's own metal workshops. The bending of the cold rolled stainless steel sheets and welding work was carried out externally. To integrate the attachments for the

Figure 5.19: Hub-side overview of cascade casing

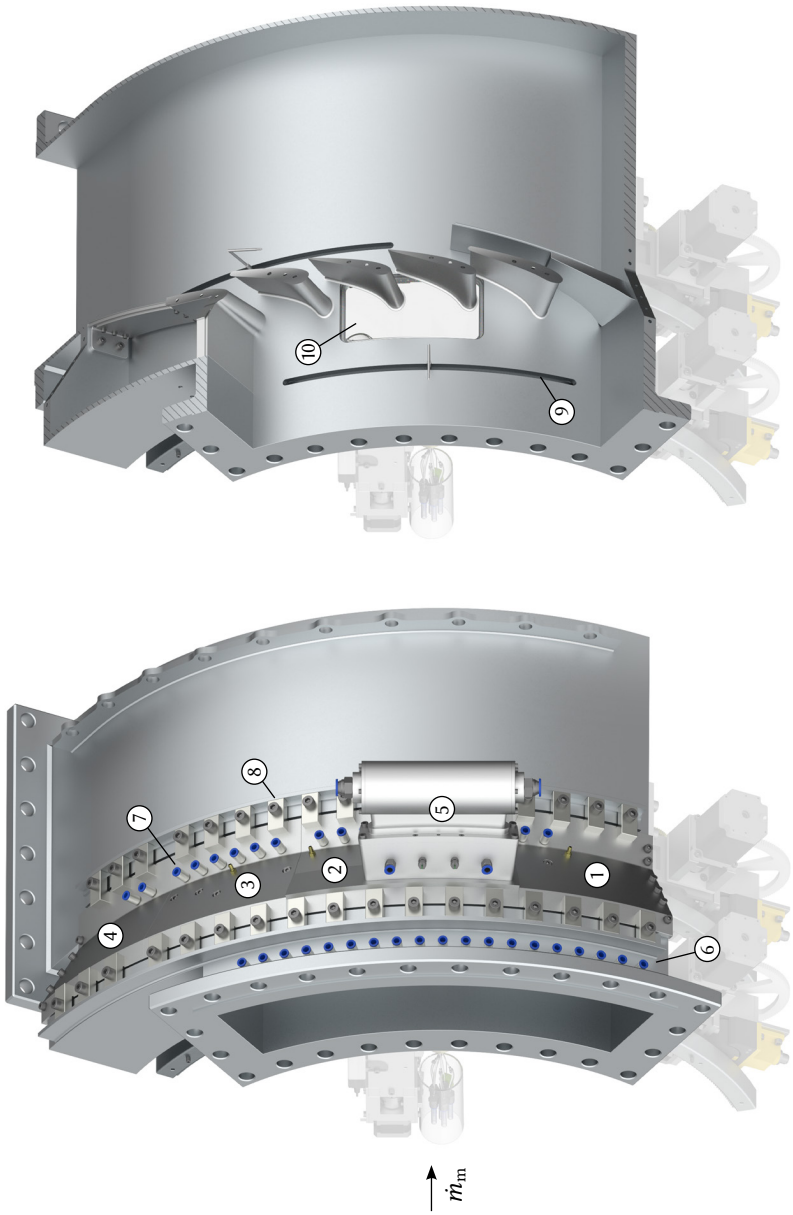

① – ④ Milled endwall segments
⑤ Purge slot plenum
⑥ Static pressure tap ring inlet
⑦ Static pressure tap ring outlet
⑧ Clamp-based endwall mounting
⑨ Slotted holes for probe access
⑩ Optical access

Figure 5.20: Shroud-side overview of cascade casing

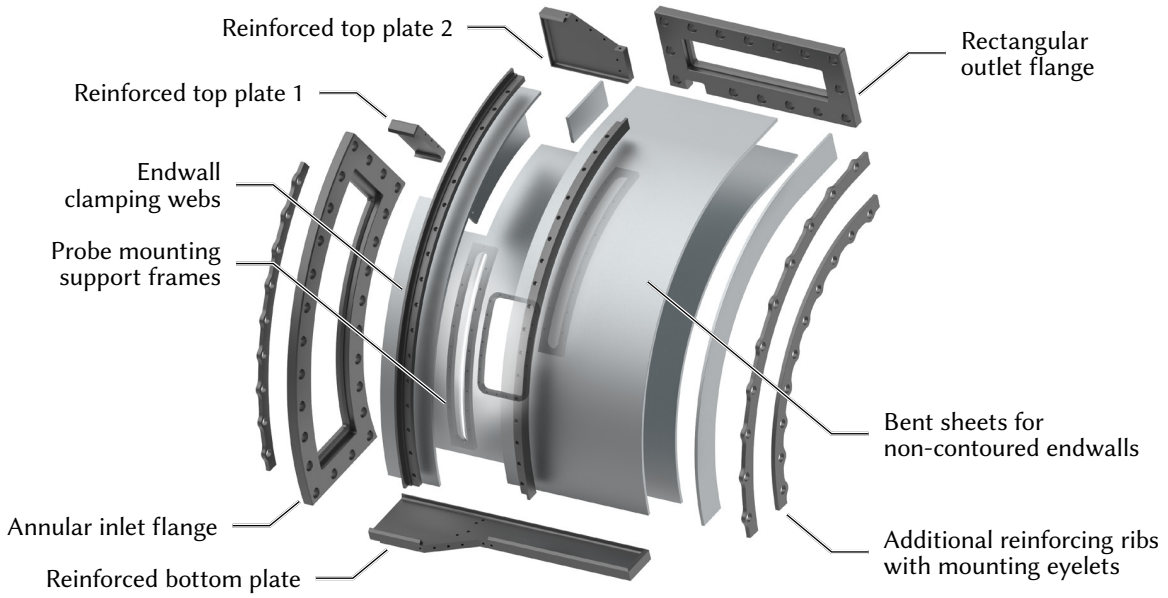

Figure 5.21: Exploded view of the annular cascade casing

probe traversing system and the optical access, mounting frames with threaded bores were welded on. These frames were provided with a thickness allowance so that they could be precisely machined to a defined radius after welding. The openings required for optical access and the probe feed-through were laser-cut out before bending. The webs necessary for clamping the milled endwall segments further stiffen the structure. Both annular and rectangular flanges were designed as socket-weld flanges with a thickness of 20 mm. The latter was provided with a cutout to match the trajectory of the outlet probe traversing rack. The sheets were welded both inside (groove) and outside (fillet) to the flanges. To avoid a tripping effect of the internal welding on the flow, the seams were surface ground.

A finite element analysis has shown that the highest equivalent stresses are present at the transition from the endwall to the bottom. To reduce the load on the welded joints, the bottom and top plates were, therefore, designed in the style of a welding neck flange with a long-tapered hub allowing the sheets to be butt welded, as this kind of joint is advantageous over a fillet weld in terms of force flux. [158]. In addition, to minimize the notch effect caused by the change in cross-section, the bottom and top plates are provided with a fillet edge of 5 mm at the endwall transition. To increase the dimensional stability, the bottom and top plates were given a thickness surcharge of 9 mm. To improve the torsional stiffness of the casing, reinforcing ribs were spot-welded in the circumferential direction. Integrated ring eyelets ease transport and assembly as they serve as suspension points.

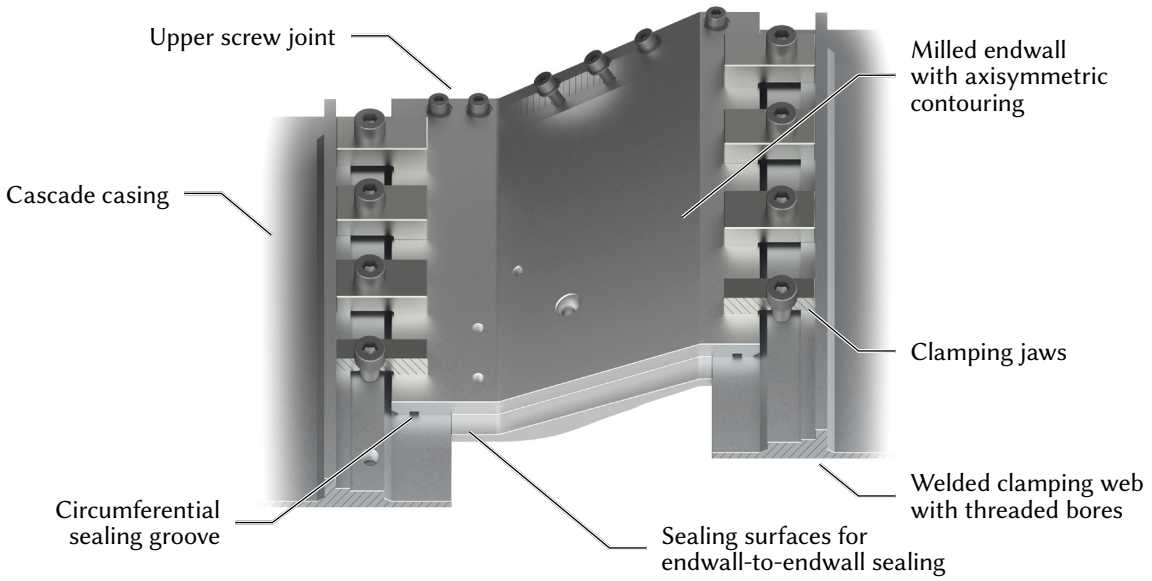

Figure 5.22: Detail of endwall clamping and sealing

A strength verification of the final weld design was performed with a commercial tool that assesses the load on the welded joints through finite element analysis based on the so-called structural stress concept: The stress in the volumetric model is calculated at a specific distance from the weld and extrapolated to the weld root [159]. The extrapolated stress is then checked against the requirements specified in the German FKM guideline [160].[11]

Endwall clamping: To integrate the milled endwall segments into the cascade casing, a clamping mechanism consisting of 34 single jaws was developed, as this design is more forgiving of manufacturing variations in the welded structure. The design of the clamping and sealing mechanism is depicted in Figure 5.22: The clamping jaws are screwed onto the two circumferential, stepped webs while being supported along the raised outer surface. To minimize the surface pressure on the aluminum endwalls, the clamping faces were made as large as possible and provided with a radius that matches the outer radius of the endwall segments. The endwall inserts and the cascade casing are sealed to each other in the circumferential direction by a round cord. The endwall-to-endwall sealing is realized by an overlapping surface sealing in the style of a tongue and groove joint. Threaded holes have been added to the top and bottom plate of the cascade casing in order to the tightness between the upper or lower endwall segments and the casing by the additional screw joints.

11 The FKM guideline "Computational Strength Verification of Machine Components" is a guideline published by the Research Council for Mechanical Engineering (FKM) that provides a standardized method for determining the strength of mechanical components.

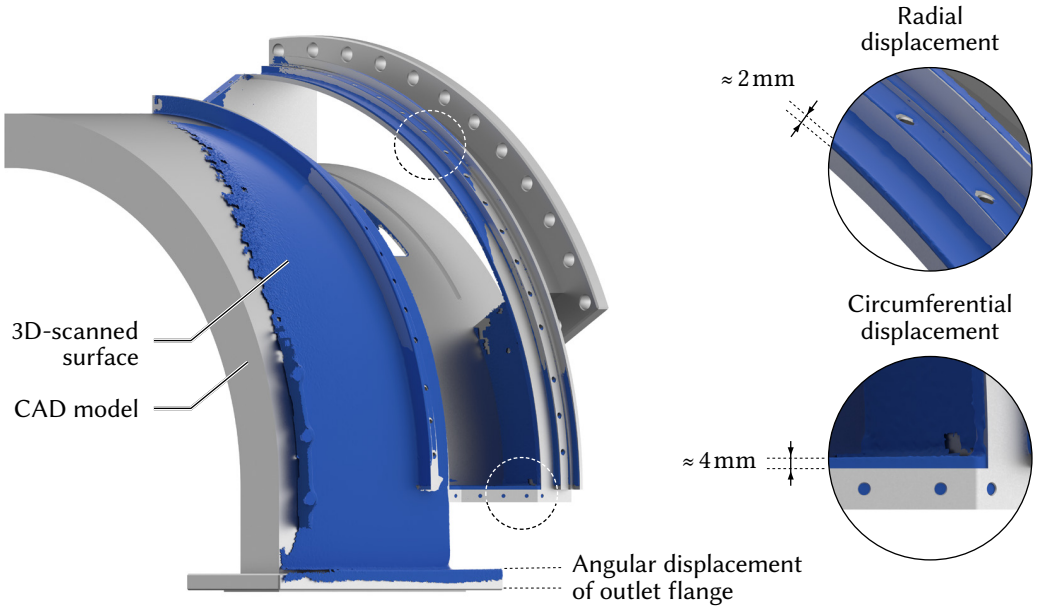

Figure 5.23: Annular cascade casing with superimposed 3D scan

To estimate the strength of the assembly, a finite element analysis was conducted on the assembly of the clamping jaw, screw connection, and clamping web. It was assumed that the M8 bolting (strength class A2-70) was applied with a preload force of 8 kN, equivalent to a tightening torque of approximately 11 Nm [161]. At a maximum static chamber pressure of 1.5 bar, the endwalls are subjected to a force of 13.5 kN, so each of the 34 clamps is roughly loaded with a radial force on the clamping surface of about 400 N, ignoring the additional screw connections at the top and bottom of the cascade. The extra bending of the clamp jaw under operating conditions slightly reduces the force reaction acting on the bolt so that overloading can be ruled out. However, the bending in the clamp results in high equivalent stresses of about 200 MPa at the through-hole. To repeatedly withstand these high stresses, the jaws were made from high-strength cold work steel (1.2842/AISI O2) and subsequently chromated for corrosion protection.

Manufacturing challenges and mechanical rework: The dimensions of the manufactured cascade casing differ from the CAD model due to weld shrinkage and tolerances during partial assembly. To minimize the initial deformation, the casing was first adjusted using hydraulic stamps after the welding work was completed. To evaluate the extent of the final deviations, the casing was captured using a handheld 3D scanner (Creaform Go!SCAN 3D) with a volumetric resolution of approximately 0.1 mm related to the component dimensions. The outcome of the 3D scan on the shroud is shown in Figure 5.23: As a result of the high heat input along the fillet welds of the clamping webs, the shroud endwalls at the inlet and outlet have deformed in the radial direction by a maximum of 2 mm. Consequently, the second top plate has shifted by 4 mm in the circumferential direction. A milling post-

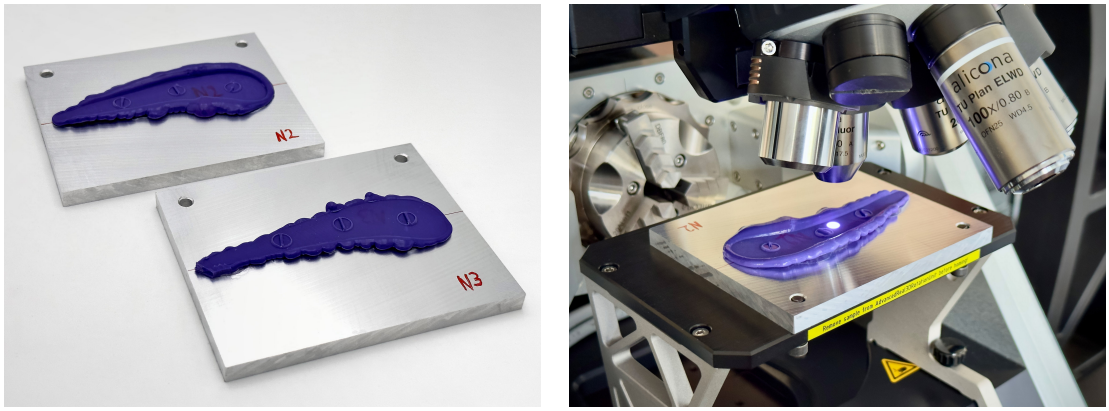

Figure 5.24: Impressions of the gaps between the vane roots and hub endwall and measurement of the height profile using focus variation

processing of the shroud radii on the casing was not pursued, as this would inevitably have resulted in a step at the inner transition from the casing to the endwall insert. Instead, the large clamping force of the jaws allowed the single endwall segments to be matched to the actual contour within their elastic deformability, with the first endwall segment being manually reworked to fit into the casing.

The deformation of the end wall also caused the channel height to exceed the nominal dimension by up to 2 mm. Inserting the vanes in their originally specified dimensions would have created a gap between the vane roots and the hub endwall, resulting in a leakage flow from the pressure side to the suction side. This leakage flow was expected to compromise the vane aerodynamics. Therefore, the gap between each vane and the endwall was replicated using a medical impression material (Kettenbach Panasil contact) before the height profile was mapped using a focus variation measuring device (Alicona InfiniteFocus), as shown in Figure 5.24. This allowed the split vane roots to be individually customized for subsequent 3D printing. Using customized vane roots also ensures that the two central vanes do not exert excessively high clamping forces on the adjacent sight glass.

As previously mentioned, the surface of the welded-on mounting frames was subsequently machined on a 3-axis milling machine to ensure a uniform radius over the entire circumference. This is particularly important for the functioning of the circumferential probe traversing, as a warpage of the screwed aluminum guiding cheeks (see Figure 5.39) would have resulted in a tightening of the moving parts. Furthermore, the internal surfaces of the optical access cutout were milled to ensure a precise fit between the window and the opening.

5.5.2 Lower and Upper Cascade Geometry

The design of the lower and upper cascade geometry follows the final results of the numerical optimization with the integration of the adapted vane geometry, the lower tailboard, and the separation edges. As shown in Figure 5.25, the simplified lower vane is bolted to the bottom plate. Due to the high sensitivity of flow periodicity to the circumferential extension, the lower tailboard is adjustable in 0.5°

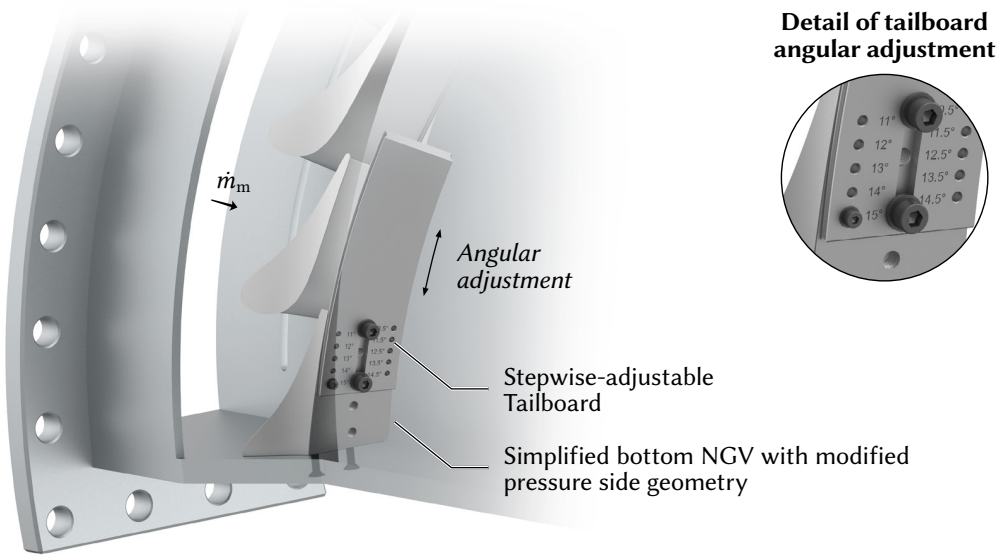

Figure 5.25: Lower tailboard with angular adjustment

increments between 10.5° and 15°. According to numerical results, the tailboard is loaded with 35 N during operation. To minimize the deflection of the 4 mm thick sheet, the tailboard was therefore made of stainless steel and bolted to the lower vane at two points. To seal the flow passage from the recirculation zone, it was provided with a sealing groove on both sides. A pitch-wise modification of the tailboard is possible in principle but requires the vane and tailboard to be replaced by a modified version.

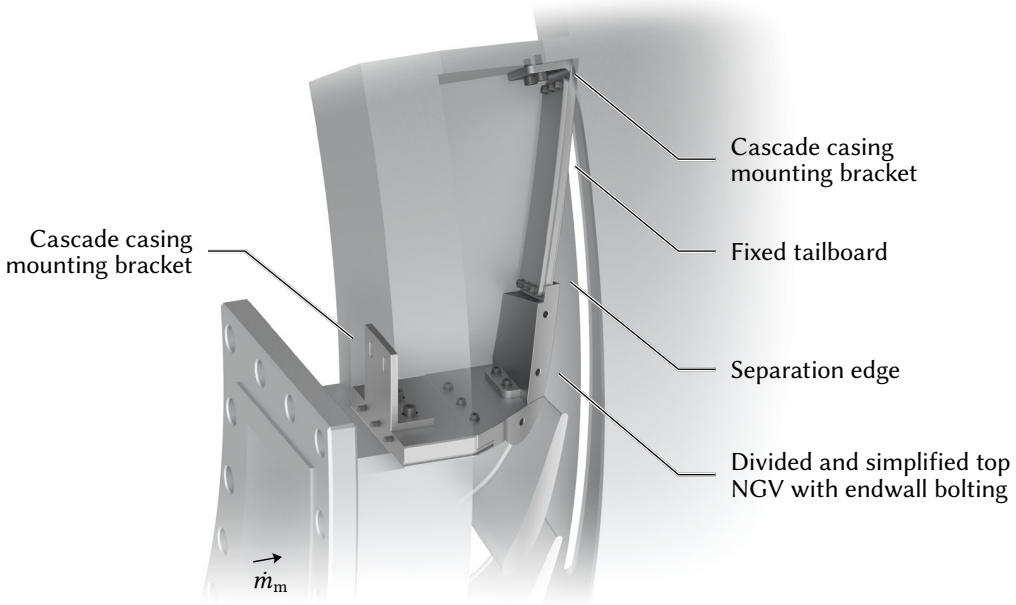

Figure 5.26: Upper cascade geometry

The upper cascade geometry is shown in Figure 5.26. Due to its complex shape, it was made from several parts, minimizing the material consumption. Conservatively assuming that ambient pressure is present in the cavity between the upper cascade limitation and the cascade casing, the structure is facing a load of approximately 700 N. Therefore, it is secured to both the housing and the end walls using multiple bolts and reinforced with additional brackets.

5.5.3 Central Passage Endwall for Film Cooling Effectiveness Measurements

The central endwall segment in Figure 5.27 is used for conducting film cooling effectiveness measurements. It extends over two passages to minimize the influence of abutting edges of the adjacent segments, especially at the passage exit. The vane roots were integrated into the endwall to prevent damage to the otherwise thin-walled fillet, which could have impacted passage aerodynamics. The vanes are pinned to the endwall for precise positioning and secured with bolts at the back. The final vane design was modified to consist of two parts for easier production, with the vane body made of aluminum and the back-cut fillet on the hub being 3D-printed. As with the linear cascade, the endwall is equipped with pressure taps to validate the results of the PSP measurement and to assess the periodicity of the flow by comparing it to pressure taps in neighboring passages. The pressure taps in the central passage also serve as marker points for robot-based position adjustments and as grid points for the post-processing algorithm used to map the image data to the 3D model. Conventional manufacturing methods were not feasible for the slot inserts due to a lack of fixturing options, so they were 3D-printed from a temperature-resistant polymer with an operating temperature of up to 250 °C using a multi-jet printer (3D Systems ProJet 2500 Plus). The free mold design allowed all slot

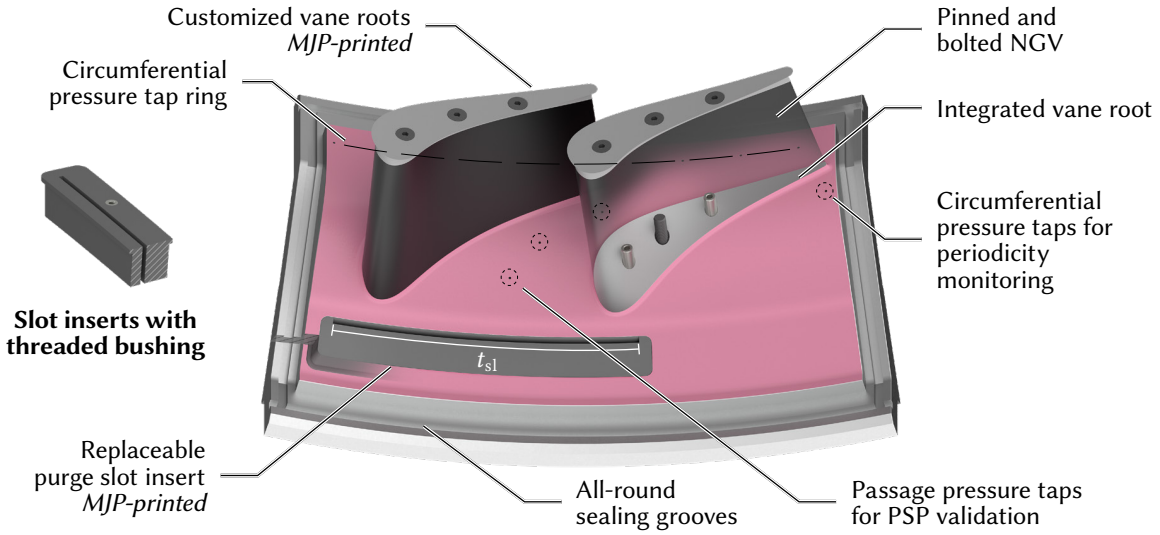

Figure 5.27: Central passage endwall with replaceable purge slot insert and PSP coating

inserts to be made in a single piece. Furthermore, the low thermal conductivity of $0.25\,\mathrm{W\,m^{-1}\,K^{-1}}$ leads to reduced heat dissipation to the coolant, which in turn lowers the measurement uncertainty of the heat transfer measurement campaign.

The inserts are placed into the endwall from the outside, with a circumferential step providing support in the radial direction. For easy removal, metal threaded bushings have been incorporated into the inserts. The optimal transition fit between the inserts and endwall cutout was achieved by iteratively adjusting the printing dimensions through a series of test prints.[12] As with the linear cascade, the circumferential length of the slot had to be limited for design reasons but also because of the restriction of the foreign gas supply, while with regard to periodicity, the slot should optimally extend over all passages. In the present case, the circumferential length of the slot t_{sl} was chosen to provide an overlap of 15 % into each of the adjacent passages, i.e., $t_{\mathrm{sl}}/t_{\mathrm{s}} = 1.3$.

5.5.4 Purge Slot Plenum

Earlier investigations at the slot outlet using a custom Pitot tube suggested that the plenum geometry of the linear cascade had a significant influence on the circumferential flow profile. However, conducting the measurement was difficult not only due to limited accessibility but also because the flow profile was considerably affected by the pressure field within the passage. Since CFD calculations, to be presented below, confirmed the findings of the measurement, the plenum design for the annular cascade was fundamentally revised. To evaluate the new design approach in comparison to the previous design without curvature influence, it was linearized for the CFD calculation.

Linear cascade plenum design: The plenum of the linear cascade was adapted from previous investigations by Müller et al. [9] on a linear cascade with cylindrical vanes and is shown in Figure 5.28. The four-part assembly is supplied with coolant via two push-in fittings. In the transition section, which is designed as a diffuser, the coolant is directed into the rectangular plenum after passing through a woven turbulence grid ($d = 0.4\,\mathrm{mm}$, $M = 1\,\mathrm{mm}$) enhancing the turbulent mixing. It then enters the interchangeable slot insert, which is kept in place by a clamping body integrated into the plenum assembly. The diffuser of the transition section has an outlet-to-inlet ratio of approximately 4.3 and an opening angle of 45° with respect to the center axis, thus considerably exceeding the recommendations of Mehta and Bradshaw [138].

The numerical model for evaluating the linear plenum design is explained in detail below since significant parts of the fluid volume and relevant boundary conditions correspond to the linearized geometry of the new design. Exemplary results of the calculation are shown in the right part of Figure 5.28 by means of the normalized velocity distribution on the center section plane for $BR = 1.0$. As expected, the flow separates as it enters the diffuser. The turbulence grid causes the two flow cones

12 In contrast to the original CAD model shown here, an additional circumferential sealing groove was integrated into the slot inserts to suppress parasitic flow from the plenum into the passage (see Figures C.11 and C.12).

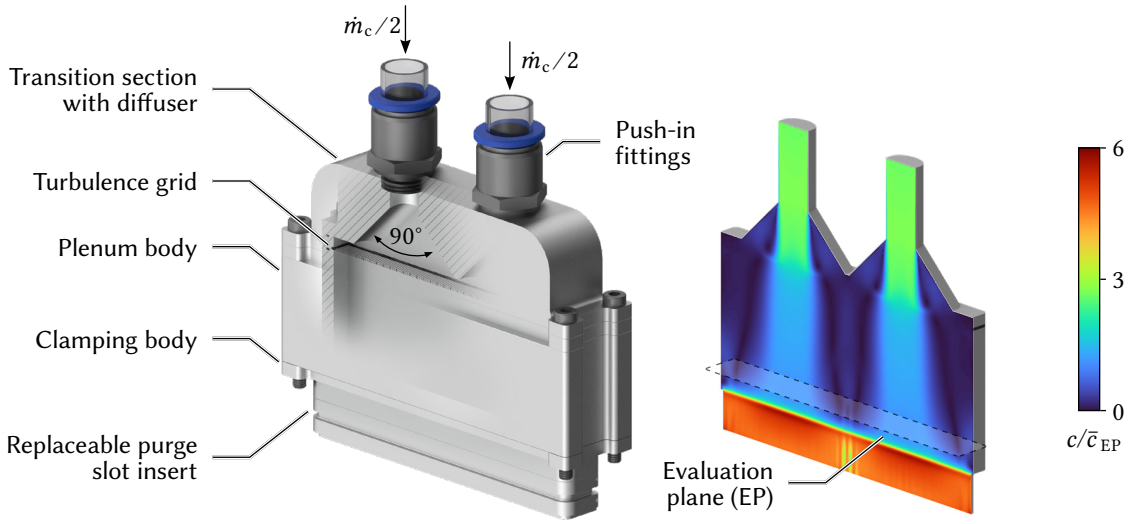

Figure 5.28: Purge slot plenum of linear cascade with numerically calculated velocity distribution ($BR = 1.0$)

to widen slightly, but complete mixing does not occur in the plenum. Instead, large recirculation zones emerge in the center and along the sides of the plenum body. As a result, the velocity distribution is clearly profiled when the coolant enters the slot. As expected, the flow is equalized within the perpendicular slot ($W = 2\,\text{mm}$) due to viscous and turbulent effects, but local streaks with significantly reduced flow velocity emerge from it and enter the main flow. It cannot be answered within the scope of this analysis whether the coolant streaks described in the previous Chapter are attributable to these effects or whether small surface defects at the edge of the slot outlet are the cause of it.

To suppress separation for all blowing ratios, the diffuser angle would have to be reduced to less than 7.5°. This would have increased the total height of the transition section from currently 35 mm to approximately 160 mm introducing severe manufacturing and handling challenges. Therefore, a new geometry was designed and put into practice.

Annular cascade plenum design: The new concept utilizes a porous polymer sleeve for a homogeneous feed to the plenum. The final design of this new approach is shown in Figure 5.29: The coolant enters the porous polyethylene sleeve, which is enclosed by a thin-walled lengthwise semi-open inner tube, through two opposing push-in fittings. The tube and sleeve are encased on both sides by a lid, which is screwed to the outer tube. The high pressure drop in the porous medium causes the coolant to be evenly discharged through the sleeve into the cavity between the inner and outer tubes. The coolant then flows along the inside of the outer tube and exits into the transition section, which is bonded to the slotted outer tube. To prevent the coolant from bypassing the porous sleeve, the inner assembly is sealed with a surface seal attached to the face of the sleeve and an O-ring fitted to the outside of the inner tube. A turbulence screen is installed after the cross-section expansion in the transition section, increasing the mixing in the plenum.

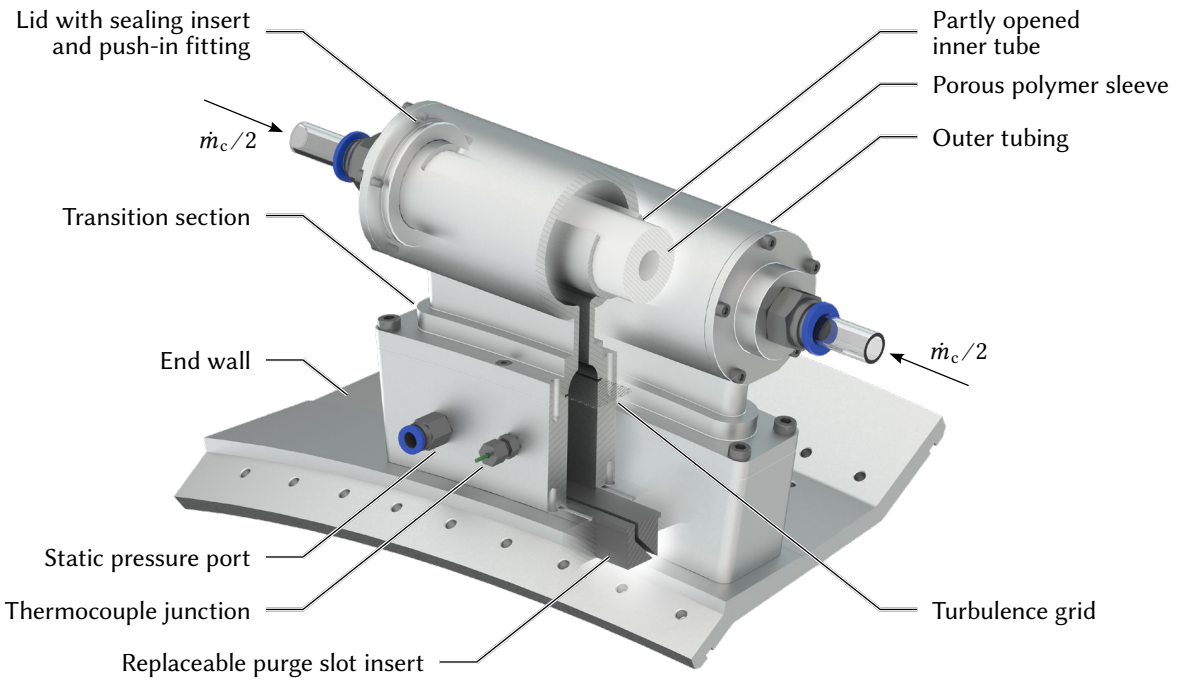

Figure 5.29: Purge slot plenum of the annular cascade

An O-ring integrated into the endwall seals the plenum-endwall contact surface while sealing between the plenum body and the transition section is provided by a surface seal. The slot insert is fixed by the plenum body, eliminating the need for a separate clamping body. Dual measurement accesses for pressure and temperature allow monitoring of the coolant flow parameters. The entire assembly, with all metal parts being made from aluminum, is bolted into the endwall with four screws and can therefore be quickly loosened for changing the slot insert. All parts are pinned together for clear positioning.

Numerical evaluation: For a numerical evaluation of both plenum designs, the flow was modeled using the domain depicted in Figure 5.30. As mentioned before, the annular plenum design was linearized for an unbiased comparison with the original design. Since the near-exit profile of the coolant flow is to be investigated and consequently should not be influenced by a boundary condition at the slot exit, the domain was extended by a main flow channel, with flow parameters similar to the passage inlet flow at the cascade operating point. All calculations were performed under steady-state conditions with the commercial solver ANSYS CFX (2019 R3).

The porous sleeve was assumed to be isotropic and integrated into the computational setup as an independent porous domain connected via porous-fluid interfaces with the inner and outer cavities. The model incorporates the Forchheimer equation where the pressure loss ΔP of a flow with an

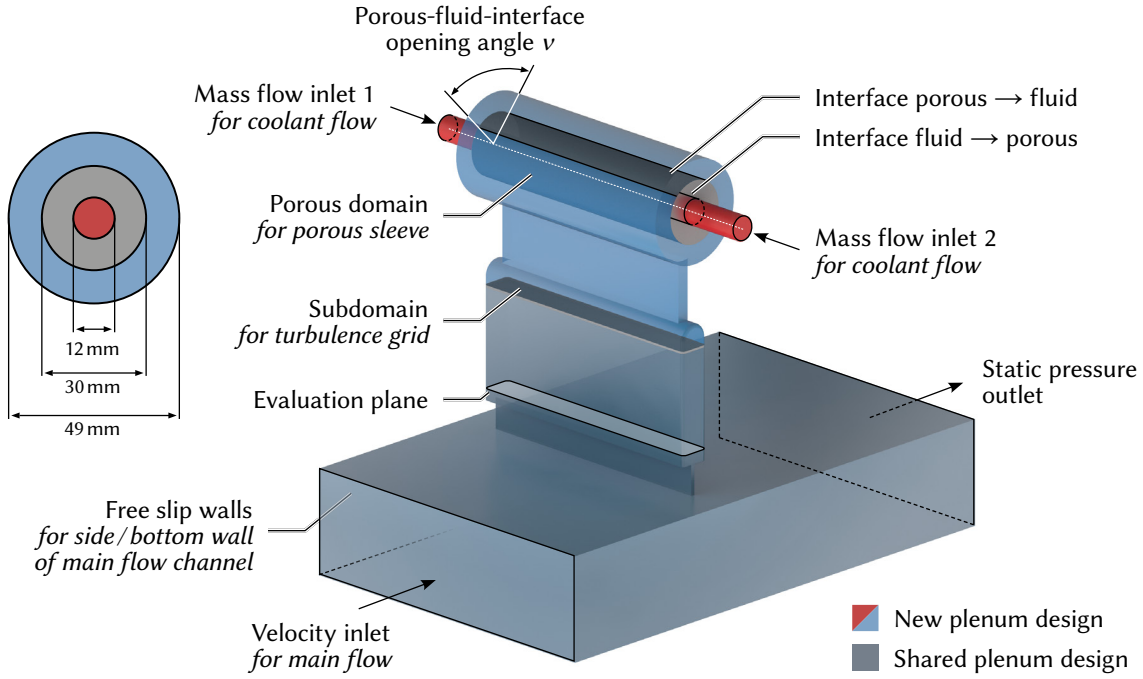

Figure 5.30: CFD domain of the linearized plenum design with porous sleeve

averaged fluid speed $\bar{c}_\mathrm{p}$ across a porous medium of the length l is described by [162]

$$-\frac{\Delta p}{l} = \frac{\mu}{k_1} \cdot \bar{c}_\mathrm{p} + k_2 \cdot \rho \cdot \bar{c}_\mathrm{p}^2 \tag{5.6}$$

with the permeability denoted as k_1 and the so-called non-Darcy flow coefficient denoted as k_2. While the first term, also known as Darcy's law and dominant at low Reynolds numbers, relates to the viscous resistance of the porous medium, the second term accounts for the flow resistance caused by the inertia of the fluid as it moves through the pores of the medium [163].

To reflect the influence of the turbulence grid, a subdomain (thickness 1 mm) with source terms for the pressure loss and turbulent kinetic energy was integrated according to Roach [139]. These and further main parameters of the calculation are summarized in the following Table 5.9.

To assess the homogeneity of the coolant flow in the plenum for all blowing ratios, the node-based velocity distribution on the evaluation plane drawn in Figure 5.30 was first interpolated to a regular grid. The evaluation plane was set 5 mm above the slot inlet, as an evaluation at the slot outlet would be biased by the mixing processes within the slot geometry, i.e., the findings could not be generalized to other slot geometries. To allow the results of all blowing ratio configurations to be aggregated, the velocity distribution was normalized with the respective mass flow average on the evaluation plane. The distribution of the free flow of each plenum configuration is then compared with regard to flow homogeneity using statistical measures such as the standard deviation $\overline{\sigma}$ and span $\overline{SP}$, both averaged over all blowing ratios.

Table 5.9: CFD setup for the analysis of the linearized plenum design

Parameter	Value	Parameter	Value
Viscous model	k-ω SST	$p_{\mathrm{m,out}}$	1.6 bar
Time	steady-state	BR	0.25 ... 1.5
Porous domain	see Table 5.11	β_{g}	0.51
c_{m}	25 m s^{-1}	k_{g}	1.44
Inlet turbulence	5 %	T_{in}	30 °C

The numerical investigation of the new plenum design was conducted for three different opening angles ν and three porous domain setups with increasing flow resistance (see Table 5.11), which reflects the commercial availability of porous sintered materials such as polyethylene, bronze, or stainless steel.

As the results of the CFD calculations should be independent of the mesh configuration, a mesh sensitivity study was conducted for three meshes of increasing node numbers. All meshes were generated using the ANSYS Meshing Tool (2019 R3). The multi-domain mesh consists of both tetrahedral and hexahedral elements, the latter one used for sweepable parts of the domain. The boundary layers in the fluid domains were resolved by a maximum number of 10 prism layers, with the first layer thickness being chosen according to the requirements of the k-ω SST turbulence model. For the sensitivity analysis, both integral and pointwise variables, namely the mass flow averaged pressure loss between the inlet and evaluation plane and the velocity at the center of the evaluation plane, were assessed. The setup and the results of the analysis are summarized in the following Table 5.10.

The analysis shows that the changes in the considered variables would already be tolerable from mesh 1 (coarse) to mesh 2 (medium). Further refinement reduces the percentage deviation to less than 1 %. For this reason, all further calculations were conducted with the medium mesh settings.

Table 5.10: Mesh sensitivity analysis for medium loss configuration with $\nu = 90°$ and $BR = 1$

Parameter	Mesh 1	Mesh 2	$\Delta_{2\text{-}1}$	Mesh 3	$\Delta_{3\text{-}2}$
No. of mesh nodes	1.44×10^5	3.79×10^6	162.3 %	7.52×10^6	98.3 %
y^+	< 5	< 3		< 3	
$\overline{p}_{\mathrm{s,in}} - \overline{p}_{\mathrm{EP}}$	100.2 mbar	102.0 mbar	1.8 %	102.6 mbar	0.6 %
$c_{\mathrm{EP,center}}$	5.439 m s^{-1}	5.497 m s^{-1}	1.1 %	5.490 m s^{-1}	−0.1 %

Table 5.11 compares the results of the three porous-domain variants with the design of the linear cascade (LIN) and a lossless setup, where the porous domain is replaced with a continuous fluid domain. The inhomogeneity of the LIN design, already visible in the velocity distribution in Figure 5.28, is also reflected in the statistical values: The local velocity scatters on average by 25 % around the reference value and spans a range of almost 77 % relative to the normalized average value.

Table 5.11: Influence of porous domain settings for $\nu = 90°$

Parameter	LIN	Lossless	Low loss	Med loss	High loss
Porosity β /%	-	-	60	50	40
Permeability k_1 /m^2	-	-	250×10^{-12}	50×10^{-12}	5×10^{-12}
Non-Darcy flow coefficient k_2 /m^{-1}	-	-	0.2×10^6	1×10^6	10×10^6
Pressure loss ΔP at $BR = 1.0$ /mbar	-	2.2	19.5	102	826.2
$\overline{\sigma}\left(c_{EP,lat}/\bar{c}_{EP}\right)$	0.247	0.061	0.035	0.036	0.039
$\overline{SP}\left(c_{EP,lat}/\bar{c}_{EP}\right)$	0.769	0.248	0.153	0.167	0.168

All porous configurations perform significantly better than the old plenum design, as the standard deviation drops to as low as 0.035 for the low-loss sleeve. The span is lowered to approximately 15 % relative to the normalized average value. The differences between the porous variants are marginal, with the low-loss configuration yielding the best results. The comparison with the lossless variant shows that the absence of the sleeve worsens the homogeneity of the flow. The improvement is, therefore, not solely attributable to the new plenum geometry, although even the lossless design performs considerably better than the old plenum design. The choice of the porous sleeve should therefore be based on the associated pressure drop as well as on commercial availability.[13]

The influence of the opening angle ν is depicted in Table 5.12: The aforementioned also applies here: A smaller opening angle ν reduces the effective flow cross-section of the porous sleeve and thus increases the average flow velocity u. As a result, the pressure loss according to equation 5.6 increases significantly for smaller opening angles. However, this is not associated with an improvement in homogeneity. On the contrary, the variant with $\nu = 90°$ performs best, therefore being adopted for the final design of the annular plenum. Again, the aforementioned applies: The differences between the individual porous setups are marginal compared to the improvement over the design of the linear cascade.

The plenum design must ensure a uniform feeding of the slot independent of the coolant mass flow. Complementing the aggregated evaluation of the different setups, Figure 5.31 shows the normalized velocity distribution of the final geometry for three blowing ratios. The depiction of the central

13 In the present case, a polyethylene sleeve is used that was provided free of charge. Unfortunately, the manufacturer does not provide data on permeability and the non-Darcy flow coefficient. However, own measurements of the fitted sleeve have shown that with a pressure loss of approximately 80 mbar at $BR = 1$, the sleeve can be classified between the low-loss and medium-loss variants.

Table 5.12: Influence of opening angle ν for medium loss configuration

Parameter	**LIN**	$\nu = 30°$	$\nu = 60°$	$\nu = 90°$
Pressure loss ΔP at $BR = 1.0$ /mbar	-	232.1	141.7	102
$\overline{\sigma}\,(c_{EP,lat}/\bar{c}_{EP})$	0.247	0.037	0.044	0.036
$\overline{SP}\,(c_{EP,lat}/\bar{c}_{EP})$	0.769	0.177	0.179	0.167

section plane is supplemented by an additional plane that intersects the tubes in the radial direction. There are no noteworthy differences between the various blowing ratios. Owing to the constructively conditioned step at the junction between the outer tube and the transition section, streaks of reduced flow velocity with slightly different characteristics arise and propagate into the lateral areas of the plenum. In addition, the figure also illustrates the purpose of the two-sided coolant supply: The mutual stagnation effect causes the kinetic energy of the two streams to be converted symmetrically to the center of the sleeve. This results in a symmetrical flow through the sleeve, which would not have been possible with a single-sided supply.

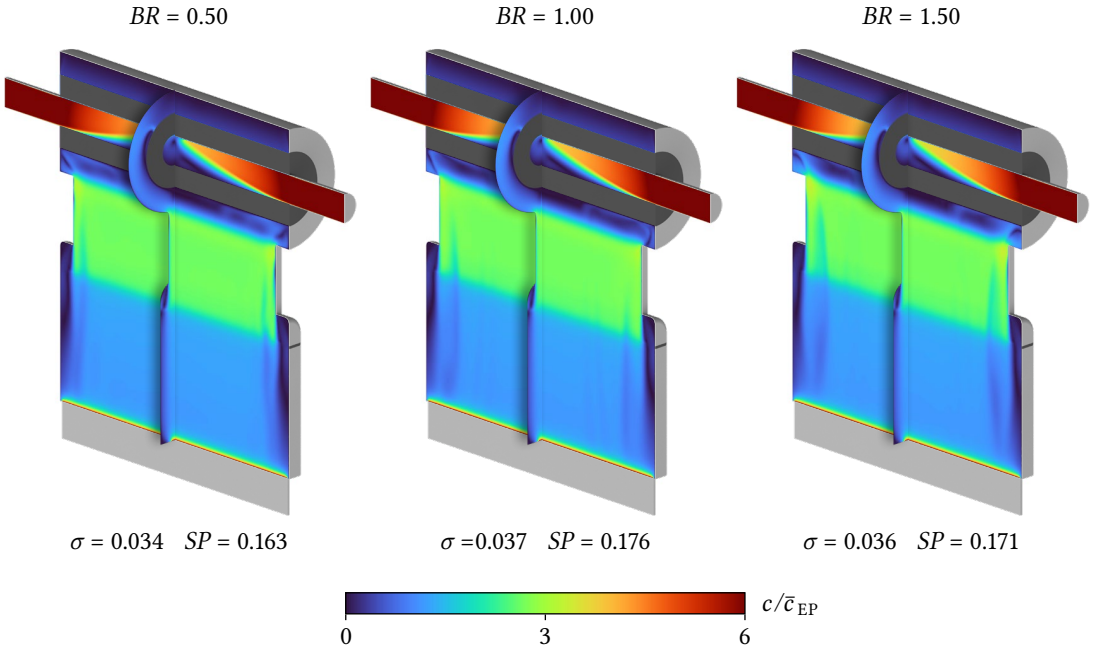

Figure 5.31: Normalized plenum velocity distribution for final parameter setup with $\gamma = 90°$

5.5.5 Central Passage Endwall for Heat Transfer Measurements

Based on the experience with the linear measurement module, the annular measurement module for heat transfer measurements was fundamentally revised. As already explained in section 4.8, the new design must be leak-proof even at high cooling water flow rates and provide at least one reliable reference point for temperature calibration of the IR camera. Furthermore, parasitic heat fluxes, e.g., fluxes from respectively into the slot insert altering the coolant temperature downstream of the measurement location, must be minimized.

During the process of redesign, the use of an electric heating solution, e.g., in the form of heating foil or heating cartridges, was also considered. Although this approach has been taken by some authors such as Werschnik et al. [164], it was rejected for several reasons: First, electric heating implies the reversal of the heat flow, limiting the operational bandwidth of the test setup ($DR \leq 1$). Secondly, surface heating elements are clearly inferior in terms of power density[14] as Kapton or silicone heating foils are usually limited to $0.8\,\mathrm{W\,cm^{-2}}$. For comparison, the cooling water setup presented in the following section provides a specific cooling power of more than $4\,\mathrm{W\,cm^{-2}}$ allowing higher temperature differences between the flow-facing side and the bottom of the auxiliary wall to be realized under steady-state conditions. In addition, different heat flow configurations can be implemented with a tempering liquid since the measuring module can operate in cooling as well as in heating mode. Cartridge heaters are able to produce more heat per unit area than heating foils, but the heat output is, by principle, very local, resulting in an inhomogeneous temperature distribution in the base body.

Design overview: Figure 5.32 illustrates the design of the annular heat transfer measurement module. To satisfy the above-mentioned requirements, i.e., to reduce the measurement uncertainty, the tempered base body and, thus, the measuring area were reduced in size. They extend from the passage entrance to the passage exit. By structurally separating the slot insert and the tempered base body, one source of possible leakage and parasitic heat fluxes into the slot insert was eliminated.

The design of the annular measurement module adopts some characteristics of the linear measurement module: While the endwall is made of stainless steel to reduce parasitic heat fluxes, the cooled base body is fabricated from copper to facilitate a homogeneous temperature distribution. The flow-facing surface of the endwall is covered with an ETFE coating (final thickness 0.5 mm), both serving as an auxiliary wall for the measurement insert and isolating the stainless steel endwall for a further reduction of parasitic heat fluxes. After coating, the assembly is over-milled to ensure a constant coating thickness and a seamless surface.

On account of the simplified geometry, the base plate is inserted into a milled pocket of the endwall and can be sealed with a single circumferential sealing cord. Two M8 mounting holes, also serving as measuring points for temperature monitoring, allow high surface pressure between the seal and the sealing surface so that leak proofing is ensured even at high cooling water flow rates. A surrounding

14 Refer for example to https://freek-heaters.com/products/flexible-heaters/kapton-polyimide-heaters/

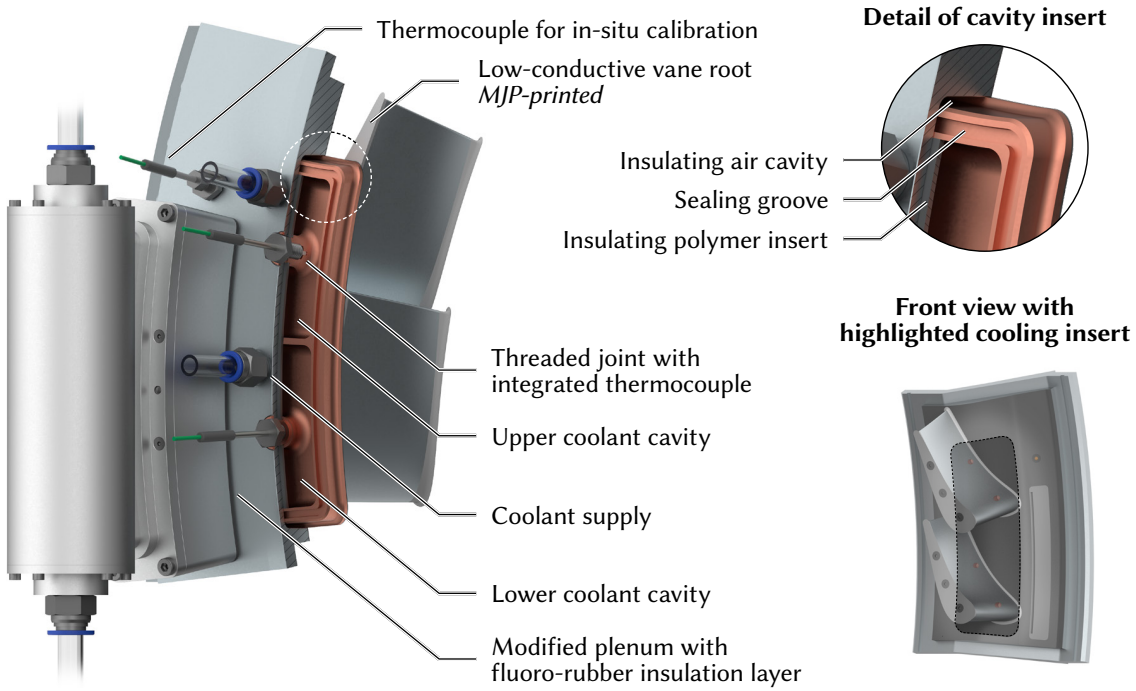

Figure 5.32: Heat transfer measurement module for the annular cascade

air cavity reduces the heat exchange between the base plate and the endwall. The cooling cavity is split into two sections, facilitating flow guidance and, thus, preventing the emergence of recirculation zones. To minimize the heat transfer between the cavity and the surrounding endwall, each cavity is equipped with a polymer insert that is supported by a step around the mounting hole.

The temperature calibration point for the IR camera was placed above the slot insert. To prevent the open measuring tip of the thermocouple from being exposed to a large radial temperature gradient, the metal endwall is not coated at the elevated piercing point. For better heat conduction, the measuring tip is encapsulated with highly conductive epoxy (Omega CC High Temperature Cement). After assembly, the entire endwall is painted with a thin coating to achieve a defined emissivity. Here, the Nextel Velvet Coating 811-21, for which detailed emissivity measurements are available [129], has proven itself in the field of IR thermography.

According to the manufacturer, the production of a curved zinc sulfide IR window with the size of the optical access (see Figure 5.19) is not economically feasible. For this reason, the solution shown in Figure 5.33 was developed, which follows the work of Gazzini [165]. Although inserting planar windows into the annular end wall will inevitably affect the flow, the influence should be limited to the near-hub area and, therefore, negligible.

The borosilicate window of the film cooling effectiveness measurements is replaced by an aluminum base frame in which multiple round zinc sulfide windows of different diameters but with the same thickness, i.e., with the same transmission characteristics, are inserted. The windows are positioned

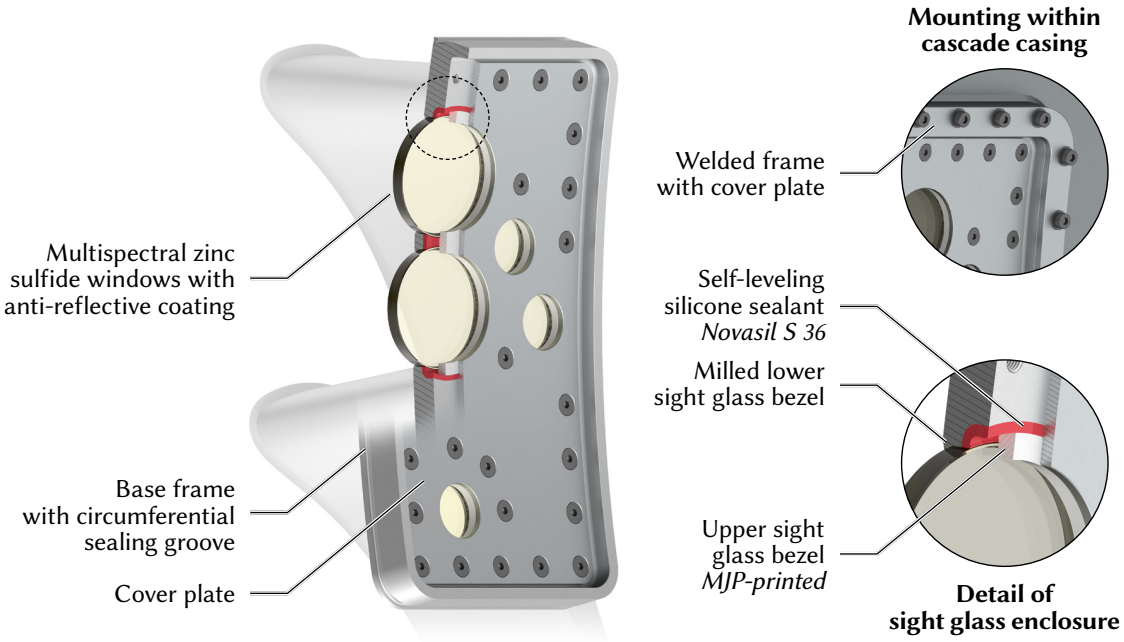

Figure 5.33: Optical access for IR thermography

such that the entire tempered endwall can be captured over a series of IR images. Another window at the level of passage P+1 ensures optical access to the temperature reference measuring point. While the windows are supported internally on a tapered step in the base frame, they are enclosed externally with 3D-printed polymer bezels allowing the entire assembly to be held in place with one continuous cover plate. To seal the windows, the cavity between the base plate and the bezel is filled with a self-leveling high-temperature silicone (Novasil S 36).

Numerical optimization: To assess the temperature distribution and to optimize the cooling water supply, a Conjugate Heat Transfer (CHT) analysis was performed, which considers both thermal conduction in the solid and convection in the fluid as well as the heat exchange between both entities. In this procedure, the problem is solved by using a calculation domain that includes both the fluid and solid regions, with the outer surface of the solid wall coinciding with the boundary of the fluid domain [166]. The domain is shown in Figure 5.34: The geometry of the base body has been slightly simplified by omitting the sealing groove and the mounting holes. It was also assumed that the narrow contact surfaces between the base body and the endwall are adiabatic. Also considered adiabatic were the parts of the base body facing the air cavity and the contact zone between the ETFE coating and the vane root. Since the powder coating is firmly and non-porously bonded to the mechanically pretreated surface of the base body, it was assumed that the thermal contact resistance at the solid-solid interface is negligible. To reflect the strong increase of the heat transfer coefficient of the main flow in the axial direction, a function $f(x_{s,ax})$ has been implemented, which approximates the distribution based on

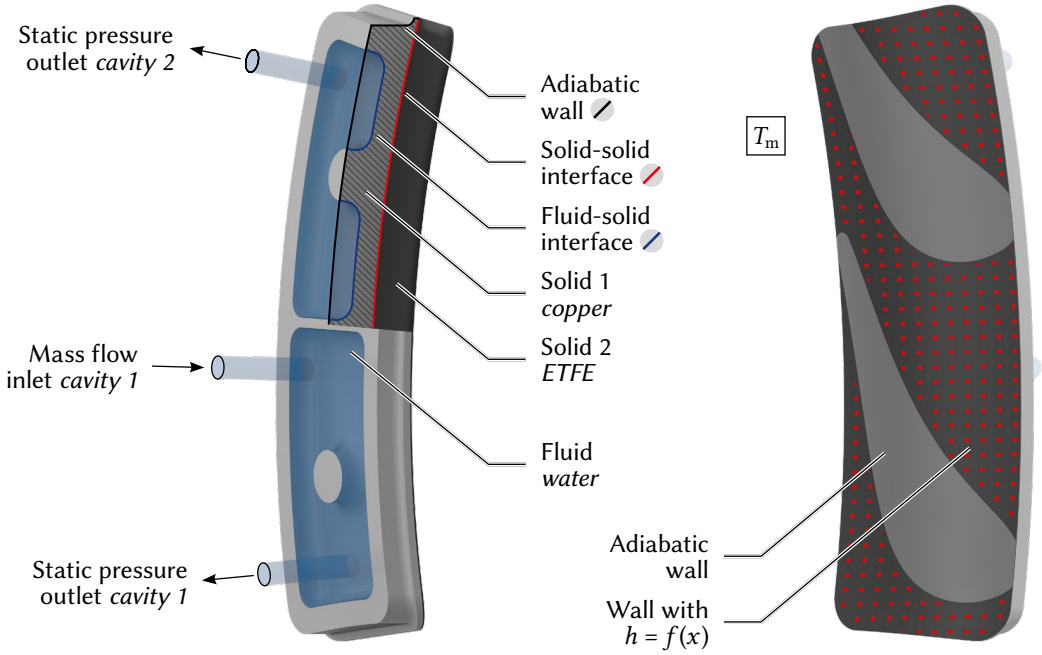

Figure 5.34: CHT domain of the simplified annular heat transfer measurement module

a numerical investigation conducted at the institute. The k-ω SST turbulence model was selected to model the turbulent flow behavior in the two cooling cavities. All calculations were performed under steady-state conditions with the commercial solver ANSYS CFX (2019 R3). Table 5.13 summarizes the boundary conditions of the analysis.

Table 5.13: CHT setup for the analysis of the annular heat transfer measurement module

Parameter	Value	Parameter	Value
Viscous model	k-ω SST	h_0	$f(x_{s,ax})$[15]
Time	steady-state	T_m	90 °C
$\dot{m}_{cl}$ per cavity	0.05 ... 0.2 kg s^{-1}	$T_{cl,in}$	10 °C
Inlet turbulence	5 %	κ_{Cu}	401 W m^{-1} K^{-1}
$p_{s,out}$	1.5 bar	κ_{ETFE}	0.25 W m^{-1} K^{-1}

15 The lateral distribution of h_0 was approximated by the following function based on CFD calculations, which were carried out as part of a student project: $-801.3\,\mathrm{W\,m^{-2}\,K^{-1}} \cdot x_{s,ax}^3 + 1172\,\mathrm{W\,m^{-2}\,K^{-1}} \cdot x_{s,ax}^2 - 42.74\,\mathrm{W\,m^{-2}\,K^{-1}} \cdot x_{s,ax} + 122.6\,\mathrm{W\,m^{-2}\,K^{-1}}$

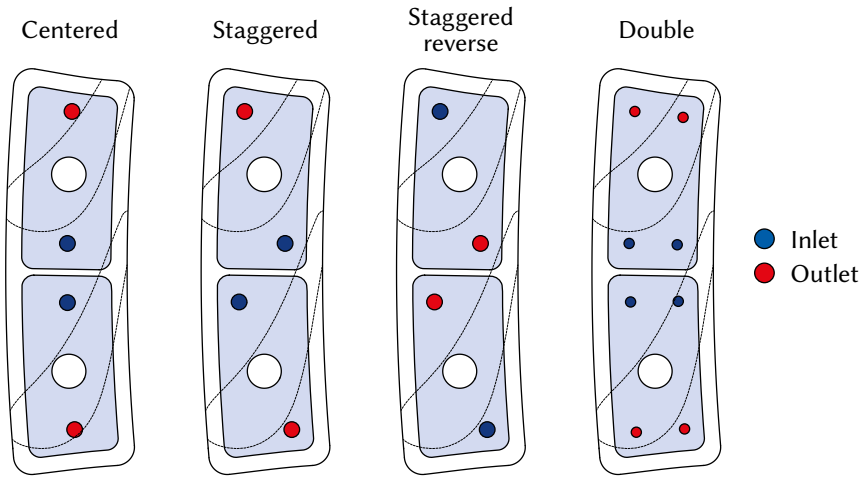

Figure 5.35: Investigated cooling variants for the evaluation of the heat transfer measurement module

For optimizing the cooling water supply based on the given base plate geometry, four variants were investigated, which differed in terms of the position and number of cooling water inlets and outlets, as shown schematically in Figure 5.35. Since this numerical investigation is to be performed in light of the requirements and assumptions underlying the heat transfer measurement campaign, the focus of the evaluation is on the homogeneity of the temperature distribution on the back side of the coating.

To ensure mesh independence, a sensitivity study was conducted for the staggered configuration with three meshes of increasing node numbers. The mesh specifications and results of this study are depicted in Table 5.14. While the coarse mesh utilizes the implemented wall functions of the turbulence model for the representation of the viscous sublayer and buffer layer region, the boundary layer was fully resolved with the medium and fine mesh. The mesh sensitivity was evaluated using the same quantities that are applied to assess the different cooling configurations, namely the average temperature difference between the water inlet temperature and the solid-solid-interface, i.e., the back of the coating, as well as the temperature span that occurs at this interface. It can be seen that the first mesh refinement is accompanied by a significant decrease in the considered quantities. The

Table 5.14: Mesh sensitivity analysis for staggered configuration with $\dot{m}_{\mathrm{cl}} = 0.15\,\mathrm{kg\,s^{-1}}$

Parameter	**Mesh 1**	**Mesh 2**	$\Delta_{2\text{-}1}$	**Mesh 3**	$\Delta_{3\text{-}2}$
No. of cavity mesh nodes	3.36×10^5	1.52×10^6	351 %	7.1×10^6	368 %
y^+	> 30	< 1		< 1	
$\overline{T}_{\mathrm{S\text{-}S}} - T_{\mathrm{cl,in}}$	0.93 K	0.84 K	−10 %	0.82 K	−1.5 %
$T_{\mathrm{S\text{-}S,max}} - T_{\mathrm{S\text{-}S,min}}$	1.2 K	0.98 K	−17.8 %	1.02 K	3.6 %

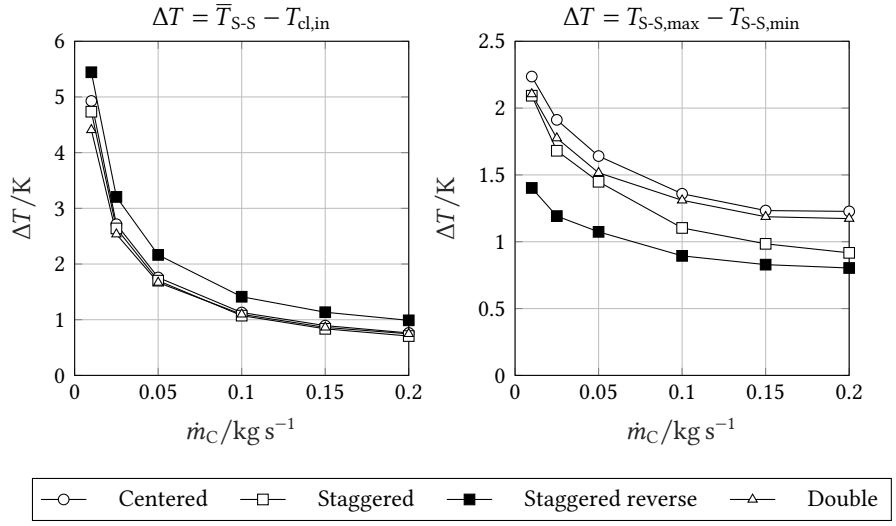

Figure 5.36: Comparison of the heat transfer measurement module variants

deviations in the results are largely caused by the fact that the temperature gradient in the viscous sublayer, which governs convective heat transfer, can only be approximated by the wall function. Further refinement entails only minor changes, especially for the averaged quantity. With respect to the accuracy required for the estimation of the cooling performance, the medium mesh thus yields sufficiently accurate results.

Figure 5.36 presents the aforementioned quantities as a function of the cooling water mass flow rate for the four cooling configurations. First of all, it is noticeable that both the averaged temperature difference and the temperature span converge asymptotically to a limiting value with increasing mass flow. The convergence against a value $> 0\,\text{K}$ is not surprising since the presence of a heat flow from the main flow via the solids into the cooling water is inevitably linked to the existence of a temperature gradient. Only in the adiabatic case, these differences would disappear. Cooling mass flows below $0.05\,\text{kg s}^{-1}$ cause these temperature differences to reach a level at which the assumption of a homogeneous temperature distribution with respect to measurement uncertainty cannot be maintained. This shall be illustrated by the example of the staggered variant: The average temperature difference between the upper and lower side of the coating is 26.1 K for $\dot{m}_{\text{cl}} = 0.01\,\text{kg s}^{-1}$ and 27.6 K for $\dot{m}_{\text{cl}} = 0.2\,\text{kg s}^{-1}$, respectively. While the error in the calculation of the local heat flux is thus about 4 % for the lowest mass flow rate, it decreases to 1.7 % for the highest mass flow rate.

When comparing the different variants, there are only small variations in the average temperature differences, with reversed staggered variant performing slightly worse than the rest. On the other hand, when considering the temperature span, this variant achieves the best results. However, at high mass flow rates, the staggered variant performs very similarly and is therefore chosen for the final configuration. For this setup, the distribution $\Delta T = T - T_{\text{cl,in}}$ at the solid-solid interface is shown in Figure 5.37: At the lowest cooling mass flow rate, the temperature difference increases significantly in the downstream part of the passage, i.e., where the highest convective heat transfer prevails. The

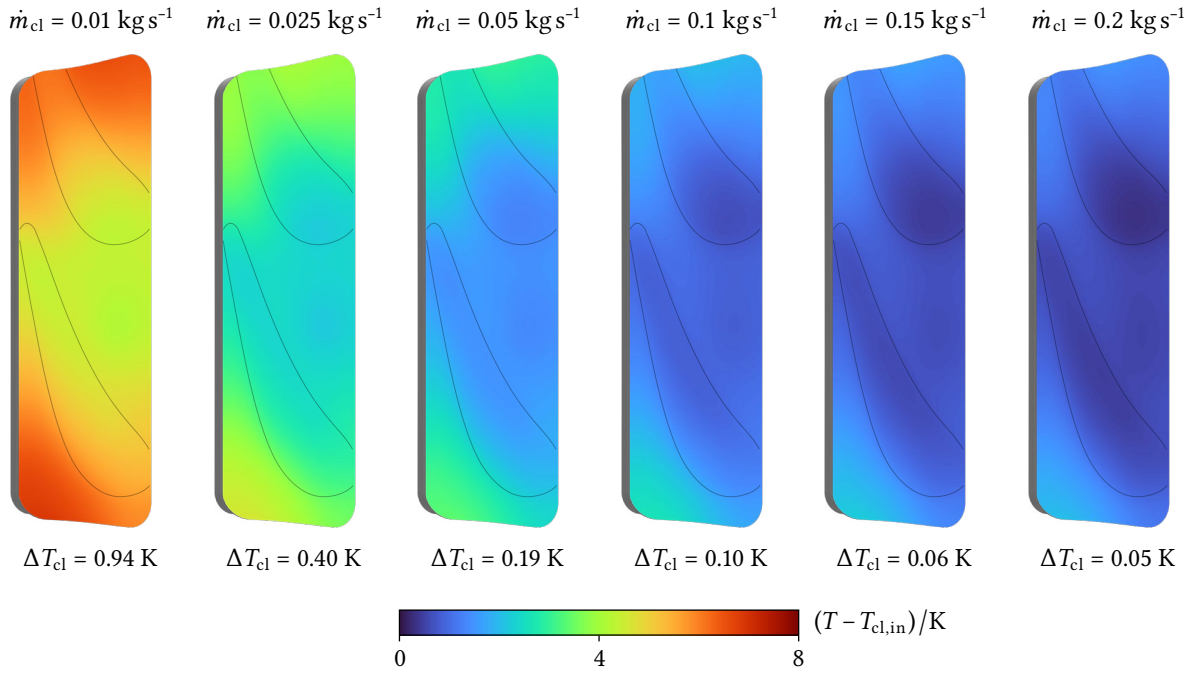

Figure 5.37: Temperature distribution of the solid-solid interface for the staggered variant

largest temperature differences occur in the adjacent passages due to their relative distance to the cooling water inlets. Although these patterns persist for higher cooling mass flows, the absolute local temperature differences are significantly lower. The leveling of local differences is also facilitated by the fact that the cooling water heats up to a lesser extent at higher mass flows, providing full cooling power at the outlet areas. The amount of heat dissipated via the cooling water remains approximately constant, as the heat flux is limited primarily by the isolation effect of the ETFE coating.

5.5.6 Five-Hole Probe Traversing

To measure the flow field at the entrance and exit of the passage, it is necessary to traverse the five-hole probes independently and with repeatable accuracy in both the axial and the circumferential direction. In addition to the kinematic requirements, the adjustment unit must seal the probe passage in the cascade casing and include features that protect the probe from being destroyed by accidental wall contact.

The probe traverse of the annular cascade consists of two units, shown in Figure 5.38. The radial unit provides a linear probe adjustment in the radial direction using a trapezoidal thread spindle which is driven by a stepper motor. The circumferential unit allows the probe to be adjusted on a circular path by means of an annular gear rack which is actuated by a spur gear. While the design of the radial adjustment unit follows the basic approach already implemented for the linear cascade by Franze [8], the circumferential adjustment had to be developed from scratch. However, the new design

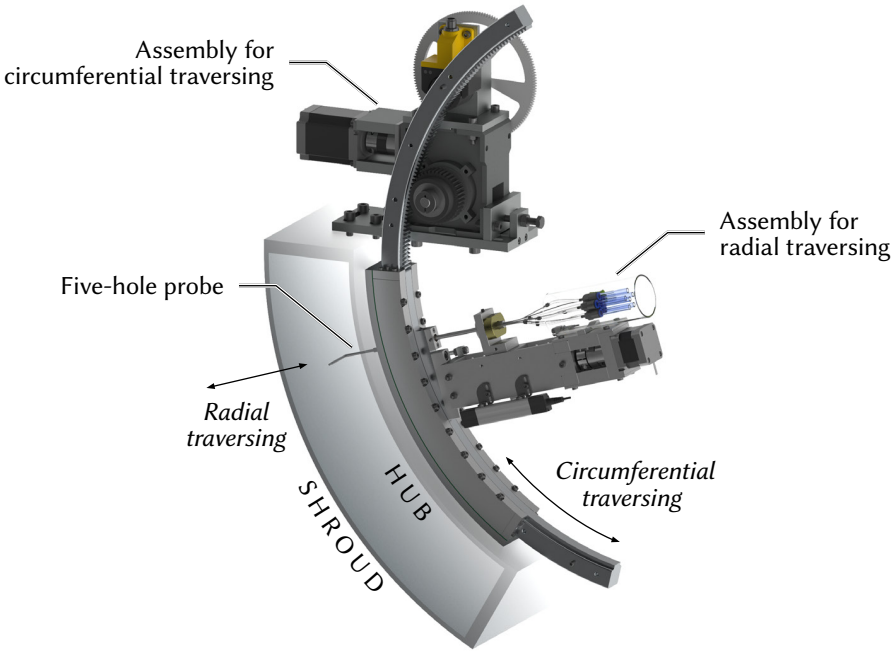

Figure 5.38: Radial and circumferential traversing units for five-hole probe field measurements

incorporates previously existing components like sensors and motors due to budget restrictions. In this context, a design was developed at the institute as part of a preliminary study, but its transferability to the new test rig was limited because the probe access was situated on the shroud but not on the hub.

Circumferential probe traversing: The centerpiece of the circumferential probe adjustment is the annular gear rack, which is guided by an assembly that is designed as a sliding guide, shown in Figure 5.39. The sliding guide consists of two identical cheeks that are bolted with the welded mounting support and enclose the gear rack. To reduce the sliding friction resistance, the internal contact surfaces of the cheeks are coated with Teflon. These narrow contact surfaces simultaneously provide a sealing function, as the rack is pressed onto the Teflon coating during operation by the pressure applied to the bottom surface. While the cheeks and covers are made from cast aluminum (EN AW 5083) due to the high demands on shape retention during the milling process, the rack is manufactured from stainless steel (1.4307/AISI 304L) for the strength of the gear teeth. To seal the rack at the two ends of the guiding cheeks and stiffen the assembly, covers with an integrated Teflon sealing package enclosing the rack are screwed onto both sides. A gasket between the mounting support, cheeks, and covers provides further sealing.

The assembly for radial adjustment of the probe is screwed onto the flat mounting platform of the rack. For sealing and guiding the probe, the rack is fitted with a fixture containing a custom-made bearing shell and a radial shaft seal, both split for easy assembly. Since the angle sensor of the driving unit does not ensure reliable absolute positioning – the gear parts can shift relative to each other

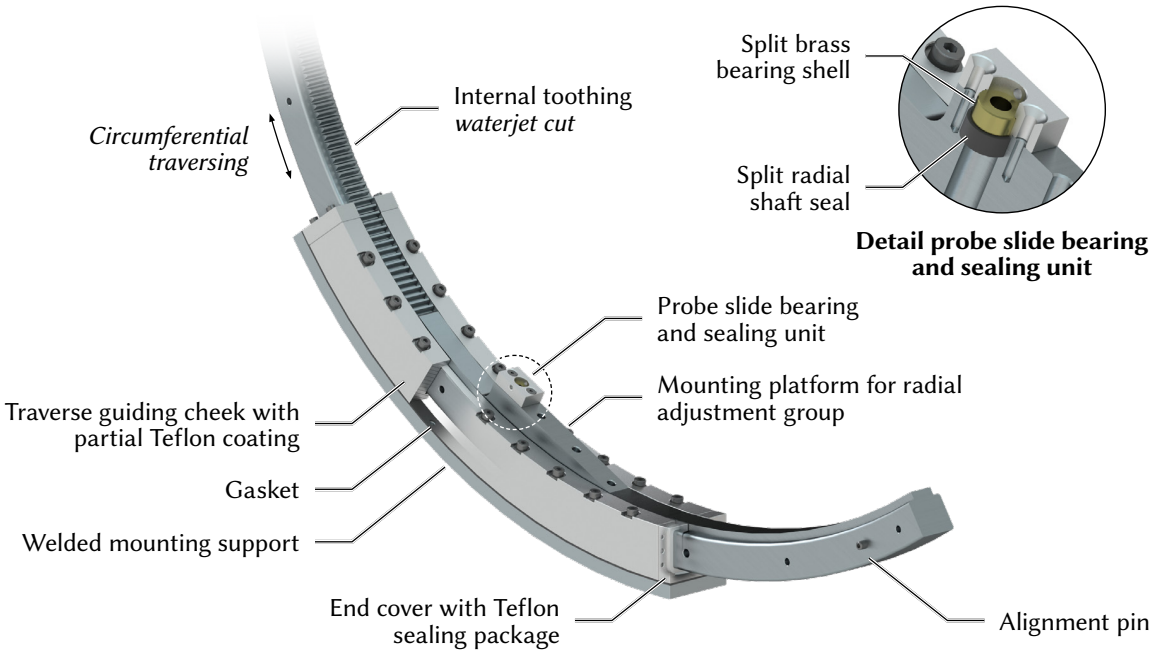

Figure 5.39: Guiding and sealing unit of the circumferential probe traversing

during assembly work – alignment pins for setting the absolute position were integrated into the rack. At the same time, the pins serve as a circumferential safeguard to mechanically block the movement of the probes outside the valid range in the event of sensor and software errors.

Manufacturing of the annular gear rack: There are a variety of manufacturing and finishing processes to produce internal gearing. For high geometric precision, internal gears are typically machined using a broaching process: This manufacturing method involves pushing and pulling a multi-toothed tool over the surface of the gear blank, which removes metal and creates the desired gear tooth shape. Since these processes require the fabrication of proprietary tools and the use of specialized machines, they tend to be expensive and are, therefore, mainly suitable for large-scale production [167]. A cost-effective alternative to classic manufacturing processes and particularly suitable for the production of prototypes is abrasive waterjet cutting, which was already utilized for the manufacturing of flanges and other parts of the test rig.

Regarding the requirements of the annular gear rack, the advantage of this process is that neither thermal energy nor mechanical stress is introduced into the component during the cutting process. The risk of component warpage, which would render the gear rack unusable due to the tight tolerances, is thereby substantially reduced. After successfully testing this method for manufacturing the gear teeth on a shortened demonstrator with the same module and inner radius, the racks were manufactured in a multi-stage process from a hot rolled stainless steel plate of 30 mm thickness. The waterjet cutter was operated with a water pressure of 3600 bar, with the opening diameter of the nozzle being 0.3 mm.

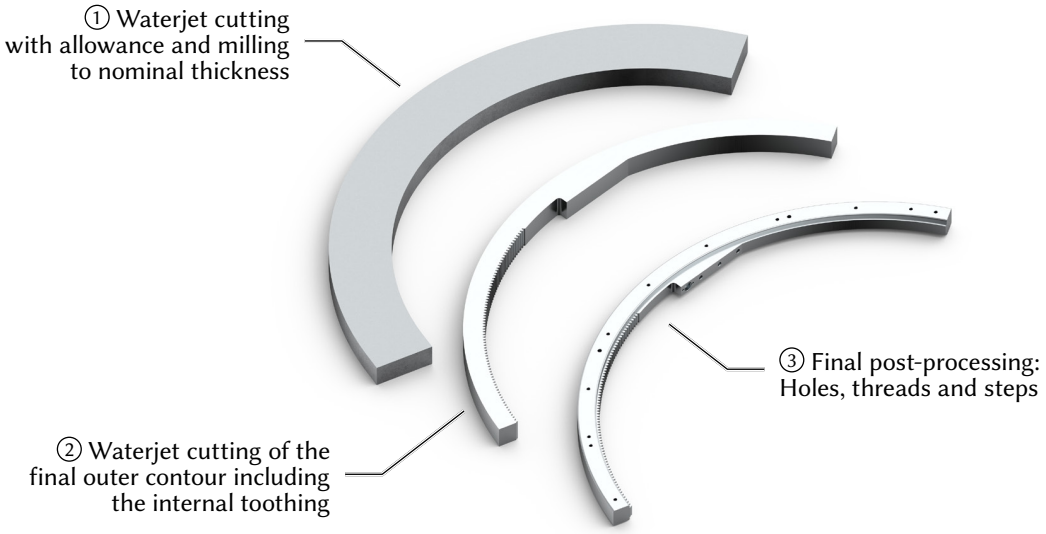

Figure 5.40: Manufacturing steps of the annular gear rack

To ensure the shape retention of the rack during manufacturing, the fabrication process was carried out in the steps illustrated in Figure 5.40: After the blank was separated by waterjet cutting from the plate and face milled from both sides to the nominal thickness of the gear rack, the final outer contour including the internal toothing was then cut out. This was followed by the final machining operation to insert the bores, threads, and steps. To improve the friction properties within the Teflon sealing package, the bottom side was honed with a face milling cutter.

Circumferential drive unit: The drive unit of the circumferential probe traversing is depicted in Figure 5.41. The annular gear rack is actuated by a spur gear flange-mounted on the output shaft of a worm gearbox. This, in turn, is connected with a stepper motor via an elastomer coupling to flatten peak loads and increase the misalignment tolerance. To measure the circumferential position, a further gear is flanged to the worm gear on the opposite shaft end, transmitting the angular displacement to an inductive angle sensor (Turck RI360P1). The entire assembly is attached to the bottom plate of the cascade casing. The mounting plate has a linear guide that can be used to position the worm gearbox and thus adjust the clearance between the gear and the rack. The specifications and parameters of the drive unit are summarized in the following Table 5.15.

The main driving gear is made from polyamide and has a steel core, allowing a high-strength shaft-hub connection, while the low-friction polyamide toothing reduces wear on the internal teeth of the annular gear rack and can be operated without lubrication. The need for a worm gearbox derives mainly from the mismatch between the maximum torque $M_{\mathrm{M,max}}$ provided by the stepper motor and the force F_{R} required to overcome the friction resistance between the rack and the guiding and sealing unit. Assuming the operating conditions from Table 5.7, the maximum torque, which is acting on

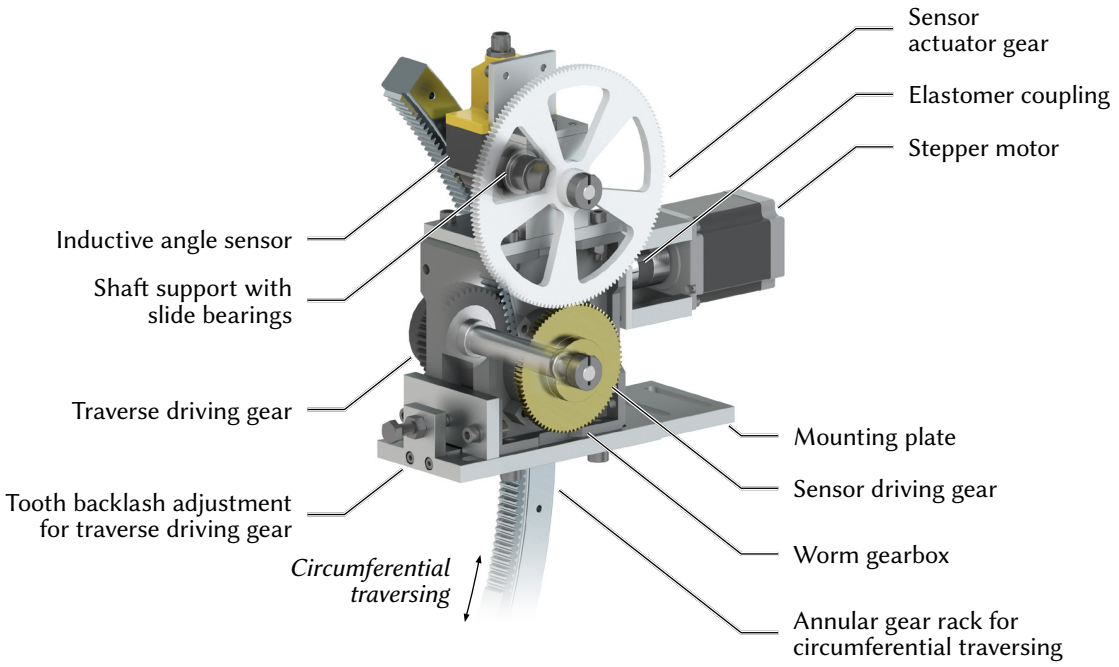

Figure 5.41: Drive unit of the circumferential probe traversing

the stepper motor, can be estimated by

$$M_S = \overbrace{\underbrace{p_{s,in} \cdot A_R \cdot \mu_R \cdot s}_{M_T \approx 1.4\,\mathrm{Nm}} \cdot \frac{d_T}{2}}^{F_R \approx 47\,\mathrm{N}} \cdot \frac{1}{\tau_W} \cdot \frac{1}{\eta_W} \approx 0.08\,\mathrm{Nm}. \tag{5.7}$$

The area A_R describes the inner surface of the gear rack that is exposed to static pressure $p_{s,in}$ during operation. The friction coefficient μ_R between the rack and the PTFE inlays of the guiding and sealing unit was assumed to be 0.05 according to Celis et al. [168]. With a safety factor of $s = 2$, the effective torques are not expected to exceed any of the above-mentioned component specifications.

The actuation of the existing angle sensors via an additional gear pair emerged from the demand to map the traversing range φ_R to the full measuring span of the sensor φ_S for reducing the angular error. The transmission ratios were therefore selected so that

$$\frac{d_S}{d_A} \approx \frac{d_T}{d_R} \cdot \frac{\varphi_S}{\varphi_R}. \tag{5.8}$$

Even though gears with involute toothing can, in principle, be mated without backlash, it actually does due to tolerances in manufacturing and installation [169]. Since backlash is usually proportional to the module, the module of the virtually torque-free angular sensor gear pair was reduced to 1 mm.

Table 5.15: Specifications of the circumferential drive unit

Parameter	Part	Symbol	Value
Module	Traverse driving gear	m_T	1.5 mm
Module	Sensor driving gear	m_S	1 mm
Reference diameter	Traverse driving gear	d_T	60 mm
Reference diameter	Annular gear rack	d_R	684 mm
Reference diameter	Sensor driving gear	d_S	80 mm
Reference diameter	Sensor actuator gear	d_A	150 mm
Transmission ratio	Worm gearbox	τ_W	25
Efficiency	Worm gearbox	η_W	0.69
Circumferential traversing range	Annular gear rack	φ_R	60°
Sensor span	Angle sensor	φ_S	360°
Allowable torque	Traverse driving gear	$M_{T,max}$	6.3 Nm
Allowable torque	Worm gearbox	$M_{W,max}$	21 Nm
Maximum torque	Stepper motor	$M_{M,max}$	0.13 Nm

The output-side spur gear was 3D-printed from plastic since gears with the required number of teeth were not available prefabricated. In addition, the pairing of brass and plastic allows the gears to be engaged closely and, thus, with as little backlash as possible.

Radial probe traversing: Figure 5.42 depicts the radial probe traversing unit: The probe is adjusted in the radial direction by means of a trapezoidal thread spindle (TR 12 × 3) which is driven by a stepper motor (Nanotec NEMA 17) with a maximum torque of 0.25 Nm. While the probe carriage containing the low-friction brass nut is guided by two parallel shafts, the spindle is supported in the casing by a locating-floating ball bearing arrangement. An elastomer coupling between the stepper motor and the shaft end of the spindle provides a high misalignment tolerance. Trapezoidal screw drives are inexpensive, have compact dimensions, and are also self-locking, so unintentional adjustment of the probe in the unpowered state of the stepper motor can be ruled out [161]. However, unlike the precise but considerably more expensive ball screws, they are affected by a backlash, so a magnetic position sensor (Sick MPA) is integrated into the traversing unit to precisely position the probe, with the magnet being attached at the bottom of the probe carriage and the sensor unit being mounted to one side panel.

Since a failure of the sensor or a glitch in the software-based probe control cannot be ruled out during operation, inductive proximity sensors (Autosen AI811) were integrated as a fail-safe, which interrupts the circuit of the stepper motor in case of proximity contact with the screw attached to the

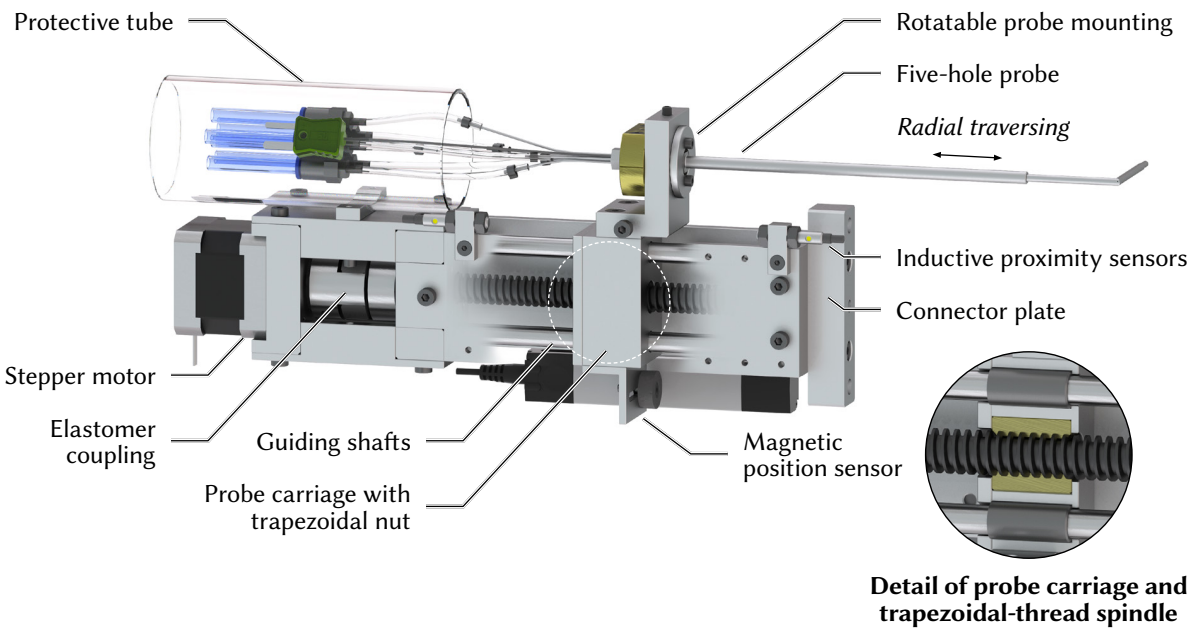

Figure 5.42: Radial probe traversing unit

probe carriage. The probe is fixed on the carriage through a rotatable two-part mounting bracket that allows the probe angle ρ to be adjusted continuously. The entire assembly is attached to the annular gear rack via a connector plate with two screws and a pin.

5.5.7 Positioning Unit for the 6-Axis Industrial Robot

During the installation of the test rig, it was found that a stationary mounting of the robot would cause difficulties in test rig handling, as accessibility to the traverse system would be considerably restricted. For this reason, a linear guide was developed that allows the robot to be moved from the recording position to a maintenance position. As shown in Figure 5.43, it consists of two linear motion guides (Mädler DA 0115 RC) that are mounted on an aluminum frame. The robot is attached to a mounting plate that is guided by four ball carriages.

The advantage of camera traversing by an industrial robot is that any recording positions can be approached with very precise repeatability. However, doing so requires that the position of the robot does not change relative to the test rig. For this reason, the mounting plate is pinned and screwed at the end positions to an adapter plate that is mounted on the frame. In addition, the screw connection provides the necessary stiffening to absorb the reaction forces of the moving robot.

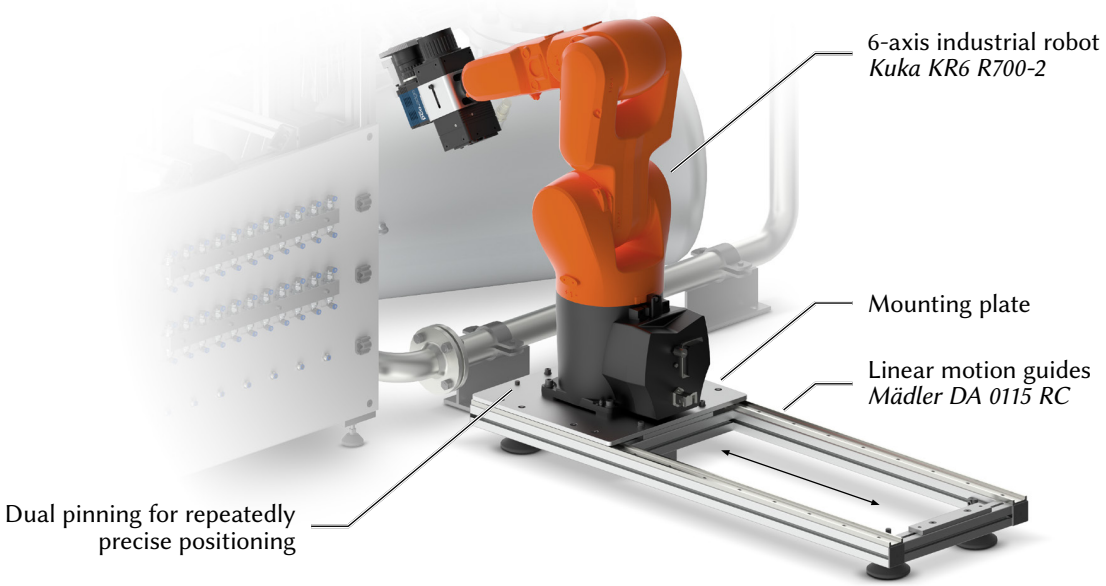

Figure 5.43: Linear positioning unit for the 6-axis industrial robot

5.6 Outlet Flow Guidance

The outlet vessel shown in Figure 5.44 was designed for an absolute pressure of 2.5 bar in accordance with DIN EN 13445. It consists of a 3 mm thick stainless steel shell (⌀ 450 mm) and torispherical heads welded on both sides. The cascade casing and piping of the chimney are connected via flange connections. A reinforcing pad was welded on to strengthen the rectangular nozzle. Two welded-on threaded sleeves allow the integration of a pressure measuring point as well as a relief valve that triggers when the design pressure is exceeded. The flow is led out of the test room via the chimney and an adjoining 90° pipe bend and fed to the existing infrastructure of the test facility.

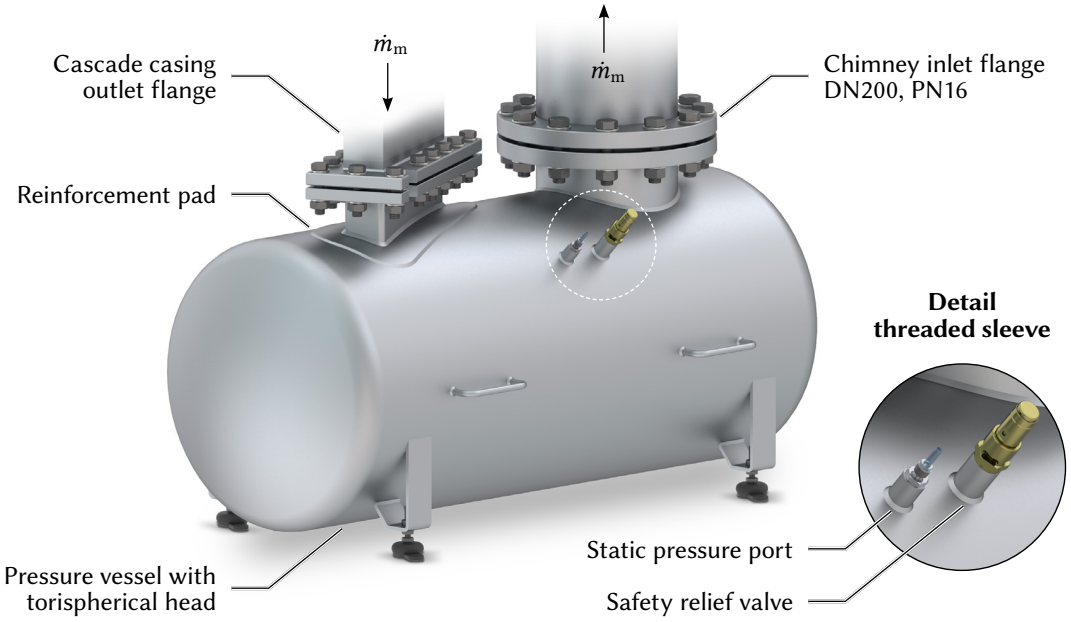

Figure 5.44: Outlet vessel

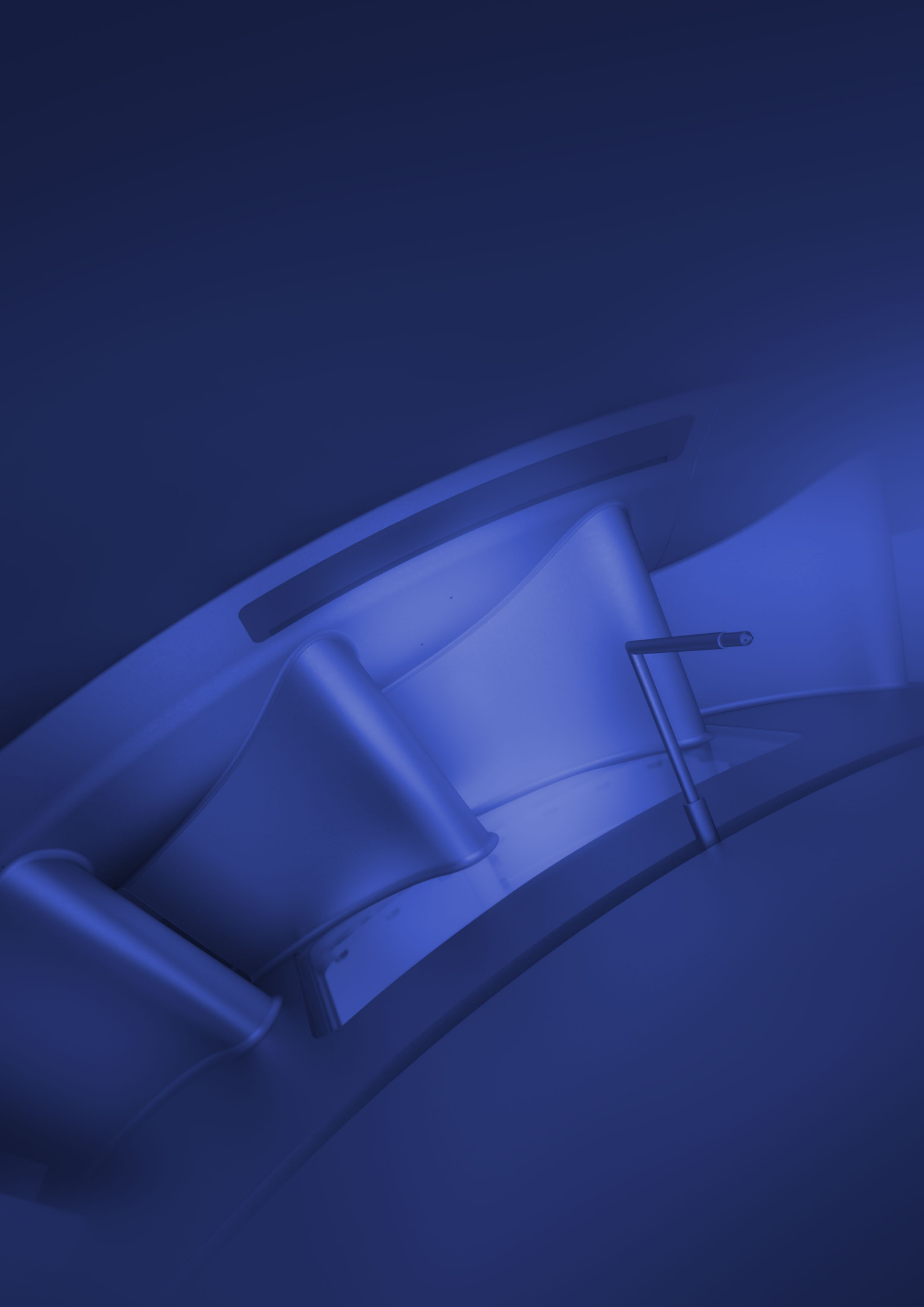

6

Summary and Outlook

Since the use of gas turbines cannot be dispensed with in the foreseeable future, ongoing development for increasing the thermal efficiency remains important. As this can be accomplished by further increasing the turbine inlet temperature, advanced internal and external cooling techniques are required to protect the highly loaded turbine components, e.g., the first nozzle guide vanes that are located just downstream of the combustion chamber.

For decades, film cooling has been a cornerstone of turbine cooling as it can protect the surface not only in the immediate vicinity of the injection but also in the downstream area. While the coolant film is typically supplied through discrete cooling holes, design-related gaps, e.g., the purge slot between the transition duct and the vane platform, can be utilized for injecting coolant. Since the coolant is drawn from the compressor, potentially offsetting thermal efficiency gains from increased turbine inlet temperatures, efficient use of the coolant is critical. In this context, experimental data obtained under engine-like flow conditions, i.e., matching the Mach and Reynolds numbers that are present in the engine, are indispensable for assessing the film cooling performance. Existing research on upstream slot injection has a blind spot, as all high-speed studies were conducted in linear cascades. This approach neglects, by principle, the influence of the radial pressure gradient that naturally occurs in swirling flows and potentially affects coolant propagation. Therefore, a high-speed annular sector cascade has been developed that is equipped with state-of-the-art nozzle guide vanes featuring endwall contouring. The new cascade allows testing the film cooling performance and aerodynamic effects of coolant flows from various upstream slot configurations, not only at engine-like Mach and Reynolds numbers but also in consideration of the radial pressure gradient. To provide baseline data for later comparison and to refine the measurement methods, which include pressure-sensitive paint, five-hole probes, and IR thermography, the development of the new cascade was preceded by extensive measurements on a linear cascade equipped with the same NGV design.

Findings and Lessons from the Linear Cascade

The measurements at the linear cascade were performed for a wide range of parameters. The purge slot was varied in terms of inclination, width, and leading-edge distance. Each slot configuration was tested at different blowing and density ratios to evaluate the influence of coolant-related parameters.

By applying the heat-mass transfer analogy, the film cooling effectiveness studies were conducted using pressure-sensitive paint. To assess the impact of coolant injection on both the near-endwall flow field and overall passage aerodynamics, oil flow visualizations, and five-hole probe measurements at the passage outlet were carried out. For the investigation of the endwall heat transfer, a measurement module was designed that implements the auxiliary wall method. It consists of a water-cooled base plate that is covered with a thin and low-conductive coating.

Oil Flow Visualizations

As intended by the design features of the NGV, the wall-near flow field of the base case (without slot) is rather unspectacular in the sense that no prominent secondary flows can be observed. With the saddle point being located in close proximity to the leading edge, it can be assumed that the strength of the horseshoe vortex is significantly attenuated. However, the injection of cooling air can cause a significant change in the near-endwall flow field, with the extent being strongly dependent on the slot geometry and the blowing ratio.

When injected through a perpendicular slot at a high blowing ratio, the coolant instantly separates and forms two prominent counter-rotating vortices originating at the leading edge and dominating the flow field at the passage inlet. This is contrasted by the results of an inclined injection, where the coolant attaches to the endwall closely behind the slot exit without forming coolant-induced vortices. The flow field further downstream is nearly identical to that of the base case. However, the formation and propagation of the horseshoe vortex seem to be mitigated, as the separation line is shifted to the pressure side of the vane root. Furthermore, the boundary layer appears to be re-energized, weakening the endwall crossflow.

Film Cooling Effectiveness

Film cooling effectiveness, both locally and averaged, is closely bonded to the blowing ratio, at least at low and medium rates ($0.25 \leq BR \leq 0.75$). At higher rates, the effectiveness gains decrease significantly as mixing with the main flow increases. This is particularly evident when the coolant is injected through a perpendicular slot, which causes the coolant to separate even at medium BR. For this reason, an inclined injection is clearly superior, especially at higher blowing ratios, as separation is suppressed.

Regardless of injecting the coolant through a perpendicular or inclined slot, the lowest blowing ratios should be avoided as the coolant is obstructed by the stagnation pressure upstream of the leading edge. Moreover, the coolant is displaced further downstream by the horseshoe vortex, leaving the thermally critical pressure-side region completely uncooled. Since this can be overcome by higher coolant momentum, a narrow slot configuration is generally superior at an equal mass flux ratio, at least until the effects of coolant separation become dominant. Concerning the slot distance to the

leading edge, the cooling coverage deteriorates progressively with increasing distance. While this is primarily due to the extended mixing length, the specific progression of the endwall contouring promotes rapid reattachment of the separated coolant for the nearest slot position. The effects of varying the density ratio are small compared to the other parameters investigated. However, as the higher density ratio is accompanied by a lower exit velocity and thus a lower momentum flux, the density ratio should be included in the analysis whenever the coolant momentum is suspected of playing a major role in the coolant distribution.

Net Heat Flux Reduction

The findings of the heat transfer measurements are limited to an evaluation of the *NHFR* due to the shortcomings of the measurement module: At medium blow ratios, the thermal load on the endwall can be significantly reduced, especially in the first half of the passage. As with the distribution of film cooling effectiveness, significant gains in heat flux reduction cannot be realized with higher *BR*. On the contrary, with the emergence of coolant-induced vortices, the results actually worsen when the coolant is injected at maximum *BR* through a perpendicular slot. This is particularly evident when moving the slot further upstream: The amplification of secondary flow is accompanied by such an increased coolant dilution that the thermal load even deteriorates locally compared to that of the base case. Especially in the case of the narrowed perpendicular slot, a reduction of the thermal load is virtually non-existent. At this point, it becomes clear why an isolated analysis of film cooling effectiveness may not provide a complete understanding of film cooling performance in certain cases, i.e., when the flow field is substantially changed by the coolant injection.

Outlet Flow Field

As a result of the aerodynamically optimized design of the investigated NGV, the local loss distribution of the base case variant is dominated by wake-induced losses, while those attributed to secondary flow are concentrated near the endwall. In contrast to previous findings for a cylindrical NGV design, the effects of coolant injection through a perpendicular slot are limited to the near-endwall region, even for the highest blowing ratio. While the local loss maximum is gradually shifted away from the endwall, the width and the loss level of the wake at the midspan remain virtually unchanged for increasing *BR*.

The flow field does not differ qualitatively much from the perpendicular injection when injecting the coolant through an inclined slot. It is, however, noticeable that the endwall boundary layer thickness is significantly reduced when compared with the base case. It stands to reason that the inclined injection introduces high-energy fluid into the boundary layer, thus counteracting the thickening.

Implications for the Annular Cascade

The linear cascade has revealed weaknesses concerning the operation and the implementation of the measurement methods that needed to be addressed for the annular cascade design. As each section of the linear cascade was constructed from multiple thick-walled stainless steel parts, handling difficulties and leakage issues arose due to weight and component warpage. Therefore, welded structures were utilized to reduce material usage while meeting safety requirements and improving leak tightness.

In terms of instrumentation and measurement method implementation, the design of the heat transfer measurement module was completely reworked as the linear design suffered from parasitic heat fluxes and cavity leakage that compromised the thermal boundary conditions of the setup. The PSP measurement setup has proven its reliability, but an additional fast-responding secondary air heater was developed to speed up the measurement sequence and reduce foreign gas consumption.

Development of the Annular Sector Cascade

The development of the annular sector cascade was divided into the preliminary numerical optimization of the wet volume and the design of the test rig itself. Since the new cascade had to be integrated into the existing test rig architecture, the design had to comply with spatial constraints that limited the length of the inlet and outlet geometry.

Numerical Optimization of the Fluid Volume

Cascades with a finite number of vanes are basically affected by periodicity issues, which must be addressed by appropriate measures such as the use of tailboards. Driven by the radial pressure gradient, annular cascades are potentially subject to a separation of the hub boundary layer downstream of the passage when discharging the flow into a constant pressure plenum. This separation may lead to blockage and flow instabilities that also affect the upstream passage flow.

For this reason, the fluid volume of the annular sector cascade was aerodynamically optimized in the preliminary design phase using CFD methods. For evaluating the periodicity of the passage flow in a unified and single-value-based manner, a benchmark approach has been developed that aggregates and weights different flow variables, such as the Mach number and the pitch angle at the inlet and outlet. The initial geometry was based on a design previously implemented by Wiers and Fransson [86] and Saha [91] in similar high-speed cascades. Instead of using tailboards, the design incorporates a dump diffuser downstream of the cascade to allow the outlet flow to develop as a free jet, with the flow angle adjusting to the downstream back pressure. Since it was not possible to achieve sufficient periodicity following this design approach, the geometry of the upper and lower channel limitations and the outlet volume were modified. The use of a tailboard at the lower passage limitation was found to be most effective in harmonizing the mass throughput. By using a short radial diffuser, which transitions the mean radius of the flow path into a linear section before discharging the flow into a constant pressure outlet vessel, flow separation could be avoided. Based on the benchmark, the final geometry provides a periodicity that exceeds the periodicity of the linear cascade.

Construction of the Annular Sector Test Rig

For reasons of tightness and weight but also for the straightforward realization of the constant-radius endwalls, the two inlet segments and the cascade casing were designed as welded structures consisting of both bent sheets and milled parts. The two inlet segments are supported by a mounting frame, which also accommodates the pressure sensors and further measurement equipment.

A screen and a honeycomb are installed in the inlet section to settle and equalize the inlet flow. To set a defined level of turbulence at the inlet of the cascade, a bar-shaped turbulence grid is integrated into the inlet section. A boundary layer suction at the hub and the shroud ensures that a new, defined boundary layer can form until the flow enters the cascade. Both the turbulence grid and the boundary layer suction are integrated as intermediate flanges into the inlet section, allowing easy installation and changeover. A measurement port in each inlet segment allows the inlet flow conditions of the cascade to be monitored.

The welded cascade casing houses both the vanes and the upper/lower channel limitations and provides optical access for the PSP and IR measurements. The operating conditions can be monitored by pressure taps, which are distributed around the perimeter at the inlet and outlet of the cascade. The cascade casing is followed by an outlet vessel, which collects the flow and guides it into the chimney.

The contoured shroud endwalls are constructed as milled segments that are inserted into the cascade casing. They are held in place by multiple clamps distributed around the perimeter. The central passage endwall segment features a replaceable, 3D-printed slot insert that allows for a quick change of slot geometry. The plenum that feeds the slot with coolant was completely redesigned, as it was found that the slot flow is adversely affected by the previous geometry used in the linear cascade. The new design makes use of a porous sleeve by which the coolant is evenly introduced into the plenum. The geometry of the sleeve, its surrounding tubes, and the porosity characteristics were optimized through numerical analysis.

The revised measurement module for the heat transfer measurements consists of a cooled copper base plate that was reduced in size to separate it from the slot insert, thus preventing leakage and parasitic heat fluxes. On account of the simplified geometry, the base plate is inserted into a milled pocket of the endwall and can be sealed with a single circumferential sealing cord. A CHT analysis was performed to evaluate the temperature homogeneity under the insulating coating and to optimize the cooling water supply to the cooling cavities in the base body. It was found that a staggered distribution of the cooling water inlets and outlets performs best, with the backside temperatures differing by less than 1 K for a cooling water mass flow of $0.1\,\mathrm{kg\,s^{-1}}$.

For the radial and circumferential movement of the five-hole probes at the inlet and outlet, traversing units were developed: The radial unit makes use of a trapezoidal spindle which is actuated by a stepper motor. Position sensors and limit switches allow a safe and precise probe movement. The circumferential movement of the probes is realized with an annular gear rack, with internal toothing manufactured by waterjet cutting. The gear rack is guided in milled cheeks that are bolted with the welded mounting support of the cascade casing. To reduce the sliding friction resistance, the internal contact surfaces of the cheeks are coated with Teflon. The rack is actuated by a spur gear flange-mounted on the output shaft of a worm gearbox. The circumferential position of the probe is measured by an inductive angle sensor actuated by another gear unit on the opposite shaft end of the worm gearbox.

The measurement setup includes an industrial robot that allows the cameras required for the PSP and IR measurements to be accurately positioned. The entire unit can be moved for maintenance purposes with a linear guide.

Outlook

The assembled and instrumented test rig is shown in Figures 6.1, 6.2 and 6.3. The next step, which is expected to be completed by the time this thesis is published, is to modify the existing measurement programs. This includes adapting the five-hole probe control to the new sensors and the modified kinematics of the underlying cylinder coordinate system. Subsequently, the inlet and outlet flow field of the cascade can be measured. If the periodicity is not yet satisfactory, the tailboard position can be adjusted. There is also potential for optimization by adjusting the suction rate of the boundary layer suction, which can help to establish a homogeneous inlet profile. The level of turbulence at the inlet should be validated using a hot-wire probe that can be inserted through the inlet probe access.

Before the PSP measurement campaign for determining the film cooling effectiveness can be carried out, suitable recording positions must first be identified. Moreover, the industrial robot must be taught to the underlying coordinate system of the test rig to provide good starting coordinates for the image mapping algorithm.

After these preparations have been completed, the isothermal measurement campaign, i.e., the PSP measurements, the aerodynamic measurements at the outlet as well as the oil flow visualizations, can be carried out for the slot configurations defined in Table 3.3. This will be followed by the instrumentation and commissioning of the heat transfer measurement module, which is currently manufactured.

Once the entire measurement campaign is completed, the question can be addressed to which extent the radial pressure gradient influences the cooling performance. Here, a comparison with the data from the linear cascade is obvious.

Future measurements on the annular cascade could include the investigation of slot geometries with forward or backward steps, as these steps can lead to a thicker endwall boundary layer, thereby intensifying secondary flow. In addition, a study of discrete cooling hole geometries is also conceivable, as the propagation of the coolant jets is also likely to be influenced by the radial pressure gradient. In order to obtain a more comprehensive picture of the passage flow, LDA measurements can be considered, with the tracer particles supplied via the probe access of the second inlet segment.

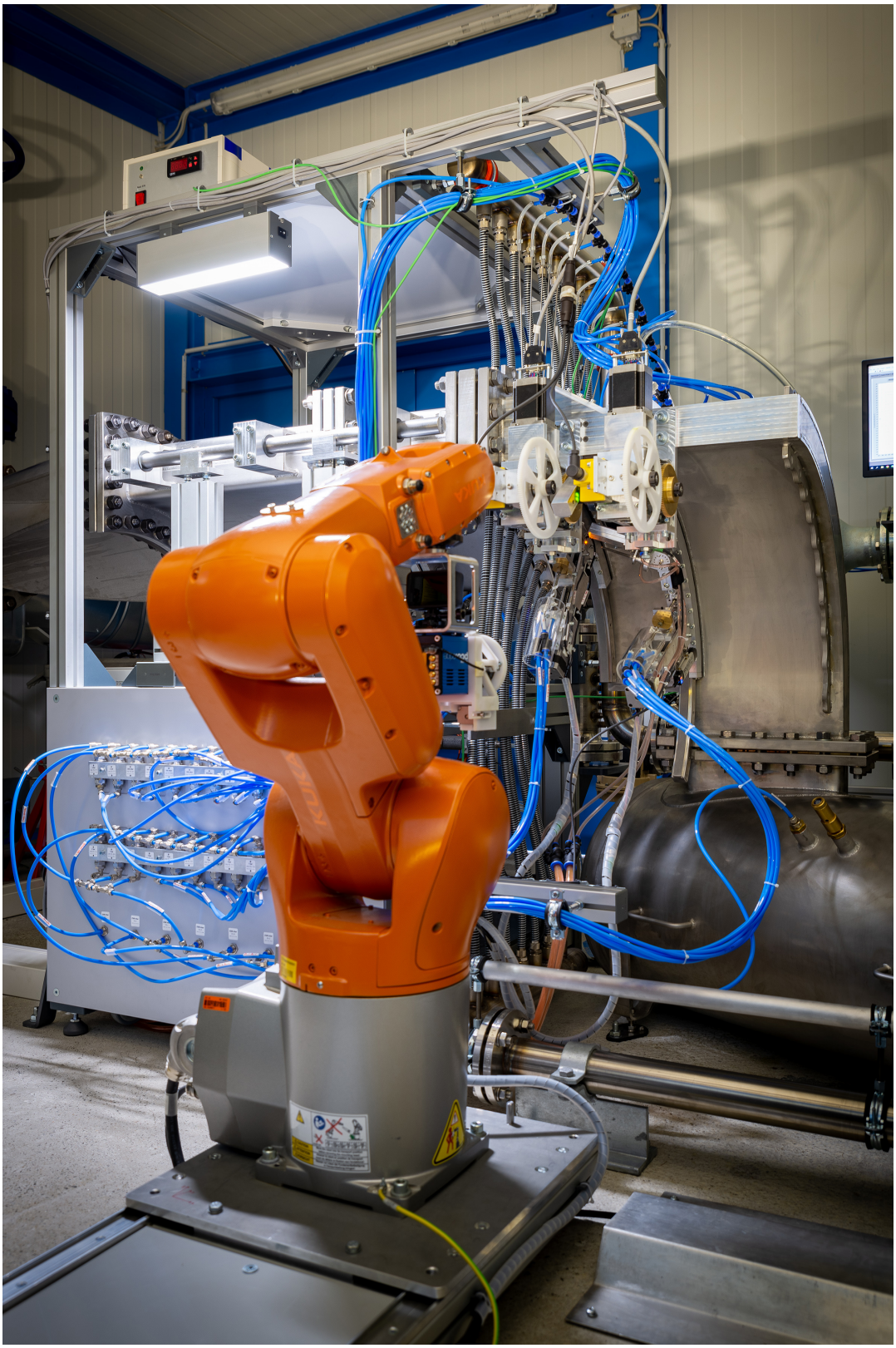

Figure 6.1: Full view of the annular test rig with industrial robot

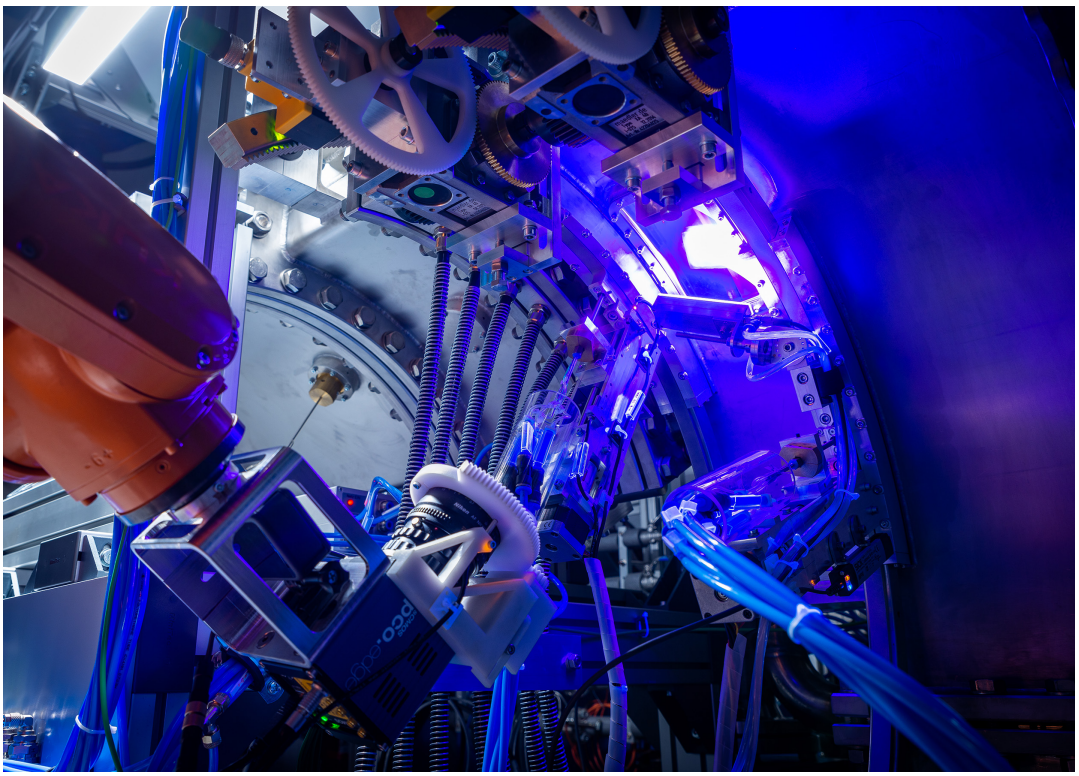

(a) Cascade casing with PSP setup

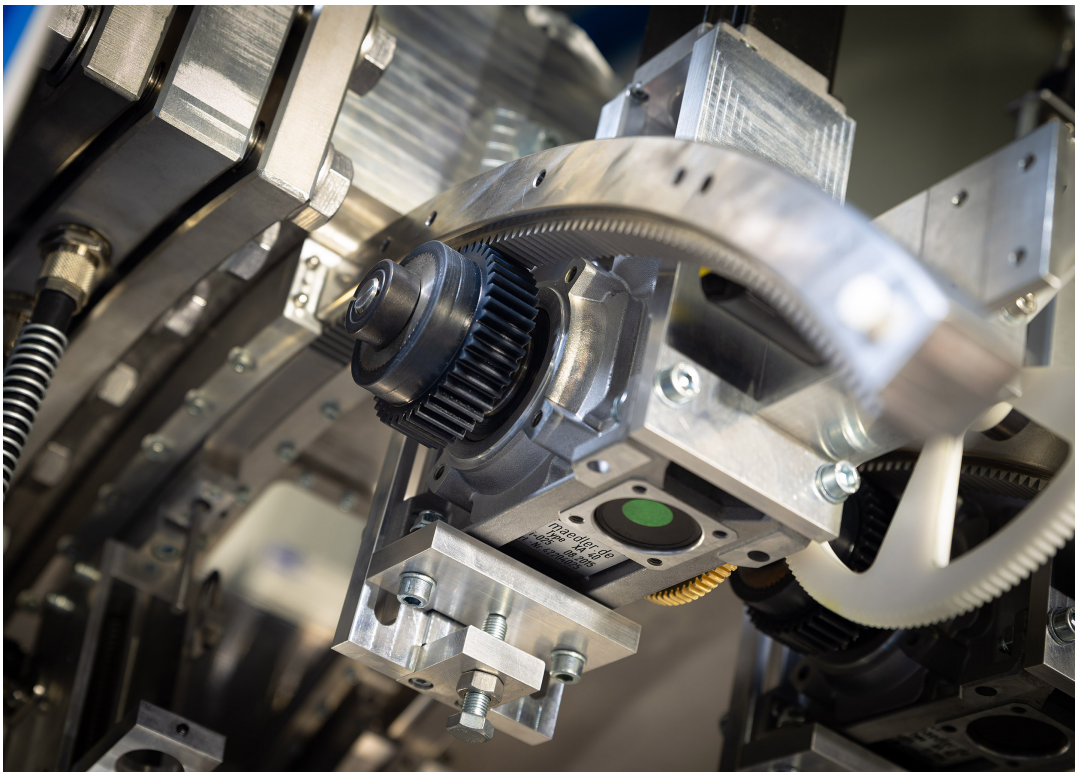

(b) Detail of circumferential probe traverse unit

Figure 6.2: Assembled and instrumented annular test rig (hub-side view)

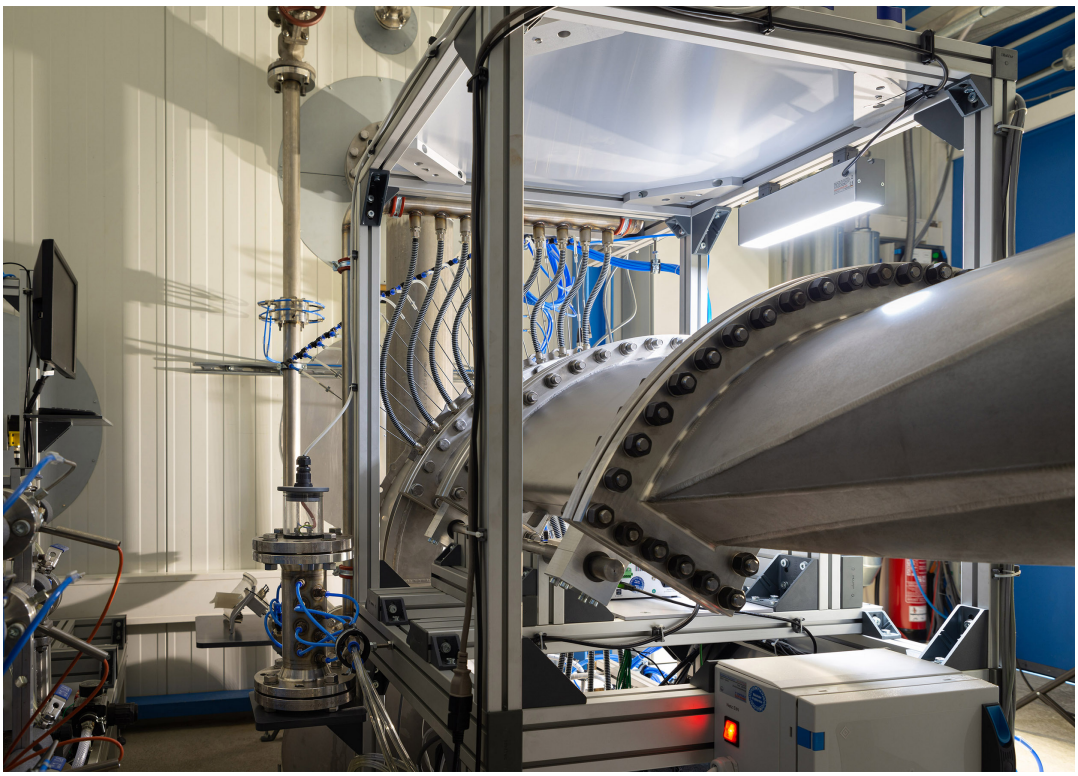

(a) Transition duct and inlet segments

(b) Partly-opened cascade casing

Figure 6.3: Assembled and instrumented annular test rig (shroud-side view)

Bibliography

[1] International Energy Agency. *Net Zero by 2050: A Roadmap for the Global Energy Sector*. May 2021. doi: 10.1787/c8328405-en.

[2] K. Takeishi. Evolution of Turbine Cooled Vanes and Blades Applied for Large Industrial Gas Turbines and Its Trend toward Carbon Neutrality. *Energies*, 15(23):8935, November 2022. doi: 10.3390/en15238935.

[3] R. J. Goldstein. Film Cooling. In *Advances in Heat Transfer*, volume 7 of *Advances in Heat Transfer*, pages 321–379. Elsevier, 1971. ISBN 9780120200078. doi: 10.1016/S0065-2717(08)70020-0.

[4] J.-C. Han, S. Dutta, and S. Ekkad. *Gas Turbine Heat Transfer and Cooling Technology*. CRC Press, November 2012. doi: 10.1201/b13616.

[5] R. Krewinkel. A Review of Gas Turbine Effusion Cooling Studies. *International Journal of Heat and Mass Transfer*, 66:706–722, November 2013. doi: 10.1016/j.ijheatmasstransfer.2013.07.071.

[6] R. Zhu, G. Zhang, S. Li, and G. Xie. Combined-Hole Film Cooling Designs Based on the Construction of Antikidney Vortex Structure: A Review. *Journal of Heat Transfer*, 143(3), December 2020. doi: 10.1115/1.4048948.

[7] C. H. Sieverding, W. V. Hove, and E. Boletis. Experimental Study of the Three-dimensional Flow Field in an Annular Turbine Nozzle Guidevane. *Journal of Engineering for Gas Turbines and Power*, 106(2):437–444, April 1984. doi: 10.1115/1.3239585.

[8] R. Franze. *Experimentelle Konzeptentwicklung und Realisierung eines Heißgasprüfstands zur Untersuchung von Filmkühlung*. PhD thesis, Technische Universität Kaiserslautern, 2016.

[9] G. Müller, C. Landfester, M. Böhle, and R. Krewinkel. Turbine Vane Endwall Film Cooling Effectiveness of Different Purge Slot Configurations in a Linear Cascade. *Journal of Turbomachinery*, 142(3):031008, February 2020. doi: 10.1115/1.4045876.

[10] C. Landfester, G. Müller, M. Böhle, and R. Krewinkel. Aerodynamic Effects of Turbine Vane End Wall Film Cooling for Different Purge Slot Configurations in a Linear Cascade. *International Gas Turbine Conference (IGTC)*, 2019.

[11] C. Landfester, G. Müller, M. Böhle, and C. Domnick. Endwall Film Cooling Effectiveness for Different Purge Slot Configurations in a Contoured Endwall Nozzle Guide Vane Stage. In *14th European Conference on Turbomachinery Fluid Dynamics and Thermodynamics*. European Turbomachinery Society, 2021.

[12] C. Landfester, G. Müller, R. Krewinkel, C. Domnick, and M. Böhle. Comparison of Film Cooling Performance for Different Purge Slot Configurations in a Cylindrical and State-of-the-Art Nozzle Guide Vane. *Journal of Turbomachinery*, 144(3), November 2021. doi: 10.1115/1.4052456.

[13] B. Lakshminarayana. *Fluid Dynamics and Heat Transfer of Turbomachinery*. Wiley, New York, 1995. ISBN 978-0-471-85546-0.

[14] L. S. Langston. Secondary Flows in Axial Turbines - A Review. *Annals of the New York Academy of Sciences*, 934(1):11–26, January 2006. doi: 10.1111/j.1749-6632.2001.tb05839.x.

[15] R. A. Graziani, M. F. Blair, J. R. Taylor, and R. E. Mayle. An Experimental Study of Endwall and Airfoil Surface Heat Transfer in a Large Scale Turbine Blade Cascade. *Journal of Engineering for Power*, 102(2):257–267, April 1980. doi: 10.1115/1.3230246.

[16] M. F. Blair. An Experimental Study of Heat Transfer and Film Cooling on Large-Scale Turbine Endwalls. *Journal of Heat Transfer*, 96(4):524, 1974. doi: 10.1115/1.3450239.

[17] W. R. Hawthorne. Rotational Flow Through Cascades. Part 1: The Components of Vorticity. *The Quarterly Journal of Mechanics and Applied Mathematics*, 8(3):266–279, 1955. doi: 10.1093/qjmam/8.3.266.

[18] L. S. Langston, M. L. Nice, and R. M. Hooper. Three-Dimensional Flow Within a Turbine Cascade Passage. *Journal of Engineering for Power*, 99(1):21–28, January 1977. doi: 10.1115/1.3446247.

[19] H. P. Wang, S. J. Olson, R. J. Goldstein, and E. R. G. Eckert. Flow Visualization in a Linear Turbine Cascade of High Performance Turbine Blades. *Journal of Turbomachinery*, 119(1):1–8, 1997. ISSN 0889-504X. doi: 10.1115/1.2841006.

[20] K. Takeishi, M. Matsuura, S. Aoki, and T. Sato. An Experimental Study of Heat Transfer and Film Cooling on Low Aspect Ratio Turbine Nozzles. *Journal of Turbomachinery*, 112(3):488–496, July 1990. doi: 10.1115/1.2927684.

[21] C. H. Sieverding. Recent Progress in the Understanding of Basic Aspects of Secondary Flows in Turbine Blade Passages. *Journal of Engineering for Gas Turbines and Power*, 107(2):248–257, April 1985. doi: 10.1115/1.3239704.

[22] R. J. Goldstein and R. A. Spores. Turbulent Transport on the Endwall in the Region Between Adjacent Turbine Blades. *Journal of Heat Transfer*, 110(4a):862–869, November 1988. doi: 10.1115/1.3250586.

[23] W. A. Eckerle and L. S. Langston. Horseshoe Vortex Formation Around a Cylinder. *Journal of Turbomachinery*, 109(2):278–285, April 1987. doi: 10.1115/1.3262098.

[24] O. P. Sharma and T. L. Butler. Predictions of Endwall Losses and Secondary Flows in Axial Flow Turbine Cascades. *Journal of Turbomachinery*, 109(2):229–236, April 1987. doi: 10.1115/1.3262089.

[25] J. Moore and R. Y. Adhye. Secondary Flows and Losses Downstream of a Turbine Cascade. *Journal of Engineering for Gas Turbines and Power*, 107(4):961–968, October 1985. doi: 10.1115/1.3239842.

[26] S. Friedrichs, H. P. Hodson, and W. N. Dawes. Distribution of Film-cooling Effectiveness on a Turbine Endwall Measured Using the Ammonia and Diazo Technique. *Journal of Turbomachinery*, 118(4):613–621, October 1996. doi: 10.1115/1.2840916.

[27] C. Baker. The Turbulent Horseshoe Vortex. *Journal of Wind Engineering and Industrial Aerodynamics*, 6(1-2):9–23, July 1980. doi: 10.1016/0167-6105(80)90018-5.

[28] G. A. Zess and K. A. Thole. Computational Design and Experimental Evaluation of Using a Leading Edge Fillet on a Gas Turbine Vane. *Journal of Turbomachinery*, 124(2):167–175, April 2002. doi: 10.1115/1.1460914.

[29] M. E. Deich, A. D. Zaryankin, G. A. Filippov, and N. F. Zatsepin. Method of Increasing the Efficiency of Turbine Stages with Short Blades. *Teploenergetikia*, 2:240–254, 1960.

[30] A. Duden, I. Raab, and L. Fottner. Controlling the Secondary Flow in a Turbine Cascade by Three-Dimensional Airfoil Design and Endwall Contouring. *Journal of Turbomachinery*, 121(2): 191–199, April 1999. doi: 10.1115/1.2841301.

[31] T. W. Simon and J. D. Piggush. Turbine Endwall Aerodynamics and Heat Transfer. *Journal of Propulsion and Power*, 22(2):301–312, March 2006. doi: 10.2514/1.16344.

[32] J. S. Ewen, F. W. Huber, and J. P. Mitchell. Investigation of the Aerodynamic Performance of Small Axial Turbines. *Journal of Engineering for Power*, 95(4):326–332, October 1973. doi: 10.1115/1.3445739.

[33] F. C. Kopper, R. Milano, and M. Vanco. Experimental Investigation of Endwall Profiling in a Turbine Vane Cascade. *AIAA Journal*, 19(8):1033–1040, August 1981. doi: 10.2514/3.51032.

[34] V. Dossena, A. Perdichizzi, and M. Savini. The Influence of Endwall Contouring on the Performance of a Turbine Nozzle Guide Vane. *Journal of Turbomachinery*, 121(2):200–208, April 1999. doi: 10.1115/1.2841302.

[35] E. Boletis. Effects of Tip Endwall Contouring on the Three-Dimensional Flow Field in an Annular Turbine Nozzle Guide Vane: Part 1—Experimental Investigation. *Journal of Engineering for Gas Turbines and Power*, 107(4):983–990, October 1985. doi: 10.1115/1.3239845.

[36] A. A. Thrift, K. A. Thole, and S. Hada. Effects of an Axisymmetric Contoured Endwall on a Nozzle Guide Vane: Convective Heat Transfer Measurements. *Journal of Turbomachinery*, 133 (4), April 2011. doi: 10.1115/1.4002966.

[37] M. G. Rose. Non-Axisymmetric Endwall Profiling in the HP NGV's of an Axial Flow Gas Turbine. In *Volume 1: Turbomachinery*. American Society of Mechanical Engineers, June 1994. doi: 10.1115/94-gt-249.

[38] N. W. Harvey, M. G. Rose, M. D. Taylor, S. Shahpar, J. Hartland, and D. G. Gregory-Smith. Nonaxisymmetric Turbine End Wall Design: Part I— Three-Dimensional Linear Design System. *Journal of Turbomachinery*, 122(2):278–285, February 1999. doi: 10.1115/1.555445.

[39] J. C. Hartland, D. G. Gregory-Smith, N. W. Harvey, and M. G. Rose. Nonaxisymmetric Turbine End Wall Design: Part II—Experimental Validation. *Journal of Turbomachinery*, 122(2):286–293, February 1999. doi: 10.1115/1.555446.

[40] G. I. Mahmood and S. Acharya. Measured Endwall Flow and Passage Heat Transfer in a Linear Blade Passage With Endwall and Leading Edge Modifications. In *Volume 6: Turbo Expo 2007, Parts A and B*, pages 917–930. ASMEDC, 2007. ISBN 0-7918-4795-0. doi: 10.1115/GT2007-28179.

[41] H. Sauer, R. Mülller, and K. Vogeler. Reduction of Secondary Flow Losses in Turbine Cascades by Leading Edge Modifications at the Endwall. *Journal of Turbomachinery*, 123(2):207–213, February 2000. doi: 10.1115/1.1354142.

[42] S. Becz, M. S. Majewski, and L. S. Langston. Leading Edge Modification Effects on Turbine Cascade Endwall Loss. In *Volume 6: Turbo Expo 2003, Parts A and B*. ASMEDC, January 2003. doi: 10.1115/gt2003-38898.

[43] L. Kubendran and W. Harvey. Juncture Flow Control using Leading-Edge Fillets. In *3rd Applied Aerodynamics Conference*. American Institute of Aeronautics and Astronautics, August 1985. doi: 10.2514/6.1985-4097.

[44] W. J. Devenport, N. K. Agarwal, M. B. Dewitz, R. L. Simpson, and K. Poddar. Effects of a Fillet on the Flow past a Wing-body Junction. *AIAA Journal*, 28(12):2017–2024, December 1990. doi: 10.2514/3.10517.

[45] J. D. Denton and L. Xu. The Exploitation of Three-dimensional Flow in Turbomachinery Design. *Proceedings of the Institution of Mechanical Engineers, Part C: Journal of Mechanical Engineering Science*, 213(2):125–137, February 1998. doi: 10.1243/0954406991522220.

[46] S. Harrison. Secondary Loss Generation in a Linear Cascade of High-Turning Turbine Blades. *Journal of Turbomachinery*, 112(4):618–624, October 1990. doi: 10.1115/1.2927702.

[47] M. T. Schobeiri, A. Suryanarayanan, C. Jermann, and T. Neuenschwander. A Comparative Aerodynamic and Performance Study of a Three-Stage High Pressure Turbine With 3-D Bowed Blades and Cylindrical Blades. In *Volume 5: Turbo Expo 2004, Parts A and B*. ASMEDC, January 2004. doi: 10.1115/gt2004-53650.

[48] D. G. Bogard and K. A. Thole. Gas Turbine Film Cooling. *Journal of Propulsion and Power*, 22(2): 249–270, 2006. ISSN 0748-4658. doi: 10.2514/1.18034.

[49] S. Baldauf, A. Schulz, and S. Wittig. High-Resolution Measurements of Local Heat Transfer Coefficients From Discrete Hole Film Cooling. *Journal of Turbomachinery*, 123(4):749–757, February 1999. doi: 10.1115/1.1387245.

[50] M. E. Crawford, W. M. Kays, and R. J. Moffat. Full-coverage Film Cooling—Part I: Comparison of Heat Transfer Data for Three Injection Angles. *Journal of Engineering for Power*, 102(4): 1000–1005, October 1980. doi: 10.1115/1.3230334.

[51] S. W. Burd, C. J. Satterness, and T. W. Simon. Effects of Slot Bleed Injection Over a Contoured Endwall on Nozzle Guide Vane Cooling Performance: Part II — Thermal Measurements. In *Volume 3: Heat Transfer, Electric Power, Industrial and Cogeneration*. American Society of Mechanical Engineers, May 2000. doi: 10.1115/2000-gt-0200.

[52] B. Sen, D. L. Schmidt, and D. G. Bogard. Film Cooling With Compound Angle Holes: Heat Transfer. *Journal of Turbomachinery*, 118(4):800–806, 1996. ISSN 0889-504X. doi: 10.1115/1.2840937.

[53] J.-C. Han. Fundamental Gas Turbine Heat Transfer. *Journal of Thermal Science and Engineering Applications*, 5(2), May 2013. doi: 10.1115/1.4023826.

[54] K. Thole, A. Sinha, D. Bogard, and M. Crawford. Mean Temperature Measurements of Jets with a Crossflow for Gas Turbine Film Cooling Application. *Rotating Machinery Transport Phenomena*, 01 1992.

[55] K. Wieghardt. *Hot-air Discharge for De-icing*. United States. Army Air Forces. AAF Trans. No. F-TS-919-RE, Wright Field, Air Material Command, 1946.

[56] A. Perdichizzi. Mach Number Effects on Secondary Flow Development Downstream of a Turbine Cascade. *Journal of Turbomachinery*, 112(4):643–651, October 1990. doi: 10.1115/1.2927705.

[57] D. Granser and T. Schulenberg. Prediction and Measurement of Film Cooling Effectiveness for a First-Stage Turbine Vane Shroud. In *Volume 4: Heat Transfer, Electric Power, Industrial and Cogeneration*. American Society of Mechanical Engineers, June 1990. doi: 10.1115/90-gt-095.

[58] A. F. Chen, C.-C. Shiau, and J.-C. Han. Turbine Blade Platform Film Cooling With Simulated Swirl Purge Flow and Slashface Leakage Conditions. *Journal of Turbomachinery*, 139(3), December 2016. doi: 10.1115/1.4034985.

[59] S. W. Burd and T. W. Simon. Effects of Slot Bleed Injection Over a Contoured Endwall on Nozzle Guide Vane Cooling Performance: Part I — Flow Field Measurements. In *Volume 3: Heat Transfer, Electric Power, Industrial and Cogeneration*. American Society of Mechanical Engineers, May 2000. doi: 10.1115/2000-gt-0199.

[60] F. Kost and M. Nicklas. Film-Cooled Turbine Endwall in a Transonic Flow Field: Part I — Aerodynamic Measurements. *Journal of Turbomachinery*, 123(4):709–719, February 2001. doi: 10.1115/1.1400112.

[61] M. Nicklas. Film-Cooled Turbine Endwall in a Transonic Flow Field: II — Heat Transfer and Film-Cooling Effectiveness. *ASME Turbo Expo 2001: Power for Land, Sea, and Air*, Volume 3: Heat Transfer; Electric Power; Industrial and Cogeneration(2001-GT-0146), 2001. doi: 10.1115/2001-gt-0146.

[62] L. J. Zhang and R. S. Jaiswal. Turbine Nozzle Endwall Film Cooling Study Using Pressure-sensitive Paint. *Journal of Turbomachinery*, 123(4):730–738, February 2001. doi: 10.1115/1.1400113.

[63] R. Oke, T. Simon, T. Shih, B. Zhu, Y. L. Lin, and M. Chyu. Measurements Over a Film-Cooled, Contoured Endwall With Various Coolant Injection Rates. In *Volume 3: Heat Transfer, Electric Power, Industrial and Cogeneration*. American Society of Mechanical Engineers, June 2001. doi: 10.1115/2001-gt-0140.

[64] W. F. Colban, K. A. Thole, and G. Zess. Combustor Turbine Interface Studies: Part I — Endwall Effectiveness Measurements. *Journal of Turbomachinery*, 125(2):193–202, April 2003. doi: 10.1115/1.1561811.

[65] D. G. Knost and K. A. Thole. Adiabatic Effectiveness Measurements of Endwall Film-cooling for a First-stage Vane. *Journal of Turbomachinery*, 127(2):297–305, April 2005. doi: 10.1115/1.1811099.

[66] N. D. Cardwell, N. Sundaram, and K. A. Thole. The Effects of Varying the Combustor-Turbine Gap. *Journal of Turbomachinery*, 129(4):756–764, July 2006. doi: 10.1115/1.2720497.

[67] F. Kost and A. Mullaert. Migration of Film-Coolant From Slot and Hole Ejection at a Turbine Vane Endwall. In *Volume 3: Heat Transfer, Parts A and B*. ASMEDC, January 2006. doi: 10.1115/gt2006-90355.

[68] J. D. Piggush and T. W. Simon. Heat Transfer Measurements in a First-stage Nozzle Cascade Having Endwall Contouring: Misalignment and Leakage Studies. *Journal of Turbomachinery*, 129(4):782–790, August 2007. doi: 10.1115/1.2720506.

[69] S. P. Lynch and K. A. Thole. The Effect of Combustor-Turbine Interface Gap Leakage on the Endwall Heat Transfer for a Nozzle Guide Vane. *Journal of Turbomachinery*, 130(4), 2008. ISSN 0889-504X. doi: 10.1115/1.2812950.

[70] A. A. Thrift, K. A. Thole, and S. Hada. Effects of an Axisymmetric Contoured Endwall on a Nozzle Guide Vane: Adiabatic Effectiveness Measurements. *Journal of Turbomachinery*, 133(4), April 2011. doi: 10.1115/1.4002965.

[71] A. A. Thrift, K. A. Thole, and S. Hada. Effects of Orientation and Position of the Combustor-Turbine Interface on the Cooling of a Vane Endwall. *Journal of Turbomachinery*, 134(6), 2012. ISSN 0889-504X. doi: 10.1115/1.4004817.

[72] K. Takeishi, Y. Oda, and S. Kozono. Experimental Study of Leakage Flow on Flow Field and Film Cooling of High Pressure Turbine Blade Platform. In *Volume 5B: Heat Transfer*. American Society of Mechanical Engineers, June 2015. doi: 10.1115/gt2015-42898.

[73] G. Barigozzi, H. Abdeh, A. Perdichizzi, M. Henze, and J. Krueckels. Aerothermal Performance of a Nozzle Vane Cascade With a Generic Nonuniform Inlet Flow Condition – Part II: Influence of Purge and Film Cooling Injection. *Journal of Turbomachinery*, 139(10), 2017. ISSN 0889-504X. doi: 10.1115/1.4036437.

[74] G. Barigozzi, A. Perdichizzi, L. Abba, and L. Pestelli. Platform Film Cooling Investigation on an HP Nozzle Vane Cascade With Discrete Shaped Holes and Slot Film Cooling. In *Volume 7B: Heat Transfer*. American Society of Mechanical Engineers, September 2020. doi: 10.1115/gt2020-14629.

[75] T. E. Biesinger and D. G. Gregory-Smith. Reduction in Secondary Flows and Losses in a Turbine Cascade by Upstream Boundary Layer Blowing. In *Volume 1: Aircraft Engine; Marine; Turbomachinery; Microturbines and Small Turbomachinery*. American Society of Mechanical Engineers, May 1993. doi: 10.1115/93-gt-114.

[76] A. Maekawa, R. Magoshi, and Y. Iwasaki. Development and In-house Shop Load Test Results of M701G2 Gas Turbine. In *International Gas Turbine Congress 2003, Tokyo*, 2003.

[77] A. Krichbaum, H. Werschnik, M. Wilhelm, H.-P. Schiffer, and K. Lehmann. A Large Scale Turbine Test Rig for the Investigation of High Pressure Turbine Aerodynamics and Heat Transfer With Variable Inflow Conditions. In *Volume 2A: Turbomachinery*. American Society of Mechanical Engineers, June 2015. doi: 10.1115/gt2015-43261.

[78] C. Hirsch, editor. *Advanced Methods for Cascade Testing*, volume 328 of *AGARDograph*. North Atlant. Treaty Org. AGARD, Neuilly sur Seine, 1993. ISBN 92-835-0717-7.

[79] R. I. Lewis. *Turbomachinery Performance Analysis*. Elsevier Science & Technology Books, 1996. doi: 10.1016/b978-0-340-63191-1.x5000-4.

[80] R. Goldstein, E. Eckert, and F. Burggraf. Effects of Hole Geometry and Density on Three-Dimensional Film Cooling. *International Journal of Heat and Mass Transfer*, 17(5):595–607, May 1974. doi: 10.1016/0017-9310(74)90007-6.

[81] T. Povey, T. V. Jones, and M. L. G. Oldfield. On a Novel Annular Sector Cascade Technique. *Journal of Turbomachinery*, 129(1):175–183, March 2004. doi: 10.1115/1.2372766.

[82] E. Boletis and C. H. Sieverding. Experimental Study of the Flow Field Behind an Annular Turbine Nozzle Guide Vane With and Without Downstream Rotor. In *Volume 1: Turbomachinery*. American Society of Mechanical Engineers, June 1984. doi: 10.1115/84-gt-15.

[83] R. G. Williamson, S. H. Moustapha, and J. P. Huot. The Effect of a Downstream Rotor on the Measured Performance of a Transonic Turbine Nozzle. *Journal of Turbomachinery*, 108(2): 269–274, October 1986. doi: 10.1115/1.3262047.

[84] L. C. Squire. Effects of Probe Supports on Measurements in Steam Turbines. In *Volume 1: Turbomachinery*. American Society of Mechanical Engineers, June 1986. doi: 10.1115/86-gt-213.

[85] S. H. Wiers and T. H. Fransson. Experimental Investigation of the Periodicity in a Sector of an Annular Turbine Cascade. In *XV. Bi-Annual Symposium on Measuring Techniques in Transonic and Supersonic Flow in Cascades and Turbomachines*, 2001.

[86] S. H. Wiers and T. H. Fransson. A New Annular Sector Cascade Test Facility to Investigate Steady State Cooling Effects. In *14th International Symposium in Measuring Techniques for Transonic and Supersonic Flow in Cascades and Turbomachines*, 1998.

[87] R. Saha, J. Fridh, T. Fransson, B. I. Mamaev, and M. Annerfeldt. Experimental Studies of Leading Edge Contouring Influence on Secondary Losses in Transonic Turbines. In *Volume 8: Turbomachinery, Parts A, B, and C*. American Society of Mechanical Engineers, June 2012. doi: 10.1115/gt2012-68497.

[88] U. R. Rådeklint and C. S. Hjalmarsson. A New Test Facility for Testing of Cooled Gasturbine Components. In *Volume 2: Aircraft Engine; Marine; Microturbines and Small Turbomachinery*. American Society of Mechanical Engineers, 1998. ISBN 978-0-7918-7863-7. doi: 10.1115/98-GT-557.

[89] V. Krivonosova, A. Lebedev, N. Simin, M. Zolotogorov, and N. Kortikov. Experimental and Numerical Analysis of High Temperature Gas Turbine Nozzle Vane Convective and Film Cooling Effectiveness. In *Volume 5: Heat Transfer, Parts A and B*. ASMEDC, January 2011. doi: 10.1115/gt2011-45294.

[90] J. E. Dees, J. A. Tallman, M. A. Heminger, and D. Wilde. Validation of Surface Pressure Predictions for Nozzle Airfoil and Endwall Film Cooling Design Using Transonic Cascade Measurements. In *Volume 3C: Heat Transfer*. American Society of Mechanical Engineers, June 2013. doi: 10.1115/gt2013-94921.

[91] R. Saha. *Aerodynamic Investigation of Leading Edge Contouring and External cooling on a Transonic Turbine Vane*, volume 14:04 of *Trita-KRV*. Industrial Engineering and Management, KTH Royal Institute of Technology, Stockholm, 2014. ISBN 978-91-7595-240-6.

[92] W. J. G. Bräunling. *Flugzeugtriebwerke*. Springer Berlin Heidelberg, 2015. doi: 10.1007/978-3-642-34539-5.

[93] S. H. Chue. Pressure Probes for Fluid Measurement. *Progress in Aerospace Sciences*, 16(2):147–223, 1975. ISSN 03760421. doi: 10.1016/0376-0421(75)90014-7.

[94] P. O. A. L. Davies. The Behaviour of a Pitot Tube in Transverse Shear. *Journal of Fluid Mechanics*, 3(05):441, February 1958. doi: 10.1017/s0022112058000112.

[95] S. D. Grimshaw and J. V. Taylor. Fast Settling Millimetre-Scale Five-Hole Probes. In *Volume 6: Ceramics, Controls, Diagnostics and Instrumentation, Education, Manufacturing Materials and Metallurgy*. American Society of Mechanical Engineers, June 2016. doi: 10.1115/gt2016-56628.

[96] P. M. Ligrani, B. A. Singer, and L. R. Baun. Spatial Resolution and Downwash Velocity Corrections for Multiple-Hole Pressure Probes in Complex Flows. *Experiments in Fluids*, 7(6):424–426, June 1989. doi: 10.1007/bf00193427.

[97] T. J. Dudzinski and L. N. Krause. Flow-direction Measurement with Fixed-position Probes. Technical report, NASA Technical Memorandum, 1969.

[98] A. L. Treaster and A. M. Yocum. The Calibration and Application of Five-hole Probes. Technical report, The Pennsylvania State University, Institute for Science and Engineering, January 1978.

[99] R. G. Dominy and H. P. Hodson. An Investigation of Factors Influencing the Calibration of 5-Hole Probes for 3-D Flow Measurements. In *Volume 1: Turbomachinery*. American Society of Mechanical Engineers, 1992. ISBN 978-0-7918-7893-4. doi: 10.1115/92-GT-216.

[100] H. Schlichting and K. Gersten. *Grenzschicht-Theorie: Mit 22 Tabellen*. Springer, Berlin and Heidelberg, 10th edition, 2006. ISBN 978-3-540-23004-5.

[101] W. Tollmien. Berechnung turbulenter Ausbreitungsvorgänge. *ZAMM - Journal of Applied Mathematics and Mechanics / Zeitschrift für Angewandte Mathematik und Mechanik*, 6(6):468–478, 1926. doi: 10.1002/zamm.19260060604.

[102] S. W. Lee and T. J. Yoon. An Investigation of Wall-proximity Effect using a Typical Large-Scale Five-Hole Probe. *KSME International Journal*, 13(3):273–285, March 1999. doi: 10.1007/bf02970486.

[103] T. Liu, J. P. Sullivan, K. Asai, C. Klein, and Y. Egami. *Pressure and Temperature Sensitive Paints*. Springer International Publishing, 2nd edition, 2021. doi: 10.1007/978-3-030-68056-5.

[104] M. M. Ardasheva, L. B. Nevskii, and G. E. Pervushin. Measurement of Pressure Distribution by Means of Indicator Coatings. *Journal of Applied Mechanics and Technical Physics*, 26(4):469–474, 1986. doi: 10.1007/bf01101626.

[105] L. J. Zhang and M. Fox. Flat Plate Film Cooling Measurement using PSP and Gas Chromatograph Techniques. In *Proceedings of the fifth ASME/JSME Joint Thermal Engineering Conference*, San Diego, CA (US), July 1999. American Society of Mechanical Engineers.

[106] L. Zhang, M. Baltz, R. Pudupatty, and M. Fox. Turbine Nozzle Film Cooling Study Using the Pressure Sensitive Paint (PSP) Technique. In *Volume 3: Heat Transfer; Electric Power; Industrial and Cogeneration*. American Society of Mechanical Engineers, June 1999. doi: 10.1115/99-gt-196.

[107] J. H. Bell, E. T. Schairer, L. A. Hand, and R. D. Mehta. Surface Pressure Measurements using Luminescent Coatings. *Annual Review of Fluid Mechanics*, 33(1):155–206, January 2001. doi: 10.1146/annurev.fluid.33.1.155.

[108] R. Goldstein, R. Rask, and E. Eckert. Film Cooling with Helium Injection into an Incompressible Air Flow. *International Journal of Heat and Mass Transfer*, 9(12):1341–1350, December 1966. doi: 10.1016/0017-9310(66)90132-3.

[109] W. Burns and J. Stollery. The Influence of Foreign Gas Injection and Slot Geometry on Film Cooling Effectiveness. *International Journal of Heat and Mass Transfer*, 12(8):935–951, August 1969. doi: 10.1016/0017-9310(69)90156-2.

[110] E. Schmidt. Verdunstung und Wärmeübergang. *Gesundheits-Ingenieur*, 52:525, 1929. doi: 10.1016/0017-9310(76)90003-x.

[111] D. R. Pedersen, E. R. G. Eckert, and R. J. Goldstein. Film Cooling With Large Density Differences Between the Mainstream and the Secondary Fluid Measured by the Heat-Mass Transfer Analogy. *Journal of Heat Transfer*, 99(4):620–627, November 1977. doi: 10.1115/1.3450752.

[112] W. M. Kays, M. E. Crawford, and B. Weigand. *Convective Heat and Mass Transfer*. McGraw-Hill Higher Education, Boston, 4th edition, 2005. ISBN 0071238298.

[113] T. V. Jones. Theory for the Use of Foreign Gas in Simulating Film Cooling. *International Journal of Heat and Fluid Flow*, 20(3):349–354, June 1999. doi: 10.1016/s0142-727x(99)00017-x.

[114] A. Javed, N. Rajan, and D. Chakraborty. Behaviour of turbulent Prandtl/Schmidt number in compressible mixing layer. *Proceedings of the Institution of Mechanical Engineers, Part G: Journal of Aerospace Engineering*, 229(7):1349–1359, August 2014. doi: 10.1177/0954410014547441.

[115] J.-C. Han and A. P. Rallabandi. Turbine Blade Film Cooling Using PSP Technique. *Frontiers in Heat and Mass Transfer*, 1(1), June 2010. doi: 10.5098/hmt.v1.1.3001.

[116] D. Charbonnier, P. Ott, J. Jonsson, F. Cottier, and T. Köbke. Experimental and Numerical Study of the Thermal Performance of a Film Cooled Turbine Platform. *ASME Turbo Expo 2009: Power for Land, Sea, and Air*, Volume 3: Heat Transfer, Parts A and B(GT2009-60306):1027–1038, 2009.

[117] D. Mendoza. An analysis of CCD camera noise and its effect on pressure sensitive paint instrumentation system signal-to-noise ratio. In *ICIASF'97 Record. International Congress on Instrumentation in Aerospace Simulation Facilities*. IEEE, 1997. doi: 10.1109/iciasf.1997.644647.

[118] J. H. Bell and B. G. McLachlan. Image Registration for Pressure-sensitive Paint Applications. *Experiments in Fluids*, 22(1):78–86, 1996. ISSN 0723-4864. doi: 10.1007/BF01893308.

[119] J. P. Hubner and B. F. Carroll. Application of Dual Sorption Theory to Pressure-Sensitive Paints. *AIAA Journal*, 35(11):1790–1792, November 1997. doi: 10.2514/2.32.

[120] R. Pawluczyk. Holographic Diffusers. In R. A. Lessard, editor, *SPIE Proceedings*. SPIE, January 1994. doi: 10.1117/12.166350.

[121] C. Lüdecke and D. Lüdecke. *Thermodynamik*. Springer Berlin Heidelberg, 2020. doi: 10.1007/978-3-662-58800-0.

[122] P. R. N. Childs, J. R. Greenwood, and C. A. Long. Heat Flux Measurement Techniques. *Proceedings of the Institution of Mechanical Engineers, Part C: Journal of Mechanical Engineering Science*, 213 (7):655–677, July 1999. doi: 10.1177/095440629921300702.

[123] G. M. Carlomagno and G. Cardone. Infrared Thermography for Convective Heat Transfer Measurements. *Experiments in Fluids*, 49(6):1187–1218, August 2010. doi: 10.1007/s00348-010-0912-2.

[124] T. Astarita, G. Cardone, and G. Carlomagno. Infrared Thermography: An Optical Method in Heat Transfer and Fluid Flow Visualisation. *Optics and Lasers in Engineering*, 44(3-4):261–281, March 2006. doi: 10.1016/j.optlaseng.2005.04.006.

[125] B. Laveau. *Investigation of the Heat Transfer Patterns on the Vane Endwall of an Axial Turbine*. PhD thesis, ETH Zurich, 2014.

[126] E. Gartenberg and A. S. Roberts. Twenty-five Years of Aerodynamic Research with Infrared Imaging. *Journal of Aircraft*, 29(2):161–171, March 1992. doi: 10.2514/3.46140.

[127] G. Gaussorgues. *Infrared Thermography*. Springer Netherlands, 1994. doi: 10.1007/978-94-011-0711-2.

[128] W. Minkina and D. Klecha. Atmospheric Transmission Coefficient Modelling in the Infrared for Thermovision Measurements. *Journal of Sensors and Sensor Systems*, 5(1):17–23, January 2016. doi: 10.5194/jsss-5-17-2016.

[129] A. Adibekyan, E. Kononogova, C. Monte, and J. Hollandt. High-Accuracy Emissivity Data on the Coatings Nextel 811-21, Herberts 1534, Aeroglaze Z306 and Acktar Fractal Black. *International Journal of Thermophysics*, 38(6), April 2017. doi: 10.1007/s10765-017-2212-z.

[130] H. Choe, W. M. Kays, and R. J. Moffat. Turbulent Boundary Layer on a Full-Coverage Film-Cooled Surface: An Experimental Heat Transfer Study with Normal Injection. Technical Report NASA-CR-2642, NASA, 1976.

[131] M. Gritsch, S. Baldauf, M. Martiny, A. Schulz, and S. Wittig. The Superposition Approach to Local Heat Transfer Coefficients in High Density Ratio Film Cooling Flows. In *Volume 3: Heat Transfer; Electric Power; Industrial and Cogeneration*. American Society of Mechanical Engineers, 1999. ISBN 978-0-7918-7860-6. doi: 10.1115/99-GT-168.

[132] C. Y. Yap, C. K. Chua, Z. L. Dong, Z. H. Liu, D. Q. Zhang, L. E. Loh, and S. L. Sing. Review of Selective Laser Melting: Materials and Applications. *Applied Physics Reviews*, 2(4):041101, December 2015. doi: 10.1063/1.4935926.

[133] J. G. Kaufman. Aluminum Alloys. In *Handbook of Materials Selection*, pages 89–134. John Wiley & Sons, Inc., 2002. doi: 10.1002/9780470172551.ch4.

[134] F. R. Menter. Two-equation Eddy-viscosity Turbulence Models for Engineering Applications. *AIAA Journal*, 32(8):1598–1605, August 1994. doi: 10.2514/3.12149.

[135] R. Reviol, R. Franze, M. Böhle, K. Takeishi, and A. Wiedermann. Cross Flow Effects on Endwall Heat Transfer in Film-Cooled Turbine Nozzle Guide Vanes. *ASME Turbo Expo 2013: Turbine Technical Conference and Exposition*, Volume 3B: Heat Transfer(GT2013-94898), 2013. doi: 10.1115/gt2013-94898.

[136] J. P. Gostelow. *Cascade Aerodynamics*. Pergamon international library of science, technology, engineering and social studies. Pergamon Pr, Oxford, 1st edition, 1984. ISBN 978-0080204284.

[137] F. Cardarelli. *Materials Handbook*. Springer London, 2nd edition, 2008. doi: 10.1007/978-1-84628-669-8.

[138] R. Mehta and P. Bradshaw. Design Rules for Small Low Speed Wind Tunnels. *The Aeronautical Journal*, 83(827):443–453, 1979.

[139] P. E. Roach. The Generation of Nearly Isotropic Turbulence by Means of Grids. *International Journal of Heat and Fluid Flow*, 8(2):82–92, 1987. ISSN 0142727X. doi: 10.1016/0142-727X(87)90001-4.

[140] R. Mehta. The Aerodynamic Design of Blower Tunnels with Wide-angle Diffusers. *Progress in Aerospace Sciences*, 18:59–120, January 1979. doi: 10.1016/0376-0421(77)90003-3.

[141] N. T. Basse. Turbulence Intensity and the Friction Factor for Smooth- and Rough-wall Pipe Flow. *Fluids*, 2(2):30, June 2017. doi: 10.3390/fluids2020030.

[142] P. Stephan, S. Kabelac, M. Kind, D. Mewes, K. Schaber, and T. Wetzel, editors. *VDI-Wärmeatlas*. Springer Berlin Heidelberg, 2019. doi: 10.1007/978-3-662-52989-8.

[143] L. F. Moody. Friction Factors for Pipe Flow. *Journal of Fluids Engineering*, 66(8):671–678, November 1944. doi: 10.1115/1.4018140.

[144] L. Prandtl. Attaining a Steady Air Stream in Wind Tunnels. techreport, NACA Technical Memorandums, United States. National Advisory Committee for Aeronautics, October 1933.

[145] K. E. G. Wieghardt. On the Resistance of Screens. *Aeronautical Quarterly*, 4(2):186–192, August 1953. doi: 10.1017/s0001925900000871.

[146] E. M. Laws and J. L. Livesey. Flow Through Screens. *Annual Review of Fluid Mechanics*, 10(1): 247–266, 1978. ISSN 0066-4189. doi: 10.1146/annurev.fl.10.010178.001335.

[147] G. B. Schubauer, W. G. Spangenberg, and P. S. Klebanoff. Aerodynamic Characteristics of Damping Screens. Technical report, NACA Technical Notes, 1950.

[148] J. Groth and A. V. Johansson. Turbulence reduction by screens. *Journal of Fluid Mechanics*, 197: 139–155, December 1988. doi: 10.1017/s0022112088003209.

[149] J. Scheiman and J. D. Brooks. Comparison of Experimental and Theoretical Turbulence Reduction from Screens, Honeycomb, and Honeycomb-screen Combinations. *Journal of Aircraft*, 18(8): 638–643, 1981. ISSN 0021-8669. doi: 10.2514/3.57538.

[150] J. B. Barlow, W. H. Rae, and A. Pope. *Low-Speed Wind Tunnel Testing*. Wiley, New York and Weinheim, 3rd edition, 1999. ISBN 978-0-471-55774-6. URL `http://www.loc.gov/catdir/description/wiley031/98028891.html`.

[151] T. Kurian and J. H. M. Fransson. Grid-generated Turbulence Revisited. *Fluid Dynamics Research*, 41(2):021403, March 2009. doi: 10.1088/0169-5983/41/2/021403.

[152] M. S. Uberoi. Effect of Grid Geometry on Turbulence Decay. *Physics of Fluids*, 10(6):1216, 1967. doi: 10.1063/1.1762265.

[153] H. E. Cekli and W. van de Water. Tailoring Turbulence with an Active Grid. *Experiments in Fluids*, 49(2):409–416, January 2010. doi: 10.1007/s00348-009-0812-5.

[154] M. Gad-El-Hak and S. Corrsin. Measurements of the Nearly Isotropic Turbulence behind a Uniform Jet Grid. *Journal of Fluid Mechanics*, 62(1):115–143, January 1974. doi: 10.1017/s0022112074000607.

[155] G. Comte-Bellot and S. Corrsin. The Use of a Contraction to Improve the Isotropy of Grid-Generated Turbulence. *Journal of Fluid Mechanics*, 25(4):657–682, August 1966. doi: 10.1017/s0022112066000338.

[156] M. S. Mohamed and J. C. Larue. The Decay Power Law in Grid-generated Turbulence. *Journal of Fluid Mechanics*, 219(-1):195, October 1990. doi: 10.1017/s0022112090002919.

[157] I. Bajsic, J. Kutin, and T. Zagar. Response Time of a Pressure Measurement System with a Connecting Tube. *Instrumentation Science & Technology*, 35(4):399–409, July 2007. doi: 10.1080/10739140701436579.

[158] V. Schuler and J. Twrdek. *Praxiswissen Schweißtechnik*. Springer Fachmedien Wiesbaden, 2019. doi: 10.1007/978-3-658-24266-4.

[159] C. Gebhardt. *Praxisbuch FEM mit ANSYS Workbench: Einführung in die lineare und nichtlineare Mechanik*. Hanser, München, 2nd edition, 2014. ISBN 978-3446439191.

[160] Forschungskuratorium Maschinenbau. *Rechnerischer Festigkeitsnachweis für Maschinenbauteile*. Verband Deutscher Maschinen- und Anlagenbau, 7th edition, 2021. ISBN 9783816307433.

[161] W. Steinhilper and B. Sauer. *Konstruktionselemente des Maschinenbaus 1: Grundlagen der Berechnung und Gestaltung von Maschinenelementen*. Springer, 2006. ISBN 9783540220336.

[162] J. Bear. *Modeling Phenomena of Flow and Transport in Porous Media*. Springer International Publishing, 2018. doi: 10.1007/978-3-319-72826-1.

[163] J. Bear. *Dynamics of Fluids in Porous Media*. Dover, 1988. ISBN 0486656756.

[164] H. Werschnik, T. Ostrowski, J. Hilgert, M. Schneider, and H.-P. Schiffer. Infrared Thermography to Study Endwall Cooling and Heat Transfer in Turbine Stator Vane Passages using the Auxiliary Wall Method and Comparison to Numerical Simulations. *Quantitative InfraRed Thermography Journal*, 12(2):219–236, 2015. ISSN 1768-6733. doi: 10.1080/17686733.2015.1066135.

[165] S. L. Gazzini. *Infrared Thermography for Endwall Heat Transfer Measurements*. PhD thesis, ETH Zürich, 2017.

[166] S. V. Patankar. *Numerical Heat Transfer and Fluid Flow*. McGraw-Hill Book Company, 1980. doi: 10.1201/9781482234213.

[167] K. Gupta, R. F. Laubscher, and N. K. Jain. *Advanced Gear Manufacturing and Finishing*. Elsevier Science & Technology Books, 2017. ISBN 9780128044605.

[168] J.-P. Celis, H. Czichos, R. S. Cowan, K.-H. Habig, and A. Fischer. *Tribologie-Handbuch Tribometrie, Tribomaterialien, Tribotechnik*. Springer Vieweg. in Springer Fachmedien Wiesbaden GmbH, 2015. ISBN 9783834822369.

[169] H. Wittel, D. Muhs, D. Jannasch, and J. Voßiek. *Roloff/Matek Maschinenelemente*. Springer Vieweg, 22nd edition, 2015. ISBN 9783658090814.

[170] G. Natsui, Z. Little, J. S. Kapat, J. E. Dees, and G. Laskowski. A Detailed Uncertainty Analysis of Adiabatic Film Cooling Effectiveness Measurements Using Pressure-Sensitive Paint. *Journal of Turbomachinery*, 138(8), mar 2016. doi: 10.1115/1.4032674.

[171] F. Vinnemeier, L. Simon, and W. Koschel. Correction Method for the Head Geometry Influence of a Five-Hole Pressure Probe on the Measurement Results. *Technisches Messen*, 57:296–303, 1990.

List of Figures

List of Tables

Measurement Uncertainty

Since this work focuses on the development of the new annular sector test rig, a distinction would have to be made between the linear and annular cascade for a detailed evaluation of all measurement uncertainties and their underlying contributors since the measurement setup has been changed for the new test rig. This applies in particular to the IR measurement setup, where the measurement module has been completely redesigned. For this reason, the evaluation of the measurement uncertainties in the present context is primarily intended to identify the main contributors to the uncertainties of the individual measurement methods.

The following table A.1 lists the pressure sensors used. All differential pressure sensors were previously calibrated with a pressure calibrator to compensate for offsets and non-linearities in the measurement chain.

Table A.1: Overview of pressure sensors

Group	**Type**	**Span** /mbar	**Total Error** /%	**Primary application**
MEAS D5100	Differential	0…350	±1	Endwall pressure taps
MEAS D5100	Differential	0…1000	±1	Five-hole probe (outlet)
MEAS D5100	Differential	0…2000	±1	Orifices coolant flow
AMS 5812	Differential	−55…55	±1.5	Five-hole probe (inlet)
AMS 5812	Differential	0…21	±1.5	Prandtl probe (inlet)
Wika A-10	Absolut	0…2500	±1	Fluid properties (main flow)
Cerabar M	Absolut	0…10 000	±0.6	Fluid properties (coolant)

A.1 Film Cooling Effectiveness

In an uncertainty analysis of the PSP measurement technique for the determination of the film cooling effectiveness, two aspects have to be distinguished: On the one hand, uncertainty arises from the experimental setup and the error contributions of individual components in the measurement chain. A detailed breakdown of these errors can be found in a study by Natsui et al. [170]. In addition, uncertainties of a more fundamental nature arise from the application of the heat-mass transfer analogy since a unity turbulent Lewis number is usually assumed when applying PSP in the context of film cooling measurements. Addressing the validity of this assumption is beyond the scope of this work. However, the experimental uncertainties that are encountered in the concrete application of the measurement technique in the test rig will be explained in the following.

Temperature-related errors The luminescence response of the paint is not only a function of pressure but also of temperature. To account for the influence of the latter in the measurement, the color is therefore calibrated for a range of temperatures as described in Chapter 3.4.2. In the subsequent measurement, an individual calibration curve can then be interpolated for the temperature relevant at the time of measurement.

Temperature-related measurement errors due to erroneous temperature readings can already occur during calibration. They are not only dependent on the individual measurement error of the temperature sensors used but can also result from the fact that the effective temperature at the surface of the calibration body deviates from the temperature at the location of the temperature measurement. However, in the present case, this influence is minimized by using a highly conductive copper plate and by placing the thermocouple as close to the surface as possible.

Consequently, an error in the determination of the temperature at the time of measurement also contributes to the overall measurement uncertainty. Here, a distinction must be made between a global measurement error and local deviations. The former is mainly caused by the erroneous determination of the main flow temperature. Furthermore, it must be taken into account that the temperature level can change after the test rig is switched off, resulting in a temperature offset between the wind-on and the reference image. However, in the present case, this offset can be determined by the thermocouples installed close to the endwall surface. In the subsequent evaluation, the recorded reference intensities are corrected to the temperature level of the wind-on image.

Local temperature deviations result from the influence of the recovery temperature at the evaluation point, especially under high-speed conditions. In principle, this can be assessed iteratively using the pressure distribution obtained from the first iteration of the PSP evaluation. However, the associated intensity changes occur to the same extent for the injection of air and foreign gas, i.e., the determination of partial pressures is equally biased. Accordingly, the calculation of η_{ad} is not affected.

Another uncertainty arises from temperature deviations between the main flow and the coolant, and to an even greater extent, from deviations between the air and foreign gas injection. The main challenge here is to compensate for the temperature drop that occurs when high-pressure cylinder gas

is depressurized to the test rig pressure level. For this reason, secondary air heaters were integrated into the test rig to continuously monitor and readjust the temperature of the coolant. Here, too, uncertainties appear in the form of erroneous temperature readings.

In the measurement setup of the linear cascade, the measured deviation between each coolant and the main flow could be limited to less than 1 K. In view of the measurements to be carried out in the annular cascade, it can be assumed that this value can be further reduced by using the additional fast-responding secondary air heater that is installed just upstream of the purge slot plenum. Irrespective of this, it is, in principle, possible to implement an iterative correction that utilizes the local mixing temperature that can be obtained in the first iteration from the film cooling effectiveness values.

Displacement-related errors While a deformation of the endwall and the vane can be ruled out in the current measurement setup, the displacement of the test rig between the wind-on and reference state is a major source of error since it would result in an erroneous relation of the local intensity values. A subsequent correction using image registration algorithms is only useful if the offset is either very small or perspective influences are of minor importance. In the present case, a purely post-correction would be insufficient due to the three-dimensional expansion of the contoured endwall. The implementation of the industrial robot enables precise re-positioning of the camera. In this process, the displacement of the test rig relative to a reference state is determined before the final image is recorded. This is done by tracking the pressure taps visible on the endwall and transmitting the position offset to the industrial robot. For the linear cascade, the residual displacement found in post-processing was less than 1 px and could be compensated by a simple image transformation.

In addition, there is a risk that the displacement of the test stand will also locally change the intensity of the excitation unless the position of the excitation source is readjusted. In the present case, the UV lights are attached to the probe traversing units that are mounted to the test section. Consequently, the relative position of the UV lights remained virtually unchanged even for large test rig displacements.

Further sources of error Uncertainties in both calibration and subsequent measurement arise from the photodetector noise of the sCMOS camera. While dark current and pattern noise is addressed by the black image, the effects of random noise can be mitigated by averaging a sequence of images, with the signal-to-noise ratio increasing in proportion to the square root of the number of images. Regarding the influence of the pressure sensors used in the calibration, a systematic error would result in a horizontal shift of the calibration curves. For low partial pressures, corresponding to high values of η_{ad}, the associated uncertainty increases. Another source of error is related to the influence on the excitation intensity, as the luminance of the excitation source may be unstable. To minimize these fluctuations, which are mainly caused by self-heating, the UV-LED lights are water-cooled. The aging of the paint and the degradation due to continuous excitation must also be taken into account. In the present case, calibration and measurement are performed within a few days. Since the total excitation time for the whole measurement campaign adds up to only about 2 hours, no negative effects are to be expected, according to the aforementioned study by Natsui et al. [170].

A.2 Heat Transfer Measurements

The measurement uncertainties associated with heat transfer investigations can be divided into two main groups: First, there are uncertainties in the application of IR thermography. According to the manufacturer, the IR camera has a measurement accuracy of 2 K within the measurement range. However, it should be noted that this is a systematic measurement error that can be compensated by in-situ calibration. The thermal resolution of the camera is much higher and amounts to 0.04 K. In addition to these measurement errors, the consideration of the radiometric chain has a significant impact on the validity of the IR measurement since the emissivity of the surface and the transmission properties of the transmission path affect the temperature reading. Because the thermocouples could not be used for in-situ calibration of the linear measurement module, only the transmission properties of the IR window that were determined ex-situ could be considered. As a result, the absolute temperature level could not be reliably measured. The measurement module for the annular cascade was therefore adapted (see Chapter 5.5.5) so that future measurements can be calibrated in situ.

The application of the auxiliary wall method involves measurement uncertainties related to the validity of both thermal and geometric assumptions: Since the local wall heat flux is determined by the conductive heat transport in the auxiliary wall, deviations in the thermal properties of the auxiliary wall contribute to the total uncertainty. This includes the thermal conductivity of the coating material, which is assumed to be isotropic. Second, there is uncertainty in the local coating thickness. This is considered to be constant because the coating was milled to the nominal dimension using a CNC milling machine with an accuracy of ≤ 0.01 mm, which corresponds to 2 % of the nominal layer thickness. To validate this assumption, a laser profilometer measurement of the coating thickness on the annular module is planned. With respect to the shortcomings of the linear measurement module described in Chapter 4.6.1, the largest contributor to the measurement uncertainty is the local mismatch of the backside temperature of the auxiliary wall. Due to the reduced cooling water flow, the downstream parts of the passage could not be sufficiently cooled. As a result, the heat transfer coefficients were not meaningful because the local heat fluxes were significantly overestimated. The new measurement module solves this problem with a new sealing concept. In addition, to further reduce the measurement uncertainty, the actual wall heat fluxes can be determined using the CHT model already used for the dimensioning. The approximated temperature distribution on the flow side can then be replaced by the temperature data from the IR measurement.

A.3 Five-Hole Probe Measurements

A fundamental concern with five-hole probe measurements is blockage of the flow channel so that the flow field being measured is affected by the presence of the probe. The use of an L-shaped probe, as featured here, moves the blockage downstream, reducing the effects of blockage in the measurement

plane. An influence on the flow can also be expected if the probe is used in close proximity to a wall. For this reason, a distance of approximately two probe head diameters is always maintained during measurements, which also protects the probe from damage due to wall contact.

Another measurement error arises from the fact that the peripheral holes are located at different positions in the measurement plane. The magnitude of this error depends on the size of the probe head in relation to the pressure gradients present at the measurement location. To address this error, the pressures measured at the peripheral holes can be interpolated to the position of the central hole in post-processing, as described, e.g., in a study by Vinnemeier et al. [171].

Because the probe pressures are recorded with the pressure sensors mentioned above, the errors associated with the pressure reading also apply here. While systematic measurement errors are compensated by calibrating the pressure sensors, readout noise is minimized by averaging 50 individual measurements at each measurement point.

Benchmark Results

Table B.1: Single results of selected base geometry variants

Variant	ΔF_j/%				$\Delta Ma_{i,\mathrm{In}}$/%				$\Delta Ma_{i,\mathrm{Le}}$/%				$\Delta Ma_{i,\mathrm{Out}}$/%				$\Delta \dot{m}_i$/%				$\Delta \beta_j$/°			
	N1	N2	N3	N4	P-2	P-1	P+1	P+2	P-2	P-1	P+1	P+2	P-2	P-1	P+1	P+2	P-2	P-1	P+1	P+2	N1	N2	N3	N4
BA-IN	6.0	1.2	-1.6	-5.6	-1.0	0.0	0.2	1.7	8.1	0.3	-1.1	0.3	8.7	4.0	-5.9	2.9	7.0	1.5	-1.4	-3.6	0.2	-0.7	-0.4	1.1
BA-01	8.8	2.7	-3.9	-7.6	-0.2	0.5	0.0	2.0	13.9	2.8	-3.0	5.6	16.9	7.7	9.6	49.4	12.8	4.4	-4.4	0.7	-1.3	-2.7	-1.6	2.4
BA-02	5.4	0.6	-1.1	-2.9	-0.6	0.4	0.8	2.6	8.1	0.0	0.4	3.2	6.1	2.4	-1.9	5.5	7.2	1.7	-0.1	-0.7	1.0	0.5	1.1	2.5
BA-03	4.8	-0.1	-1.5	-1.6	-0.7	0.3	0.8	2.6	8.1	0.1	0.9	4.2	4.2	0.4	-0.5	9.1	7.5	1.8	0.4	0.5	0.9	0.5	1.4	2.8
BA-04	4.5	-0.4	-2.2	-1.8	-1.0	0.0	0.4	2.3	8.0	-0.4	0.4	4.3	3.8	-0.1	0.5	11.3	7.5	1.5	0.1	0.6	0.4	0.1	1.0	2.5
BA-05	4.5	-0.4	-2.2	-1.9	-1.0	0.0	0.4	2.3	8.3	-0.2	0.6	4.5	4.0	0.0	0.9	13.1	7.8	1.5	0.0	0.8	0.4	0.0	1.0	2.6
BA-06	4.5	-0.4	-2.2	-1.8	-1.0	0.0	0.4	2.3	8.3	-0.2	0.5	4.5	3.7	-0.1	0.4	11.7	7.7	1.6	0.1	0.7	0.4	0.0	1.0	2.5
BA-07	4.5	-0.5	-2.2	-1.8	-1.0	0.0	0.4	2.3	8.1	-0.4	0.6	4.3	3.9	-0.1	0.3	11.3	7.6	1.4	0.1	0.6	0.4	0.1	1.0	2.5
BA-08	4.4	-0.4	-2.2	-1.8	-1.0	0.0	0.5	2.3	8.0	-0.3	0.6	4.3	3.6	-0.3	0.2	11.0	7.3	1.4	0.0	0.6	0.5	0.1	1.1	2.6
BA-09	4.5	-0.5	-2.2	-1.8	-1.0	0.0	0.4	2.3	8.1	-0.2	0.6	4.5	4.0	-0.1	0.6	11.5	7.6	1.5	0.1	0.7	0.4	0.1	1.0	2.6
BA-10	4.4	-0.4	-2.2	-1.8	-1.0	0.0	0.4	2.3	8.3	-0.1	0.8	4.3	3.8	-0.2	-0.3	-2.6	7.6	1.5	0.1	0.3	0.4	0.0	0.9	2.4

Table B.2: Single results of selected baffle geometry variants with $x_{ex} = 300\,mm$

Variant	$\Delta F_j/\%$				$\Delta Ma_{i,In}/\%$				$\Delta Ma_{i,Le}/\%$				$\Delta Ma_{i,Out}/\%$				$\Delta \dot{m}_i/\%$				$\Delta\beta_j/^\circ$			
	N1	N2	N3	N4	P-2	P-1	P+1	P+2	P-2	P-1	P+1	P+2	P-2	P-1	P+1	P+2	P-2	P-1	P+1	P+2	N1	N2	N3	N4
BAF-01	4.4	-0.4	-2.2	-1.8	-1.0	0.0	0.4	2.3	8.1	-0.1	0.6	4.4	3.7	-0.1	0.5	11.4	7.6	1.5	0.1	0.6	0.4	0.1	1.0	2.5
BAF-02	4.5	-0.4	-2.2	-1.8	-1.0	0.0	0.4	2.3	8.2	-0.3	0.9	4.6	4.1	-0.1	0.5	11.9	7.6	1.5	0.1	0.6	0.4	0.1	1.0	2.5
BAF-03	4.5	-0.4	-2.2	-1.8	-1.0	0.0	0.4	2.3	8.3	-0.3	0.4	4.4	3.6	-0.2	0.5	11.5	7.8	1.6	0.1	0.8	0.4	0.0	1.0	2.6
BAF-04	4.5	-0.5	-2.3	-1.7	-0.9	0.0	0.4	2.3	8.7	-0.1	0.7	4.6	3.7	-0.3	0.7	6.8	8.0	1.6	0.1	0.8	0.3	0.0	1.0	2.6
BAF-05	4.4	-0.6	-2.2	-1.6	-0.9	0.0	0.5	2.4	8.7	-0.1	0.7	4.7	3.5	-0.3	0.8	4.9	8.1	1.6	0.2	0.9	0.3	0.0	1.1	2.6
BAF-06	4.5	-0.4	-2.2	-1.9	-1.0	0.0	0.4	2.3	8.6	-0.3	0.7	4.3	3.7	0.0	0.0	-3.1	7.9	1.5	0.0	0.4	0.3	-0.1	0.9	2.4
BAF-07	4.5	-0.4	-2.2	-1.9	-0.9	0.0	0.4	2.3	8.4	-0.1	0.4	3.9	3.8	-0.1	-0.3	-5.8	8.0	1.6	0.0	0.3	0.2	-0.1	0.8	2.4
BAF-08	4.4	-0.5	-2.2	-1.8	-1.0	0.0	0.4	2.3	8.2	-0.2	0.6	4.3	3.9	-0.2	0.3	2.7	7.7	1.5	0.1	0.6	0.4	0.0	1.0	2.5
BAF-09	3.7	-0.2	-1.9	-1.5	-0.5	0.0	0.2	1.6	6.8	-0.1	0.4	2.3	4.0	-0.1	-0.8	-3.3	5.9	1.5	0.1	0.1	-0.9	-1.3	-0.6	0.5
BAF-10	4.6	-0.7	-2.2	-1.7	-0.4	0.1	0.2	1.5	7.8	-0.2	0.4	2.3	3.5	-0.3	-0.7	-3.9	7.2	1.4	0.2	0.1	-1.4	-1.6	-0.8	0.4
BAF-11	6.7	-0.1	-3.5	-3.0	1.6	1.0	0.0	1.2	23.9	1.9	1.0	3.4	3.1	-0.6	-0.9	-4.2	22.9	3.6	0.1	0.2	-6.1	-6.0	-3.7	-1.1

Table B.3: Single results of selected base geometry variants with modified upper bfs design

Variant	$\Delta F_j/\%$				$\Delta Ma_{i,\mathrm{In}}/\%$				$\Delta Ma_{i,\mathrm{Le}}/\%$				$\Delta Ma_{i,\mathrm{Out}}/\%$				$\Delta \dot{m}_i/\%$				$\Delta\beta_j/^\circ$			
	N1	N2	N3	N4	P-2	P-1	P+1	P+2	P-2	P-1	P+1	P+2	P-2	P-1	P+1	P+2	P-2	P-1	P+1	P+2	N1	N2	N3	N4
BA-BFS-01	3.6	-0.2	-1.9	-1.5	-0.6	0.0	0.3	1.6	6.0	-0.3	0.4	3.0	3.1	-0.3	0.7	13.2	5.3	1.3	0.1	0.8	-0.7	-1.0	-0.3	0.8
BA-BFS-02	3.6	-0.2	-1.9	-1.5	-0.7	0.0	0.3	1.6	6.2	-0.3	0.6	2.8	3.2	-0.2	0.6	5.8	5.2	1.3	0.0	0.7	-0.7	-1.0	-0.3	0.8
BA-BFS-03	3.6	-0.2	-1.9	-1.5	-0.6	0.0	0.3	1.6	6.5	-0.2	0.5	2.9	3.0	-0.2	0.3	-0.3	5.5	1.4	0.1	0.7	-0.8	-1.1	-0.4	0.7
BA-BFS-04	3.6	-0.2	-1.9	-1.5	-0.6	0.0	0.3	1.6	6.1	-0.2	0.4	2.7	3.1	-0.2	0.3	-0.2	5.3	1.3	0.0	0.6	-0.7	-1.1	-0.4	0.7

Table B.4: Single results of selected tailboard geometry variants based on geometry BA-BFS-04

Variant	ΔF_j/%				$\Delta Ma_{i,\mathrm{In}}$/%				$\Delta Ma_{i,\mathrm{Le}}$/%				$\Delta Ma_{i,\mathrm{Out}}$/%				$\Delta \dot{m}_i$/%				$\Delta\beta_j$/°			
	N1	N2	N3	N4	P-2	P-1	P+1	P+2	P-2	P-1	P+1	P+2	P-2	P-1	P+1	P+2	P-2	P-1	P+1	P+2	N1	N2	N3	N4
TB-01	10.6	-2.0	-4.3	-4.3	-0.1	0.2	0.2	1.6	9.8	-0.2	0.3	2.9	1.8	0.7	1.0	1.2	8.9	1.5	-0.3	0.5	-2.0	-2.1	-1.1	0.4
TB-02	1.6	-0.3	-0.6	-0.7	-0.5	0.0	0.3	1.7	6.7	-2.1	0.2	2.7	-0.9	0.7	1.1	1.2	5.9	-0.6	-0.3	0.5	-1.2	-0.8	-0.3	0.8
TB-03	-6.8	1.3	2.8	2.7	-1.4	-0.4	0.5	1.8	0.1	-4.0	-0.3	2.0	-3.8	0.8	1.0	1.5	-0.2	-2.3	-0.3	0.5	0.8	1.3	1.1	1.5
TB-04	-2.0	1.6	0.1	0.3	-0.9	-0.1	0.3	1.7	4.0	-1.4	0.1	2.5	2.5	0.3	0.8	0.9	3.2	0.3	-0.2	0.6	-0.1	-0.3	0.1	1.0
TB-05	2.1	0.6	-1.5	-1.2	-0.6	0.0	0.3	1.6	6.5	-0.2	0.4	3.0	3.2	0.0	0.5	0.3	5.4	1.3	-0.1	0.6	-0.8	-1.1	-0.4	0.7
FIN	-2.0	1.6	0.1	0.2	-0.9	-0.1	0.3	1.7	4.2	-1.3	0.1	2.5	3.2	0.4	0.9	0.8	3.3	0.4	-0.2	0.6	-0.1	-0.3	0.1	1.0
FIN-OP	-2.1	1.7	0.2	0.3	-0.9	-0.1	0.3	1.7	4.1	-1.4	0.1	2.4	3.3	0.4	0.9	1.0	3.2	0.3	-0.2	0.5	-0.1	-0.3	0.1	1.0
FIN-OP-FINE	-1.9	1.5	0.1	0.3	-0.9	-0.1	0.3	1.7	4.2	-1.3	0.2	2.6	3.0	0.3	0.9	1.1	3.3	0.3	-0.2	0.6	-0.2	-0.3	0.1	1.0
Linear cascade	0.7	-0.4	0.4	1.2	-2.7	-0.5	1.3	4.6	4.4	0.4	0.6	2.4	-0.8	-0.5	0.8	-1.2	3.6	0.6	0.3	1.3	0.3	0.2	0.2	1.4

Manufactured and Assembled Parts

Figure C.1: Assembled PSP calibration chamber

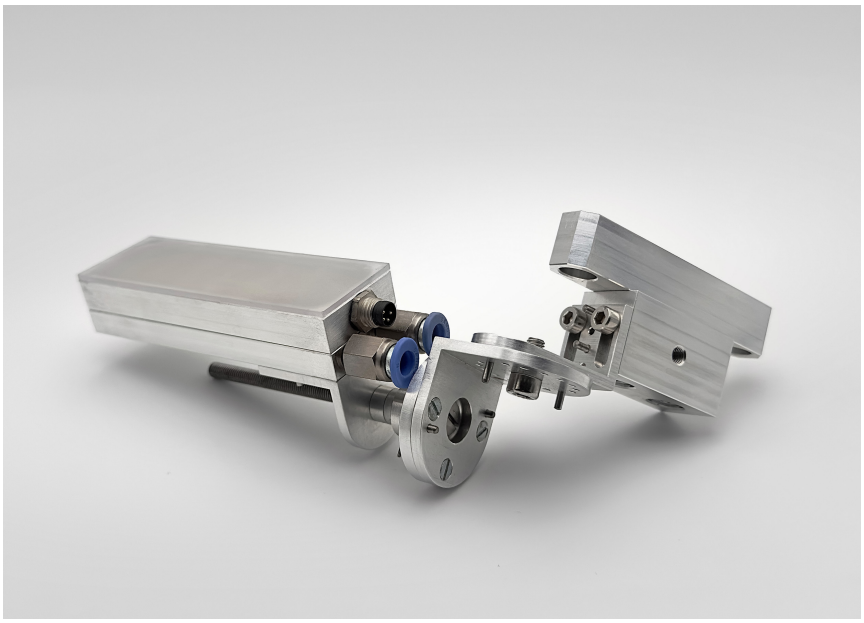

Figure C.2: Assembled UV LED floodlight

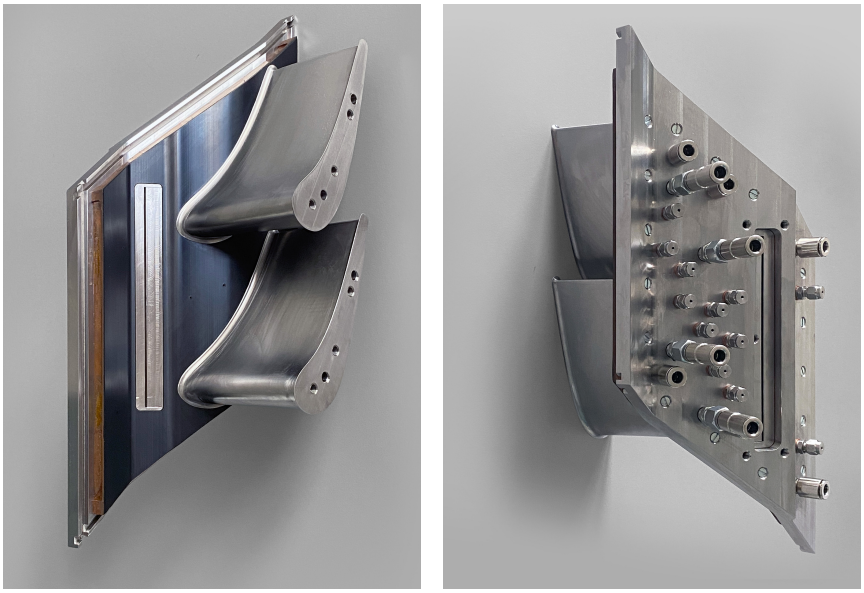

Figure C.3: Assembled heat transfer measurement module for the linear cascade

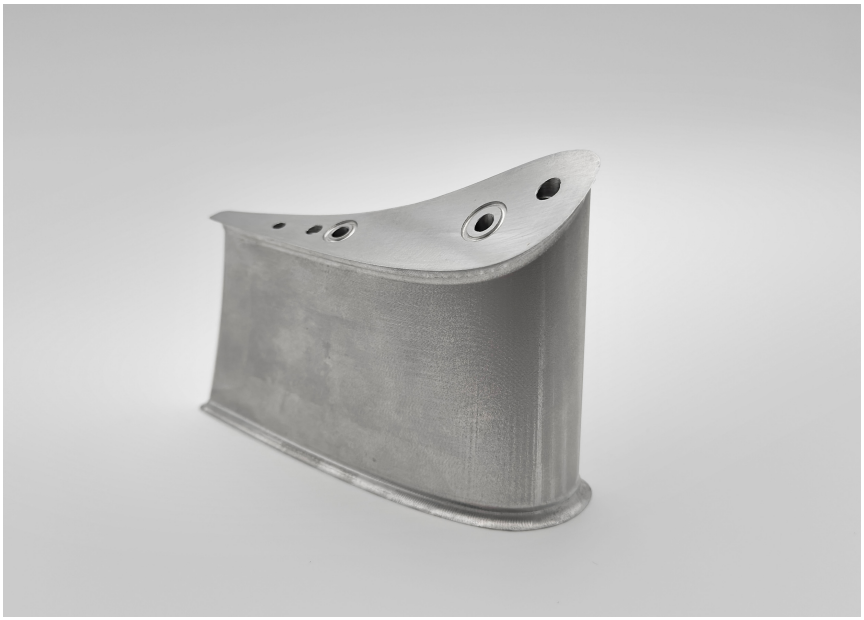

Figure C.4: Printed aluminum NGV with coolant cavity

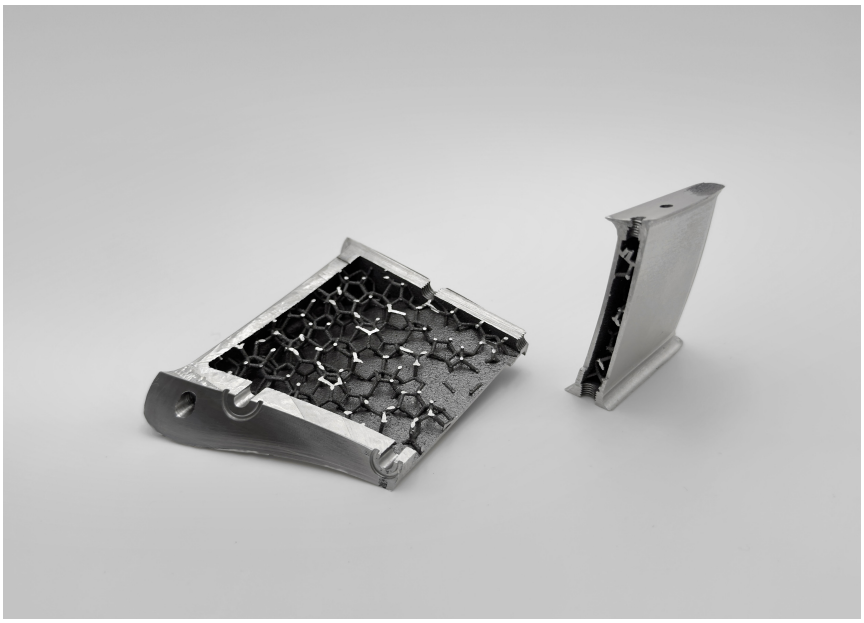

Figure C.5: Printed aluminum NGV separated for examination purposes

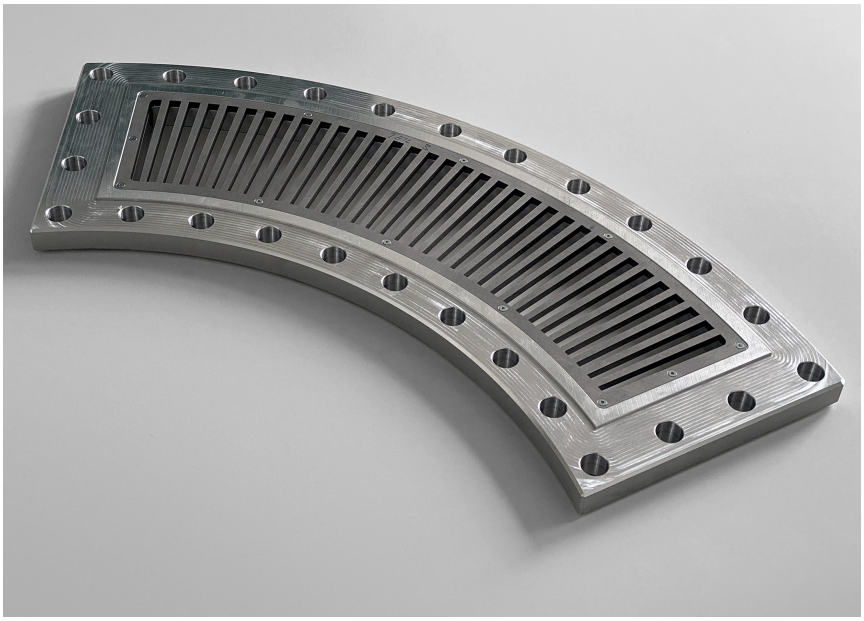

Figure C.6: Assembled annular turbulence grid

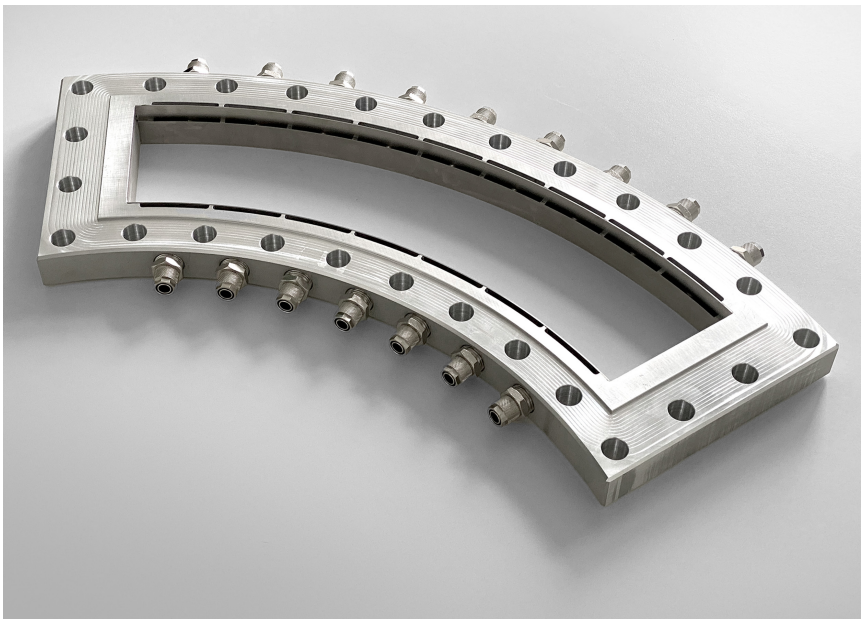

Figure C.7: Assembled annular boundary layer suction

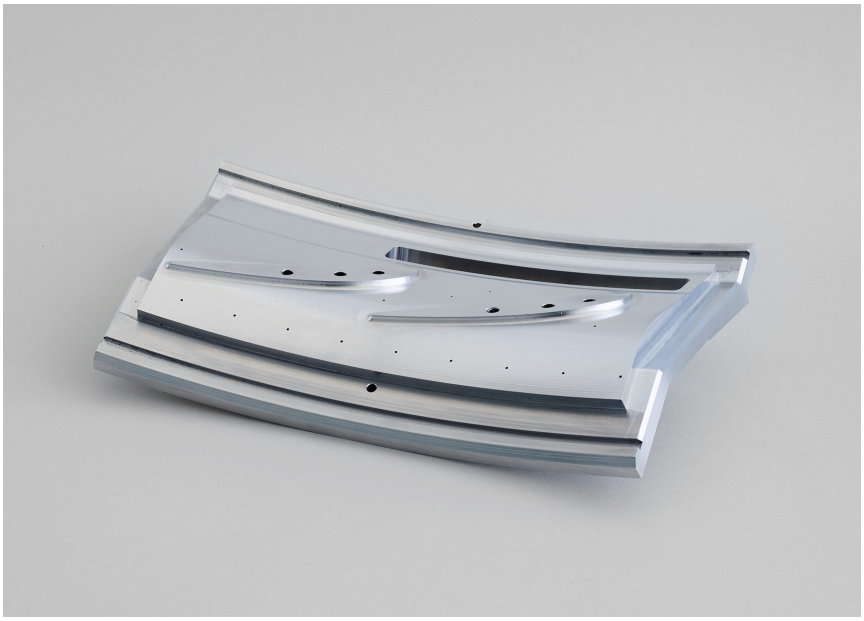

Figure C.8: Manufactured central passage endwall of the annular cascade

Figure C.9: Assembled central passage endwall with PSP coating

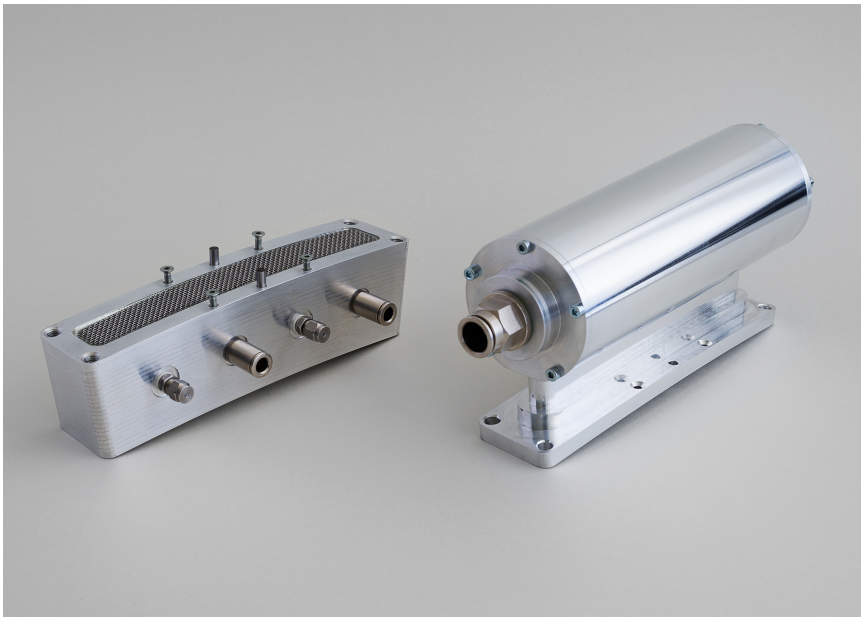

Figure C.10: Assembled purge slot plenum of the annular cascade

Figure C.11: MJP-printed purge slot inserts for the annular cascade

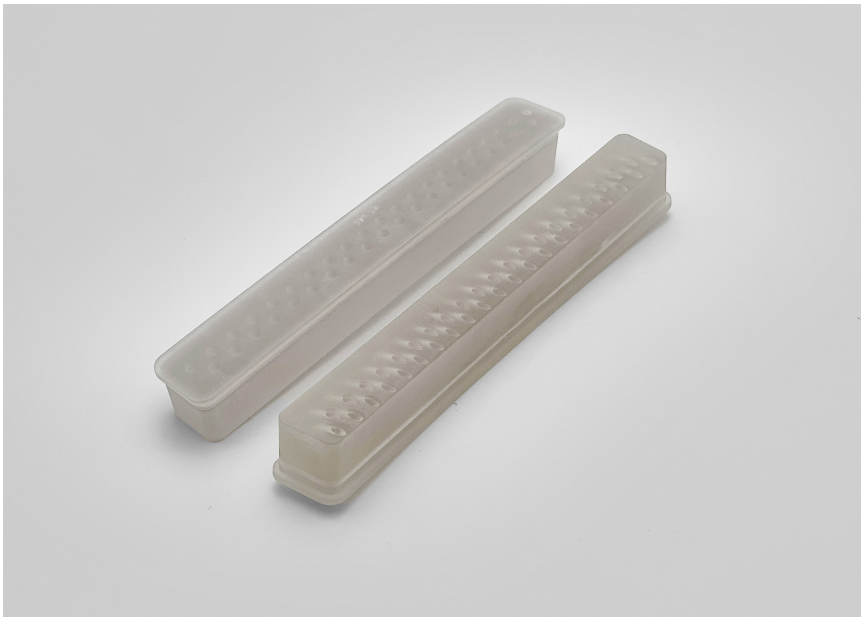

Figure C.12: MJP-printed inserts with film cooling holes for the annular cascade

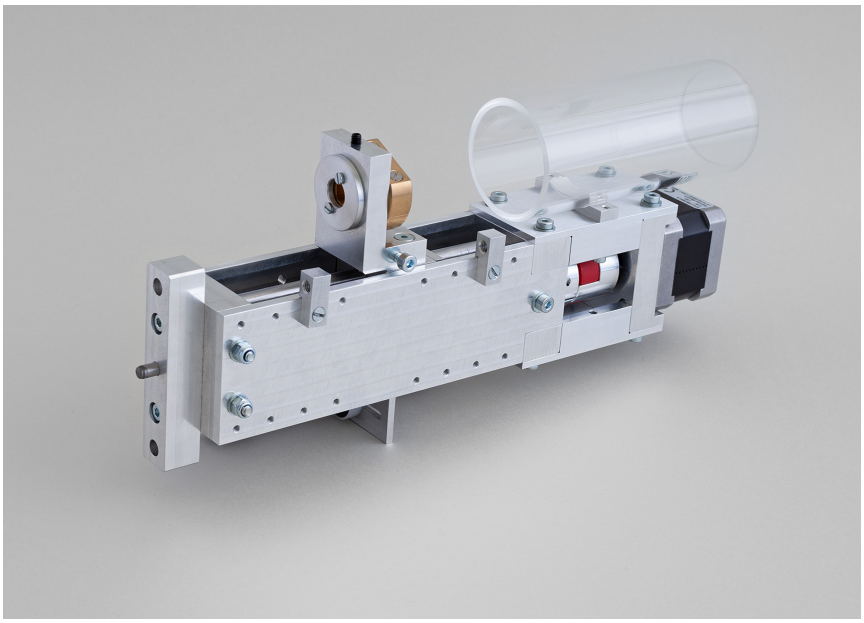

Figure C.13: Assembled radial probe traversing unit

Figure C.14: Manufactured gear rack of the circumferential probe traversing

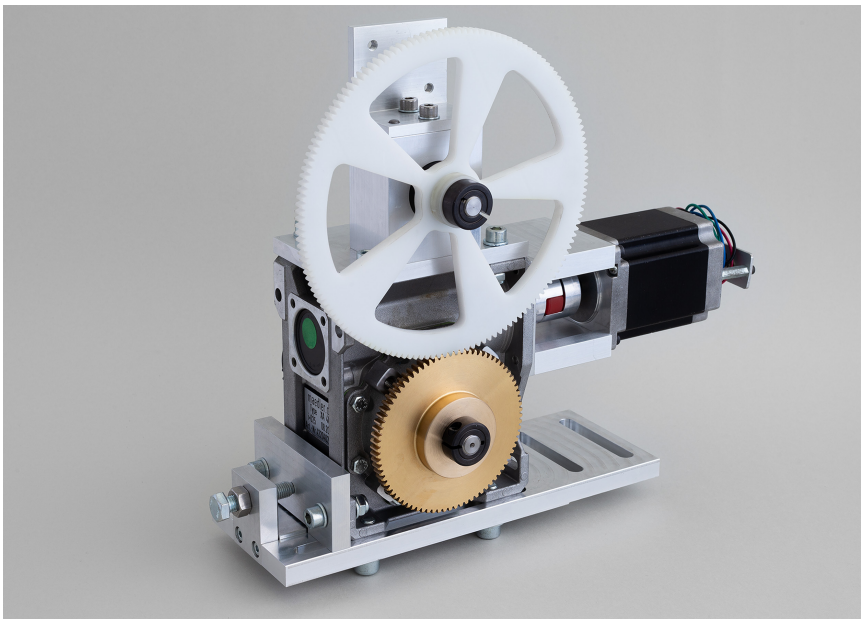

Figure C.15: Assembled drive unit of the circumferential probe traversing

Biographical Appendix

Supervised Undergraduate Theses

Sebastian Schmoll	Voruntersuchung zur Anwendbarkeit der Pressure Sensitive Paint Messtechnik an einem Heißgasprüfstand	2017
Christian Leffler	Messtechnische Optimierung einer Kalibriervorrichtung für Fünflochsonden unter Verwendung von 3D-Druckverfahren	2019
Sebastian Schmoll	Auslegung und Implementierung eines Massenstromzählers in die Grenzschichtabsaugung eines Heißgasprüfstandes	2019
Christoph Pinger	Messtechnische Optimierung einer Freifeldmessung zur Bestimmung von Strömungsablösungen in einer Windkanaldüse mittels Fünflochsonde	2019
Yannick Mansky	Experimentelle Untersuchung zu den Einflüssen von Casing Treatment auf die Sekundärströmungen eines Verdichterprofils	2019
Gregor Volk	Untersuchung des natürlichen und erzwungenen laminar-turbulenten Grenzschichtumschlags mithilfe von Infrarot-Thermografie	2020
Benedikt Rauber	Entwicklung eines Algorithmus zur projektiven Transformation von Bilddaten in den dreidimensionalen Raum	2020

Patrick Lindner	Entwicklung einer kompakten motorischen Fokusverstellung	2020
Maximilian Kölzer	Entwicklung und Erprobung von Mehrlochsonden unter Verwendung von Edelstahl-Kapillaren	2020
Gregor Kuhlbusch, Jonas Krautkrämer	Externe Kühlung in Gasturbinen – Überblick über die Arten und Anwendungsgebiete sowie Ansätze zur experimentellen Untersuchung	2020
Christina Lignowski	Numerische Untersuchung der parametrischen Randbedingungen im Rahmen der Hilfswandmethode zur Bestimmung von Wärmeübergängen	2021
Christian Fuchs	Konzepterstellung und Konstruktion eines gekrümmten Messmoduls zur Bestimmung der Wärmebelastung einer Turbinenseitenwand bei Leckagespalt-Ausblasung	2022
Moritz Klappenberger	Untersuchung des Einflusses passiver Strömungselemente auf den Strömungsabriss eines NACA-Profils mittels IR-Thermografie und Particle Image Velocimetry (PIV)	2022
Prinon Chowdhury	Numerische Untersuchung des Einflusses einer Seitenwandkonturierung und Schaufelfußverrundung auf die Sekundärströmung einer hochbelasteten Turbinenschaufel	2022
Tim Ettrich	Numerische Untersuchung der Filmkühleffektivität und Wärmebelastung einer Turbinenschaufel bei Filmkühlung durch Leckagespalt-Ausblasung	2023

Own Publications

A. Baum, **C. Landfester**, C. Berger and M. Böhle (2017). A Critical Comparison of Numerical and Experimental Results for the Examination of a Cascade Consisting of NACA 65-010 1% Profiles. *Fluids Engineering Division Summer Meeting 2017 (FEDSM)*, (V01AT03A020).

G. Müller, **C. Landfester**, R. Krewinkel and M. Böhle (2018). COOREFLEX-turbo 3.3.5: Untersuchung von Krümmungseinflüssen filmgekühlter Schaufelsegmente einer Industriegasturbine in einem Heißgasprüfstand. *Schlussbericht: 01.10.2015-31.03.2018*.

G. Müller, **C. Landfester**, M. Böhle and R. Krewinkel (2019). Turbine Vane Endwall Film Cooling Effectiveness of Different Purge Slot Configurations in a Linear Cascade. *ASME Turbo Expo 2019: Turbomachinery Technical Conference and Exposition*, Volume 5B: Heat Transfer, (GT2019-90236).

C. Landfester, G. Müller, M. Böhle and R. Krewinkel (2019). Aerodynamic Effects of Turbine Vane Endwall Film Cooling for Different Purge Slot Configurations in a Linear Cascade. *International Gas Turbine Conference 2019 (IGTC)*, (IGTC-201-60).

G. Müller, **C. Landfester**, M. Böhle and R. Krewinkel (2020). Turbine Vane Endwall Film Cooling Effectiveness of Different Purge Slot Configurations in a Linear Cascade. *Journal of Turbomachinery*, 142(3):031008.

C. Landfester, G. Müller, M. Böhle and C. Domnick (2021). Endwall Film Cooling Effectiveness for Different Purge Slot Configurations in a Contoured Endwall Nozzle Guide Vane Stage. *14th European Conference on Turbomachinery Fluid Dynamics and Thermodynamics 2021*, (ETC2021-654). European Turbomachinery Society.

C. Landfester, G. Müller, R. Krewinkel, C. Domnick and M. Böhle (2021). Comparison of Film Cooling Performance for Different Purge Slot Configurations in a Cylindrical and State-of-the-Art Nozzle Guide Vane. In *ASME Turbo Expo 2021: Turbomachinery Technical Conference and Exposition*, Volume 5B: Heat Transfer, (GT2021-59229).

C. Landfester, G. Müller, R. Krewinkel, C. Domnick and M. Böhle (2021). Comparison of Film Cooling Performance for Different Purge Slot Configurations in a Cylindrical and State-of-the-Art Nozzle Guide Vane. *Journal of Turbomachinery*, 144(3):031014

S. Schukmann, **C. Landfester** and M. Böhle (2022). Investigation of Vortex-Generator Induced Flow Structures on a Flat Plate using IR Thermography, Particle Image Velocimetry and Oil Flow Visualization. *International Conference on Fan Noise, Aerodynamics, Applications and Systems 2022 (FAN)*

Curriculum Vitae

Education

05/2014 – 01/2017	Master of Science in Industrial Engineering and Management at University of Kaiserslautern
04/2016 – 10/2016	Stay abroad at Jianghan University Wuhan, China
10/2008 – 04/2014	Bachelor of Science in Industrial Engineering and Management at University of Kaiserslautern
08/2005 – 07/2008	Apprenticeship as media designer for digital and print media at Moog, Moog & Morgenstern, Koblenz
2005	Abitur at Wilhelm-Remy-Gymnasium, Bendorf

Work Experience

02/2017 – today	Research assistant at the Institute of Fluid Mechanics and Turbomachinery, University of Kaiserslautern
01/2011 – 01/2017	Student assistant at the Dean's Office, Faculty of Business Studies and Economics, University of Kaiserslautern